School of Civil and Mechanical Engineering

Experimental and Numerical Studies of the Seismic Performance of Precast Segmental Concrete Columns

Chao Li

This thesis is presented for the Degree of
Doctor of Philosophy
of
Curtin University

January 2019

Declaration

To the best of my knowledge and belief this thesis contains no material previously published by any other person except where due acknowledgment has been made.

This thesis contains no material which has been accepted for the award of any other degree or diploma in any university.

Signature: Chao Li

Date: 18/01/2019

ABSTRACT

Traditional cast-in-situ construction method normally includes a lot of construction works on site such as preparing formworks, tying steel cages and casting concrete. These activities are time consuming and can significantly influence the traffic. Precast segmental column has been proposed to accelerate the construction speed, which is especially critical in busy urban areas with heavy traffic. It is becoming more and more popular and attractive recently considering its numerous advantages. However, the applications are mainly limited to the areas of low seismicity due to the lack of understanding on its performance under seismic loadings.

The studies carried out in this thesis concentrate on investigating the seismic performance of precast segmental column, including the static performance under cyclic loading and dynamic response under seismic excitations. Quasi-static cyclic tests are carried out to evaluate the effects of different designs on its seismic performance. The most vulnerable components and failure modes of precast segmental columns are identified. Basalt fibre reinforced polymer (BFRP) and tension-only external energy dissipation (TEED) devices are used to improve its seismic performance. Extensive numerical studies are also carried out to investigate its performances under uniaxial and biaxial cyclic loadings. Finally, shake table tests are conducted to investigate its dynamic responses under bidirectional seismic excitations.

In the first part of this thesis (Chapter 2), five segmental columns are tested under cyclic loading to investigate the performances of segmental columns under cyclic loadings with reference to the monolithic column. In particular, the effects of different design parameters on the performance of the segmental column are investigated, including the energy dissipation (ED) bars, posttension force in the tendon, segment number, and the shear keys. The test results demonstrate that the segmental columns have better ductility and smaller residual drift compared to the monolithic column. However, they have lower energy dissipation capability than the monolithic column due to the fact that more concrete damages and reinforcement yielding are developed in the monolithic column. It is also found that the concrete segments experience excessive compression at the toes of the segments due to the joint openings, resulting in concrete compressive failure at the joints.

To overcome the disadvantages of low energy dissipation and excessive concrete compressive failure, Tension-only External Energy Dissipation (TEED) devices and basalt fibre-reinforced polymer (BFRP) wrapped segments are proposed to be used in the segmental column. The TEED device is designed to improve the energy dissipation ability of the column while keeping the residual displacement small. The BFRP is used to wrap the segments to mitigate the damage of the segments. Quasi-static cyclic tests are performed to examine the effectiveness of the proposed method (Chapter 3). The test results demonstrate that the combined use of the BFRP and TEED can improve the seismic performance of the segmental column. In particular, BFRP can effectively reduce the damages of the segments and TEED devices can increase the energy dissipation capacity of the segmental column without significantly increasing the residual displacement due to the non-buckling design of the devices.

In order to further investigate the seismic performance of segmental column, numerical studies are conducted (Chapter 4). The numerical models are developed and validated against the test results of two large scale segmental columns under cyclic loading. Afterwards, parametric studies are carried out to systematically investigate the effects of bonded and unbonded tendon, posttension force level, confinement of the segments, and other parameters on the performance of segmental columns. In addition, shape memory alloy (SMA) bars are also adopted and investigated as ED bars to increase the energy dissipation. It is found that the bonded tendon results in stress concentration in the tendon and decreases the ductility of the column. Higher posttension force results in higher strength and energy, but lower ductility. The SMA bars are effective to increase the energy dissipation capacity of the column while keeping the residual displacement small.

Although many experimental and numerical studies have been carried out to study the uniaxial cyclic performance of the segmental columns, the biaxial seismic performance of the segmental column, however, is rarely investigated. In reality, the seismic excitation has three components. Using the performance of the segmental column under uniaxial loading to predict the structural response during an earthquake may lead to inaccurate results. Therefore, the performance of the segmental column subjected to biaxial cyclic loadings is investigated in Chapter 5. Six biaxial cyclic loading paths are applied to a numerical model to investigate the influence of different

biaxial cyclic loading combinations. The results demonstrate that the biaxial cyclic loading paths have significantly influences on the strength, ductility and energy dissipation of the segmental column.

Shake table tests allow direct observation of the dynamic behaviours of segmental columns under seismic ground excitations. Only limited shake table tests have been carried out on the precast segmental columns. Moreover, only uniaxial ground motions are used in these tests. Shake table test on the segmental column under bidirectional earthquake motions is carried out in this study (Chapter 6). A monolithic column is also tested for comparison. It is interesting that significant twisting occurred to the segmental column under the bidirectional earthquake motions during the test, indicating that the friction between the joints is not enough to resist the torsional moment induced by the unsymmetrical damages in the segments and the bidirectional earthquake loadings. This has not been observed in previous studies. To prevent the twisting, shear keys between the segments are proposed to be installed at the joints between the segments, and they are proved to be effective according to the results of the numerical simulations.

ACKNOWLEDGEMENT

First and foremost, my sincerest and deepest gratitude goes to my supervisor John Curtin Distinguished Professor Hong Hao for the continuous support, great patience, and invaluable encouragement throughout these years. Your wisdom, broad vision and wise guidance have made my PhD study a valuable journey to gain knowledge and broaden my mind. It is a priceless treasure for my future career and life. Thank you, Professor Hao.

I am also thankful to my co-supervisor Dr. Kaiming Bi for your advices, suggestions and invaluable help during this research. Thanks also go to Dr. Xihong Zhang and Mr. Do Van Tin for the help during the cyclic tests in the structural lab at the University of Western Australia. The technical assistance from Mr. Jim Waters is also gratefully acknowledged. The help from Mr Taixiang Zhao and Andrew Joseph, final year students from Curtin University, during the cyclic tests is gratefully appreciated. Thanks go to Mr. Yaoliang Li for the beneficial discussion of numerical modelling. Special thanks also go to members in Prof. Hao's group for their help and suggestions during the shake table tests that carried out in the Structural Dynamics Lab at Curtin University, including Dr. Wensu Chen, Dr. Jun Li, Dr. Thong Pham, Mr. Cheng Yuan and Mir Abdul Kuddus. Final year students of Curtin University Mr. Timothy McGilligan and Kevin Eng-Long Ee are also acknowledged for their active participation and help during the shake table tests. Thanks also go to the technicians in the lab of Curtin University for their technical support. Hanson Australia and Delta Corporation Limited are also gratefully acknowledged for providing us the concrete and posttension strands, respectively.

I would also like to thank the group members of Prof. Hao's research group at Curtin University. It is a great thing to be a member of this dynamic group where I received invaluable comments and suggestions throughout this study. I would like to express my thanks to Dr. Jun Li, Yifei Hao, Bipin Shrestha, Kinzang Thinley, Shuyang Chen, Qingfei Meng, Xingyu Fan, Musaad Zaheer, Haoran Zuo, Do Van Tin, Zhejian Li, Hamid Matin Nikoo, Yianqiang Cui, Yijun Chen, Cheng Yuan, Feng Shi, Duy Tan Le, Gao Fan, Ruisheng Ma, Huawei Li, Mir Abdul Kuddus, as well as the visiting scholars including Professor Chao Zhang, Xueyuan Yan, Jianrong Yang, Linqi Huang,

Sujing Yuan, Shenglan Ma, Jing Zhang, Lufeng Zhao, Pinghe Ni, Chuang Cui, Lizhong Song, Dangxiong Wang, Jian Cui, Mei Li and Jiefu Liu.

I am thankful to Australian Research Council (ARC) for providing the financial support to this research through a Discovery Project. Thanks must also go to the head of the Civil Engineering, Dr. Andrew Whyte, and chair of my thesis committee, Prof. Hamid Nikraz. Thanks also go to Curtin University and China Scholarship Council for providing the scholarship for my PhD study. I would also want to thank Mrs. Sucy Leong, Mrs. Evelyn Wong, Mr. Frankie Sia, Ms. Cheryl Cheng and Ms. Ying Hong Lin as the administrative officers. Thanks also go to the IT and library support from Curtin University.

Last but not the least, I would like to express my deepest gratitude to my parents, Zhian Li and Xiuqiong Fan, for your unconditional love and constant encouragement.

LIST OF PUBLISHED WORK AND WORK PREPARED FOR PUBLICATIONS

The list of published paper and work prepared for publications, with the full bibliographic citations in the order they appear in the thesis, are listed below.

Chapter 2

Li, C., Hao, H., Zhang, X., & Bi, K. (2017). Experimental study of precast segmental columns with unbonded tendons under cyclic loading. *Advances in Structural Engineering*, 2017:1369433217717119.

Chapter 3

Li, C., Bi, K., Hao, H., Zhang, X., & Do, T. V. (2018). Cyclic test and numerical study of precast segmental concrete columns with BFRP and TEED. *Bulletin of Earthquake Engineering*, doi:10.1007/s10518-019-00597-1

Chapter 4

Li, C., Hao, H., & Bi, K. (2017). Numerical study on the seismic performance of precast segmental concrete columns under cyclic loading. *Engineering Structures*, 148, 373-386. doi.org/10.1016/j.engstruct.2017.06.062

Chapter 5

Li, C., Hao, H., & Bi, K. (2018). Seismic performance of precast concrete-filled circular tube segmental column under biaxial lateral cyclic loadings. *Bulletin of Earthquake Engineering*. 17(1), 271-296. doi:10.1007/s10518-018-0443-4

Chapter 6

Li, C., Bi, K., & Hao, H., (2019). Seismic Performances of Precast Segmental Column under Bidirectional Earthquake Motions: Shake Table Test and Numerical Evaluation. *Engineering Structures*, 2019:187:314-28.

LIST OF RELEVANT ADDITIONAL PUBLICATIONS

The list of additional publications relevant to the thesis, with the full bibliographic citations, is given below.

Li, C., Hao, H., & Zhang, X., (2017). *Analysis of precast segmental concrete columns with unbonded post-tensioned tendons under cyclic loading.* Proceedings of the 16th World Conference on Earthquake Engineering, Santiago, Chile.

Li, C., Hao, H., & Zhang, X., (2017). *Cyclic tests of precast segmental concrete columns with unbonded post-tensioned tendons.* Proceedings of the 16th World Conference on Earthquake Engineering, Santiago, Chile.

Li, C., Hao, H., & Bi, K. (2017). *Numerical study on the precast concrete filled steel tubular (CFST) segmental column under biaxial cyclic loadings.* Proceeding of Australian Earthquake Engineering Society annual conference 2017, Canberra, ACT, Australia.

Li, C., Hao, H., Zhang, X., Bi, K. & Do, T. V., (2017). *Experimental study of precast BFRP-wrapped segmental concrete columns with external ED device under eccentric cyclic loading.* Proceeding of Australian Earthquake Engineering Society annual conference 2017, Canberra, ACT, Australia.

Bi, K., **Li, C.**, & Hao, H. (2018). *Seismic performance of precast segmental columns: shake table tests.* Proceeding of Australian Earthquake Engineering Society annual conference 2018, Perth, WA, Australia.

Zhang, X., Hao, H., & **Li, C.** (2016). The effect of concrete shear key on the performance of segmental columns subjected to impact loading. *Advances in Structural Engineering*, 1369433216650210.

Zhang, X., Hao, H., & **Li, C.** (2016). Experimental investigation of the response of precast segmental columns subjected to impact loading. *International Journal of Impact Engineering*, 95, 105-124.

Zhang, X., Hao, H., & **Li, C.** (2018). Multi-hazard resistance capacity of precast segmental columns under impact and cyclic loading. *International Journal of Protective Structures*, 9(1), 24-43.

Zhang, X., Hao, H., **Li, C.**, & Do, T. V. (2018). Experimental study on the behavior of precast segmental column with domed shear key and unbonded Post-Tensioning tendon under impact loading. *Engineering Structures*, 173, 589-605.

Kuddus, M. A., Li, J., Hao, H., **Li, C**., & Bi, K. (2019). Target-free vision-based technique for vibration measurements of structures subjected to out-of-plane movements. *Engineering Structures*, 190, 210-222.

STATEMENT OF CONTRIBUTION OF OTHERS

The overall scope and the related research methodologies of this research were defined by Prof. Hong Hao. The works presented in the thesis were primarily carried out by the candidate, Mr. Chao Li, which include conducting experimental tests, developing numerical models, analyzing results and preparing the manuscripts. Contributions of the co-authors are described as follows.

Chapter 2 and Chapter 3

Prof. Hong Hao helped in defining the scope of the experimental tests. The financial support to the experiments was provided by ARC Discovery Project (DP 150104346). The first author and Dr. Xihong Zhang prepared and tested the specimens as presented in chapter 2 and chapter 3. Mr. Do Van Tin provided help in the tests presented in chapter 3. Based on the test results, the first author prepared the manuscripts with the reviewing and editing efforts spent by Prof. Hong Hao, Dr. Kaiming Bi and Dr. Xihong Zhang to improve the quality of the manuscripts.

Chapter 4 and Chapter 5

In chapters 4 and 5, Prof. Hong Hao ascertained the objectives of the studies through critical evaluation. The first author developed the numerical model and then conducted the numerical studies. Prof. Hong Hao and Dr. Kaiming Bi provided uninterrupted intellectual support and suggestions throughout these studies. The manuscripts were written by the first author and revised by Prof. Hong Hao and Dr. Kaiming Bi.

Chapter 6

In chapter 6, the experimental tests were conceived by Prof. Hong Hao, who defined the scope of the work and secured the use of shake tables in the Structural Dynamics Lab at Curtin University. The financial support to the tests was also provided by ARC Discovery Project (DP 150104346). The experiments were conducted by the first author with the continuous intellectual support from Prof. Hong Hao and Dr. Kaiming Bi. The first author developed the numerical model to supplement the test results and

then prepared the manuscript, which was then revised and edited by Prof. Hong Hao and Dr. Kaiming Bi.

TABLE OF CONTENTS

ABSTRACTi

ACKNOWLEDGEMENT iv

LIST OF PUBLISHED WORK AND WORK PREPARED FOR PUBLICATIONS vi

LIST OF RELEVANT ADDITIONAL PUBLICATIONS vii

STATEMENT OF CONTRIBUTION OF OTHERS ix

TABLE OF CONTENTS xi

LIST OF FIGURES xiv

LIST OF TABLES xix

CHAPTER 1 INTRODUCTION 20

1.1 Background 20

1.2 Research Objectives 24

1.3 Research Outline 25

1.4 References 26

CHAPTER 2 EXPERIMENTAL STUDY OF PRECAST SEGMENTAL COLUMNS WITH UNBONDED TENDONS UNDER CYCLIC LOADING... 29

2.1 Abstract 29

2.2 Introduction 29

2.3 Experimental setup 32

2.3.1 Specimen design 32

2.3.2 Experimental setup 34

2.4 Test results and analysis 36

2.4.1 Column damage 36

2.4.2 Hysteretic curve 39

2.4.3 Residual drift 45

2.4.4 Backbone curve 46

2.4.5 Hysteretic energy dissipation and equivalent viscous damping ratio .. 47

2.4.6 Prestress tendon force 50

2.5 Conclusions 53

2.6 References 53

CHAPTER 3 CYCLIC TEST AND NUMERICAL STUDY OF PRECAST SEGMENTAL CONCRETE COLUMNS WITH BFRP AND TEED 56

3.1 Abstract 56

3.2 Introduction 56

3.3 Experimental program 60
3.3.1 Specimen design 60
3.3.2 Test setup and loading protocol 63
3.4 Test results and discussions 66
3.4.1 Observed damage patterns 66
3.4.2 Hysteretic curves and backbone curves 67
3.4.3 Hysteretic energy dissipation and equivalent viscous damping ratio 69
3.5 Numerical study 72
3.5.1 Modelling details 72
3.5.2 Numerical results 75
3.6 Summary and conclusions 77
3.7 References 78

CHAPTER 4 NUMERICAL STUDY ON THE SEISMIC PERFORMANCE OF PRECAST SEGMENTAL CONCRETE COLUMNS UNDER CYCLIC LOADING 83

4.1 Abstract 83
4.2 Introduction 83
4.3 Numerical modelling 87
4.3.1 Model description 87
4.3.2 Finite element model 88
4.4 Validation of the numerical models 95
4.5 Parametric study 98
4.5.1 Influence of bonding conditions of prestress tendons 100
4.5.2 Influence of total axial force 103
4.5.3 Influence of confinement 104
4.5.4 Influence of the number of segments 107
4.5.5 Influence of energy dissipation (ED) bars 108
4.5.5.1 Mild steel 109
4.5.5.2 SMA 111
4.6 Conclusions 117
4.7 References 118

CHAPTER 5 SEISMIC PERFORMANCE OF PRECAST CONCRETE-FILLED CIRCULAR TUBE SEGMENTAL COLUMN UNDER BIAXIAL LATERAL CYCLIC LOADINGS 122

5.1 Abstract 122
5.2 Introduction 122
5.3 Numerical model 125
5.3.1 Model description 125
5.3.2 Numerical modelling details 127
5.3.3 Model validation 130
5.4 Biaxial loading protocols 132

5.5 Biaxial modelling results 134
5.5.1 Damages and hysteretic curves 134
5.5.2 Backbone curve 138
5.5.3 Residual displacement 141
5.5.4 Relationships between bidirectional lateral forces 142
5.5.5 Energy dissipation 144

5.6 Discussion 146
5.6.1 Minimize the residual displacement 146
5.6.2 Effect of axial loading ratio 148

5.7 Summary and conclusions 151

5.8 References 152

CHAPTER 6 SEISMIC PERFORMANCES OF PRECAST SEGMENTAL COLUMN UNDER BIDIRECTIONAL EARTHQUAKE MOTIONS: SHAKE TABLE TEST AND NUMERICAL EVALUATION 157

6.1 Abstract 157

6.2 Introduction 157

6.3 Column designs and constructions 160
6.3.1 Column design 161
6.3.2 Construction and material properties 163

6.4 Shake table test setup 166
6.4.1 Shake table and column installation 166
6.4.2 Instrumentation 167
6.4.3 Input ground motions 169

6.5 Test results 172
6.5.1 Observed damage 172
6.5.2 Variations of the fundamental periods 175
6.5.3 Drift responses 176
6.5.4 Residual twisting angle and residual displacement 177
6.5.5 Posttension force 181

6.6 Numerical study 182
6.6.1 Numerical model 182
6.6.2 Model validation 184
6.6.3 Shear keys to mitigate torsional responses 186

6.7 Summary and conclusions 188

6.8 References 189

CHAPTER 7 CONCLUSIONS AND RECOMMENDATIONS 193

7.1 Main findings 193

7.2 Recommendations for future works 196

LIST OF FIGURES

Figure 2-1 (a). Specimen schematic drawing, (b). Section of monolithic, (c). Section of 5seg, 5segED and 7seg, (d). Section of 5segkey and 7segkey. 33
Figure 2-2 (a) Sketch of test setup; (b) Photo of test setup.....35
Figure 2-3 Specimen damage: (a) monolithic column; (b) 5seg; (c) 5segED; (d) 7seg; (e) 5segkey; (f) 7segkey.....39
Figure 2-4 Hysteretic curve of columns at different drift ratios: (a) monolithic column; (b) 5seg; (c) 5segED; (d) 7seg; (e) 5segkey; (f) 7segkey.....44
Figure 2-5 Mechanism of unsymmetrical damage.....44
Figure 2-6 Residual drift of specimens.....46
Figure 2-7 Backbone curve of all specimens.....47
Figure 2-8 (a) Cumulative energy dissipation of the specimens, (b) Equivalent viscous damping ratio 50
Figure 2-9 Tendon force histories (a) 5seg, (b) 5segED, (c) 7seg, (d) 5segkey, (e) 7segkey.....52
Figure 3-1 Schematic drawings of the specimens (a) elevation view, (b) cross section and (c) details of the segment and domed-shape shear key 62
Figure 3-2 Details of TEED device.....63
Figure 3-3 (a) Photograph of the testing setup; (b) Schematic of the testing setup...65
Figure 3-4 Loading sequence.....65
Figure 3-5 Views of the three columns after test: (a) S0, (b) S1 and (c) S2.....67
Figure 3-6 Hysteretic curves of the three columns: (a) S0, (b) S1, (c) S2.....69
Figure 3-7 Backbone curves of the columns.....69
Figure 3-8 Cumulative energy dissipation of the columns 70
Figure 3-9 Schematic figure for the parameters of equivalent viscous damping ratio 72
Figure 3-10 Equivalent viscous damping ratios of the columns.....72
Figure 3-11. FE models of the three columns: (a) S0, (b) S1, (c) S2.....74
Figure 3-12. Comparison of the damages of the column: (a) S0 in the test, (b) S0 in FEM 76

Figure 3-13. Comparison of the tested and FEM hysteretic curves: (a) S0, (b) S1, (c) S2 76
Figure 3-14. Comparison of the tested and FEM backbone curves: (a) S0, (b) S1, (c) S2 77
Figure 4-1 Design details of the specimens: (a) JH1; (b) Cross section; (c) JH3 88
Figure 4-2 Relationship between parameters in CDP model 93
Figure 4-3 Cyclic loading history 95
Figure 4-4 The FE models (a) JH1; and (b) JH3 95
Figure 4-5 Comparisons of damage pattern of JH1: (a) concrete damage in the second segment (Hewes & Priestley, 2002); (b) concrete crush below the steel jacket (Hewes & Priestley, 2002); (c) axial strain of the numerical model 97
Figure 4-6 Comparisons of the simulated hysteretic curves with the experimental results: (a) JH1; (b) JH3 97
Figure 4-7 (a) Hysteretic curves of B1 and B2; (b) Cumulative energy dissipation capacity of B1 and B2 102
Figure 4-8 Stress of the tendon: (a) B1; and (b) B2 102
Figure 4-9 (a) Hysteretic curves of P1-P5; (b) cumulative energy dissipation of P1-P5 104
Figure 4-10 (a) Hysteretic curves of C1-C3; (b) cumulative energy dissipation of C1-C3 106
Figure 4-11 Bulge in the steel jacket observed in the test and simulation 106
Figure 4-12 Stress distributions of the steel jackets C1 to C3 107
Figure 4-13 (a) Hysteretic curves of S1-S3; (b) cumulative energy dissipation of S1-S3 108
Figure 4-14 (a) A schematic of arrangement of the added ED bars; (b) ED bars in the FE model 110
Figure 4-15 Comparison of hysteretic curves: (a) E1 to E6; (b) E1 and E6 111
Figure 4-16 Cumulative energy dissipation capacity of E1 to E6 111
Figure 4-17 Idealized constitutive model of super-elastic SMA 113
Figure 4-18 Comparison of hysteretic curves: (a) SE1 to SE6; (b) SE1 and SE6 ... 115
Figure 4-19 Cumulative energy dissipation capacity of SE1 to SE6 115
Figure 4-20 Comparison of the hysteretic curves of E6 and SE6 116
Figure 4-21 Comparison of stress-strain curves of mild steel and SMA bars 116

Figure 4-22 Joint openings and deformation of the SMA bars when the column is in push and pull direction 116
Figure 5-1 Design details of the column (after (Chou et al., 2013)) 126
Figure 5-2 Numerical model of the column 130
Figure 5-3 Uniaxial lateral loading: (a) displacement amplitude; (b) loading path (UC) 130
Figure 5-4 Comparison of numerical and experimental hysteretic curves 131
Figure 5-5 Comparison of the energy dissipation at each drift between the numerical and experimental results 131
Figure 5-6 Loading protocols for biaxial cyclic load path: (a) BC1, (b) BC2, (c) BC3, (d) BC4, (e) BC5, (f) BC6 133
Figure 5-7 Damage distributions at the bottom segment of the column under different loading paths (at the end of the simulation) 135
Figure 5-8 Hysteretic curves of segmental column under different biaxial loading paths 138
Figure 5-9 Backbone curves of the columns (a) X direction, (b) Y direction 140
Figure 5-10 Schematic of the strength degradation 140
Figure 5-11 Maximum residual displacements of the column under different loading paths 142
Figure 5-12 Relationships between the forces in the X and Y directions (red dash circle: maximum lateral strength of the column under UC; solid line: biaxial loading relationships in the X and Y directions) 143
Figure 5-13 Cumulative energy dissipation of the column under different loading paths 145
Figure 5-14 Normalized energy dissipation of the column under different loading paths at different drift ratios 146
Figure 5-15 Constitutive model for SMA 147
Figure 5-16 Hysteretic curves of segmental column with mild steel and SMA bars under biaxial loading path BC4 148
Figure 5-17 Comparison of the cumulative energy dissipation of the column with mild steel and SMA bars 148
Figure 5-18 Backbone curves of the column under uniaxial loading with various levels of axial loading ratios 150

Figure 5-19 Backbone curves of the column under biaxial loading with various levels of axial loading ratios: (a) X direction (b) Y direction 150
Figure 6-1 Design details of the tested columns (a) monolithic column; (b) segmental column 163
Figure 6-2 Construction of the specimens: (a) arrangement of rebars for the monolithic column, (b) formwork for the monolithic column, (c) monolithic column after curing, (d) formwork for the segmental column, (e) posttensioning setup of the segmental column, (f) base slabs and top mass slabs before casting, (g) base slabs and top mass slabs after casting 165
Figure 6-3 (a) Shake tables alignment and levelling, (b) base concrete block installed, (c) column ready to be installed, (d) installation of the mass blocks, (e) final setup of the column 167
Figure 6-4 Arrangement of the sensors: (a) front view; (b) top view 169
Figure 6-5 One pair of the bidirectional inputs (maximum PGA=0.2g): (a) N-S (X) direction; (b) E-W (Y) direction; (c) Acceleration response spectra 171
Figure 6-6 Comparisons of the input and outputs: (a) accelerations; (b) displacements; (c) Fourier spectra 172
Figure 6-7 Damage of the monolithic column: (a), PGA 0.9g; (b-c), PGA 1.0g..... 174
Figure 6-8 Damage of the segmental column: (a-b), PGA 0.7g; (c-d), PGA 0.8g .. 174
Figure 6-9 Measured first vibration periods of the columns prior to each test 176
Figure 6-10 Drift time histories of the two columns (a-b), PGA 0.2g; (c-d), PGA 0.7g 177
Figure 6-11. Intensity vs resultant drift responses of the two columns 177
Figure 6-12 Residual twisting angles of the two columns 179
Figure 6-13 Schematic drawing of the stiffness centre change due to asymmetric damage 179
Figure 6-14 Schematic drawing of the influence of twisting on the residual displacement 180
Figure 6-15 Residual displacements of the two columns: (a) in each direction; (b) resultant residual displacements 181
Figure 6-16 The posttension force versus displacements of the segmental column (PGA=0.7g) 182
Figure 6-17 The Maximum and minimum posttension forces in the tests 182
Figure 6-18 Numerical model 184

Figure 6-19 Absolute displacement response comparisons: (a-b) PGA=0.2g; (e-f) PGA=0.5g; relative displacement response comparisons: (c-d) PGA=0.2g; (g-h) PGA=0.5g 185
Figure 6-20 Twisting angles of the column from the test and numerical simulation 186
Figure 6-21 Steel shear key system between the segments: (a-b) schematic drawing of the shear keys, (c) modelling of the shear keys 187
Figure 6-22 Twisting angles of the column with and without shear keys 188

LIST OF TABLES

Table 2-1 Summary of specimen designs 33
Table 2-2 Material properties 34
Table 3-1 Summary of design details 63
Table 3-2 Material properties 63
Table 3-3 Input parameters 73
Table 4-1 Properties of the materials 90
Table 4-2 Plasticity parameters for CDP in ABAQUS 91
Table 4-3 Modelling results and errors of lateral forces at each drift ratio 98
Table 4-4 Specimens with different design parameters 99
Table 4-5 Parameters for SMA 112
Table 4-6 Quantitative comparisons of E6 and SE6 115
Table 5-1 Material properties of the column 127
Table 5-2 Strength degradation in comparison with the maximum strength (%) 141
Table 5-3 Material properties of SMA 147
Table 5-4 Summary of the strengths and strength degradations of the columns under different loading cases 151
Table 6-1 Scale factors for the column 162
Table 6-2. Properties of the materials 166
Table 6-3. Sensor details 168

CHAPTER 1 INTRODUCTION

1.1 Background

Conventional cast in place construction involves many time consuming activities such as formwork preparation, working platform installation, concrete casting, and formwork removal, which can cause serious traffic delays, environmental impact to the construction site, and disruptions to social and economic activities. In addition, construction quality can be also affected due to the complex on site conditions. In comparison, prefabricated structures can significantly reduce the construction time as it shifts most of the construction works to the prefabrication factory. Compared to the traditional construction method, it has many advantages such as less construction time, minimal traffic disruption, less environmental impact, better quality control, and safer working conditions. Due to these attractive advantages, it is becoming more and more popular around the world. Precast segmental column is one of the prefabricated structures which has been proposed as substructures to accelerate the bridge construction speed. Many applications can be found around the world. However, they are mainly limited to areas of low seismicity due to the fact that its performance under seismic loading have not been fully understood yet (Hewes & Priestley, 2002). Rigorous research on the performance of precast segmental column is necessary before using it in earthquake prone areas.

A typical precast segmental column normally consists of precast concrete segments and posttensioned tendon that used to clamp all the segments together. Some studies have been carried out to investigate the seismic performance of precast segmental columns (Billington & Yoon, 2004; Chou & Chen, 2006; ElGawady et al., 2010; Hewes & Priestley, 2002; Yamashita & Sanders, 2009). Hewes and Priestley (2002) carried out cyclic tests on the precast segmental columns with unbonded tendons. The bottom segment was confined with steel jacket with various thicknesses to mitigate the concrete damage. The test results showed that the residual displacements of the specimens were small. Minor spalling damage was developed and the column with thicker jacket performed better in terms of ductility. Billington and Yoon (2004) tested segmental columns with shear keys between the segments. Ductile fiber-reinforced cement-based composite (DRFCC) was used in the plastic hinge regions. It was found that the DFRCC was able to increase the energy dissipation of the system and maintain

its integrity better than the traditional concrete. Chou and Chen (2006) tested two precast concrete filled tube (CFT) segmental columns, in which fixed axial force ratio and the same number of segments were used for the two columns. Ou et al. (2009) investigated the influences of axial load and ED bar ratio on the performance of precast segmental columns with hollow square cross section. It should be noted that many design factors could potentially affect the performance of segmental column, however each of the above mentioned study focused on studying one or two of these factors. Since different materials, dimensions, axial loads, and testing methods were used in different previous studies, it is not easy to have direct comparisons. Chapter 2 in the present study carries out cyclic tests on five segmental columns with different designs to investigate the effects of different design parameters on the performance of precast segmental columns.

After a strong earthquake event, large residual displacement can make it difficult or even impossible to repair the bridge structures. For example, about 100 reinforced concrete columns were totally demolished after the Hyogo-ken Nanbu earthquake in 1995 because the residual drifts of these columns were larger than 1% and it was difficult to set and align the superstructures back to their original positions (Kawashima et al., 1998). Experimental results of previous studies have revealed that the precast posttensioned segmental column has excellent self-centring ability due to the restoring force provided by the posttensioned tendon, which is an important advantage for the post-earthquake retrofit activities (Ou et al., 2009). The experimental results, on the other hand, also demonstrated that the energy dissipation capacity of the segmental column is smaller than the monolithic column (Bu et al., 2015; ElGawady et al., 2010). The reason is that the longitudinal steel bars are discontinuous across the joints, when the lateral load is applied to the segmental column, openings are developed at the joints between the segments instead of causing concrete tensile cracks and steel bar yielding as observed in the monolithic column. Extra energy dissipation (ED) devices are therefore necessary to increase the energy dissipation capacity of the segmental column. In terms of the ED devices, both the internal embedded bars and external ED devices have been used by previous studies. For example, Ou et al. (2009) proposed using internal bonded mild steel bars as ED bars across the joints to increase the energy dissipation capacity of the segmental column. It was found that the ED bars were effective to increase the energy dissipation capacity

of the column. However, they might also increase the residual displacement of the column. Similar observations were also found in some other studies (Bu et al., 2015; Wang et al., 2008). Moreover, the internal ED bars are difficult to be repaired and replaced after damage during a severe earthquake event. To overcome this problem, replaceable external ED devices were proposed and investigated by some researchers (Chou & Chen, 2006; ElGawady & Sha'lan, 2010; Marriott et al., 2009). In these studies, reduced steel angle plates or fuse type dissipaters were used. The use of the external ED devices was found to be effective to increase the energy dissipation capacity of the precast segmental column. However, buckling of the external ED devices was found during the test when the devices were under compression and the residual displacements of the segmental columns were relatively large. Chapter 3 in this study proposes tension-only external ED (TEED) devices to increase the energy dissipation capacity of the segmental column while preventing buckling damage and keeping the residual displacement small with the special designed TEED devices.

Due to the joint opening and rocking behaviour of the segments, excessive stress can be developed at the toes of the segments. As a result, concrete crushing and spalling damages were observed in the previous tests. Various strengthening technics were used to mitigate such damage, including using high performance concrete (Billington & Yoon, 2004; Ichikawa et al., 2016), confining the segments with steel jacket (Chou & Chen, 2006; Hewes & Priestley, 2002), and using replaceable rubber hinge at the bottom of the column (Varela & Saiidi, 2016a). Fibre-reinforced polymer (FRP) was also adopted in some studies to confine the segments (ElGawady et al., 2010; Guo et al., 2015; Motaref et al., 2013). The FRPs used in the previous studies included carbon fibre-reinforced polymer (CFRP) and glass fibre-reinforced polymer (GFRP). Recently, basalt FRP (BFRP) has attracted increasing attention due to its low cost and good mechanical properties. It is a potential material that can be used as an alternative to strength the segments. In Chapter 3, BFRP is adopted to wrap the segments in order to mitigate the concrete damage of the segments.

Besides the experimental studies, numerical simulation is another approach to understand the performance of the column. A series of numerical modelling methods have been used to simulate the behaviour of segmental columns. Wang et al. (2008) developed two dimensional (2D) finite element (FE) model to capture the behaviour

of four precast segmental columns by using ABAQUS, in which only the last cycle of the hysteretic curve was compared. Dawood et al. (2011) developed 3D FE models in ABAQUS, and the backbone curves of the test and modelling results were compared. Nikbakht et al. (2014) adopted ANSYS to build a 3D model. Ou et al. (2007) developed 3D model in ABAQUS. Other fibre-based models by using OpenSees were also investigated in some studies (Cai et al., 2018; Wang et al., 2014). It should be noted that some influencing factors such as the bonding condition of the tendon and confinement to the segments were not considered. Hence, further developing a reliable numerical model to investigate the influences of different designs on the performance of segmental column is still necessary. In Chapter 4, detailed 3D numerical models are developed by using ABAQUS. The numerical models are validated against previous cyclic test results first and then used for parametric studies. Comprehensive numerical simulations are carried out to investigate the influences of different design parameters on the cyclic performance of the segmental column.

Even though there have been many studies on the cyclic behaviour of the precast segmental column, most of them only considered uniaxial cyclic loading. Study on the bidirectional performance of the segmental column is not available in the literature. Some previous experimental and numerical studies have been carried out to investigate the bidirectional performance of traditional monolithic concrete columns (Bousias et al., 1995; Qiu et al., 2002; Rodrigues et al., 2015; Rodrigues et al., 2013; Shirmohammadi & Esmaeily, 2015) and thin wall steel columns (Goto et al., 2009; Ucak & Tsopelas, 2014). It was found the bidirectional loadings affect the performance of these columns significantly in terms of strength, ductility and energy dissipation capacity. As the segmental column is different from the monolithic column, to understand its biaxial performance, it is necessary to investigate the performance of the segmental column under bidirectional loadings and to evaluate the effect of load path on the performance of such column. In Chapter 5, the biaxial performance of the segmental column is investigated through numerical studies. A numerical model of a segmental column under uniaxial cyclic loading is first developed and validated. Then different commonly used biaxial cyclic loading paths are applied to the numerical model to assess the biaxial performance of the segmental column. The influences of load paths and axial load ratios on the biaxial performance of the segmental column are also investigated.

Although the cyclic performance of the precast segmental column has been investigated extensively, its real dynamic responses, however, are rarely studied. A few shake table tests have been carried out in some studies. For example, Yamashita and Sanders tested on a 1/4 scaled precast segmental column and it was found the specimen showed good ductility and small residual displacement (Yamashita & Sanders, 2009). Motaref et al. (2013) tested segmental columns with the plastic hinge strengthened by damage-resilient material including elastomeric pad, ECC and carbon fibre-reinforced polymer (CFRP). Moustafa and ElGawady (2018) tested the segmental hollow-core FRP-concrete-steel (HC-FCS) columns on the shake table. Varela and Saiidi (2016b) carried out shake table tests on two 1/4-scale columns with replaceable plastic hinges incorporating ECC and SMA bars. However, it should be noted that only uniaxial earthquake excitation was used in these tests. Due to the nature of the earthquake, the columns are inevitably subjected to the multi-component motions during the earthquake. The performance of the segmental column under multi-component earthquake motions may be different from those observed from the column under uniaxial earthquake motion. Therefore, it is necessary to carry out shake table tests on the segmental column under multi-component earthquake input to better understand its seismic performance. In Chapter 6, shake table tests and numerical simulations are carried out to investigate the dynamic response of the precast segmental column. A monolithic column is also tested as a reference.

1.2 Research Objectives

The primary objective of this study is to investigate the seismic performance of precast posttensioned segmental concrete column. To achieve this goal, experimental tests including cyclic tests and shake table tests are carried out. Numerical simulations are also conducted to perform intensive parametric studies of the influences of various design parameters and loading conditions on the performances of segmental columns. The specific research works and objectives of this study include:

1) Investigating the influences of energy dissipation bars, number of segments, shear keys and prestressing force on the performance of segmental columns.
2) Studying the effectiveness of using BFRP to mitigate the compressive damage of the concrete, and studying the effectiveness of enhancing the energy

dissipation capacity of the segmental column by using the newly proposed buckling resistant tension-only energy dissipation device (TEED) devices.

3) Developing numerical models to reliably simulate the responses of segmental column under cyclic loading. Investigating the effects of various design details on the performance of segmental columns through comprehensive parametric studies.
4) Investigating the effects of biaxial cyclic loadings on the performance of the segmental column and the effect of different loading paths on its performance.
5) Investigating the dynamic response of segmental columns subjected to biaxial ground excitations by conducting shake table tests and numerical simulations on the segmental column.

1.3 Research Outline

This thesis comprises seven chapters. The contents of the six chapters following the introductory chapter are described below:

Chapter 2 presents the experimental tests on one monolithic column and several segmental columns with different designs. The differences between the performance of monolithic and segmental columns are compared and discussed in terms of hysteretic curves, backbone curves, energy dissipation and residual drift. The influences of different designs on the cyclic performance of segmental columns are also discussed.

Chapter 3 presents the proposed methods for strengthening the segments with BFRP and increasing the energy dissipation capacity of the column with the newly proposed TEED to achieve a better seismic performance.

Chapter 4 develops and calibrates the numerical models of segmental columns. The effects of the bonding condition of the tendon, axial force ratio, confinement to the segments, segment number and energy dissipation bar ratio are investigated through comprehensive parametric studies. The use of Shape Memory Alloy (SMA) to increase the energy dissipation and minimize the residual displacement are also discussed in this chapter.

Chapter 5 investigates the influences of biaxial cyclic loadings on the performance of segmental columns. A numerical model is developed and different biaxial loading paths are applied to the validated numerical model. The effects of the biaxial loading paths on the performance of the segmental column are discussed.

Chapter 6 carries out shake table tests on both monolithic column and segmental column under bidirectional earthquake motions. The dynamic responses of segmental column subjected to the bidirectional seismic excitations are assessed and compared with the monolithic column. The effectiveness of using multiple shear keys between the segments to reduce the twisting of the segmental column is investigated through numerical simulations.

Chapter 7 summarizes the concluding remarks of the current study, as well as recommendations for the future research.

This thesis is compiled by a connection of technical papers prepared by the candidate during the research. Therefore, Chapter 2 to 6 can be read independently, and consist of some repeated information and literature review.

1.4 References

Billington, S. L., & Yoon, J. (2004). Cyclic response of unbonded posttensioned precast columns with ductile fiber-reinforced concrete. *Journal of Bridge Engineering, 9*(4), 353-363.

Bousias, S. N., Verzeletti, G., Fardis, M. N., & Gutierrez, E. (1995). Load-path effects in column biaxial bending with axial force. *Journal of Engineering Mechanics, 121*(5), 596-605.

Bu, Z. Y., Ou, Y. C., Song, J. W., Zhang, N. S., & Lee, G. C. (2015). Cyclic Loading Test of Unbonded and Bonded Posttensioned Precast Segmental Bridge Columns with Circular Section. *Journal of Bridge Engineering*, 04015043.

Cai, Z.-K., Zhou, Z., & Wang, Z. (2018). Influencing factors of residual drifts of precast segmental bridge columns with energy dissipation bars. *Advances in Structural Engineering*, 1369433218780545.

Chou, C. C., & Chen, Y. C. (2006). Cyclic tests of post-tensioned precast CFT segmental bridge columns with unbonded strands. *Earthquake Engineering & Structural Dynamics, 35*(2), 159-175.

Dawood, H., ElGawady, M., & Hewes, J. (2011). Behavior of segmental precast posttensioned bridge piers under lateral loads. *Journal of Bridge Engineering, 17*(5), 735-746.

ElGawady, M., Booker, A. J., & Dawood, H. (2010). Seismic behavior of posttensioned concrete-filled fiber tubes. *Journal of Composites for Construction, 14*(5), 616-628.

ElGawady, M., & Sha'lan, A. (2010). Seismic behavior of self-centering precast segmental bridge bents. *Journal of Bridge Engineering, 16*(3), 328-339.

Goto, Y., Muraki, M., & Obata, M. (2009). Ultimate state of thin-walled circular steel columns under bidirectional seismic accelerations. *Journal of Structural Engineering, 135*(12), 1481-1490.

Guo, T., Cao, Z., Xu, Z., & Lu, S. (2015). Cyclic Load Tests on Self-Centering Concrete Pier with External Dissipators and Enhanced Durability. *Journal of Structural Engineering, 142*(1), 04015088.

Hewes, J. T., & Priestley, M. N. (2002). *Seismic design and performance of precast concrete segmental bridge columns* (No. SSRP-2001/25). Retrieved from University of California, San Diego, CA:

Ichikawa, S., Matsuzaki, H., Moustafa, A., ElGawady, M. A., & Kawashima, K. (2016). Seismic-Resistant Bridge Columns with Ultrahigh-Performance Concrete Segments. *Journal of Bridge Engineering*, 04016049.

Kawashima, K., MacRae, G. A., Hoshikuma, J.-i., & Nagaya, K. (1998). Residual displacement response spectrum. Journal of Structural Engineering, 124(5), 523-530.

Marriott, D., Pampanin, S., & Palermo, A. (2009). Quasi-static and pseudo-dynamic testing of unbonded post-tensioned rocking bridge piers with external replaceable dissipaters. *Earthquake Engineering & Structural Dynamics, 38*(3), 331-354.

Motaref, S., Saiidi, M. S., & Sanders, D. (2013). Shake table studies of energy-dissipating segmental bridge columns. *Journal of Bridge Engineering, 19*(2), 186-199.

Moustafa, A., & ElGawady, M. A. (2018). Shaking Table Testing of Segmental Hollow-Core FRP-Concrete-Steel Bridge Columns. *Journal of Bridge Engineering, 23*(5), 04018020.

Nikbakht, E., Rashid, K., Hejazi, F., & Osman, S. A. (2014). A numerical study on seismic response of self-centring precast segmental columns at different post-tensioning forces. *Latin American Journal of solids and structures, 11*(5), 864-883.

Ou, Y. C., Chiewanichakorn, M., Aref, A. J., & Lee, G. C. (2007). Seismic performance of segmental precast unbonded posttensioned concrete bridge columns. *Journal of Structural Engineering, 133*(11), 1636-1647.

Ou, Y. C., Wang, P. H., Tsai, M. S., Chang, K. C., & Lee, G. C. (2009). Large-scale experimental study of precast segmental unbonded posttensioned concrete bridge columns for seismic regions. *Journal of Structural Engineering, 136*(3), 255-264.

Qiu, F., Li, W., Pan, P., & Qian, J. (2002). Experimental tests on reinforced concrete columns under biaxial quasi-static loading. *Engineering Structures, 24*(4), 419-428.

Rodrigues, H., Arêde, A., Furtado, A., & Rocha, P. (2015). Seismic behavior of strengthened RC columns under biaxial loading: An experimental characterization. *Construction and Building Materials, 95*, 393-405. doi:http://dx.doi.org/10.1016/j.conbuildmat.2015.07.149

Rodrigues, H., Arêde, A., Varum, H., & Costa, A. G. (2013). Experimental evaluation of rectangular reinforced concrete column behaviour under biaxial cyclic loading. *Earthquake Engineering & Structural Dynamics, 42*(2), 239-259. doi:10.1002/eqe.2205

Shirmohammadi, F., & Esmaeily, A. (2015). Performance of reinforced concrete columns under bi-axial lateral force/displacement and axial load. *Engineering Structures, 99*, 63-77. doi:http://dx.doi.org/10.1016/j.engstruct.2015.04.042

Ucak, A., & Tsopelas, P. (2014). Load Path Effects in Circular Steel Columns under Bidirectional Lateral Cyclic Loading. *Journal of Structural Engineering, 141*(5), 04014133.

Varela, S., & Saiidi, M. (2016a). A bridge column with superelastic NiTi SMA and replaceable rubber hinge for earthquake damage mitigation. *Smart Materials and Structures, 25*(7), 075012.

Varela, S., & Saiidi, M. (2016b). Resilient deconstructible columns for accelerated bridge construction in seismically active areas. *Journal of Intelligent Material Systems and Structures*, 1045389X16679285.

Wang, J. C., Ou, Y. C., Chang, K. C., & Lee, G. C. (2008). Large-scale seismic tests of tall concrete bridge columns with precast segmental construction. *Earthquake Engineering & Structural Dynamics, 37*(12), 1449-1465.

Wang, Z., Ge, J., & Wei, H. (2014). Seismic performance of precast hollow bridge piers with different construction details. *Frontiers of Structural and Civil Engineering, 8*(4), 399-413.

Yamashita, R., & Sanders, D. H. (2009). Seismic performance of precast unbonded prestressed concrete columns. *ACI Structural Journal, 106*(06).

CHAPTER 2 EXPERIMENTAL STUDY OF PRECAST SEGMENTAL COLUMNS WITH UNBONDED TENDONS UNDER CYCLIC LOADING

2.1 Abstract

Precast segmental column has attracted a lot of research interests over the past two decades. It has become more and more popular in construction industry to achieve fast construction, improve construction quality and reduce environmental impact. Many factors including the energy dissipation bar, number of segments, prestressing force and shear keys could affect the performance of segmental column, but each of previous studies normally focused on investigating one or two of these factors. Since different previous studies used different materials, different structural dimensions, different axial loads and different testing methods, it is difficult to have comprehensive comparisons. Moreover, limited studies indicated that shear keys had insignificant influences on performances of segmental columns subjected to cyclic loadings, while other studies revealed shear keys contribute to resisting impact loads but could lead to more severe damage due to stress concentration. In this study, cyclic tests were carried out to systematically assess the performance of segmental columns. Special attentions were paid on the influences of shear keys on column responses. Five scaled segmental columns with different designs were tested to study their damage mode, hysteretic behaviour, residual drift and energy dissipation capacity. One monolithic column was also tested as a reference. Test results showed that comparing with the monolithic column the segmental columns exhibited better ductility and smaller residual drift, indicating better seismic performance, but segmental columns had less loading capacity and absorbed less energy. The influences of different designs including energy dissipation bar between adjacent segments, number of segments, prestressing force level in the tendon and concrete shear key on the seismic performance of segmental column were investigated and discussed.

2.2 Introduction

Conventional construction of reinforced concrete buildings and bridges normally includes erecting working platform, installation of structural forms, fabrication and

placing steel reinforcement, casting concrete, concrete curing and removing formworks. All of these procedures have to be finished onsite which take much time and can be significantly affected by weather conditions. The associated labour hours and equipment for conventional constructions are also significant. To accelerate the construction speed, prefabrication systems are becoming more and more popular. Precast segmental concrete column is one of them. Compared with traditional cast-in-situ columns, precast segmental columns have various advantages. They can minimize site disruption, increase construction speed, reduce weather-related time delays, enhance construction quality and minimize environmental impact (Mashal et al., 2013). In addition, since most of the components are precast off-site in the factories, new materials such as fibre-reinforced concrete and ultra-high strength concrete which normally require careful mixing or high-temperature curing could be applied on precast segmental columns. Despite all these advantages, the applications of segmental column are mainly limited in areas of low seismicity since its performance under earthquake loading is not yet well understood (Motaref et al., 2010). Considering the advantages of segmental column, in recent years, many studies have been carried out to better understand its behaviour under earthquake ground excitations for its further applications in seismic regions (Chou et al., 2013; ElGawady & Dawood, 2012; Motaref et al., 2010; Shim et al., 2008; Tazarv & Saiid, 2015).

Previous studies on the seismic performance of segmental columns normally include experimental tests (Billington & Yoon, 2004; Chou & Chen, 2006; Ou et al., 2009) and numerical simulations (Dawood et al., 2011; Nikbakht et al., 2014). These studies revealed that some factors could affect the performance of segmental columns. These factors include the prestressing force, the number of segments, shear keys, and energy dissipation bars. Limited studies indicated that the friction forces between the segments are enough to resist the shear forces of the column induced by seismic ground excitations (Mashal et al., 2013). Therefore, plain segments without shear keys are commonly considered in the previous studies (Chou & Chen, 2006; ElGawady et al., 2010a; Hewes & Priestley, 2002; Yamashita & Sanders, 2009). However, during the service life of the column, other extreme loading conditions such as vehicle collision, barge impact, and blast loading may induce significantly large shear forces in the column as compared to the seismic ground excitations. Therefore proper designs with sufficient shear resistance between segments are often needed. A recent study

revealed that including shear key in the segmental column, while effectively increases the shear resistance and reduces the relative deformation between segments subjected to lateral impact loadings, leads to stress concentration, which may cause more severe damage to concrete segments (Zhang et al., 2016). The influences of shear key on segmental column performances under seismic loadings therefore need to be studied. In previous studies, different number of segments were used by different researchers. For example, twelve segments with small height of 50 mm were used in one study (Ichikawa et al., 2016). While less number of segments with large segment height were used by other researchers (Bu et al., 2015; Chou & Chen, 2006; Ou et al., 2010) or even a single segment (Marriott et al., 2009). Because these studies used different segmental column models, comparisons of the results are not enough to draw conclusions on the influences of the segment number on the performances of segmental columns. Only limited studies can be found in previous literature that investigated the influence of segment number (ElGawady et al., 2010b; ElGawady & Sha'lan, 2010). Further study on the number of segments is therefore also needed. Similarly, since the integrity of segmental column largely depends on the posttensioned tendon, prestressing force level is another important factor for segmental columns. Only very limited studies investigate the influences of prestress level on the performance of segmental column. Dawood et al. (2014) carried out parametric study on segmental column through numerical simulations. It was found that by increasing the prestressing force level the maximum strengths of the column was increased, but the ultimate drift was reduced, which indicated that the ductility of the specimen was decreased. In this study, columns with different levels of prestressing force were tested to experimentally investigate the effect of prestressing force on the performance of segmental columns.

The present study was designed to systematically investigate the influence of these factors. Segmental columns with the same dimensions but different segment number, different prestress levels, with or without shear key and ED bar were designed and tested so as to systematically study the performance of segmental columns under cyclic loading. The respective pros and cons of the designs are examined through the experimental study.

2.3 Experimental setup

2.3.1 Specimen design

Six specimens including five segmental columns and one reference monolithic column were designed and tested under lateral cyclic loading. A prototype column was scaled with the scaling factor of 1/4 (Zhang et al., 2016). As shown in Figure 2-1 (a), the first column was a traditional monolithic column which was used as a reference to compare the hysteretic behaviour between monolithic column and precast segmental columns. The second column was a precast segmental column with five segments. The third specimen was the same as the second one but with bonded ED bars across the segment joints. For the column with ED bars, holes were left in the segments before casting. The ED bars were inserted into the holes and the holes were then grouted with cementitious materials so that the ED bars could be bonded with the surrounding concrete. The fourth specimen had seven segments without ED bars or shear keys, and the fifth specimen consisted of five segments with concrete shear keys. The sixth specimen had seven segments with shear keys. The detailed dimension of the shear key is shown in Figure 2-1 (d). All the columns are named based on the segment numbers and other design details. For example, 5segED means that specimen has five segments and ED bars across the joints; 7segkey represents the column has seven segments and shear keys. Figure 2-1 (b, c, d) shows the typical cross sections of the tested specimens. All of the six columns have the same cross section and height, i.e. 100 mm × 100 mm and 800 mm (H). For the column with shear keys, trapezoid concrete shear keys with upper and bottom length of 40 and 60 mm, and a height of 20 mm were used. All the columns adopted four ribbed mild steel bars with a diameter of 6mm as the longitudinal reinforcement. For the monolithic column, the longitudinal reinforcement bars were continuous while for the segmental columns the reinforcements were discontinuous at the segment joints. For the segmental columns, two starter bars were used between the footing and the base segments to connect the base segment to the footing in the lateral loading direction. A seven-wire high strength prestress strand with a diameter of 9.3 mm was placed in the duct which was embedded at the centre of the segmental column. The area of the tendon was 54.7 mm^2. The transverse stirrups had a diameter of 4 mm. The dimension of the footings was 400 mm × 400 mm × 140 mm (length × width × height) for all the columns. Table 2-1

summarizes the design details of all the six columns. Table 2-2 gives the material properties of the six specimens.

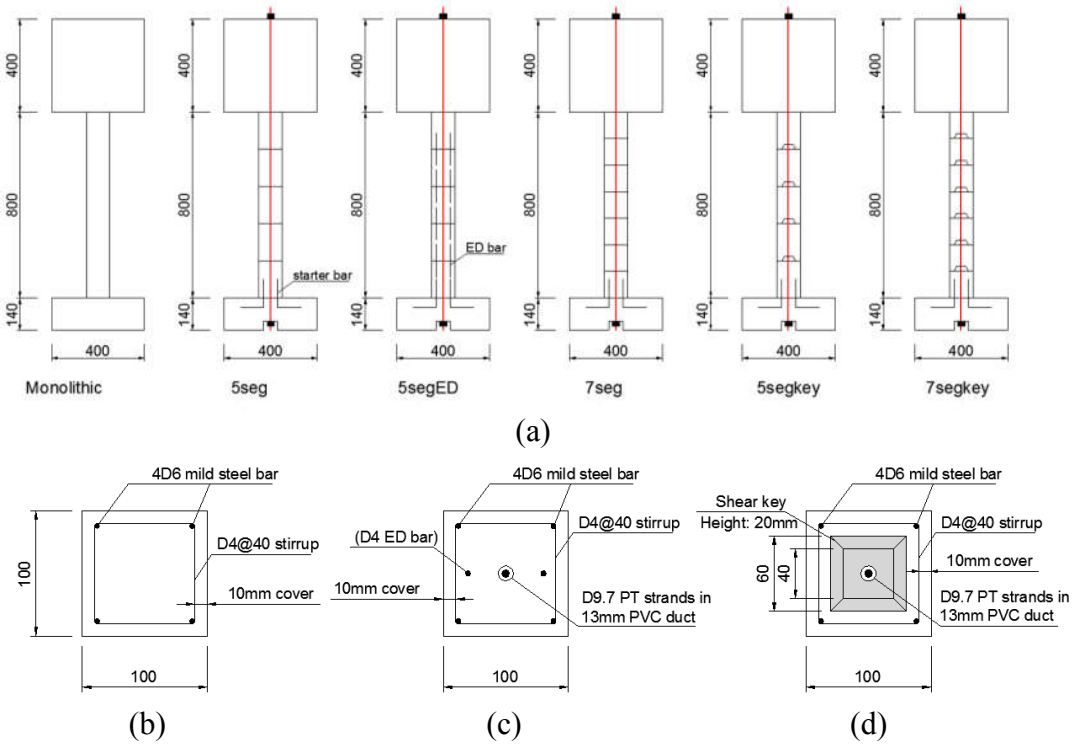

Figure 2-1 (a). Specimen schematic drawing, (b). Section of monolithic, (c). Section of 5seg, 5segED and 7seg, (d). Section of 5segkey and 7segkey.

Table 2-1 Summary of specimen designs

No.	Name	Height (mm)	No. of segments	Reinforcement				*PT force
				Longitudinal	ρ(%)	Transvers	ρ(%)	
1	Monolithic	800	-	4D6	1.13	D4@40	1.57	-
2	5seg	800	5	-	-	D4@40	1.57	30kN
3	5segED	800	5	2D4 (ED bars)	0.25	D4@40	1.57	30kN
4	7seg	800	7	-	-	D4@40	1.57	30kN
5	5segkey	800	5	-	-	D4@40	1.57	25kN
6	7segkey	800	7	-	-	D4@40	1.57	30kN

*PT stands for prestressed tendon

Table 2-2 Material properties

Material	ρ (kg/m3)	E (GPa)	f_c' (MPa)	f_t or f_y (MPa)
Concrete	2400	30	34	5
Longitudinal rebar	7800	200	-	500
Stirrup	7800	200	-	300
Prestress tendon	7850	195	-	1860

2.3.2 Experimental setup

The specimens were cast and prepared carefully in the laboratory. After all the specimens were cured, the segments were sanded to achieve flat and smooth surfaces. The levels of each column were also checked before they were installed on the testing frame. During the test, the footing was firmly fixed onto the test frame. Then the segments were stacked one by one, and the prestress tendon was inserted through the duct embedded at the centre of each segment. A 450 kg top mass was added to the top of the column. After placing the top mass, the prestress tendon was stressed with a hydraulic jack. The applied post-tension (PT) forces for all the specimens are shown in Table 2-1. The posttensioning level was controlled by a pressure monitor on the pump and also a load cell at the top of the tested specimen.

Figure 2-2 illustrates the setup of the testing system. The entire system was built on a large rigid steel beam. To be different from previous cyclic tests, a specially designed 'yielding arm' (as shown on the left hand side of Figure 2-2) was made to hold the top of the column. The arm was composed of two hinges, a rigid horizontal beam and a vertical column. It will hold the top of tested column to restrain it from rotation once the column was under the action of the actuator. The two hinges ensure the arm will 'yield' and not provide other reactions to the column. The actuator was supported by a frame on the right hand side of the testing system, which will push and pull the top of the column to apply the cyclic loading. Each end of the actuator was tied to a ball hinge to release accidental out-of-plane bending to protect the actuator during the test.

A load cell was installed on the actuator to measure the applied cyclic load. Another load cell was positioned on top of the column to monitor the change in prestressing force. The displacement was measured by a linear variable differential transformer (LVDT) behind the tested specimen.

The specimens were tested under a series of drift amplitude including 0.25%, 0.375%, 0.5%, 0.75%, 1.0%, 1.5%, 2.0%, 3.0%, 4.0%, 5.0%, 6.0% and 7.0%, respectively. The drift is denoted as the displacement at the lateral load point divided by the distance between the column base and the loading point. The loading point was 800 mm above the column base. Different specimens may fail at different drift ratios, so the exact limited drift ratio for each specimen was determined during the test. Each drift level was repeated three times in order to examine the strength degradation of the columns under the same drift ratio. During the tests, concrete cracks were carefully inspected and marked.

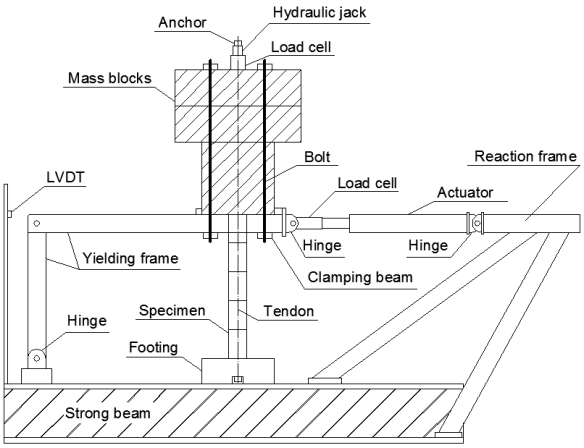

(a)

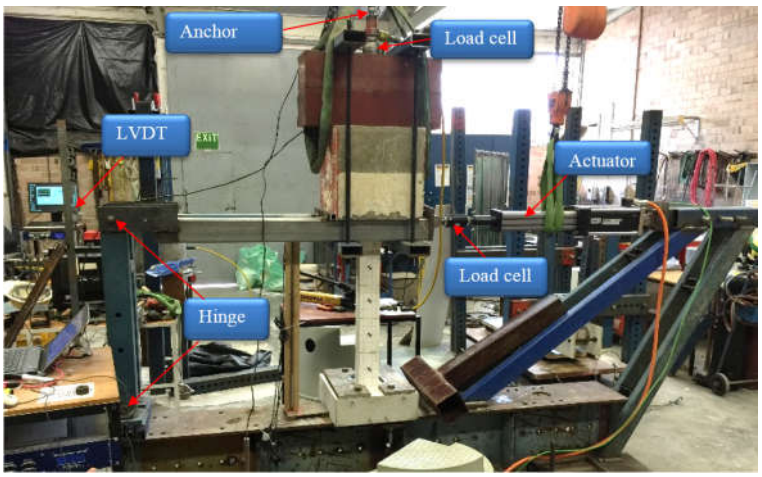

(b)

Figure 2-2 (a) Sketch of test setup; (b) Photo of test setup

2.4 Test results and analysis

Test results of the segmental columns and the monolithic column are presented in this section. Firstly, qualitative observations including column damages under cyclic loadings are given. Then, the hysteric curves, the residual drift, the energy dissipation capacity and the prestressing force histories are provided and discussed in detail.

2.4.1 Column damage

Figure 2-3 (a) shows the cracks and damage of the monolithic column after the test. Flexural horizontal cracks were spotted at very early stage of the test. Flexural cracks appeared at the base of the column and extended to about 70mm above the footing at 0.5% drift ratio. As the drift level increased, more and more cracks were formed along the column. Because of the restraint at the top of the column, a lot of cracks and concrete crushing damage were also found on the column near the top flange. At 5% drift ratio, the lateral strength of the column dropped significantly due to the damage of concrete and fracture of the longitudinal reinforcement. The test was stopped at 5% drift ratio to prevent collapse of the whole testing system.

The segmental column 5seg was composed of five segments without shear keys or ED bars. Only starter bars were used to connect the base segment to the footing. It was designed to represent the most common segmental columns studied in literature. Figure 2-3 (b) shows the observed column damage. The openings of the column were mainly located at the joint between the two bottom segments and the joint between the top mass and the top segment (column-mass joint). Since the bending moment at the base and the top of the column were the largest under double curvature bending, both of the column-footing and column-mass joints tended to open. However, the starter bars across column-footing joint restricted the opening, so the joint between the two bottom segments opened instead of the column-footing joint. At 7% drift, serious damage was found at the base segment and the top segment due to large compressive stress in the concrete segments. No obvious damage was found in the rest segments since insignificant openings were observed between these segments.

The column 5segED had five segments and ED bars across the joints. Figure 2-3 (c) shows the damage pattern of the column 5segED after the test. Comparing with column 5seg without ED bars, the response and damage of column 5segED was

different. Due to the placement of ED bars across the segmental joints, the column performed more like a rocking column and rocked at the base and top joints. At 7% drift ratio, the toes of the base and top segment were damaged. In addition, the starter bars between the footing and the base segment were also fractured.

The specimen 7seg was designed to compare the influence of the number of segments on the performance of the segmental column. Figure 2-3 (d) shows the damage and failure of the column 7seg. Generally, the behaviour of this column was similar to that of column 5seg in terms of the joint opening locations and damage mode. Notably, relative slippage was found between the two bottom segments. Slip between the two base segments was about 1.5 mm and did not increase because the prestress tendon at the centre of the column prevented the segments from further slipping. The slip phenomenon indicated that the friction force between the segments was not sufficient to withstand the lateral shear force for the column 7seg.

The column 5segkey consisted of five segments with concrete shear key. Figure 2-3 (e) shows the damage of the column. As the drift ratio increased to 7%, concrete damage was not obvious. The damage of the concrete mainly concentrated at the column-mass joint. The other segments remained almost intact. It was noted that with the shear keys across the joints, no shear slip was found between all the segments, which demonstrated the effectiveness of shear key in providing the shear resistance and preventing segment slippage. The column 5segkey performed similarly to column 5seg. However, it experienced less concrete crush damage and less cracks than column 5seg due to lower initial prestressing force level.

The column 7segkey was designed to investigate the influence of shear keys on the performance of the segmental column with seven segments. As shown in Figure 2-3 (f), concrete near the joint of two bottom segments of column 7segkey crashed in both push and pull directions. Stirrups were exposed due to excessive damage to covering concrete. As mentioned above, slippage between segments in column 7seg without shear keys was observed, while this did not occur in 7segkey with shear keys. It proved that the shear keys were effective in preventing the slippage between segments. However, the column 7segkey experienced serious damage and the strength dropped significantly at 6% drift level. This was because of stress concentration around the shear key which led to the concrete crushing damage. Similar observations were also

made on segmental columns under impact loads (Zhang et al., 2016). Both of these observations indicate that shear key in segmental column prevents possible shear slippage between segments, however, the shear key also causes stress concentrations, which may lead to serious concrete damage. Modification to the shape of the shear key will be made in the future study to minimize stress concentration and hence reduce concrete crushing damage near the joints between the segments.

(a)	
(b)	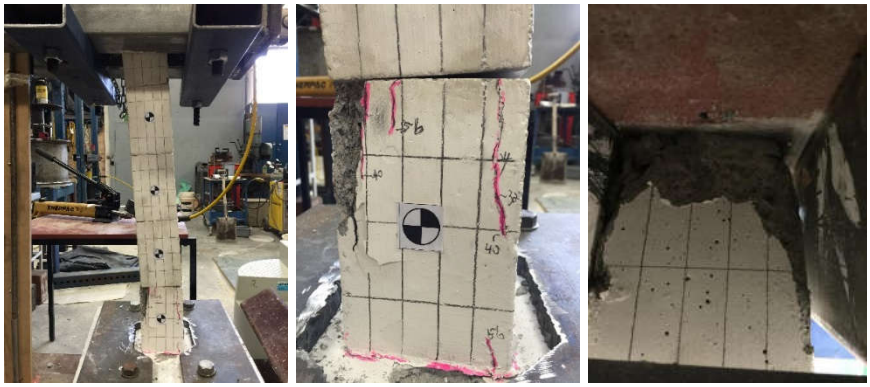
(c)	

(d)	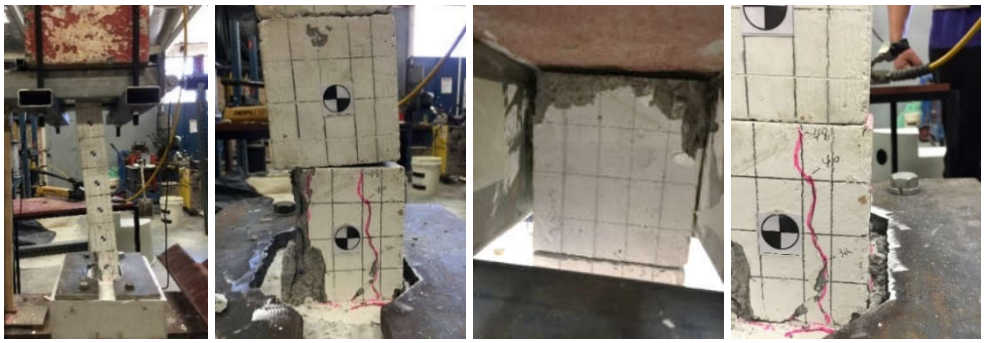
(e)	
(f)	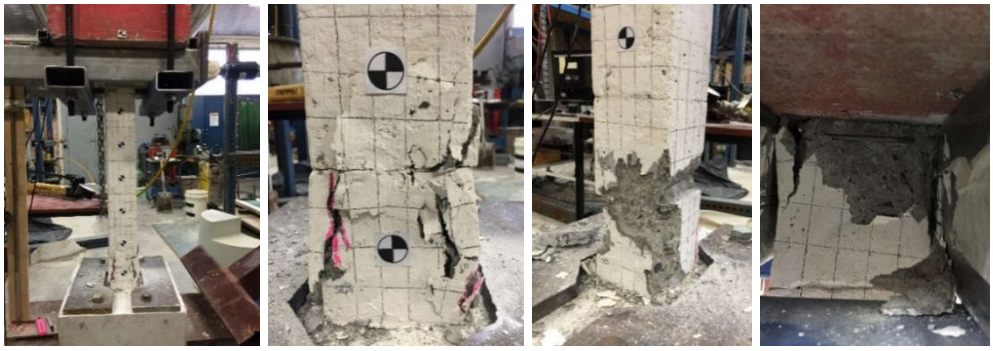

Figure 2-3 Specimen damage: (a) monolithic column; (b) 5seg; (c) 5segED; (d) 7seg; (e) 5segkey; (f) 7segkey

2.4.2 Hysteretic curve

The hysteretic curve of the monolithic column is shown in Figure 2-4 (a). Significant non-linear force-displacement relationship starts after 0.75% drift ratio. The ultimate strength of the column reached about 6 kN and -4.8 kN for the push and pull directions at the drift level of 2%. This asymmetrical lateral force was probably caused by unsymmetrical damage of the column during the test in push and pull directions, which could be relatively more apparent for small specimens tested in the present study. Strength degradation can be observed in the repeated loading cycles at the same drift level. At the ultimate drift of 5%, the lateral strength of the column dropped to

approximately 2.5 kN. The hysteretic curve of the monolithic column encloses a large area which indicates that the column dissipated a lot of energy. However, the residual drift is also large which makes it difficult to retrofit after the earthquake.

The hysteretic curves for the column 5seg with five segments before 5% drift and the maximum drift are shown in Figure 2-4 (b). Before 5% drift ratio, the response of the column under lateral cyclic loading showed a typical flag-shaped hysteretic curve. The area enclosed by the hysteretic loops was relatively small which indicated that the energy dissipated by this column was smaller than that of the monolithic column. Compared with the monolithic column, the prestress tendon in the column could pull the column back to almost its initial position after removing the applied lateral load. As a result, the residual drift of the segmental column was much smaller than that of the monolithic column. The maximum strength reached about 4.8kN and -5.5kN for the push and pull directions at the drift level of 5%. After 5% drift level, the strength and stiffness of the column dropped significantly. Also it can be seen from Figure 2-4 (b) that when the drift ratio was larger than 5%, obvious residual drift could be observed, especially for the push side with positive force and displacement. This can be explained by the serious damage of the push side of the base segment as shown previously in Figure 2-3 (b). At the ultimate drift of 7%, due to crush of the concrete near the joint between the two base segments and the column-mass joint, the lateral load dropped to only about 2.6 kN and -4.2 kN for the push and pull directions, respectively. It should be noted that in the push side, the strength of the column dropped more significantly. This is because the push side of the base segment was damaged more severely. A more detailed explanation can be made as following, as shown in Figure 2-5, assuming that the segments rotated rigidly and opening developed at the interface between the two bottom segments. At the same drift level, the rotation angle of the top segment in the push and pull directions should be the same. When serious damage occurred in the push direction, the force arm L1 became shorter than the force arm L2 in the pull direction. Additionally, the elongation of the prestress tendon was also shorter in the push direction which directly decreased the prestressing force. The reduction of the force arm and the prestressing force both contributed to the loss of the column resistance and resulted in faster drop of column resistance in the push direction.

The hysteric relationship of column 5segED is shown in Figure 2-4 (c). This column was designed to investigate the effectiveness of the energy dissipation bars on increasing the energy absorption capacity of the segmental column. The strength was about 4.7 kN and -5.6 kN, respectively, for the push and pull directions at the drift of 5%. At the ultimate drift of 7%, the lateral strength in the push and pull direction dropped to 2.45kN and 3.65kN, respectively, which could be attributed to the fracture of the starter bar as observed in the test. The present results are consistent with those in previous study (Ou et al., 2009), i.e., adding ED bars will increase energy absorption capacity, but also increase the residual deformation owing to the plastic deformation of the ED bar. More tests and numerical simulations are needed to derive optimized design of ED bars to achieve a compromise for large energy dissipation and relative small residual deformation.

The hysteretic curves for the column 7seg are shown in Figure 2-4 (d). This column also showed outstanding self-centring ability compared with the monolithic column. In the push direction, specimen 7seg reached its maximum strength at 3% drift level with a magnitude of 5.6 kN while in the pull direction the maximum strength was 4.6 kN at the drift of 5%. When the drift level reached 7%, the remaining lateral strength of the specimen was only 3.7 kN in the push direction, which means that the strength dropped 34% of the maximum strength. While in the pull direction the remaining strength was 4.0 kN, the corresponding strength degradation was 13% of the maximum strength. The strength of the column in the push direction dropped faster than the strength in the pull direction. This again was mainly because of the unsymmetrical damage of the column in the push and pull direction, which was similar to that observed in column 5seg and the mechanism is displayed in Figure 2-5.

The hysteretic curves for the column 5segkey before 5% drift and 7% drift are shown in Figure 2-4 (e). Since the initial prestressing force in the tendon was jacked to only 25 kN, the recorded maximum strength of the column was therefore relatively smaller than that of the column with 30 kN prestressing force. At the drift of 4%, the column reached its maximum strength, which were about 3.5 kN and -4.2 kN for the push and pull directions, respectively. After 5% drift level, the strength and stiffness of the column dropped slowly. At the drift of 7%, the lateral strength dropped to about 3.1 kN and -4.1 kN for the push and pull direction. From the phenomenon observed during

the test as shown in Figure 2-3 (e), this column experienced less concrete damage due to smaller axial force in comparison with other segmental columns. Therefore, for the segmental column, the tendon force needs to be carefully designed since it strongly influences the seismic performance of the segmental columns including the damage level, lateral strength and ductility.

The hysteretic curves for the column 7segkey before 5% drift and 6% drift are shown in Figure 2-4 (f). In the push direction, specimen 7segkey reached its maximum strength at 4% drift level with a magnitude of 3.9 kN while in the pull direction the maximum strength was -5.6 kN at the drift of 5%. At 6% drift, the strength of the column dropped significantly and the test was stopped at this drift level. From the observed phenomenon of the specimen as shown in Figure 2-3 (f), the column underwent severe concrete crush in the two bottom segments and the top segment. Compared with the column 7seg without shear key, column 7segkey experienced more significant damage. Stress concentration around the corners of the shear keys may be the main reason that caused such damage.

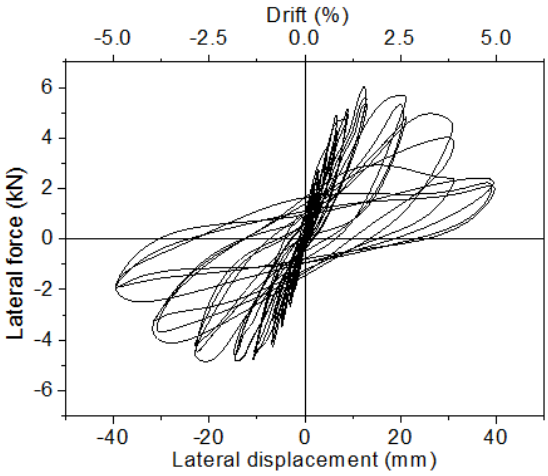

(a)

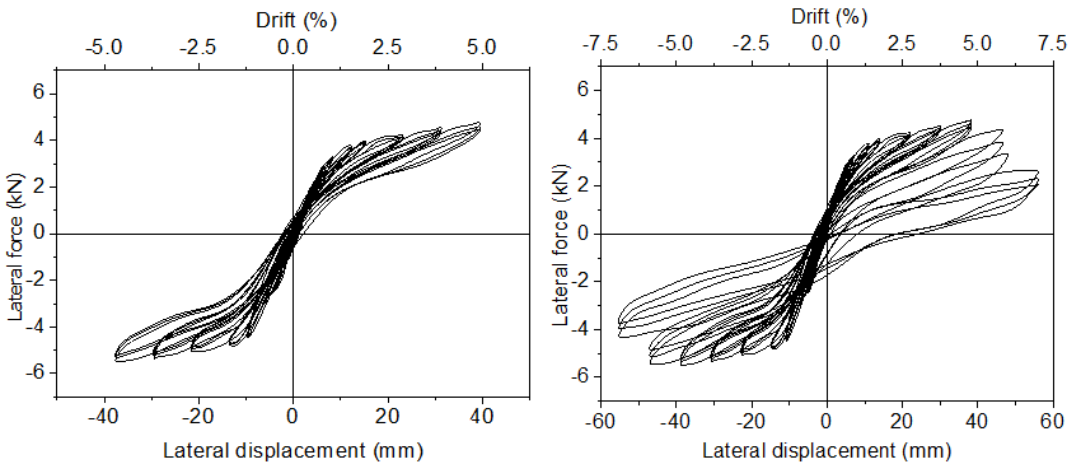
Drift (%)
-5.0 -2.5 0.0 2.5 5.0
Lateral force (kN)
6 4 2 0 -2 -4 -6
-40 -20 0 20 40
Lateral displacement (mm)
Drift (%)
-7.5 -5.0 -2.5 0.0 2.5 5.0 7.5
Lateral force (kN)
6 4 2 0 -2 -4 -6
-60 -40 -20 0 20 40 60
Lateral displacement (mm)

(b)

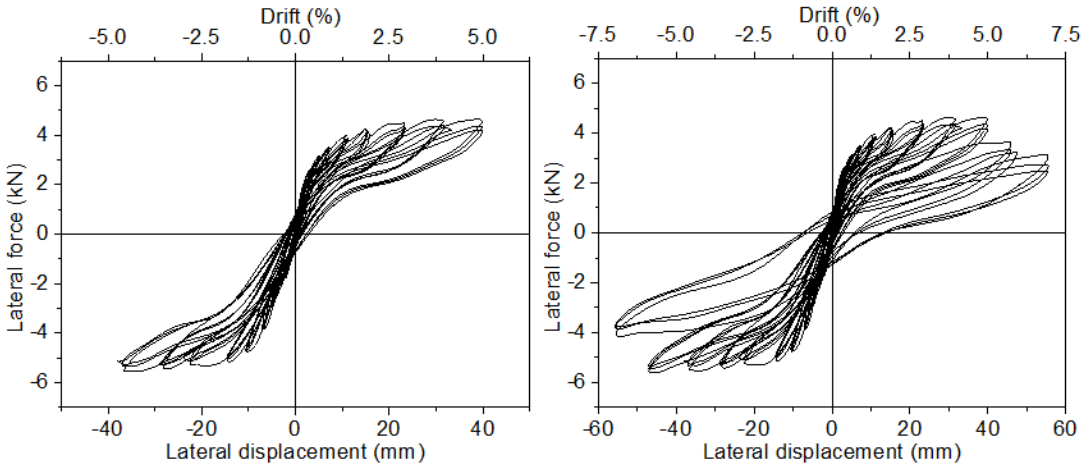
Drift (%)
-5.0 -2.5 0.0 2.5 5.0
Lateral force (kN)
6 4 2 0 -2 -4 -6
-40 -20 0 20 40
Lateral displacement (mm)
Drift (%)
-7.5 -5.0 -2.5 0.0 2.5 5.0 7.5
Lateral force (kN)
6 4 2 0 -2 -4 -6
-60 -40 -20 0 20 40 60
Lateral displacement (mm)

(c)

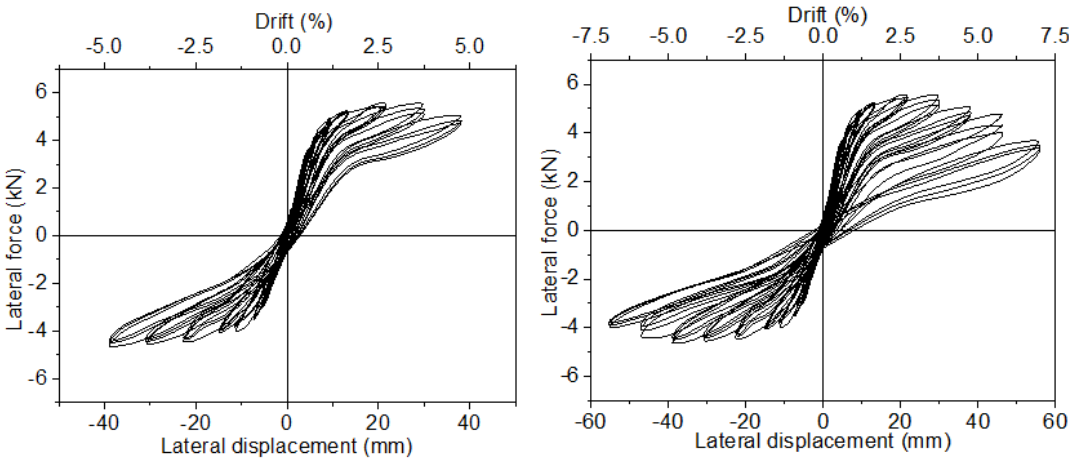
Drift (%)
-5.0 -2.5 0.0 2.5 5.0
Lateral force (kN)
6 4 2 0 -2 -4 -6
-40 -20 0 20 40
Lateral displacement (mm)
Drift (%)
-7.5 -5.0 -2.5 0.0 2.5 5.0 7.5
Lateral force (kN)
6 4 2 0 -2 -4 -6
-60 -40 -20 0 20 40 60
Lateral displacement (mm)

(d)

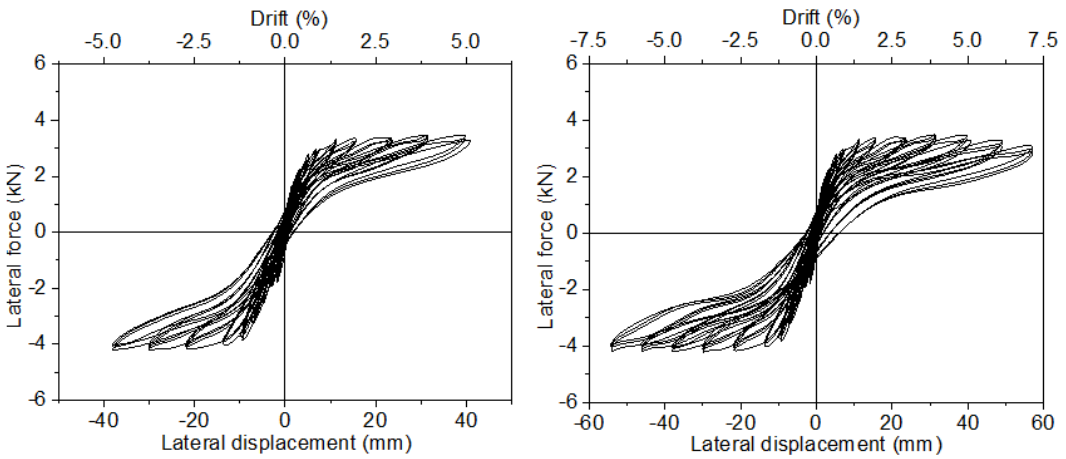

(e)

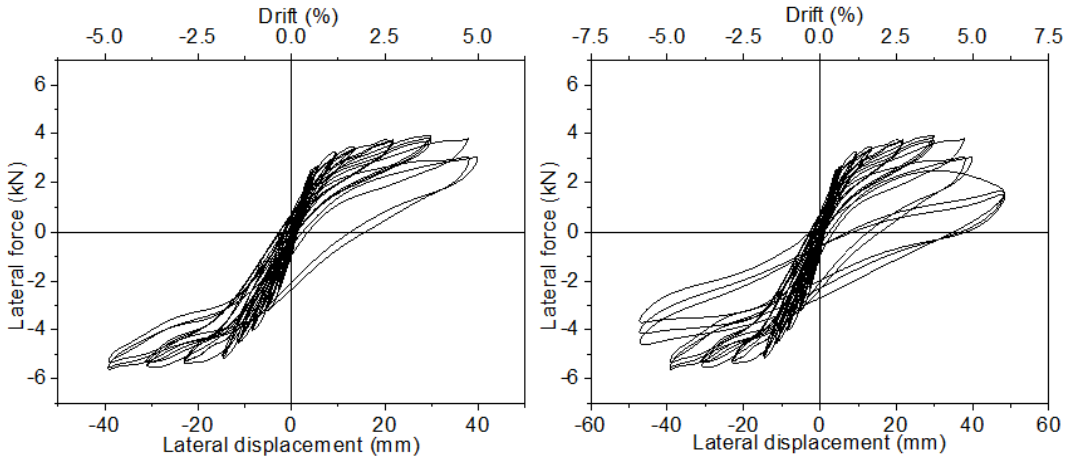

(f)

Figure 2-4 Hysteretic curve of columns at different drift ratios: (a) monolithic column; (b) 5seg; (c) 5segED; (d) 7seg; (e) 5segkey; (f) 7segkey

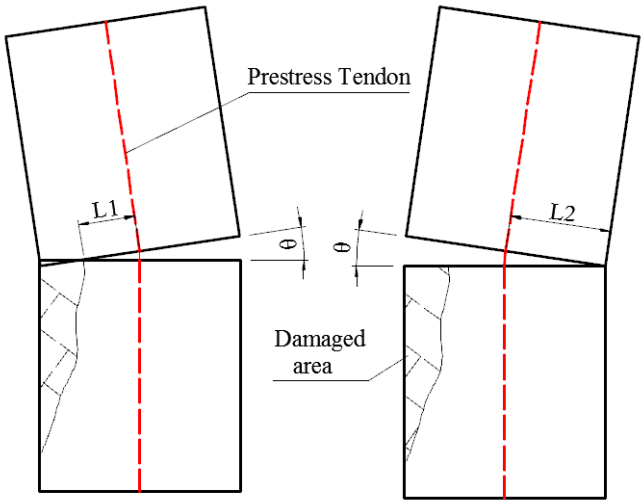

Figure 2-5 Mechanism of unsymmetrical damage

2.4.3 Residual drift

To quantify and compare the performance of the tested segmental columns in terms of residual drift, the averaged positive and negative (push and pull) residual drifts for each column at different drift levels are summarized and plotted against the corresponding applied lateral drifts in Figure 2-6.

As shown in Figure 2-6, the residual drifts of the monolithic column are similar to those of the segmental columns until the applied drift ratio increased to 2%. At 5% drift ratio the residual drift of the monolithic column reached about 2.9% which was almost 58% of the total applied lateral drift, indicating that the monolithic column had a poor self-centring ability. Due to the unbonded post-tensioned tendon, the residual drifts of the segmental columns were much smaller than that of the monolithic column. At 4% drift ratio, the residual drift of the segmental columns was about 0.16%. For the specimen 5seg, the residual drift remained quite small before 6% drift ratio. It increased gradually and reached about 0.36% at 6% drift ratio. Then at 7% drift ratio, the residual drift increased quickly as a result of significant damage of the base segment and the loss of the prestressing force. In comparison, the column 5segED with mild steel energy dissipation bars across the joint had slightly higher residual drift than that of column 5seg before 5% drift which could be the results of plastic deformation of the ED bars. At 6% drift ratio, the residual drift reached about 0.55%. Then at 7% drift ratio, the residual drift increased quickly as a result of the plastic deformation of the starter bars and ED bars as well as the concrete crush of the base and top segments. For the column 5segkey, the residual drift remained small till the end of the test, reaching only about 0.52% at 7% drift ratio. This was because the concrete damage of this column was minor. Column 7seg had similar residual drift as column 5seg before 4% drift ratio, after which lower residual displacements were found on column 7seg comparing with column 5seg. This is because of different levels of concrete damage and prestressing force loss in the two columns. The residual drift of column 7segkey increased quickly after 4% drift ratio because of severe concrete crush damage of the two base segments. At 5% applied drift, about 0.75% residual drift was measured on column 7segkey. And the recorded residual drift increased significantly to about 2.5% as the applied drift ratio increased to 6%. This was because shear keys resulted in more concrete damage, which was more apparent on segmental columns with more segments as observed above. In summary, all the segmental columns had much smaller

residual drift than the monolithic column at the same drift level. Column 7segkey experienced a substantially larger residual deformation than column 5segkey because of more serious damages to concrete segments in 7segkey column due to stress concentration. In the current design, the dimension of the shear key in both the five segments and seven segments columns are the same, but the dimensions of the segments in the two columns are different. Larger shear key relative to the concrete segment resulted in more prominent stress concentration and hence led to more severe damage.

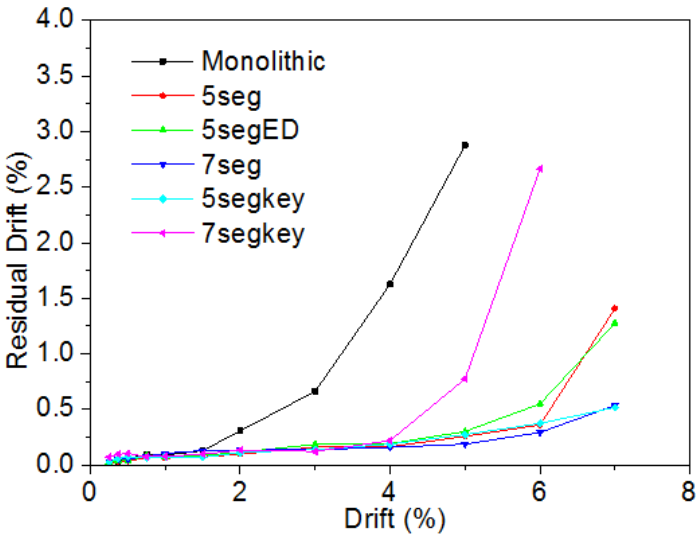

Figure 2-6 Residual drift of specimens

2.4.4 Backbone curve

The average maximum lateral strengths for all the tested columns at each drift level are summarized and plotted in Figure 2-7. Among all the columns, the monolithic column showed the highest maximum strength. However, the strength of the monolithic column degraded quickly after the column suffered damage. As shown, right after it reached the peak strength of 5.4 kN at 2% drift, the column strength began to decrease quickly. The segmental columns had smaller strength as compared to the monolithic column but they all showed larger deformation ability, indicating that they had much better ductility than monolithic column. Except the column 5segkey with smaller prestressing force, all the other segmental columns had similar backbone curve. By comparing the backbone curves of column 5seg and 5segED, it can be found that adding ED bars across the joints increased the initial stiffness and the strength of

the column before 5% drift level. After 5% drift ratio, the strength of the 5segED started to drop, which could be caused by the yielding of the starter bar between the footing and base segment as shown in Figure 2-3 (c). The column 7seg had slightly higher lateral strength than column 5seg at small drift levels but after 4% drift level column 5seg had higher loading capacity. This was because the 5seg column experienced more damage and prestressing force loss at small drift levels while the 7seg column suffered more severe damage at large drift. The column 5segkey with 25 kN prestressing force had smaller lateral strength compared with other segmental columns. However, this column showed almost no strength decrease till the end of the test, indicating that it had better ductility than other columns. These results indicate that increasing the prestressing force increases the load-carrying capacity of the column but may reduce the ductility of the column. The column 7segkey had smaller lateral strength than the column 7seg and the column failed at the 6% drift level. As explained above, this was because of the excessive concrete crushing damage due to stress concentration caused by shear keys.

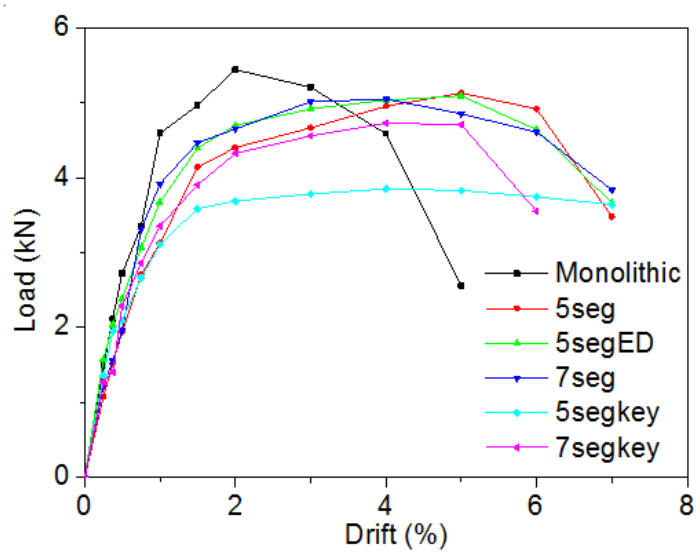

Figure 2-7 Backbone curve of all specimens

2.4.5 Hysteretic energy dissipation and equivalent viscous damping ratio

Energy dissipation is a major issue when studying the earthquake resistance capacity. The energy dissipated by a column can be calculated by integrating the area of the hysteretic loops. The cumulative energy dissipation of the columns in the current tests was derived and shown with respect to the drift ratio in Figure 2-8 (a). As shown, when

the drift ratio was lower than 5%, the monolithic column dissipated more energy than the segmental columns due to more plastic deformations. At 5% drift ratio, the accumulated energy dissipation of the monolithic column was 1249.6 kN.mm. The accumulated energy dissipation of the segmental column 5seg at this drift ratio was 450.53 kN.mm, which was 64% less compared with the monolithic column. As discussed above, this was mainly because more concrete cracks were formed on the monolithic column. The plastic deformation and the fracture of the longitudinal reinforcement also consumed a large amount of imposed energy. In comparison, in the segmental column the flexural induced cracks were replaced by the joint openings. Since less concrete damage and reinforcement yielding occurred in the segmental column, less energy was dissipated. To improve the energy dissipation capability of segmental column, ED bars were introduced in column 5segED. As shown, at 5% drift ratio the cumulative energy consumed by the column 5segED with ED bars was significantly increased to 626 kN.mm, which was 39% higher than that of column 5seg without ED bars. As the drift ratio further increased, more energy was dissipated by the segmental column with ED bars. At 7% drift, the accumulated energy dissipated by the column 5segED was about 1356.9 kN.mm. It should be pointed out that despite monolithic column could consume more hysteric energy at relatively low drift ratio, it failed at 5% drift while the segmental column 5seg and 5segED both survived the test at 7% drift. The influence of segment number can be found by comparing column 5seg and 7seg. Before 6% drift, the cumulative energy dissipated by column 7seg was higher than column 5seg. For example, at 5% drift, column 7seg dissipated 531.4 kN.mm energy while column 5seg dissipated 450.5 kN.mm energy. From the observed damage phenomenon, the base segment of column 7seg experienced much more damage than the base segment of column 5seg. Moreover, column 7seg has more joints and relative movement at joints also contribute to energy dissipation. However, after 6% drift, more energy was dissipated by column 5seg. This might be caused by propagation of cracks and significant loss of prestressing force due to the concrete damage at the anchorage zone in this column after 6% drift, leading to a large amount of energy dissipation. The column 5segkey dissipated slightly higher amount of energy than the specimen 5seg before 5% drift. This was probably because of more concrete damage and interface friction inside the segments around the shear key. After 5% drift level, the energy dissipated by the specimen 5seg increased faster, reaching 1084.8 kN.mm at 7% drift, which was 18% higher than 5segkey. This is because of the severe

damage of the base segment of column 5seg. The column 7segkey had a significant increase in energy dissipation after 4% drift. From the observed phenomenon and hysteretic curve, this column experienced serious damage and significant strength degradation after this drift level, resulting large energy dissipation.

The hysteretic energy dissipation is represented by the area (A_h) of the hysteretic curve. Suggested by Priestley et al. (Priestley et al., 1996), an equivalent viscous damping ratio is defined as:

$$\xi_{eq} = \frac{A_h}{2\pi V_m \Delta_m} = \frac{A_h}{2\pi K_{eff} \Delta_m^2} = \frac{A_h}{4\pi A_e} \tag{2.1}$$

$$V_m = \frac{|V_{max}|+|V_{min}|}{2} \tag{2.2}$$

$$\Delta_m = \frac{|\Delta_{max}|+|\Delta_{min}|}{2} \tag{2.3}$$

$$K_{eff} = \frac{V_m}{\Delta_m} \tag{2.4}$$

where ξ_{eq} is the equivalent viscous damping ratio; A_h is the area of the hysteretic loop or the energy dissipation per cycle; V_m and Δ_m are the average peak force and displacement; K_{eff} is the effective stiffness of an equivalent linear elastic system; A_e is the elastic strain energy.

Figure 2-8 (b) shows the equivalent viscous damping ratio of the tested specimens. Since the lateral displacements at the beginning of the test were only 2-3 mm which was quite small and might lead to large error while computing the equivalent viscous damping ratio, the results were therefore only given for drift ratios after 0.5%. The equivalent viscous damping ratios of the columns show a slight decrease at small drift ratios. Similar results were also observed by other researchers (ElGawady & Sha'lan, 2010; Guo et al., 2015). Guo et al. gave a brief explanation on this initial decrease of the equivalent viscous damping ratio (Guo et al., 2015). Possible explanations could be made as follows. When the drift ratio was small, the columns were still in elastic condition, the main source of the energy dissipation came from the system (such as friction). With the increase of drift ratio, the average peak force and displacement (V_m and Δ_m) for each drift level increased quickly while the column still did not show quite obvious nonlinear behaviour thus the energy dissipation (A_h) would not increase too

much. According to Equation (2.1), the equivalent viscous damping ratio decreased gradually. The equivalent viscous damping ratio of the monolithic column reached 20.85% at the drift ratio of 5%. In comparison, the segmental columns had much smaller equivalent viscous damping ratio at this drift level, reaching approximately around 4% to 8%. Comparing column 5seg and column 5segED, the equivalent viscous damping ratio of column 5segED was higher than 5seg due to the placement of ED bars. For instance, at 5% drift the ED bars increased the ξ_{eq} value of column 5segED to about 5.6% which was approximately 35% more than that of column 5seg without ED bars. The column 7seg and 7segkey had similar value of ξ_{eq} before 4% drift level. Afterwards, column 7segkey started to experience serious concrete damage which dissipated a large amount of energy and also reduced the strength of the column. As a result, ξ_{eq} of column 7segkey increased significantly, reaching 14.3% at 6% drift ratio.

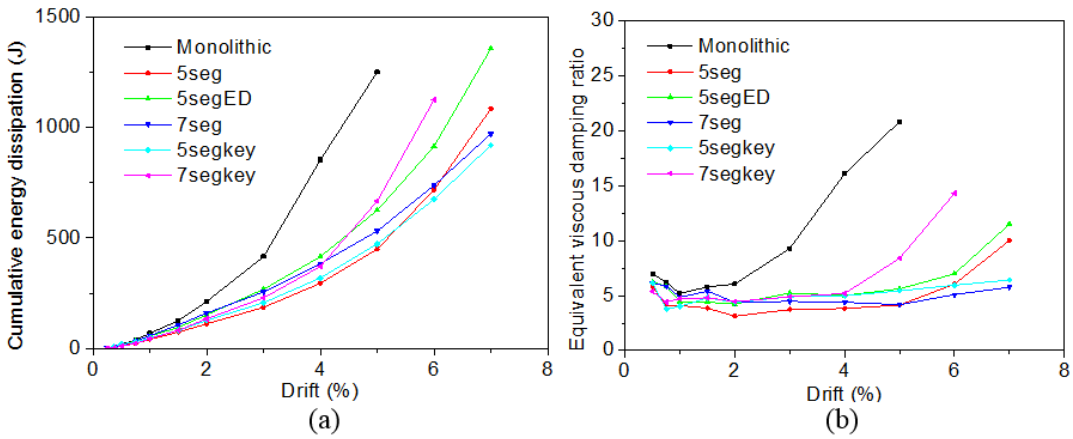

Figure 2-8 (a) Cumulative energy dissipation of the specimens, (b) Equivalent viscous damping ratio

2.4.6 Prestress tendon force

All the segmental columns tested in this study used unbonded post-tensioned tendons. The measured tendon force-drift histories of the columns under lateral cyclic loading were shown in Figure 2-9. The initial force for the tendon was labelled by a horizontal red dash line in the figure. Since the tendon was placed at the centre of the column, when the column was pushed and pulled in two directions the prestress tendon elongated as the column was forced to deform sideways. The measured force in the tendon therefore showed a V-shape relationship with the applied drift. The damage of

columns near the segmental joints resulted in plastic deformation of the column, which led to the loss of prestress in the tendon. In addition, damage and plastic deformation in the concrete near the anchorage area and possible slip of the anchorage could also result in the loss of prestressing force in the tendon. As shown in Figure 2-9 (a), for column 5seg the prestressing force started to drop obviously under repeated loading at 6% drift ratio. As the drift ratio further increased to 7%, significant drop of prestressing force was observed. The drop of prestressing force directly decreased the lateral strength of column which could be observed in Figure 2-4 (b). Similarly, for column 5segED, significant prestressing force loss happened at 7% drift. The same decrease trend of the column strength was observed in Figure 2-4 (c). The prestressing force history of column 7seg was shown in Figure 2-9 (c). Serious unsymmetrical damage of the base segment could be the reason for unsymmetrical prestressing force history. For column 5segkey, the prestressing force history was stable. No sudden prestressing force loss was observed. For column 7segkey, as shown in Figure 2-9 (e), significant prestressing force loss started after 5% drift ratio. The two base segments were damaged seriously, as shown in Figure 2-3 (f), which loosened the tendon and decreased the prestressing force. The strength of the column 7segkey was affected and underwent significant drop after 5% drift. To sum up, for the segmental column the effective prestressing force is closely related to the lateral strength. Carefully design of the prestressing force and anchorage of the tendon should be made to avoid sudden loss of prestressing force which would results in sudden loss of column strength.

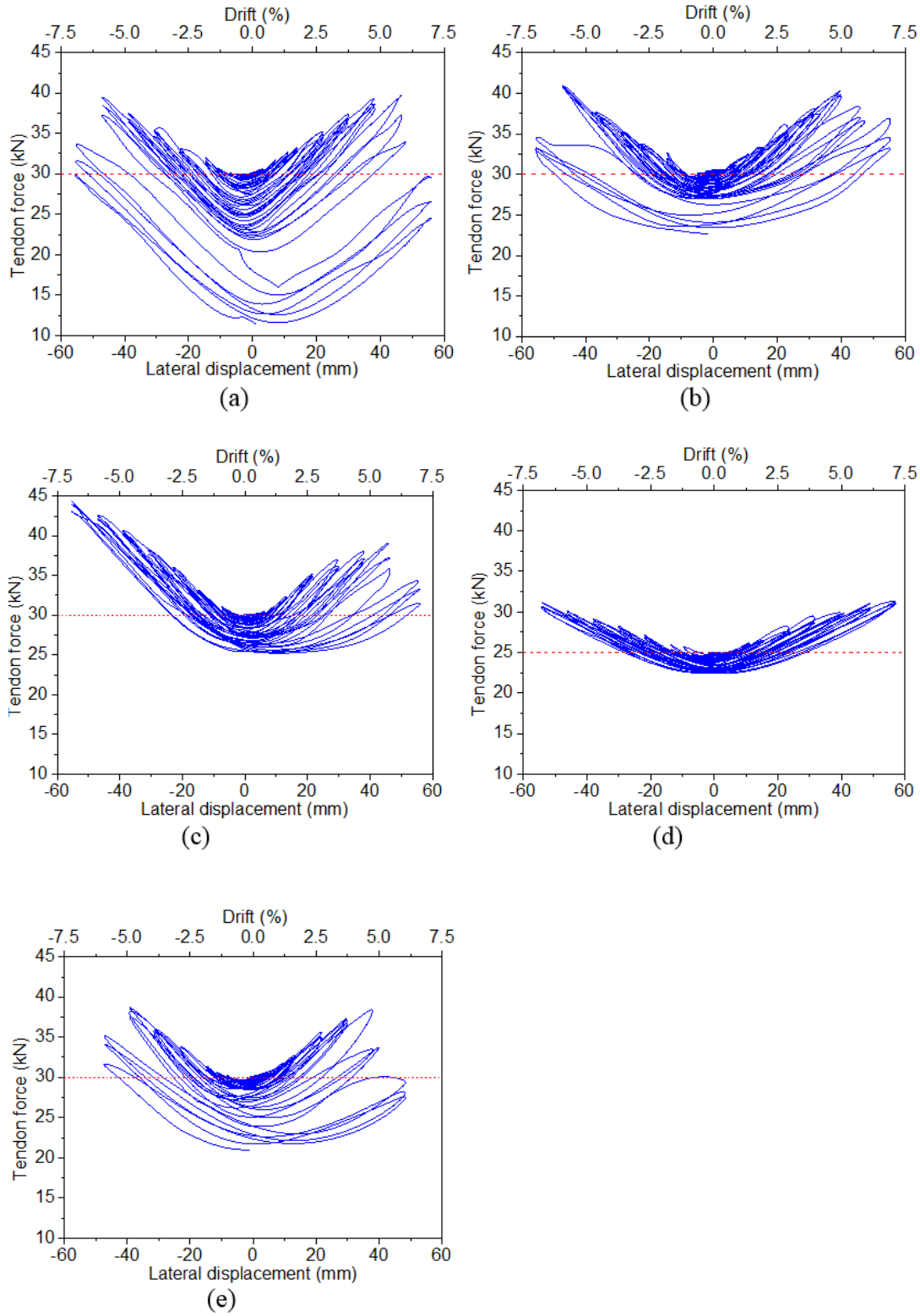

Figure 2-9 Tendon force histories (a) 5seg, (b) 5segED, (c) 7seg, (d) 5segkey, (e) 7segkey

2.5 Conclusions

This article presents results from a comprehensive experimental study that systematically investigates the seismic performance of segmental columns under lateral cyclic loading. Six columns with different designs but the same overall dimensions were tested to examine the influences of different parameters on the performances of segmental columns. Based on the experimental results, it was concluded that monolithic column failed due to flexural cracks, crushing of concrete, and fracture of longitudinal reinforcement bars while segmental columns failed primarily due to concrete compression damage near the joints. Segmental columns showed much better ductility compared with monolithic column. Due to restoring force provided by the prestress tendon, segmental columns had much smaller residual drifts comparing with that of the monolithic column. Using ED bars across all the joints, the accumulated energy dissipation and equivalent viscous damping ratio of the column could be increased. The segmental column with ED bars had slightly higher residual drift than the specimen without ED bars, but it was still small in comparison with the monolithic column. Lower prestressing force level resulted in lower maximum strength but less column damage and better ductility. The segmental column with five segments and seven segments had similar performance. The loss of the tendon force resulted in a drop of the column strength and significantly increase of the residual drift. Shear keys were able to prevent the slippage between the segments, but stress concentration could be developed near the shear keys, which could cause more crushing damage to the concrete segments. Further studies are needed to better examine the pros and cons of shear keys, which may be critical to resist lateral impact forces for the column.

2.6 References

Billington, S. L., & Yoon, J. (2004). Cyclic response of unbonded posttensioned precast columns with ductile fiber-reinforced concrete. *Journal of Bridge Engineering, 9*(4), 353-363.

Bu, Z. Y., Ou, Y. C., Song, J. W., Zhang, N. S., & Lee, G. C. (2015). Cyclic Loading Test of Unbonded and Bonded Posttensioned Precast Segmental Bridge Columns with Circular Section. *Journal of Bridge Engineering*, 04015043.

Chou, C. C., Chang, H. J., & Hewes, J. T. (2013). Two-plastic-hinge and two dimensional finite element models for post-tensioned precast concrete segmental bridge columns. *Engineering Structures, 46*, 205-217.

Chou, C. C., & Chen, Y. C. (2006). Cyclic tests of post-tensioned precast CFT segmental bridge columns with unbonded strands. *Earthquake Engineering & Structural Dynamics, 35*(2), 159-175.

Dawood, H., ElGawady, M., & Hewes, J. (2011). Behavior of segmental precast posttensioned bridge piers under lateral loads. *Journal of Bridge Engineering, 17*(5), 735-746.

Dawood, H., Elgawady, M., & Hewes, J. (2014). Factors affecting the seismic behavior of segmental precast bridge columns. *Frontiers of Structural and Civil Engineering, 8*(4), 388-398.

ElGawady, M., Booker, A. J., & Dawood, H. (2010a). Seismic behavior of posttensioned concrete-filled fiber tubes. *Journal of Composites for Construction, 14*(5), 616-628.

ElGawady, M., Booker, A. J., & Dawood, H. M. (2010b). Seismic behavior of posttensioned concrete-filled fiber tubes. *Journal of Composites for Construction, 14*(5), 616-628.

ElGawady, M., & Dawood, H. (2012). Analysis of segmental piers consisted of concrete filled FRP tubes. *Engineering Structures, 38*, 142-152.

ElGawady, M., & Sha'lan, A. (2010). Seismic behavior of self-centering precast segmental bridge bents. *Journal of Bridge Engineering, 16*(3), 328-339.

Guo, T., Cao, Z., Xu, Z., & Lu, S. (2015). Cyclic Load Tests on Self-Centering Concrete Pier with External Dissipators and Enhanced Durability. *Journal of Structural Engineering, 142*(1), 04015088.

Hewes, J. T., & Priestley, M. N. (2002). *Seismic design and performance of precast concrete segmental bridge columns* (No. SSRP-2001/25). Retrieved from University of California, San Diego, CA:

Ichikawa, S., Matsuzaki, H., Moustafa, A., ElGawady, M. A., & Kawashima, K. (2016). Seismic-Resistant Bridge Columns with Ultrahigh-Performance Concrete Segments. *Journal of Bridge Engineering*, 04016049.

Marriott, D., Pampanin, S., & Palermo, A. (2009). Quasi-static and pseudo-dynamic testing of unbonded post-tensioned rocking bridge piers with external replaceable dissipaters. *Earthquake Engineering & Structural Dynamics, 38*(3), 331-354.

Mashal, M., White, S., & Palermo, A. (2013). *Quasi-static cyclic tests of Emulative Precast Segmental Bridge Piers (E-PSBP)*. Paper presented at the 2013 NZSEE Conference Wellington, New Zealand.

Motaref, S., Saiidi, M., & Sanders, D. (2010). Experimental study of precast bridge columns with built-in elastomer. *Transportation Research Record: Journal of the Transportation Research Board*(2202), 109-116.

Nikbakht, E., Rashid, K., Hejazi, F., & Osman, S. A. (2014). A numerical study on seismic response of self-centring precast segmental columns at different post-tensioning forces. *Latin American Journal of solids and structures, 11*(5), 864-883.

Ou, Y. C., Tsai, M. S., Chang, K. C., & Lee, G. C. (2010). Cyclic behavior of precast segmental concrete bridge columns with high performance or conventional steel reinforcing bars as energy dissipation bars. *Earthquake Engineering & Structural Dynamics, 39*(11), 1181-1198.

Ou, Y. C., Wang, P. H., Tsai, M. S., Chang, K. C., & Lee, G. C. (2009). Large-scale experimental study of precast segmental unbonded posttensioned concrete bridge columns for seismic regions. *Journal of Structural Engineering, 136*(3), 255-264.

Priestley, M. N., Seible, F., & Calvi, G. M. (1996). *Seismic design and retrofit of bridges*: John Wiley & Sons.

Shim, C. S., Chung, C. H., & Kim, H. H. (2008). Experimental evaluation of seismic performance of precast segmental bridge piers with a circular solid section. *Engineering Structures, 30*(12), 3782-3792.

Tazarv, M., & Saiid Saiidi, M. (2015). Low-Damage Precast Columns for Accelerated Bridge Construction in High Seismic Zones. *Journal of Bridge Engineering*, 04015056.

Yamashita, R., & Sanders, D. H. (2009). Seismic performance of precast unbonded prestressed concrete columns. *ACI Structural Journal, 106*(06).

Zhang, X., Hao, H., & Li, C. (2016). The effect of concrete shear key on the performance of segmental columns subjected to impact loading. *Advances in Structural Engineering*, 1369433216650210.

CHAPTER 3 CYCLIC TEST AND NUMERICAL STUDY OF PRECAST SEGMENTAL CONCRETE COLUMNS WITH BFRP AND TEED

3.1 Abstract

Previous studies on the seismic behaviour of precast segmental concrete column revealed that concrete crushing and spalling damages may occur at the toes of the segments due to rocking between segments at the joints. In addition, the energy dissipation capacity of segmental column is smaller than the conventional monolithic column. Energy dissipation bars therefore have been proposed to increase its energy dissipation capability. The energy dissipation bars, however, increase the residual displacement of the column, which degrades the most advantageous characteristic of precast segmental column. To solve these problems, this paper proposes wrapping the segments with basalt fibre-reinforced polymer (BFRP) to reduce the concrete compressive damage and using Tension-only External Energy Dissipation (TEED) devices to dissipate energy. Compared to other FRP materials, BFRP has better mechanical properties and costs less. The proposed TEED device can keep the residual displacement of the column at small level while improving the energy dissipation capacity of the column due to its special design. Experimental cyclic tests are carried out to examine the effectiveness of the proposed method. The results show that the damage of the segments could be effectively reduced by using BFRP, and the columns show good ductility and almost no strength degradation. The TEED devices are effective to increase the energy dissipation capacity of the column while keeping the residual displacement small.

3.2 Introduction

Bridge construction activities often cause site disruptions due to occupation of large working areas and long construction time. This is a critical problem for urban regions where traffic conditions are generally heavy. Precast segmental column has attracted extensive research interests recently as a rapid construction solution. The precast segmental column normally includes concrete segments that are precast in the prefabricated factories and posttensioned tendons which are used to connect the segments together. The onsite construction activities only include the installation of

precast segments and applying posttensioned forces to the tendons to clamp the segments. The construction time, therefore, can be greatly reduced and the traffic disruption can be significantly minimized. Moreover, since the concrete segments are prefabricated in the factories, the qualities of the segments can be better controlled and the working conditions for workers are improved. It is becoming a promising solution for rapid construction in the congested urban areas. However, due to the lack of knowledge on its seismic performance, precast segmental columns are mainly applied to the areas with low seismicity. In recent years, some studies have been carried out to investigate the seismic performance of precast segmental columns to widen its applications in earthquake prone areas (Billington & Yoon, 2004; Chou & Chen, 2006; ElGawady et al., 2010; Leitner & Hao, 2016; Li et al., 2018; Mashal & Palermo; Ou et al., 2009; Shim et al., 2008; Shim et al., 2017; Zhao et al., 2017; Zhao et al., 2018).

For the traditional monolithic concrete columns under earthquake excitations, concrete cracks, concrete spalling damages, and steel reinforcement yielding are normally developed, forming plastic hinge in the column. In comparison, for the precast segmental concrete column, when the lateral load is applied to the column, openings will be developed at the joints between the segments instead of forming the tensile concrete cracks. Due to the joint opening, the segments rock against each other and excessive compressive stress can be developed in the concrete segments at the rocking joints. Concrete crushing damage is therefore commonly observed at the column joints when the column is subjected to the seismic loadings (Bu et al., 2015; Wang et al., 2008). To reduce such damage in the segments, strengthening methods such as using high performance concrete (Billington & Yoon, 2004; Ichikawa et al., 2016), confining the segments with steel jacket (Chou & Chen, 2006; Hewes & Priestley, 2002), and using replaceable rubber hinge at the bottom of the column (Varela & Saiidi, 2016) were proposed and investigated.

Some studies also investigated the effectiveness of using fibre-reinforced polymer (FRP) to wrap the segments to mitigate the compressive damage (ElGawady et al., 2010; Guo et al., 2015; Motaref et al., 2013). According to the types of fibre material, FRP can be categorized into carbon fibre-reinforced polymer (CFRP) and glass fibre-reinforced polymer (GFRP). Recently, basalt fibre has attracted increasing attention as an alternative to the commonly used carbon and glass FRPs because of its low cost

and good mechanical properties. Basalt fibres are made from basalt rocks by melting the rocks and forming the basalt filaments. No additives are required and lower amount of energy is needed during the manufacturing process, which consequently reduces the cost and also the environmental impact. Another important advantage of BFRP is its excellent mechanical properties. Compared with glass fibres, basalt fibres have higher strength (Artemenko, 2003). It was also reported that basalt fibres have about 35-42% higher Young's modulus than glass fibres (Lopresto et al., 2011). Though the strength of basalt fibres is lower than carbon fibres, they are less brittle, and a lot cheaper than carbon fibres (Artemenko, 2003; Dhand et al., 2015). Due to these advantages, it is a promising material that can be used as an alternative among the fibre reinforcement materials available currently to strengthen the structure components in the construction industry. In this study, basalt fibre-reinforced polymer (BFRP) is adopted to strengthen the concrete segments considering its excellent mechanical properties and low cost.

Early types of precast segmental columns normally consist of posttensioned tendons and precast segments. The segments are connected by the posttensioned tendons only and no steel reinforcement passes across the joints between the segments. Previous studies revealed that this kind of design shows very good ductility and outstanding self-centring ability. However, the energy dissipation capacity of the column is low (Chou & Chen, 2006; Hewes & Priestley, 2002; Ou et al., 2009). To increase the energy dissipation ability of segmental column, internal energy dissipation (ED) bars (Guerrini et al., 2015; Li et al., 2017; Marriott et al., 2009; Ou et al., 2010; Wang et al., 2008) were proposed and investigated. For the internal ED system, corrugated tubes are placed in the formwork of the prefabricated elements before casting. These holes allow the ED bars to pass through and are grouted with cementitious materials after installation of the segments and ED bars. According to the previous studies, the internal ED bars are effective to increase the energy dissipation capacity of the precast segmental columns (Li et al., 2017; Nikbakht & Rashid, 2018; Ou et al., 2009). However, the use of internal ED bars could increase the residual displacement due to the plastic deformation (Li et al., 2017; Ou et al., 2009; Wang et al., 2008). Another disadvantage of internal ED bars is that they are difficult to be repaired and retrofitted after fracture or yielding during a severe earthquake event since they are grouted together with the concrete.

To overcome this problem, the external ED devices were then proposed (Chou & Chen, 2006; ElGawady & Sha'lan, 2010; Palermo et al., 2007; Wang et al., 2018). For example, Chou et al. (2006) tested two precast concrete filled steel tube segmental columns under cyclic loading, one of the columns had no ED device and the other one had ED devices made of Reduced-Steel-Plate (RSP). It was found that the RSP devices were effective to increase the energy dissipation capacity of the column with the equivalent viscous damping ratio increased from 6.5% to 9%. However, buckling of the RSP devices were found during compression, which resulted in larger residual displacement. Marriott et al. (2009) proposed external energy device that was similar to the buckling restrained braces (BRB) to increase the energy dissipation capacity of rocking columns. The device consisted of a mild steel round bar with reduced diameter, bolt thread parts at both ends for connection, and an external round steel tube filled with grout or epoxy to restrain buckling. Sarti et al. (2016) carried out extensive studies on similar fuse-type external energy dissipation devices and it was found that contact between the internal bar and the external steel tube could occur during compression, which caused a sway mechanism in the external restraining tube. Once the slenderness ratio became large, buckling could also happen to the device. Very recently, Wang et al. (2018) proposed using a core zone, replaceable UHPC cover plates, and replaceable dissipaters between the core zone and cover plates in the bottom segment of the precast segmental columns to achieve rapid repair after an earthquake. It was found that the replaceable dissipaters buckled during the test and the buckling deformation of the dissipaters led to a lateral extrusion force on the cover plates which finally caused bending failure of the cover plates. Serious buckling of the dissipaters also increased the residual drift of the segmental columns.

These studies have demonstrated the effectiveness of using external ED devices to increase the energy dissipation of precast segmental column. However, as mentioned above, buckling may occur to these devices when they are under compression, resulting in an increase in the residual displacement of the column. To overcome this problem, this study introduces a Tension-only External Energy Dissipation (TEED) device to increase the energy dissipation while avoiding buckling. This design concept was inspired by the non-buckling segmented brace proposed by Hao (2015). The non-buckling segmented brace consists of steel segments connected by tension only joints. It behaves similar to the conventional brace under tension, while under compression,

it can slide without or with limited resistance. Therefore, buckling of the brace can be avoided. Excellent performance was observed in the cyclic tests on this new tension-only brace member (Hao, 2015). The TEED device proposed in this study consists of a simple steel plate with a fixing hole and a sliding slot (refer to Figure 3-2). The device will elongate and dissipate energy when it is under tension, while there is no resistance when it is under compression since the connection bolt can slide in the slot, therefore buckling of the device can be avoided with such design.

This article proposes using BFRP to wrap the segments of segmental column to mitigate the compressive damage at the joints of the segments, and adopting TEED devices to increase the energy dissipation capacity of the precast segmental column. This design has the following obvious advantages compared to the previous commonly adopted methods: (1) the possible damages at the joints of the segments can be significantly reduced with low additional cost; (2) the energy dissipation capability is increased while keeping the residual displacement of column small. Quasi-static cyclic tests are performed to examine the effectiveness of the proposed method.

3.3 Experimental program

3.3.1 Specimen design

Three specimens were designed and fabricated in the present study. Figure 3-1 shows the schematic view of these specimens and Table 3-1 summarizes the design details. Column S0 was the reference column without any strengthening and energy dissipation devices. Column S1 was similar to S0 except that all the segments were wrapped with BFRP to confine the concrete segments and reduce the concrete damage. Column S2 was similar to column S1, but TEED devices were installed to increase the energy dissipation capability. The specimen was scaled from an actual column with a height of 3.2 m (Zhang et al., 2016), and the scaling factor was chosen as 1/4 considering the capacity of the loading equipment. The steel ratios were kept the same as that in the prototype column. The dimensions of the columns were restricted by the capacity of the available cyclic testing equipment in the lab, and a height of 800 mm and a cross section of 100×100 mm were selected for all the columns. Each column consisted of five segments, the height of each segment was 160 mm. It should be noted

that shear keys between the segments were found to be effective to increase the shear resistance of the segmental columns (Li et al., 2017; Zhang et al., 2016). However, previous studies also demonstrated that introducing large trapezoid-shape concrete shear keys might lead to stress concentration and result in serious damages in the concrete segments (Li et al., 2017; Zhang et al., 2016). In the present study, a domed-shape shear key with the radius of 107 mm (Figure 3-1 (c)) was designed at the bottom of each segment to improve the shear resistance of the column between the segments while minimizing the stress concentration.

Four longitudinal steel bars with a diameter of 6 mm and four transverse stirrups with 4 mm diameter were used in each segment to hold the longitudinal reinforcements. The longitudinal reinforcement ratio and volumetric stirrup ratio were 1.13% and 1.57%, respectively. It should be noted that since the longitudinal reinforcements discontinue at segment joints, they do not contribute to the lateral resistance of the column. Two starter bars with 6 mm diameter were used to connect the base segment and footing in the lateral loading direction. The longitudinal steel bars were discontinuous at the segment joints, i.e., the joints between the segments were free to open when the column was subjected to lateral loading. All the segments were precast and then stacked together one by one. A tendon that located at the centre of the column was used to clamp the segments together with posttension force. The tendon used in this study was a seven-wire high strength prestress strand with an area of 54.7 mm^2. The corresponding prestressing tendon steel ratio was 0.547%. The posttensioned tendon was anchored at a recess in the footing and the top of the mass blocks, and the dimension of the concrete footing was 400 × 400 × 140 mm (length × width × height).

The design concept of the TEED device is to allow it to take force and dissipate energy under tension while having no resistance to compression, so that the posttension tendon can pull the deformed column back to its original position and thus keeping the residual displacement of the column small. Figure 3-2 shows the design details of the TEED device. As shown, a dog-bone shape was selected to facilitate the energy dissipation. Considering the possible deformation of the columns, the total length, width and thickness of the device were selected as 114 mm, 26 mm and 2 mm, respectively. As illustrated in Figure 3-2, a circular hole was designed as a fixing end and a sliding slot hole was designed as a sliding end. The bolt in the sliding slot could

hold the device and allow the device to elongate in tension, while in compression it could slide in the slot free without any resistance. Since no compressive force could be induced in the plate, buckling of the device could be avoided. Bolts that were used to fix the TEED devices to the column were placed at the designed positions in the formwork before concrete casting.

The columns were prepared and cast in the Structural Lab in the University of Western Australia. After the curing of the segments, two layers of BFRP were wrapped to the concrete segments with epoxy resin (Sikadur 30). According to the specification as suggested in ACI 440.2R-08 (Bakis et al., 2002), the corners of the square cross section of the segments were rounded to a radius of 13 mm to avoid stress concentrations to the BFRP wrapping. The tensile strength, elastic modulus, ultimate strain, and the thickness of the BFRP were 2100 MPa, 105 GPa, 2.1% and 0.12 mm, respectively. The corresponding material properties of the concrete, steel, BFRP and prestressing strand used in the tests are summarized in Table 3-2, in which ρ is density, f_c' and f_t are the compressive and tensile strengths of concrete, f_y is the yield strength and E is Young's modulus.

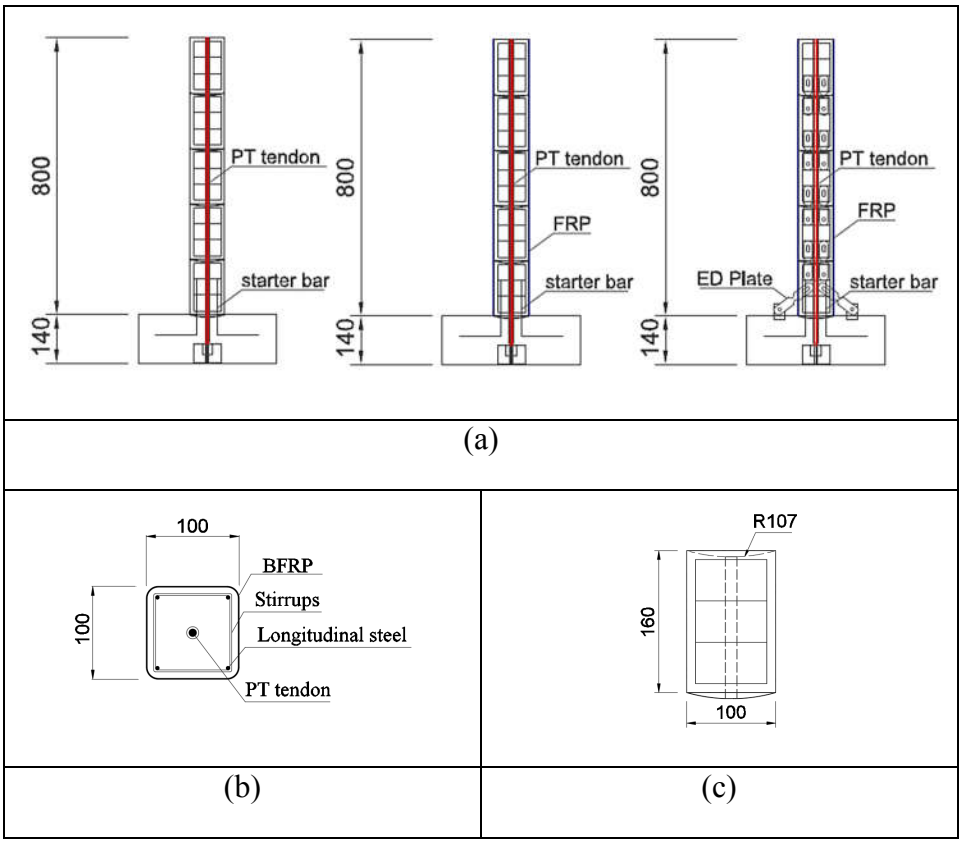

Figure 3-1 Schematic drawings of the specimens (a) elevation view, (b) cross section and (c) details of the segment and domed-shape shear key

Table 3-1 Summary of design details

Name	Strengthening	Energy dissipation	Height (mm)	Cross section (mm × mm)
S0	No	No	800	100 × 100
S1	BFRP	No	800	100 × 100
S2	BFRP	TEED	800	100 × 100

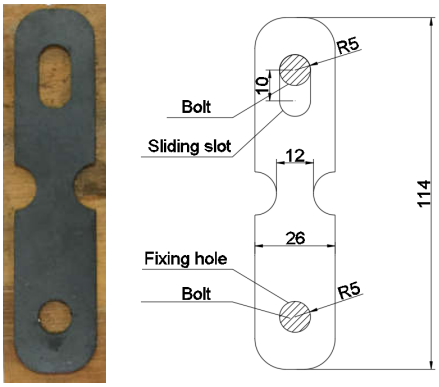

Figure 3-2 Details of TEED device

Table 3-2 Material properties

Material	ρ (kg/m^3)	f_c' (MPa)	f_t or f_y (MPa)	E (GPa)
Concrete	2400	34	3.6	30
Longitudinal rebar	7800	-	500	200
Stirrup	7800	-	300	200
ED plate	7800	-	300	200
BFRP	2500	-	2100	105
Prestress tendon	7850	-	1860	195

3.3.2 Test setup and loading protocol

Figure 3-3 shows a photograph and a schematic view of the cyclic testing system used to perform the experimental studies. As shown, the system included a strong beam, a

reaction frame, an actuator, a protection frame and three top mass blocks. The strong beam was used to fix the column and the reaction frame. The beam was firmly fixed to the strong floor in the lab. The actuator was connected to the reaction frame and the specimen. To protect the actuator, two spherical hinges were installed at both ends to release the possible bending moment. During the installation process, the tendon was first inserted to the footing which was fixed to the strong beam, and then the segments were stacked one by one. After all the segments were installed, the top mass blocks were placed onto the column. The top mass blocks included one concrete block with a dimension of 400 × 400 × 450 mm (length × width × height), and two steel blocks with dimensions of 500 × 240 × 150 mm. The total dead weight of the three mass blocks was around 450 kg. The prestressing tendon was stressed to 30 kN by a hydraulic jack after the mass blocks were placed at the correct position. The total axial force in the column was 34.55 kN, which was approximately 10.16% of the axial load capacity of the column.

After the installation of the column, displacement controlled lateral loads were applied to the column with different drift ratios including 0.25%, 0.375%, 0.5%, 0.75%, 1.0%, 1.5%, 2.0%, 3.0%, 4.0%, 5.0%, 6.0%, respectively. Here the drift ratio is defined as the displacement at the loading point divided by the distance between the top surface of the footing and the loading point. For each drift ratio, the load was repeated twice to examine the strength degradation at the same displacement amplitude. Figure 3-4 shows the loading protocol used in the tests. The lateral force applied to the column was measured by using the load cell of the actuator and the displacement of the column was recorded by the LVDT as shown in Figure 3-3 (b).

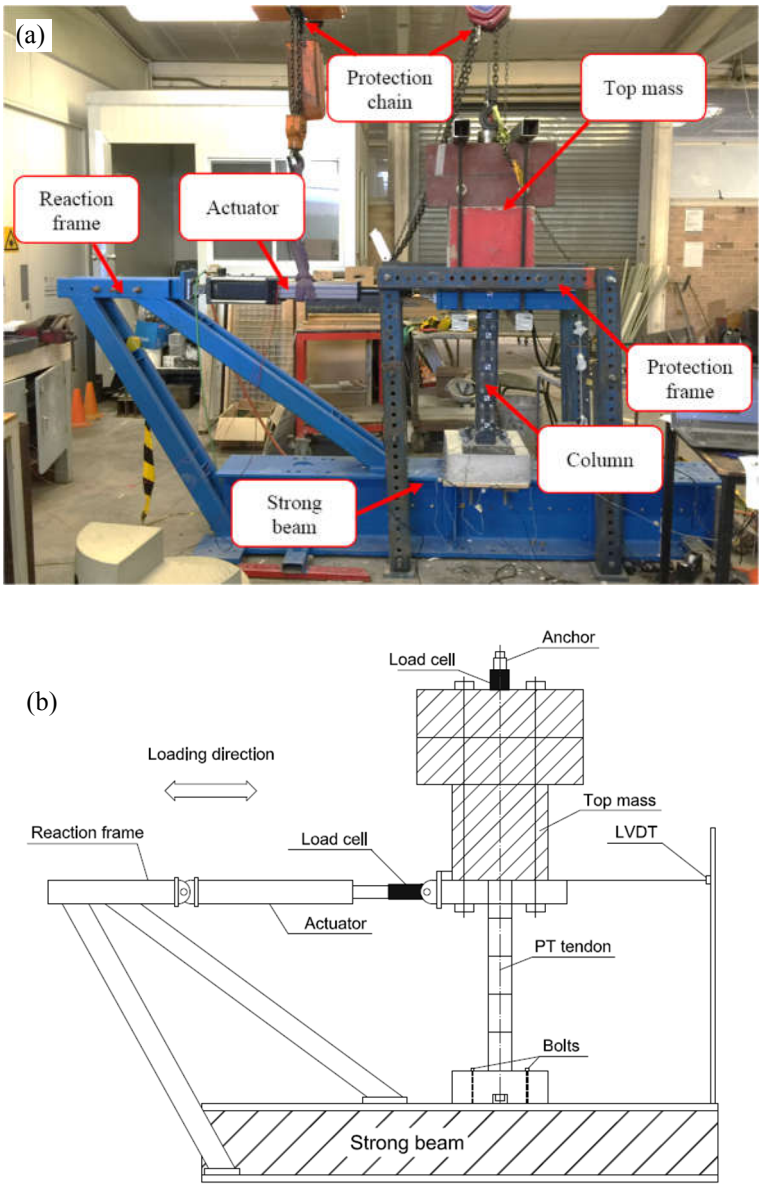

Figure 3-3 (a) Photograph of the testing setup; (b) Schematic of the testing setup

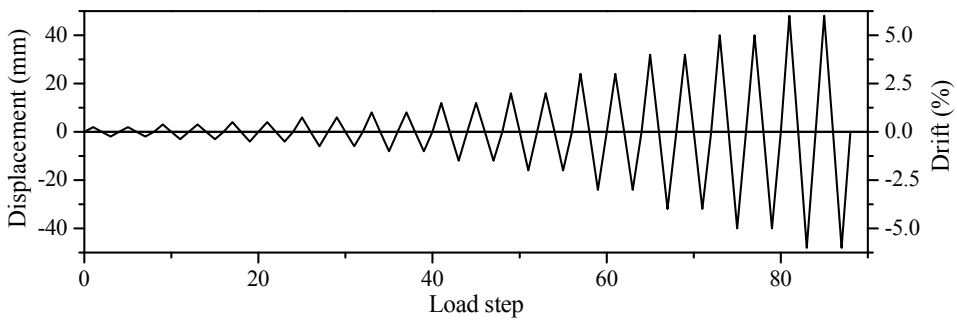

Figure 3-4 Loading sequence

3.4 Test results and discussions

3.4.1 Observed damage patterns

Figure 3-5 illustrates the damage patterns of the three columns after tests. As shown in Figure 3-5 (a), column S0 experienced concrete damage near the joint between the two bottom segments. This is because the bottom segment was connected to the footing with starter bars, opening at this joint was therefore restrained and the opening was shifted to the joint between the two bottom segments. Due to the joint opening, the toes of the segments experienced excessive compressive stress, which in turn caused the spalling and crushing damages to the concrete segments as observed in Figure 3-5 (a). Figure 3-5 (b) shows the view of column S1 at the end of the test. No visible damage was observed in the segments due to the confinement provided by BFRP, which demonstrated that BFRP was effective to strengthen the column segments and prevent the crushing and spalling damages of precast segmental column under cyclic loading. Figure 3-5 (c) shows the final view of column S2 when both BFRP and TEED were applied. Similar to the column S1, no visible damage of concrete or fracture of BFRP was observed. Also, no buckling of the TEED device was observed during the test, which demonstrated that the proposed TEED device met the design purpose. The improvement of the energy dissipation ability of the column resulted from the use of TEED devices will be discussed quantitatively in the following sections.

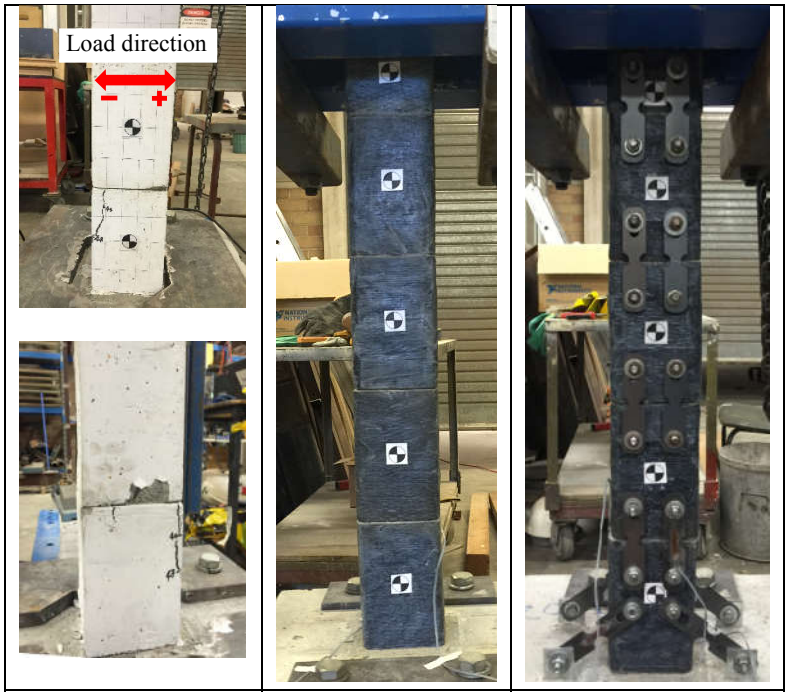

(a)	(b)	(c)

Figure 3-5 Views of the three columns after test: (a) S0, (b) S1 and (c) S2

3.4.2 Hysteretic curves and backbone curves

The hysteretic curves and backbone curves of the three columns are shown in Figure 3-6 and Figure 3-7, respectively. As shown in Figure 3-6, the columns showed very good self-centring ability and ductility, all the columns did not fail at 6% drift ratio. For column S0, it behaved linearly until the drift ratio reached approximately 0.5%. After that, the strength showed obvious nonlinearity due to the opening of the joint and damage in concrete segments. The results also show that the hysteretic curves were not exactly symmetrical and the strength in the negative displacement direction showed slight degradation after 4% drift ratio, which could be attributed to the more severe concrete damage in the negative displacement direction as shown in Figure 3-5 (a). This is also reflected in the backbone curve as shown in Figure 3-7. It can be seen that the strength of the column (the black curve in Figure 3-7) in the positive displacement direction was almost a constant (about 1.94 kN) when the drift ratio was larger than 2%. In the negative displacement direction, it reached 2.10 kN at 4% drift ratio and decreased to 2.03 kN at 6% drift ratio due to the damage in the bottom segment.

Figure 3-6 (b) shows the hysteretic curve of S1. It can be seen that the curve was almost symmetrical in the positive and negative displacement directions and the strengths in the both directions showed no obvious degradation due to the confinement of the BFRP. The maximum lateral force in the positive and negative displacement directions were 2.10 kN and 2.12 kN, respectively as shown in Figure 3-7 (the red curve), which were close to those of column S0. This is because the fibres of the BFRP were unidirectional and also discontinuous across the joints of the segments, it could provide confinement to the segments and thus prevent the cover concrete from damage but it would not directly increase the lateral loading strength of the column. However, it should be noted that column S0 experienced slight strength degradation which was not observed in column S1, indicating that the BFRP could mitigate the damages and improve the ductility of the column.

The hysteretic curve of column S2 is shown in Figure 3-6 (c) and the corresponding backbone curve is also shown in Figure 3-7 (the blue curve). As expected, the column had higher strength due to the use of TEED devices, the maximum strengths in the positive and negative displacement directions reached 2.5 kN and 2.7 kN, respectively, which were larger than those obtained in columns S0 and S1. Moreover, the area of the hysteretic curve was larger in comparison with the column S1, indicating the TEED devices were effective to increase the energy dissipation of the column.

The residual drift is an important parameter for columns because large residual displacement can impede the post-quake rescue and retrofitting activities. For the three columns, the residual displacements were quite small, with the averaged values of 2.2 mm, 2.1 mm and 2.8 mm respectively at the 6% drift ratio. This can be attributed to the prestressing tendon which could pull the columns back to the original positions. The residual displacement in column S1 was slightly smaller than S0. For the column S2, installation of the TEED device slightly increased the residual displacement compared to S1, but the increment was very small, indicating the advantage of the TEED device, i.e. it can increase the energy dissipation capacity of the column while not increasing the residual displacement significantly. This is different from other energy dissipation devices such as the internal ED bars. For example, as reported by Bu et al. (Bu et al., 2015), the residual displacement increased from 5.7 mm to 16.3 mm at 7% drift ratio when the internal ED bars were used.

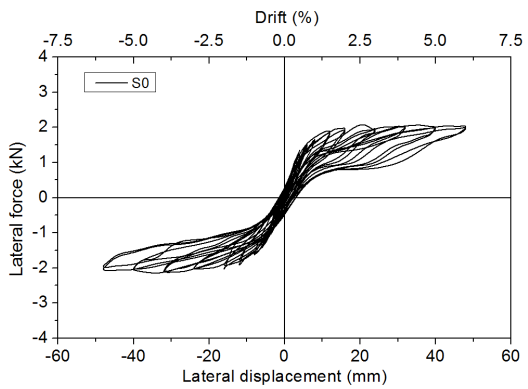

(a)

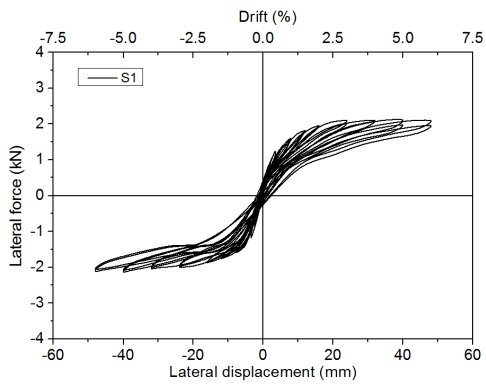

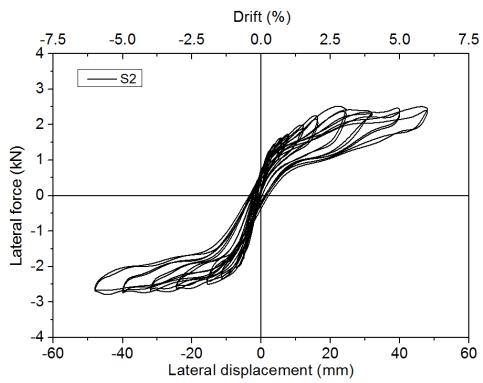

(b) (c)

Figure 3-6 Hysteretic curves of the three columns: (a) S0, (b) S1, (c) S2

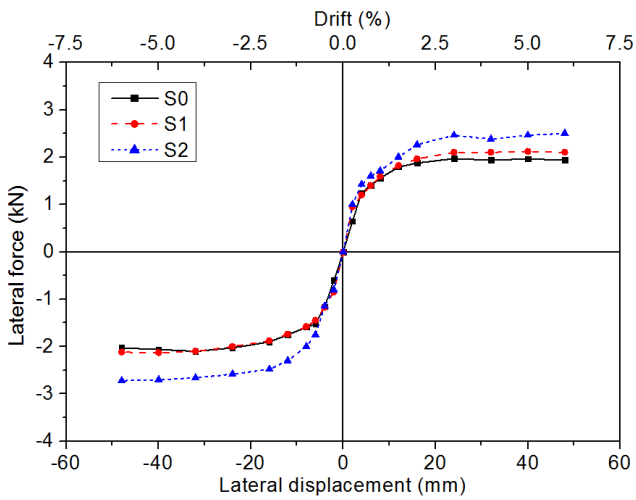

Figure 3-7 Backbone curves of the columns

3.4.3 Hysteretic energy dissipation and equivalent viscous damping ratio

The energy dissipation of the column under cyclic loading is the area enclosed by the hysteretic curves, and it can be calculated by integrating the hysteretic loops. Figure

3-8 shows the cumulative energy dissipation of the specimens. It can be observed that the columns dissipated nearly the same amount of energy when the drift ratio is less than 1% due to the very minor damage and plastic deformations of the specimens. When the drift ratios became larger, more evident differences could be observed. As shown, column S1 dissipated the least amount of energy and column S2 resulted in the most evident energy dissipation capability. In particular, the cumulative energy dissipation reached around 348.9 kN.mm, 199.3 kN.mm and 423.9 kN.mm for columns S0, S1 and S2, respectively at 6% drift ratio. Compared to S0, 42.9% less energy was dissipated by column S1 due to that less damage was developed in the segments, which again demonstrated the effectiveness of using BFRP to mitigate the concrete damage. For column S2, it can be seen that 112.7% more energy was dissipated compared to the column S1, which showed the very good energy dissipation capability of the proposed TEED device. It might worth reiterating again that the proposed device on the other hand did not significantly increase the residual displacement of the column.

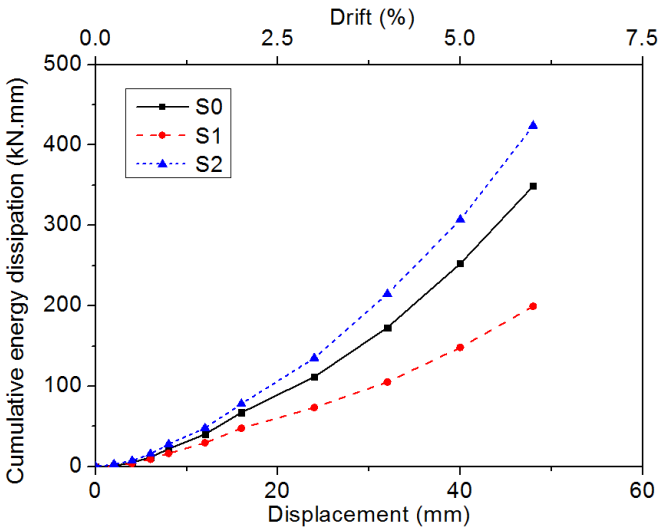

Figure 3-8 Cumulative energy dissipation of the columns

The hysteretic energy dissipation of the specimens can be evaluated by the equivalent viscous damping ratio (ξ_{eq}), which can be calculated by Equations (3.1-3.3) as suggested by Priestley et al. (Priestley et al., 1996).

$$\xi_{eq} = \frac{A_h}{2\pi V_m \Delta_m} = \frac{A_h}{2\pi K_{eff} \Delta_m^2} = \frac{A_h}{4\pi A_e} \tag{3.1}$$

$$V_m = \frac{|V_{max}| + |V_{min}|}{2} \tag{3.2}$$

$$\Delta_m = \frac{|\Delta_{max}| + |\Delta_{min}|}{2} \tag{3.3}$$

where A_h is the energy dissipation of each cycle; V_m is the average peak force and Δ_m is the corresponding displacement of each cycle; K_{eff} is the stiffness of the equivalent linear elastic system; A_e is the elastic strain energy. Figure 3-9 shows a schematic drawing of the parameters described above and Figure 3-10 shows the calculated equivalent viscous damping ratios of the three columns. It can be found that column S1 resulted in the smallest equivalent damping ratio among the three columns due to the limited energy dissipation as shown in Figure 3-8. For columns S0 and S2, similar damping ratios were obtained and the values ranged from 6.1% to 7.9% as shown in Figure 3-10. However, it should be noted that the damping mechanisms of the two columns were different. For the column S0, the large damping was because of the concrete damage at the joints, while for column S2, it mainly came from the energy dissipation devices, i.e. the TEEDs and starter bars. It also should be noted that though more energy was dissipated by column S2 compared to column S0 at the same drift ratio as shown in Figure 3-8, the equivalent damping ratios of the two columns were however similar. This is because as defined in Equation (3.1), besides the dissipated energy, ξ_{eq} is also related to the lateral force (V_m in Equation (3.2)). For column S2, though more energy was dissipated, the strength of the column was also larger compared to S0. In summary, based on the discussions above, the BFRP could effectively minimize the damage of the column. With the added TEED devices, the energy dissipation capability of the column was evidently increased, while the residual displacement was only slightly increased compared to the original column S0. All these results demonstrate the effectiveness and advantages of using BFRP and TEED to improve the seismic performances of precast segmental columns.

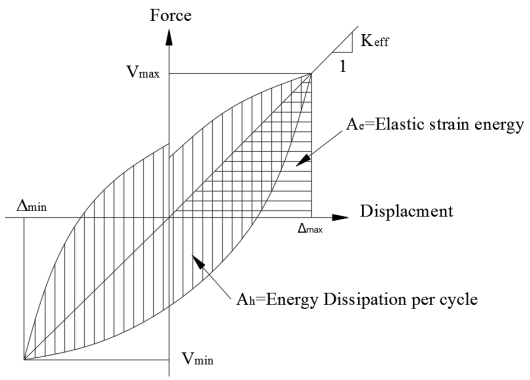

Figure 3-9 Schematic figure for the parameters of equivalent viscous damping ratio

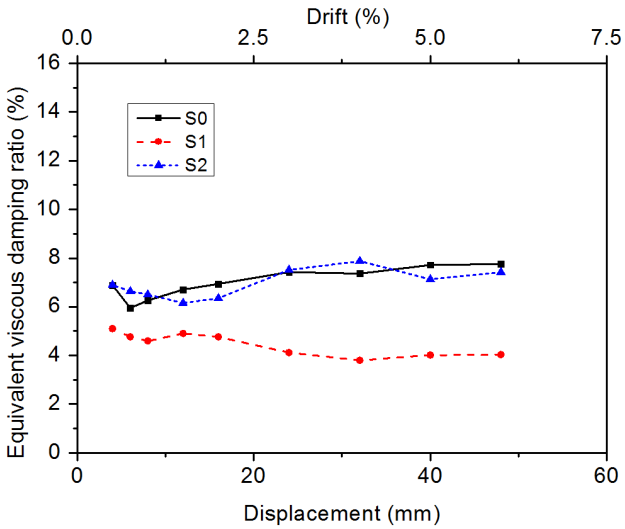

Figure 3-10 Equivalent viscous damping ratios of the columns

3.5 Numerical study

In this part, three dimensional (3D) finite element (FE) models are developed to simulate the behaviours of the precast segmental columns tested in the present study. The commercially available FE program ABAQUS/Standard (Simulia, 2012) is adopted to perform the simulations. In particular, the modelling details of each component of the column and the interactions between different parts are described and summarized first, then the numerical results are compared with the test results in section 3.5.2.

3.5.1 Modelling details

Figure 3-11 shows the FE models of the three columns. The concrete components, including the precast concrete segments, footing, loading block, are modelled by the

3D solid elements (C3D8R) in the present study. After the mesh convergence tests, the mesh sizes are chosen as 10 mm for the column segments, 30 mm for the footing and 50 mm for the loading block. In ABAQUS, the concrete damaged plasticity model (CDP) is the most suitable one to simulate the performance of the reinforced concrete structures under repeated cyclic loading (Simulia, 2012), which is therefore adopted in this study. The CDP model needs the inputs of five plasticity parameters and the uniaxial stress-strain relationship of the concrete. The five plasticity parameters are the dilation angle (ψ), the flow potential eccentricity (e), the ratio of initial equibiaxial compressive yield stress to initial uniaxial compressive yield stress (σ_{b0}/σ_{c0}), the coefficient to define the shape of the deviatoric cross-section (K_c), and the viscosity parameter (μ). Table 3-3 summaries the definitions and values of these parameters as suggested in some previous study (Demir et al., 2016). For the concrete stress-strain relationship, the model proposed by Mander et al. (1988) is used for column S0 for the normal concrete segments and the model provided in ACI 440.2R-08 (Bakis et al., 2002) is adopted for columns S1 and S2 for the BFRP confined concrete.

Table 3-3 Input parameters

Parameter	Value	Explanation (Simulia, 2012)
ψ	30	Dilation angle
e	0.1	Flow potential eccentricity
σ_{b0}/σ_{c0}	1.16	The ratio of initial equibiaxial compressive yield stress to initial uniaxial compressive yield stress
K_c	0.6667	The coefficient determining the shape of the deviatoric cross-section
μ	0.0001	Viscosity parameter

The longitudinal reinforcements and transverse reinforcements are modelled as truss elements (T3D2). No bond slip between the steel and concrete is considered in the simulation, and 'embedded constrains' in ABAQUS are used to model such behaviour. Since there was a gap between the tendon and the reserved hole in the concrete segments, the prestressing tendon is modelled as 3D solid elements (C3D8R) to more realistically simulate the gap between the tendon and the segments (Li et al., 2017).

Surface to surface contact elements are used to model the contact between the tendon and the segments. For the column S2 with TEED devices, solid elements were used to model the TEED devices, and a mesh size of 3 mm is selected. The bolts that cast in the segments to connect the TEED devices are also modelled as solid elements and surface to surface contact elements are adopted for the interactions between the TEED devices and the bolts. The classical elastic-perfectly plastic stress-strain material model is used for the steel material (Nikbakht et al., 2015). For the column S1 and S2 with BFRP confinement, the FRP jacket is modelled by the membrane elements (M3D4R). Linear elastic laminar material property is assigned to the elements in the fibre hoop direction, which is defined to simulate the confinement effect of the FRP jacket. The material parameters for the BFRP are listed in Table 3-2. No bond slip is considered between the FRP and the concrete, and 'tie' constrain is used to connect the concrete and FRP jacket (Yuan et al., 2017). To model the joint openings of the segmental column under cyclic loading, surface to surface contact elements are adopted again. Hard contact and tangential friction are used to model the normal contact between the surfaces and the tangential behaviour, respectively. The friction coefficient of the tangential contact is assumed to be 0.5 as recommended by some previous studies (e.g. (Dawood et al., 2011)). For the boundary condition, the fixed footing is modelled by constraining the bottom and top surface of the footing. The anchorages of the tendons are modelled by embedding two ends of the tendons in the surrounding concrete.

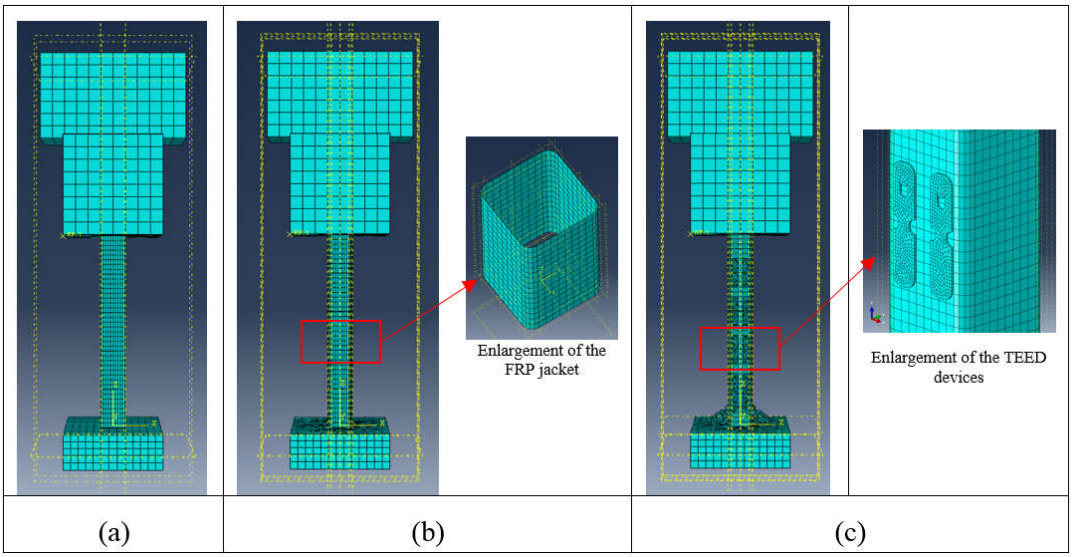

Figure 3-11. FE models of the three columns: (a) S0, (b) S1, (c) S2

3.5.2 Numerical results

Figure 3-12 compares the damage patterns of column S0 observed in the test and in the numerical simulation. Comparisons of the damage patterns of column S1 and S2 are not given here because no obvious damages were observed in the tests and in numerical simulations. As shown, the numerical model well captures the damage developed at the joint. However, it should be noted that the damage across the section is symmetrical in the numerical simulation, the observed damage in the test was, however, not exactly symmetrical. This could be the tested specimen is not exactly symmetric in the test and minor construction imperfection may obviously influence the results considering the small dimension of the scaled specimens, while no such problem exists in the numerical simulations. This is also reflected in the hysteretic curves and backbone curves as shown in Figure 3-13 and Figure 3-14. As shown, the numerically simulated hysteretic curves and backbone curves are symmetric, while certain asymmetry exists in the experimental results. Nevertheless, reasonable matches between the testing and numerical results can be observed, which demonstrates the accuracy of the numerical models. It should be noted that some differences exist in the column S2. Generally speaking, the strength of the column is slightly larger in the numerical simulations as shown in Figure 3-13 (c) and Figure 3-14 (c). This might be because in the numerical simulation, the bolts and the TEED devices are assumed to be in perfect contact, while in the test certain imperfections or small gaps might exist between the TEED devices and the bolts, which in turn made the column S2 slightly flexible compared to the numerical model. In summary, the developed numerical models can well capture the cyclic performance of the segmental columns. It can serve as a supplementary tool for conducting experimental studies and be used to further investigate the influences of critical parameters on the seismic performances of segmental columns. In the present study, the number of layer of the BFRP, the shape, slot length and thickness of the TEED, etc might influence their performances. However, since the primary aim of the present study is to demonstrate the effectiveness of the proposed methods, these parametric studies are not included in the present paper, and will be further investigated in the future studies.

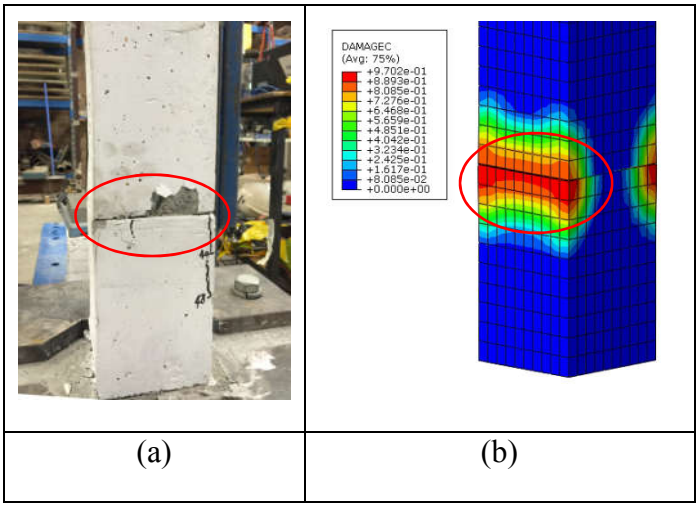

Figure 3-12. Comparison of the damages of the column: (a) S0 in the test, (b) S0 in FEM

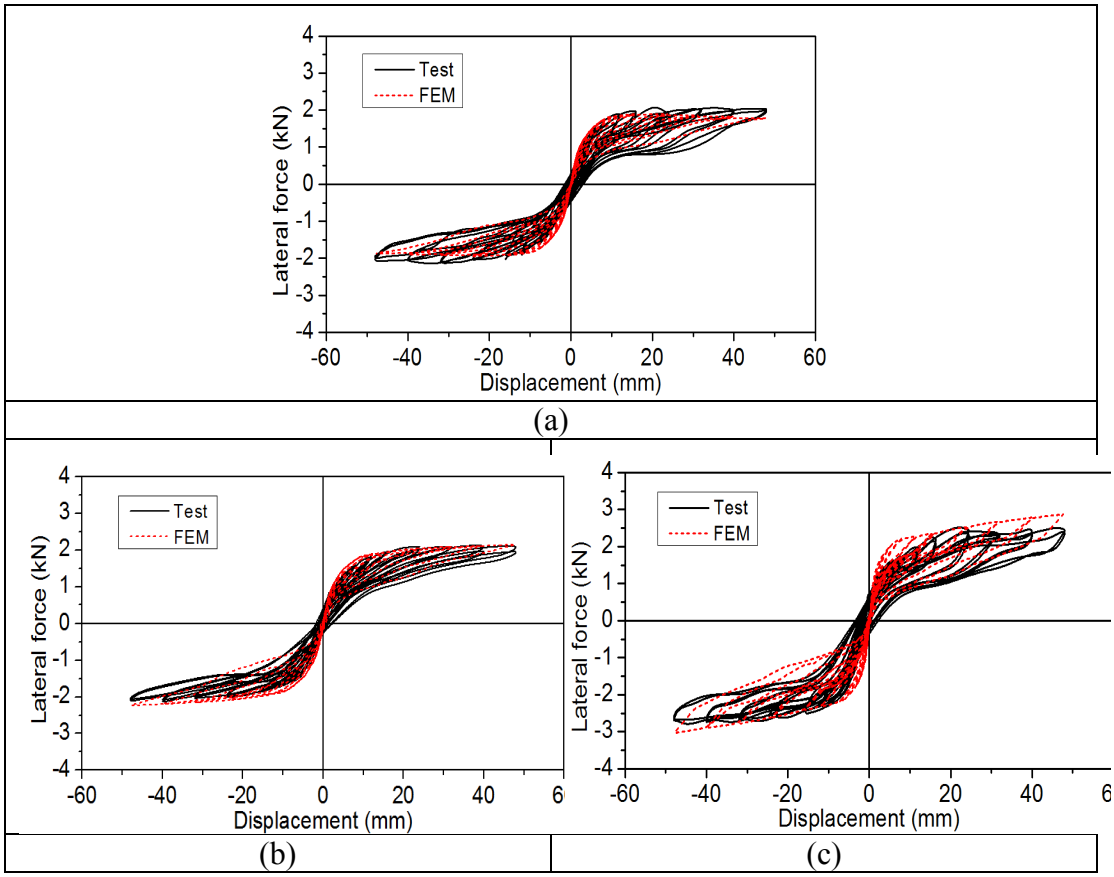

Figure 3-13. Comparison of the tested and FEM hysteretic curves: (a) S0, (b) S1, (c) S2

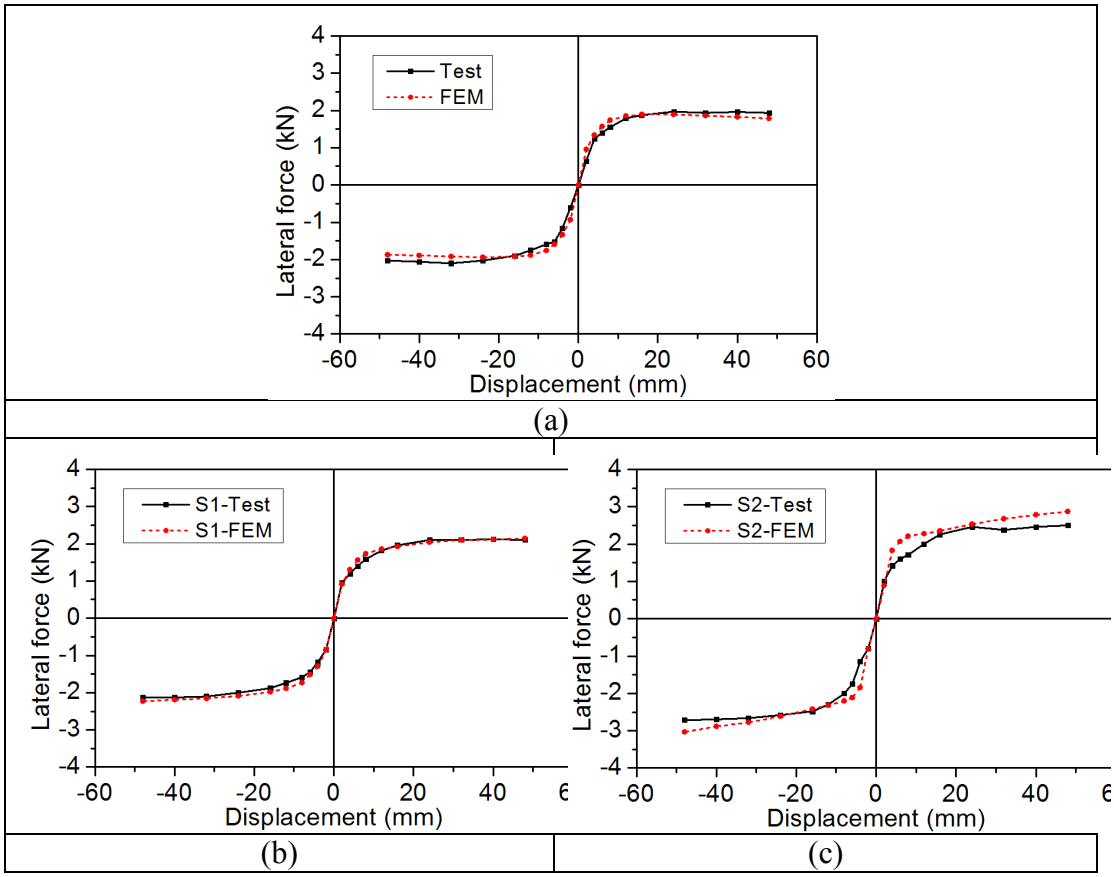

Figure 3-14. Comparison of the tested and FEM backbone curves: (a) S0, (b) S1, (c) S2

3.6 Summary and conclusions

Previous studies on the seismic behaviours of segmental columns revealed that severe concrete spalling and crushing damages may occur at the joints of the segments, and installing conventional ED devices may increase the residual displacement of the column. To overcome these problems, this chapter proposes using BFRP to wrap the concrete segments in order to mitigate the concrete damage, and using TEED devices to increase the energy dissipation capability of the column while keeping the residual displacement at a small level. Quasi-static cyclic tests are carried out to investigate the effectiveness of the proposed method. The following conclusions are drawn based on the experimental results: The conventional segmental column (S0) experienced concrete damages at the joints of the segments due to the large compressive stress induced by joint openings. When BFRP was used to wrap the segments, no obvious damage was observed (columns S1 and S2). BFRP can be an alternative of the conventionally used GFRP and CFRP wrapping sheets considering its lower cost and good mechanical properties. The specially designed TEED devices could increase the

energy dissipation capacity of the segmental column while the residual displacement was maintained at a small level. The buckling free design of the proposed TEED device was achieved and the device can be a good alternative of the conventionally used ED devices. The combined use of BFRP and TEED can obviously enhance the seismic performances of the conventional segmental column.

3.7 References

Artemenko, S. (2003). Polymer composite materials made from carbon, basalt, and glass fibres. Structure and properties. *Fibre Chemistry, 35*(3), 226-229.

Bakis, C. E., Ganjehlou, A., Kachlakev, D. I., Schupack, M., Balaguru, P., Gee, D. J., Gentry, T. R. (2002). Guide for the design and construction of externally bonded FRP systems for strengthening concrete structures. *Reported by ACI Committee, 440*(2002)

Billington, S. L., & Yoon, J. (2004). Cyclic response of unbonded posttensioned precast columns with ductile fiber-reinforced concrete. *Journal of Bridge Engineering, 9*(4), 353-363.

Bu, Z. Y., Ou, Y. C., Song, J. W., Zhang, N. S., & Lee, G. C. (2015). Cyclic Loading Test of Unbonded and Bonded Posttensioned Precast Segmental Bridge Columns with Circular Section. *Journal of Bridge Engineering*, 04015043.

Chou, C. C., & Chen, Y. C. (2006). Cyclic tests of post‐tensioned precast CFT segmental bridge columns with unbonded strands. *Earthquake engineering & structural dynamics, 35*(2), 159-175.

Dawood, H., ElGawady, M., & Hewes, J. (2011). Behavior of segmental precast posttensioned bridge piers under lateral loads. *Journal of Bridge Engineering, 17*(5), 735-746.

Demir, A., Caglar, N., Ozturk, H., & Sumer, Y. (2016). Nonlinear finite element study on the improvement of shear capacity in reinforced concrete T-Section beams by an alternative diagonal shear reinforcement. *Engineering Structures, 120*, 158-165. http://dx.doi.org/http://dx.doi.org/10.1016/j.engstruct.2016.04.029

Dhand, V., Mittal, G., Rhee, K. Y., Park, S.-J., & Hui, D. (2015). A short review on basalt fiber reinforced polymer composites. *Composites Part B: Engineering, 73*, 166-180. http://dx.doi.org/https://doi.org/10.1016/j.compositesb.2014.12.011

ElGawady, M., Booker, A. J., & Dawood, H. (2010). Seismic behavior of posttensioned concrete-filled fiber tubes. *Journal of Composites for Construction, 14*(5), 616-628.

ElGawady, M., & Sha'lan, A. (2010). Seismic behavior of self-centering precast segmental bridge bents. *Journal of Bridge Engineering, 16*(3), 328-339.

Guerrini, G., Restrepo, J. I., Massari, M., & Vervelidis, A. (2015). Seismic Behavior of Posttensioned Self-Centering Precast Concrete Dual-Shell Steel Columns. *Journal of Structural Engineering, 141*(4), 04014115. http://dx.doi.org/doi:10.1061/(ASCE)ST.1943-541X.0001054

Guo, T., Cao, Z., Xu, Z., & Lu, S. (2015). Cyclic Load Tests on Self-Centering Concrete Pier with External Dissipators and Enhanced Durability. *Journal of Structural Engineering, 142*(1), 04015088.

Hao, H. (2015). Development of a new nonbuckling segmented brace. *International Journal of Structural Stability and Dynamics, 15*(08), 1540012.

Hewes, J. T., & Priestley, M. N. (2002). *Seismic design and performance of precast concrete segmental bridge columns* (No. SSRP-2001/25). University of California, San Diego, CA:

Ichikawa, S., Matsuzaki, H., Moustafa, A., ElGawady, M. A., & Kawashima, K. (2016). Seismic-Resistant Bridge Columns with Ultrahigh-Performance Concrete Segments. *Journal of Bridge Engineering*, 04016049.

Leitner, E. J., & Hao, H. (2016). Three-dimensional finite element modelling of rocking bridge piers under cyclic loading and exploration of options for increased energy dissipation. *Engineering Structures, 118*, 74-88. http://dx.doi.org/10.1016/j.engstruct.2016.03.042

Li, C., Hao, H., & Bi, K. (2017). Numerical study on the seismic performance of precast segmental concrete columns under cyclic loading. *Engineering Structures, 148*, 373-386. http://dx.doi.org/https://doi.org/10.1016/j.engstruct.2017.06.062

Li, C., Hao, H., & Bi, K. (2018). Seismic performance of precast concrete-filled circular tube segmental column under biaxial lateral cyclic loadings. *Bulletin of Earthquake Engineering,* http://dx.doi.org/10.1007/s10518-018-0443-4

Li, C., Hao, H., Zhang, X., & Bi, K. (2017). Experimental study of precast segmental columns with unbonded tendons under cyclic loading. *Advances in Structural Engineering*, 1369433217717119.

Li, J., Hao, H., & Wu, C. (2017). Numerical study of precast segmental column under blast loads. *Engineering Structures, 134*, 125-137. http://dx.doi.org/http://dx.doi.org/10.1016/j.engstruct.2016.12.028

Lopresto, V., Leone, C., & De Iorio, I. (2011). Mechanical characterisation of basalt fibre reinforced plastic. *Composites Part B: Engineering, 42*(4), 717-723. http://dx.doi.org/https://doi.org/10.1016/j.compositesb.2011.01.030

Mander, J. B., Priestley, M. J., & Park, R. (1988). Theoretical stress-strain model for confined concrete. *Journal of structural engineering, 114*(8), 1804-1826.

Marriott, D., Pampanin, S., & Palermo, A. (2009). Quasi‐static and pseudo‐dynamic testing of unbonded post‐tensioned rocking bridge piers with external replaceable dissipaters. *Earthquake Engineering & Structural Dynamics, 38*(3), 331-354.

Mashal, M., & Palermo, A. Quasi-static cyclic testing of half-scale fully precast bridge substructure system in high seismicity.

Motaref, S., Saiidi, M. S., & Sanders, D. (2013). Shake table studies of energy-dissipating segmental bridge columns. *Journal of Bridge Engineering, 19*(2), 186-199.

Nikbakht, E., & Rashid, K. (2018). Investigation on seismic performance and functionality of self-centring post-tensioned segmental columns. *Structure and Infrastructure Engineering, 14*(6), 730-742.

Nikbakht, E., Rashid, K., Hejazi, F., & Osman, S. A. (2015). Application of shape memory alloy bars in self-centring precast segmental columns as seismic resistance. *Structure and Infrastructure Engineering, 11*(3), 297-309.

Ou, Y. C., Tsai, M. S., Chang, K. C., & Lee, G. C. (2010). Cyclic behavior of precast segmental concrete bridge columns with high performance or conventional steel reinforcing bars as energy dissipation bars. *Earthquake Engineering & Structural Dynamics, 39*(11), 1181-1198.

Ou, Y. C., Wang, P. H., Tsai, M. S., Chang, K. C., & Lee, G. C. (2009). Large-scale experimental study of precast segmental unbonded posttensioned concrete bridge columns for seismic regions. *Journal of Structural Engineering, 136*(3), 255-264.

Palermo, A., Pampanin, S., & Marriott, D. (2007). Design, modeling, and experimental response of seismic resistant bridge piers with posttensioned dissipating connections. *Journal of Structural Engineering, 133*(11), 1648-1661.

Priestley, M. N., Seible, F., & Calvi, G. M. (1996). *Seismic design and retrofit of bridges*: John Wiley & Sons.

Sarti, F., Palermo, A., & Pampanin, S. (2016). Fuse-Type External Replaceable Dissipaters: Experimental Program and Numerical Modeling. *Journal of Structural Engineering, 142*(12) http://dx.doi.org/10.1061/(asce)st.1943-541x.0001606

Shim, C. S., Chung, C. H., & Kim, H. H. (2008). Experimental evaluation of seismic performance of precast segmental bridge piers with a circular solid section. *Engineering Structures, 30*(12), 3782-3792.

Shim, C. S., Lee, S., Park, S., & Koem, C. (2017). Experiments on prefabricated segmental bridge piers with continuous longitudinal reinforcing bars. *Engineering Structures, 132*, 671-683.

Simulia, D. S. (2012). Abaqus 6.12 documentation. *Providence, Rhode Island, US,*

Sun, Z., Wang, D., Bi, K., & Si, B. (2016). Experimental and numerical investigations on the seismic behavior of bridge piers with vertical unbonded prestressing strands. *Bulletin of Earthquake Engineering, 14*(2), 501-527.

Varela, S., & Saiidi, M. (2016). A bridge column with superelastic NiTi SMA and replaceable rubber hinge for earthquake damage mitigation. *Smart Materials and Structures, 25*(7), 075012.

Wang, J., Wang, Z., Tang, Y., Liu, T., & Zhang, J. (2018). Cyclic loading test of self-centering precast segmental unbonded posttensioned UHPFRC bridge columns. *Bulletin of Earthquake Engineering*, 1-29.

Wang, J. C., Ou, Y. C., Chang, K. C., & Lee, G. C. (2008). Large - scale seismic tests of tall concrete bridge columns with precast segmental construction. *Earthquake Engineering & Structural Dynamics, 37*(12), 1449-1465.

Wang, Z., Wang, J., Tang, Y., Liu, T., Gao, Y., & Zhang, J. (2018). Seismic behavior of precast segmental UHPC bridge columns with replaceable external cover plates and internal dissipaters. *Engineering Structures, 177*, 540-555. http://dx.doi.org/https://doi.org/10.1016/j.engstruct.2018.10.012

Yuan, F., Wu, Y.-F., & Li, C.-Q. (2017). Modelling plastic hinge of FRP-confined RC columns. *Engineering Structures, 131*, 651-668. http://dx.doi.org/http://dx.doi.org/10.1016/j.engstruct.2016.10.018

Zhang, X., Hao, H., & Li, C. (2016). The effect of concrete shear key on the performance of segmental columns subjected to impact loading. *Advances in Structural Engineering*, 1369433216650210.

Zhang, X., Hao, H., Li, C., & Do, T. V. (2018). Experimental study on the behavior of precast segmental column with domed shear key and unbonded Post-Tensioning tendon under impact loading. *Engineering Structures, 173*, 589-605. http://dx.doi.org/https://doi.org/10.1016/j.engstruct.2018.07.002

Zhao, L., Bi, K., Hao, H., & Li, X. (2017). Numerical studies on the seismic responses of bridge structures with precast segmental columns. *Engineering Structures, 151*, 568-583. http://dx.doi.org/https://doi.org/10.1016/j.engstruct.2017.08.018

Zhao, L., Hao, H., Bi, K., & Li, X. (2018). Numerical Study of the Seismic Responses of Precast Segmental Column Bridge under Spatially Varying Ground Motions.

Journal of Bridge Engineering, 23(12) http://dx.doi.org/10.1061/(asce)be.1943-5592.0001319

CHAPTER 4 NUMERICAL STUDY ON THE SEISMIC PERFORMANCE OF PRECAST SEGMENTAL CONCRETE COLUMNS UNDER CYCLIC LOADING

4.1 Abstract

To accelerate construction speed, precast segmental column is becoming more and more popular in recent years due to its obvious advantages in saving construction time, reducing site disruption and controlling construction quality. However, the applications are still limited primarily in low seismic areas because its performance under earthquake loading is not well known yet. Many experimental studies have been carried out to investigate the seismic performance of segmental columns under cyclic loading. Due to the complexity in modelling such structures, numerical study of precast segmental columns subjected to seismic loads is limited. In this paper, three dimensional (3D) finite element (FE) models for two precast segmental columns are developed to predict the responses of such columns under lateral cyclic loading. The numerical models are first validated against the cyclic test results and then used to perform parametric studies. The influences of five parameters including bonding condition of the tendon, total initial axial forces level, confinement of the segments, number of segments, and energy dissipation (ED) bars on the performance of segmental columns are systematically investigated. Moreover, columns with shape memory alloy (SMA) bars are also investigated to increase the energy dissipation capacity and reduce the residual drift of the segmental columns. It is found that both mild steel and SMA bars can increase the energy absorption capacity of the column, but the SMA bars can minimize the residual drift due to its mechanical property. This study clearly identifies the influences of different factors on the performance of segmental columns. The developed numerical model can be used in the future studies to predict the seismic responses of structures with segmental columns.

4.2 Introduction

Precast construction has attracted a lot of research interests in recent years. Compared with traditional cast in situ construction method, the precast construction has many advantages. In the precast concrete systems, most of the structural elements are prefabricated in factories and then shipped to the construction site. With a few workers

and lifting equipment, the structural system can be quickly erected. As a result, the on-site construction time can be significantly reduced and hence the environmental impact is less as compared to the traditional construction method. In addition, the quality of the structure and safety for workers can be improved since most of the construction activities are carried out in prefabrication factories. Precast segmental column is one the prefabricated systems which can be used as bridge piers to improve the construction efficiency in urban areas with heavy traffic. However, it should be noted that the applications of segmental columns are still limited to areas of low seismicity due to a lack of knowledge about its performance under seismic loading. To overcome this problem many important studies have been carried out to investigate the seismic behaviour of precast segmental columns recently (Billington & Yoon, 2004; Chou & Chen, 2006; ElGawady & Dawood, 2012; Hewes & Priestley, 2002; Ou et al., 2010; Shim et al., 2008; Sideris et al., 2014; Tazarv & Saiid, 2015). Owing to the challenge in numerically modelling such columns formed up with discrete concrete blocks, most of the previous studies are based on the experimental tests.

In the precast segmental column system, the bonding condition of the prestress tendon is an important factor that has significant influence on the performance of the column. Both bonded and unbonded tendon systems have been reported in the previous studies. In the bonded tendon system, the tendon is placed in the corrugated tube and cementitious materials are injected into the corrugated tube after applying the prestressing force to the tendon. As a result, the tendon will deform together with the surrounding concrete. For the unbonded tendon system, no cementitious materials are filled in the tube. Previous studies (ElGawady et al., 2010; Ou et al., 2009) showed unbonded tendon system normally results in smaller residual drift. In comparison, bonded tendon will increase the strength of the column and yielding of the tendon can dissipate some energy (Wang et al., 2008). However, yielding of the tendon can also lead to a reduction of the axial force, which consequently decreases the friction force between the segments and thus reduces the shear resistance. Moreover, yielding of the bonded tendon is likely to result in larger residual deformation as compared to that of the unbonded tendon.

Since the segments of a segmental column are normally connected by prestress tendons, the level of prestressing force in the prestress tendon directly affects the

performance of segmental column because it provides the lateral shear resistance through friction force and also the moment resistance for the column. Two specimens with different levels of prestressing forces under the same loading conditions were reported by Ou et al. (2009). The test results showed that the column with higher prestressing force had higher ultimate strength and smaller residual drift, therefore large prestressing force is desirable in these regards. On the other hand, increasing the posttensioning force increases the axial compressive stress in the concrete of the whole column. The toes of the segments therefore may experience large compressive stress when the segments rock with respect to each other. In other words, high axial compressive stress may lead to concrete crushing failure of the column and reduce the ductility of the column. Therefore, systematic studies are needed to determine the proper posttension force level that can be applied to the segmental column.

Previous studies showed that the segmental column normally experienced compression failure at the joints of the segments due to the large compressive stress when the segments rocked between each other under cyclic loading (ElGawady & Sha'lan, 2010; Shim et al., 2008). Thus different strengthening methods were used to mitigate the damage of the column, such as using high performance concrete (Billington & Yoon, 2004), confining the segments with FRP (ElGawady et al., 2010), and confining the segments with steel jacket (Chou & Chen, 2006; Hewes & Priestley, 2002). The confinement effectiveness directly affects the confined strength of the concrete and thus affects the performance of segmental column. Therefore, it is necessary to investigate the influence of confinement for the precast segments on the performance of segmental column.

For a segmental column, the joints will open and the segments will rock between each other under seismic loading, so a segmental column with the same height but with different number of segments may have different responses due to the different locations and the different amount of openings. Thus the number of segments is another factor which may affect the seismic performance of the segmental column. However, only very limited studies have investigated the influence of this factor. Experimental study on a series of precast segmental bridge bents confined with FRP was conducted (ElGawady & Sha'lan, 2010). Among the five specimens, F-FRP1 and F-FRP3 had the same dimensions and the same designs except that specimen F-FRP1

had only one segment while specimen F-FRP3 had three segments. The test result showed that these two specimens behaved similarly. Further studies are however necessary to confirm this observation and its validity to segmental columns with other number of segments.

For a segmental column in an earthquake event, the rocking behaviour between the segmental joints reduces the damage of the whole column and the posttensioned tendons can pull the column back to its original position which minimizes the residual displacement of the column. Therefore the segmental column has better self-centring ability in comparison with the traditional monolithic column. Nevertheless, many previous studies also showed that precast segmental columns that connected only with prestress tendons dissipated very limited energy (e.g. (Ou et al., 2009)). A variety of energy dissipation devices have been proposed to increase the energy dissipation capability of segmental columns. These devices can generally be divided into two categories, i.e. the internal energy dissipation bars (Ou et al., 2010; Ou et al., 2009) and the external energy dissipation devices (Chou & Chen, 2006; Marriott et al., 2009, 2011). According to these studies, the use of energy dissipation devices increases the energy dissipation of the columns, but may also introduce more damage to the column and increase the residual displacement.

The above review reveals that many factors can affect the performance of segmental column under seismic load. To systematically investigate the influences of these factors on the behaviour of segmental columns, ideally numerical simulation is a better alterative since laboratory testing is not only time consuming but also costly. Some numerical models have been developed and reported in the literature to investigate the influences of particular factors on the performance of segmental columns. These models include fibre based model (Tazarv & Saiid, 2015), two dimensional (2D) FE model (Wang et al., 2008), and three dimensional (3D) FE model (Dawood et al., 2011; Leitner & Hao, 2016; Nikbakht et al., 2015; Ou et al., 2007). Among them, Ou et al. (2007) investigated the influence of energy dissipation bar ratios, Dawood et al. (2011) focused on predicting the backbone curves of segmental columns, and other researchers investigated the influence of different options to increase the energy dissipation capacity of the columns (Leitner & Hao, 2016). However, studies on the influences of different designs on the cyclic performance of segmental columns are

limited. The present study aims to develop an accurate numerical model and then systematically investigate the influences of different design parameters on the performance of segmental columns. Three dimensional (3D) FE models are first developed by using the ABAQUS/Standard program and the models are validated against the experimental results (Hewes & Priestley, 2002). Comprehensive parametric studies, including the influences of bonding condition of the tendon, total axial force level, confinement for the segments, number of the segments, and energy dissipation (ED) bars on the cyclic response of the segmental columns are then carried out to better understand the behaviour of segmental columns. Finally, shape memory alloy (SMA) bars are also used and investigated to increase the energy dissipation capacity and reduce the residual drift of segmental columns.

4.3 Numerical modelling

Three dimensional (3D) FE models of two segmental columns are developed by using the commercial finite element software ABAQUS/Standard (Simulia, 2012). In this part, a brief description of the models and the detailed modelling methods and procedures will be presented.

4.3.1 Model description

Three dimensional FE models are developed based on the experimental tests (Hewes & Priestley, 2002). A tall column JH1 with an aspect ratio of six and a short column JH3 with an aspect ratio of three are modelled and validated in this study. Figure 4-1 shows the design details of the two columns. For column JH1, a base segment and another three segments are connected by an unbonded prestress tendon at the centre of the column. For column JH3, the base segment is the same as JH1 while only one segment is stacked on the base segment. All the segments have a circular cross section with a diameter of 610 mm. To minimize the damage of the concrete segments, the base segments of JH1 and JH3 are confined by steel jackets with the thickness of 6mm and 2.8 mm, respectively. No steel bars are placed in the base segments. The upper segments are transversely confined by transverse reinforcement with a diameter of 9.5 mm and a spacing of 75 mm. Eight longitudinal steel bars with a diameter of 12.7 mm are also placed around the section evenly in the upper segments. The tendons used in

the columns are ASTM A779 Grade 270 prestressing strands. The total cross section area of the tendons for each column is 2665 mm^2.

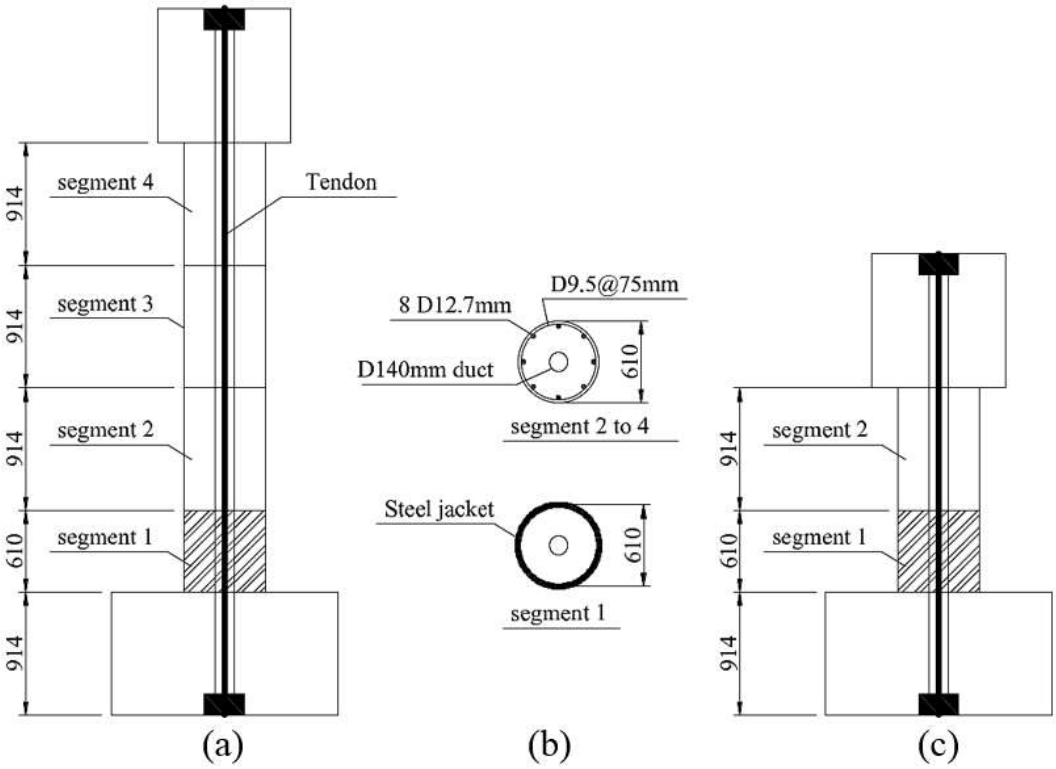

Figure 4-1 Design details of the specimens: (a) JH1; (b) Cross section; (c) JH3

4.3.2 Finite element model

All the concrete components of the column, including the column segments, footing and top mass, are modelled with the eight-node 3D brick elements (C3D8R). For the concrete material, three models are available in ABAQUS, including smeared crack model, brittle cracking model and concrete damage plasticity model (Simulia, 2012). The smeared crack model is normally applied when the concrete is subjected to monotonic loadings. The brittle cracking model assumes that the compressive behaviour is linear elastic and it is accurate for modelling brittle materials such as brittle rocks and plain concrete. The concrete damaged plasticity model (CDP) is developed primarily for the reinforced concrete structures under monotonic, cyclic and dynamic loadings (Simulia, 2012). Since the columns studied in this paper are reinforced concrete structures subjected to cyclic loading, the concrete damaged plasticity (CDP) model is therefore adopted to simulate the inelastic behaviour of the segmental columns.

In general, the CDP model is based on five plasticity parameters and two sets of the basic uniaxial data of the concrete. The five parameters ψ, e, σ_{b0}/σ_{c0}, K_c, and μ, define the yield surface function, the potential flow and the viscosity of the material. The uniaxial data are the compressive and tensile stress-strain behaviour of the concrete. Damage data which decrease the stiffness of the materials are used to describe the behaviour of the material under repeated loading. The definitions of these parameters are shown as below in sequence.

The CDP model uses the yield function developed by Lubliner et al. (Lubliner et al., 1989) and further modified by Lee and Fenves (Lee & Fenves, 1998). The evolution of the yield surface is defined by several parameters, including the ratio of the initial equibiaxial compressive strength to initial uniaxial compressive strength σ_{b0}/σ_{c0}, the parameter K_c which defines the shape of the failure surface in the deviatoric plane, and the plastic strain ε_c^{pl}. The yield function is defined as

$$F = \frac{1}{1-\alpha}(\bar{q} - 3\alpha\bar{p} + \beta(\varepsilon^{pl})\langle\hat{\bar{\sigma}}_{max}\rangle - \gamma\langle-\hat{\bar{\sigma}}_{max}\rangle) - \bar{\sigma}_c(\varepsilon_c^{pl}) = 0 \tag{4.1}$$

$$\alpha = \frac{(\sigma_{b0}/\sigma_{c0})-1}{2(\sigma_{b0}/\sigma_{c0})-1} \tag{4.2}$$

$$\gamma = \frac{3(1-K_c)}{2K_c-1} \tag{4.3}$$

$$\beta(\varepsilon^{pl}) = \frac{\bar{\sigma}_c(\varepsilon_c^{pl})}{\bar{\sigma}_t(\varepsilon_c^{pl})}(1-\alpha) - (1+\alpha) \tag{4.4}$$

where α and γ are the dimensionless constants defined by σ_{b0}/σ_{c0} and the parameter K_c. $\bar{q}$ is the Mises equivalent effective stress, $\bar{p}$ is the hydrostatic pressure stress, $\hat{\bar{\sigma}}_{max}$ is the major principle stress, $\bar{\sigma}_c$ is the effective compressive cohesion stress, $\bar{\sigma}_t$ is the effective tensile cohesion stress (Simulia, 2012).

The flow potential G used for the model is Drucker-Prager hyperbolic function. The flow potential eccentricity e and the dilation angle ψ are required to define the function:

$$G = \sqrt{(e\sigma_{t0}\tan\psi)^2 + \bar{q}^2} - \bar{p}\tan\psi \tag{4.5}$$

where ψ is the dilation angle, σ_{t0} is the uniaxial tensile stress at failure, e is a parameter, referred to as the eccentricity of the potential flow.

To define the concrete material, several parameters are required including the elastic modulus, Poisson's ratio and the plasticity parameters for CDP. Table 4-1 tabulates the material properties of the columns. Table 4-2 summarizes the fundamental plasticity parameters required by CDP model in ABAQUS which are suggested in (Demir et al., 2016; Zhu et al., 2017).

Table 4-1 Properties of the materials

	Items	JH1	JH3
Concrete	Strength (MPa)	48.7	57.3
	Elastic modulus Ec (Gpa)	33008.5	35804.6
	Poisson's ratio	0.2	0.2
Longitudinal bars	Number and arrangement	8D12.7	8D12.7
	Elastic modulus Es (Gpa)	206	206
	Yielding stress (Mpa)	410	410
	Poisson's ratio	0.3	0.3
Transverse bars	Diameter and spacing	D9.5@75	D9.5@75
	Elastic modulus Es (Gpa)	206	206
	Yielding stress (Mpa)	410	410
	Poisson's ratio	0.3	0.3
Steel jacket	Thickness (mm)	6	2.8
	Elastic modulus Es (Gpa)	206	206
	Yielding stress (Mpa)	303	290
	Poisson's ratio	0.3	0.3
Tendons	Area (mm^2)	2665	2665
	Elastic modulus Es (Gpa)	196	196
	Yielding stress (Mpa)	1860	1860
	Poisson's ratio	0.3	0.3
	Prestress level (%)	54	42

Table 4-2 Plasticity parameters for CDP in ABAQUS

Parameter	Value	Explanation (Simulia, 2012)
ψ	30	Dilation angle
e	0.1	Flow potential eccentricity
σ_{b0}/σ_{c0}	1.16	The ratio of initial equibiaxial compressive yield stress to initial uniaxial compressive yield stress
K_c	0.6667	The coefficient determining the shape of the deviatoric cross-section
μ	0.0001	Viscosity parameter

For the stress-strain relationship of the concrete, many stress-strain models have been proposed (Han et al., 2007; Hu & Schnobrich, 1989; Mander et al., 1988). Two widely used concrete stress-stain models are utilized in this study, one is the Mander's stress-strain model (Mander et al., 1988) for the stirrup confined concrete segments and the other is the model proposed by Han et al. (2007) for the bottom segments which are confined by the steel jackets. With the given material properties in Table 4-1, including the concrete characteristics compressive stress f_c' and the confinement properties (stirrup diameter, stirrup spacing, steel jacket thickness, and yield stresses), the stress-strain curves of the concrete material can be defined based on the material models in (Han et al., 2007) and (Mander et al., 1988). Since these models have been well documented in the two references, so only brief descriptions are presented here. Equation (4.6) gives a brief description of Mander's model.

$$f_c = \frac{f_{cc}' E_c \varepsilon_c / \varepsilon_{cc}}{E_{sec} + (E_c - E_{sec})(\varepsilon_c/\varepsilon_{cc})^{E_c/(E_c - E_{sec})}} \tag{4.6}$$

where f_{cc}' is the maximum compressive concrete stress and ε_{cc} is the corresponding strain, which are determined by the confining pressure provided by the stirrups. E_c is the tangent modulus of elasticity, E_{sec} is the secant modulus defined as $E_{sec} = \frac{f_{cc}'}{\varepsilon_{cc}}$. More details about the definition of the parameters can be found in reference (Mander et al., 1988).

For the steel jacket confined concrete, the constitutive law is defined as following:

$$y = \begin{cases} 2x - x^2 & (x \leq 1) \\ \frac{x}{\beta_0 (x-1)^{\eta} + x} & (x > 1) \end{cases} \tag{4.7}$$

where $x = \frac{\varepsilon}{\varepsilon_0}$, $y = \frac{\sigma}{\sigma_0}$, σ_0 is the cylinder strength of the concrete f_c', and ε_0 is the corresponding strain. β_0 and η are parameters determined by the properties of the confining steel jacket. More details about the parameters are available in (Han et al., 2007).

The tensile behaviour of the concrete is modelled as linear elastic until the tensile strength $f_t' = 0.62276\sqrt{f_c'}MPa$ is reached. The post-cracking behaviour is modelled by a linear softening until an ultimate strain of 0.2% (Dawood et al., 2011).

The CDP model in ABAQUS also needs the definition of damage variables which are designed to model the degradation of the concrete stiffness under cyclic loading. Figure 4-2 shows the typical relationship of the parameters in CDP model. E_c is the undamaged Young's modulus of the concrete, ε_c^{pl} is the plastic strain (irrecoverable), and ε_{0c}^{el} is the elastic strain (recoverable). The compression damage variable is defined as the following function (Birtel & Mark, 2006):

$$d_c = 1 - \frac{\sigma_c E_c^{-1}}{\varepsilon_c^{pl}\left(\frac{1}{b_c} - 1\right) + \sigma_c E_c^{-1}} \tag{4.8}$$

where the plastic strain $\varepsilon_c^{pl} = b_c \times \varepsilon_c^{in}$. Previous study recommended a value of 0.7 for the constant b_c, which is validated against experimental data (Birtel & Mark, 2006). The inelastic strain is defined as following: $\varepsilon_c^{in} = \varepsilon_c - \varepsilon_{0c}^{el}$, where $\varepsilon_{0c}^{el} = \sigma_c / E_c$. Relationship between these parameters is shown in Figure 4-2.

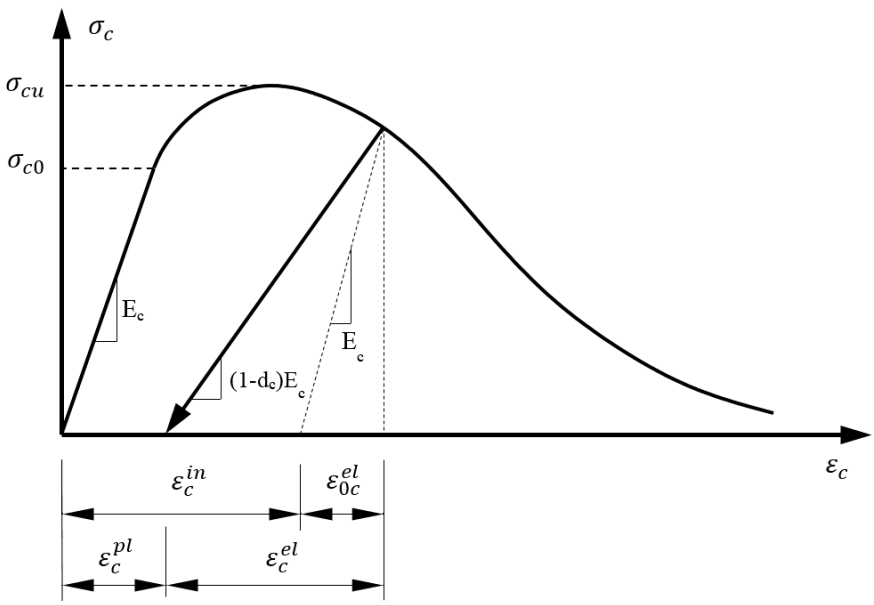

Figure 4-2 Relationship between parameters in CDP model

Similar to the compressive damage variable, the tensile damage variable is defined by the following function with a constant parameter b_t =0.1 (Birtel & Mark, 2006).

$$d_t = 1 - \frac{\sigma_t E_c^{-1}}{\varepsilon_t^{pl}\left(\frac{1}{b_t}-1\right)+\sigma_t E_c^{-1}} \tag{4.9}$$

For the steel reinforcements, steel jackets, and prestress tendons, the classical elastic-perfectly plastic stress-strain material model is adopted (Nikbakht et al., 2015), and the basic properties of each material are listed in Table 4-1. The steel reinforcements, including the longitudinal and transverse mild bars in the segments, are modelled with truss element T3D2. The reinforcements are embedded in the surrounding concrete. In other words, the slippage between the steel bars and surrounding concrete is not considered in the numerical model. The steel jacket for the base segment is modelled with shell element (S4R). The holes for the tendon in the segments have a diameter of 140mm while the diameter of the tendon is about 58mm, which leaves a gap between the tendon and the concrete segments. To realistically model the contact behaviour between the tendon and the concrete segments, the 3D brick elements (C3D8R) are chosen to model the tendon. Certain lengths of the top and base ends of the tendon are embedded into the top mass and the foundation to model the anchorage of the tendon. The initial prestress levels in the tendons are summarized in Table 4-1.

Under lateral cyclic loading, the joints of a segmental column normally experience openings. In order to model such behaviour, surface to surface contact elements are adopted. The tangential contact behaviour between the master and slave surface is modelled by tangential friction. The friction coefficient is assumed to be 0.5 between the segments (Dawood et al., 2011). The normal contact behaviour between the surfaces is modelled by hard contact. The surfaces are allowed to separate without any resistance and also able to develop compression when the surfaces are in contact. For the unbonded tendon in the column, the contact behaviour between the unbonded post tensioning tendon and the duct is also modelled with surface to surface contact elements. The tangential friction coefficient is assumed to be zero to model the unbonded behaviour between the tendon and the duct. For the bonded tendon in the following parametric study, the tendon is totally embedded in the top mass, the footing, and also all the segments so that the tendon will deform together with the surrounding concrete.

During the tests, the footing was fixed to the ground. In the model, the nodes of the footing are totally constrained to simulate the fixed boundary conditions. Three loadings need to be defined in the numerical simulation, including the prestressing force of the tendon, the axial load, and the lateral cyclic load. The prestressing force is applied to the tendon with initial stress condition. The axial load is modelled as a surface pressure and loaded on the top surface of the top mass block. The lateral displacement controlled cyclic loading is imposed to the top mass with predetermined drift ratio. The loadings in the models are the same with those in the experiment (Hewes & Priestley, 2002). Figure 4-3 shows the cyclic loading history. The whole numerical models are shown in Figure 4-4.

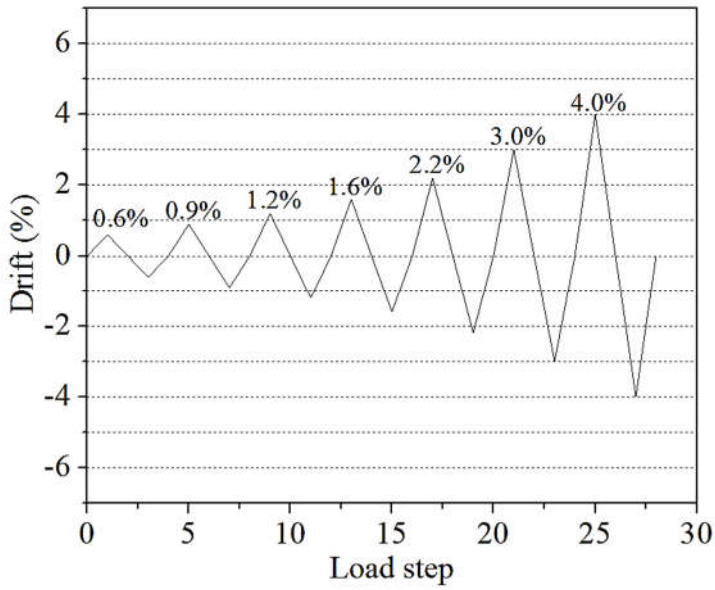

Figure 4-3 Cyclic loading history

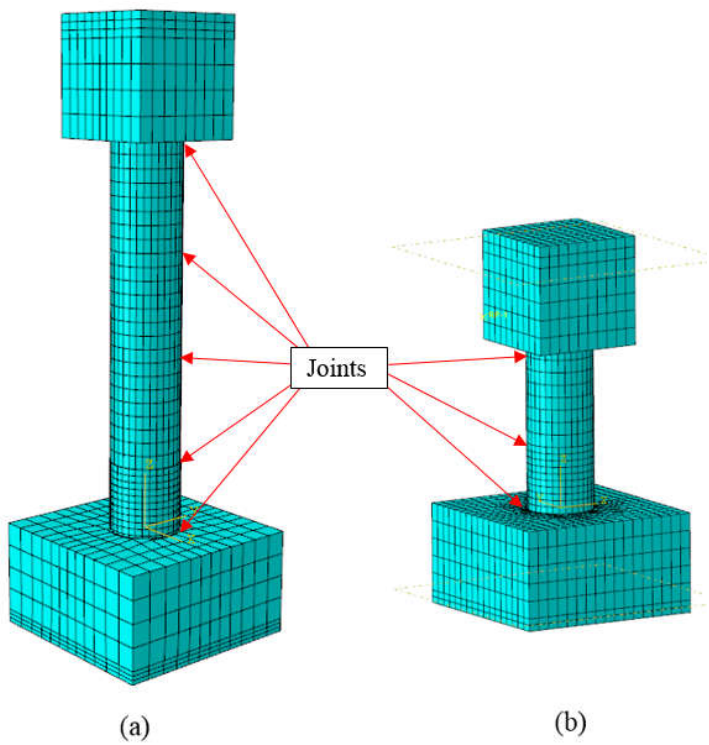

Figure 4-4 The FE models (a) JH1; and (b) JH3

4.4 Validation of the numerical models

To validate the accuracy of the numerical models, the numerical results are compared with the experimental results in terms of the damage mode and force-displacement hysteretic curves. Figure 4-5 shows the damage mode of JH1 from the test and the

numerical simulation at 3% drift ratio. It can be seen in Figure 4-5 (a) that during the experiment, a part of the cover concrete of on one side of segment two spalled at 3% drift level due to large axial compressive stress the concrete segment experienced. Numerical simulation successfully captures this damage as shown in Figure 4-5 (c). The dark area in Figure 4-5 (c) shows the concrete elements with high axial strain which is larger than the strain at the peak stress of unconfined concrete (Yuan et al., 2017). Similarly, large strain is observed in the numerical model at the joint between the footing and the base segment in Figure 4-5 (c). This is because the steel jacket of the base segment was designed to be 25mm higher than the bottom surface of the base segment to prevent contact between the steel jacket and the footing in the experiment. As expected, the concrete crush was also observed in the test at the same place, which is shown in Figure 4-5 (b). In general, the numerical model is able to capture the damage mode of the tested segmental column. Figure 4-6 shows the comparisons of the hysteretic curves of JH1 and JH3 derived from the numerical models and the experimental results. The grey curves represent the experimental results and the red dot lines stand for the modelling results. In general, good agreements are observed between the experimental and numerical results. As shown, the initial stiffness, post-yield stiffness and the lateral strength of the tested segmental columns are well captured by the numerical models. Here the word "yield" does not mean material yielding of the tendon. It is meant to describe the nonlinear force-displacement relation in the column response due to the joint opening between the segments. To quantitatively examine the results, the predicted results and the corresponding errors with respect to the testing data of the lateral force at each drift level are summarized in Table 4-3. It can be found that for JH1, the prediction errors are quite small in the positive displacement direction, while in the negative displacement direction the errors are slightly larger. By checking the experimental results carefully, it can be seen that the lateral forces are not symmetric in the positive and negative directions during the tests. For example, at 2% drift ratio, the strengths of column JH1 in the positive and negative directions are 210.4kN and 199.4kN, respectively. In comparison, the predicted values are 215.4kN and 216.2kN, respectively. The lateral strengths are almost symmetric in the numerical model while they are slightly asymmetric in the test results which could result from the unsymmetrical damage in the column and the test setup errors during the experiment. Nevertheless, the maximum error between the predicted results and the experimental results of column JH1 is about 8.4% at 2% drift

ratio, which is considered acceptable in view of the many uncertainties in performing such tests. Similarly, for column JH3, a slight discrepancy is observed between the experimental and numerical results. The maximum error between the predicted results and the experimental results is also about 8.4%, which occurs at 3% drift ratio. Overall, the numerical models are able to predict the experimental force-displacement response of the unbonded segmental columns with good precision. These comparisons verify the reliability of the numerical model in simulating the responses of segmental columns under cyclic loadings. The validated numerical models are used to systematically investigate the influences of different factors on the cyclic performance of segmental columns in the next section.

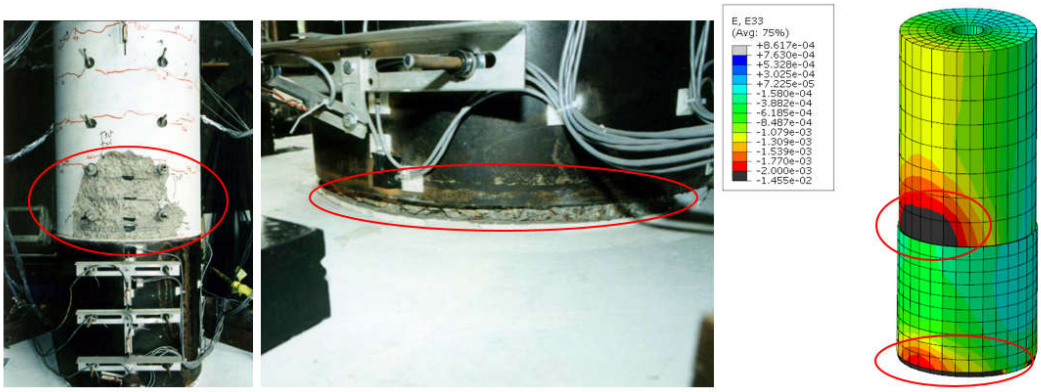

(a) (b) (c)

Figure 4-5 Comparisons of damage pattern of JH1: (a) concrete damage in the second segment (Hewes & Priestley, 2002); (b) concrete crush below the steel jacket (Hewes & Priestley, 2002); (c) axial strain of the numerical model

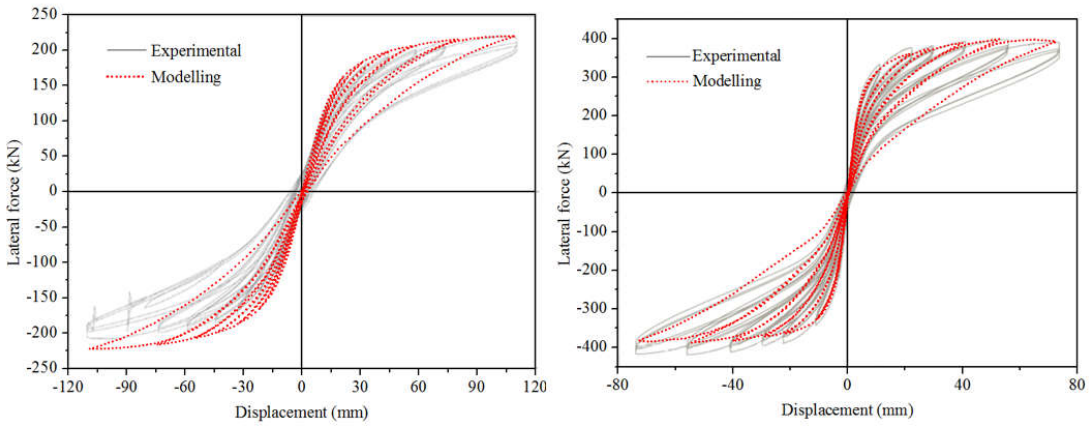

(a) (b)

Figure 4-6 Comparisons of the simulated hysteretic curves with the experimental results: (a) JH1; (b) JH3

Table 4-3 Modelling results and errors of lateral forces at each drift ratio

Drift ratio (%)	JH1			JH3		
	Experimental (kN)	Modelling (kN)	Error (%)	Experimental (kN)	Modelling (kN)	Error (%)
0.6	164.7	161.5	2	334.1	318.9	4.6
-0.6	-156.2	-164.6	5.3	-342.8	-327.1	4.6
0.9	186.7	184.1	1.4	377.5	360.5	4.5
-0.9	-175.6	-186.4	6.1	-389.7	-363.1	6.8
1.2	196.9	197.2	0.1	382.3	372.5	2.6
-1.2	-185.3	-198.6	7.2	-397.4	-371.3	6.6
1.6	206.1	205.9	0.1	393.0	389.0	1.0
-1.6	-194.9	-206.7	6	-412.6	-382.5	7.3
2	210.4	215.4	2.4	399.0	397.8	0.3
-2	-199.4	-216.2	**8.4**	-418.7	-387.2	7.5
3	217	220.3	1.5	391.0	392.8	0.5
-3	-206.3	-222.2	7.7	-417.9	-382.8	**8.4**

4.5 Parametric study

The above calibration study verified the accuracy of the numerical model, which is used here to perform parametric simulations. Without loss of generality, the calibrated segmental column JH1 is adopted here as the reference column. The influences of six parameters are investigated in the present study and the different cases are summarized in Table 4-4. The same numerical model is used for all the cases by adjusting different design parameters of the reference column.

Table 4-4 Specimens with different design parameters

No.	Bonded or Unbonded	Axial force ratio (%)	Confinement	Seg NO	Mild steel ED ratio (%)	SMA ED ratio (%)
B1 (JH1)	Unbonded	27.2	1seg-6mm	4	0	0
B2	Bonded	27.2	1seg-6mm	4	0	0
P1	Unbonded	10	1seg-6mm	4	0	0
P2	Unbonded	20	1seg-6mm	4	0	0
P3	Unbonded	30	1seg-6mm	4	0	0
P4	Unbonded	40	1seg-6mm	4	0	0
P5	Unbonded	50	1seg-6mm	4	0	0
C1(JH1)	Unbonded	27.2	1seg-6mm*	4	0	0
C2	Unbonded	27.2	1seg-3mm	4	0	0
C3	Unbonded	27.2	1seg-9mm	4	0	0
S1(JH1)	Unbonded	27.2	1seg-6mm	4	0	0
S2	Unbonded	27.2	1seg-6mm	2	0	0
S3	Unbonded	27.2	1seg-6mm	1	0	0
E1(JH1)	Unbonded	27.2	1seg-6mm	4	0	0
E2	Unbonded	27.2	1seg-6mm	4	0.23	0
E3	Unbonded	27.2	1seg-6mm	4	0.58	0
E4	Unbonded	27.2	1seg-6mm	4	0.91	0
E5	Unbonded	27.2	1seg-6mm	4	1.31	0
E6	Unbonded	27.2	1seg-6mm	4	2.32	0
SE1(JH1)	Unbonded	27.2	1seg-6mm	4	0	0
SE2	Unbonded	27.2	1seg-6mm	4	0	0.23
SE3	Unbonded	27.2	1seg-6mm	4	0	0.58
SE4	Unbonded	27.2	1seg-6mm	4	0	0.91
SE5	Unbonded	27.2	1seg-6mm	4	0	1.31
SE6	Unbonded	27.2	1seg-6mm	4	0	2.32

* 1seg-6mm means that the bottom segment is confined by a steel jacket with 6mm thickness.

4.5.1 Influence of bonding conditions of prestress tendons

As reviewed above, for the segmental column, both bonded and unbonded posttensioned (PT) tendons are commonly used to clamp the precast segments. For the bonded tendon system, steel corrugated ducts are precast in the segments. After curing the concrete, the steel tendons are inserted in the ducts and posttensioned force is applied to the tendons. Cementitious grout materials are then injected into the corrugated ducts after applying the posttensioned force. As a result, the tendon is bonded to the surrounding concrete and can then deform together with the surrounding concrete. Bonded PT tendons can protect the tendon from corrosion. However, bonded tendon may yield under earthquake ground excitation, which may not only endanger the performance of the whole structure since the tendons are the main connection between the segments and provide the lateral strength for the segmental column, but also increase the residual deformation. To investigate the influences of bonding conditions of the tendons on the performance of segmental columns, two specimens B1 and B2 are simulated and compared, in which B1 is the same as JH1 with unbonded tendons while the only difference between the two columns is that B2 has a bonded tendon. To simulate the bonded tendon in the model, the tendon is embedded in the surrounding concrete. No bond slip between the tendon and concrete is assumed in the model. Therefore, the tendon deforms together with the concrete. In numerical simulations, the columns are both loaded to 6% drift ratio. Figure 4-7 compares the hysteretic curves and the cumulative energy dissipation of the two columns. It can be seen that the specimen with bonded tendon (B2) demonstrates higher lateral strength and dissipates more energy than that of the specimen with unbonded tendon (B1). The maximum strength of column B2 occurs at 4% drift ratio and the value reaches 279.3kN. While for column B1, the strength at 4% drift ratio is 221.2kN, which is 20.8% lower than that of B2. However, after 4% drift ratio, column B2 experiences an obvious drop of strength, indicating the ductility of column B2 is not as good as that of column B1. This is because, as shown in Figure 4-8 (a), when the joints between the segments open, for the column B1 the tendon elongates and the stress of the tendon is evenly distributed along the whole tendon. Thus the stress of the tendon is not too large (maximum 1147MPa). For the column B2, however, the bonded tendon shows significant localized higher stress (maximum 1860MPa) at the segment joints as shown in Figure 4-8 (b). With higher tendon stress, the column can achieve higher

lateral strength, but the higher localized tendon stress also cause yielding of the tendon and more concrete damage which therefore results in a decrease of the strength and poor ductility. Figure 4-7 (a) also shows that the residual drift of column B2 is larger than B1. This is consistent with the results observed in previous study (Wang et al., 2008). The reason is that higher localized tendon stress causes more damage to the concrete. Moreover, yielding of the bonded tendon also contributes to the residual deformation. These are also the reason that column B2 dissipates more energy than column B1 as shown in Figure 4-7 (b). Here the energy dissipated by the column under cyclic loading is represented by the areas of the hysteretic curves. Therefore, the amount of energy absorption at each loading cycle is calculated by integrating the area of the hysteretic loop. It should be noted that the maximum lateral load applied to the column is smaller than the friction force between the segments, which means that the friction force is sufficient to resist the shear force in the column and slippage between the joint is not expected. In another word, the energy dissipated by the precast segmental column is mainly contributed by the damage of the concrete segments, possible yielding of the tendon, and yielding of the steel reinforcements. It is obvious that more severe damage of the concrete, yielding of the bonded tendon and large residual displacement make it hard to retrofit after a severe earthquake. In other words, in terms of ductility and residual drift, the column with unbonded tendon performs better than the column with bonded column. It should be noted that corrosion might be a problem for the unbounded column since the unbonded system exposes the tendon to the air and water directly. To overcome this problem, advanced corrosion resistance materials such as FRP tendons might be a viable alternative of the steel tendons.

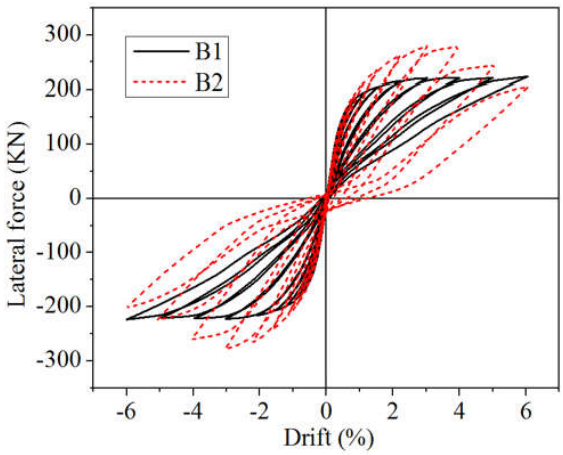

(a)

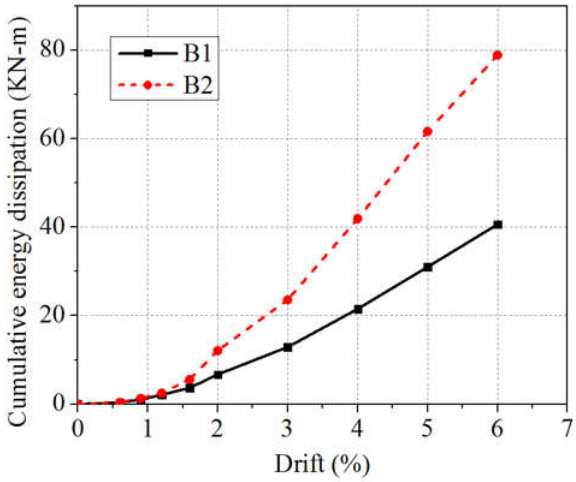

(b)

Figure 4-7 (a) Hysteretic curves of B1 and B2; (b) Cumulative energy dissipation capacity of B1 and B2

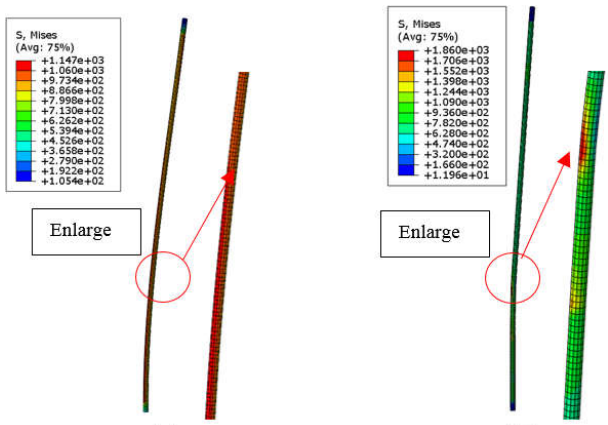

(a) (b)

Figure 4-8 Stress of the tendon: (a) B1; and (b) B2

4.5.2 Influence of total axial force

To investigate the influence of axial force levels on the performance of the segmental column, five new segmental columns P1, P2, P3, P4 and P5 with different amount of total axial forces are considered. The only difference between these columns and the reference column JH1 is the axial force ratio, as given in Table 4-4. The total axial force ratio is defined as $(F_P+F_D)/f_c'A_g$, in which F_P stands for the prestressing force, F_D represents the dead load on the column, f_c' is the strength of the concrete, and A_g is the gross section area of the column. For the external axial load resulting from gravity, the load direction is vertical and this load will have P-Δ effect when the column deforms and will result in extra moment in the column. In this study, the dead loads on the columns are kept the same and the prestressing forces are changed such that the total axial load ratio varies from 0.1 to 0.5 for column P1 to P5, respectively. Figure 4-9 (a) shows the force-displacement relationships of the specimens with different total axial force levels. It can be seen that the lateral strength of the column increases with the increase of the axial load ratio. In addition, when the axial load ratio is low, the column stiffness after yielding is positive. However, when the axial load ratio reaches certain level (0.4), the stiffness after yielding is negative, implying the drop in the column lateral strength. For example, for columns P4 and P5 with the axial load ratio of 0.4 and 0.5, respectively, the strengths of the columns start to drop after 4% drift ratio, which means the column with higher axial load ratio is less ductile compared to the one with low axial load ratio. This is because a higher initial axial stress in the concrete causes more concrete crushing damage to the segments when subjected to cyclic loading. The damage of the concrete also results in more energy dissipation as shown in Figure 4-9 (b). To summarize, the modelling results indicate that a low axial load ratio results in a low lateral strength and low energy dissipation, but high displacement capability and ductility; a high total axial load ratio, on the other hand, results in a high strength, but low ductility. This observation is similar to that of monolithic columns tested by previous researchers (Ahn & Shin, 2007; Barrera et al., 2011). Therefore to achieve a good balance, the axial load level should be carefully selected in the design.

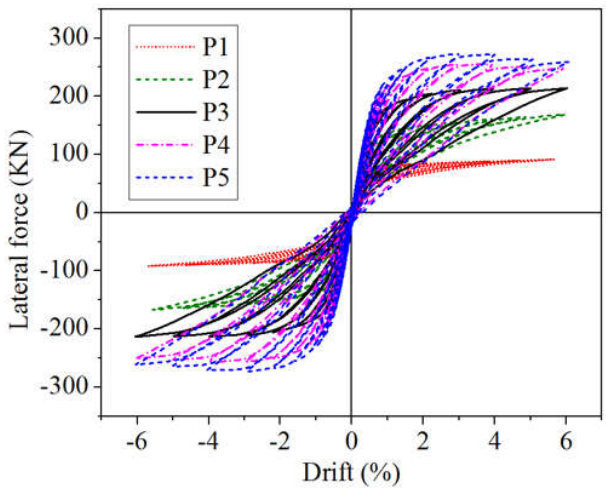

(a)

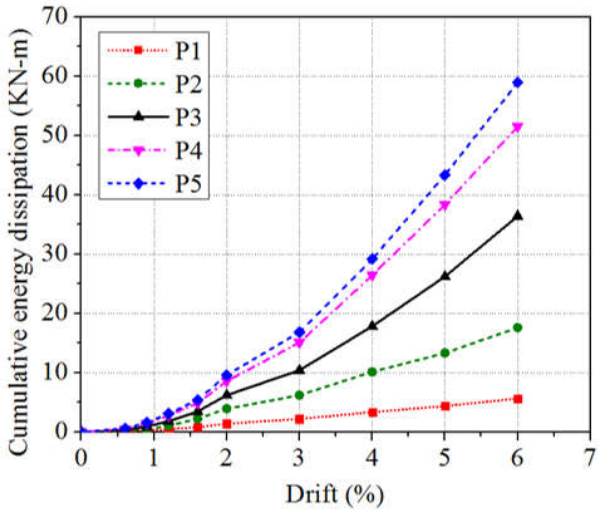

(b)

Figure 4-9 (a) Hysteretic curves of P1-P5; (b) cumulative energy dissipation of P1-P5

4.5.3 Influence of confinement

In the precast segmental column, high compressive strains are expected around the segment joints especially at the base joint. Therefore some researchers explored the effectiveness of confining the base segment of the column. For the reference column considered in this study (JH1) (Hewes & Priestley, 2002), the base segment was confined with a 6mm thick steel jacket in the test. To investigate the influence of confinement, two specimens (C2, C3), which are the same as the reference column

JH1 (C1) except for the thickness of steel jacket, are modelled. The thicknesses of the steel jackets in these two specimens are 3mm and 9mm, respectively.

Figure 4-10 shows the hysteretic curves and cumulative energy dissipations of this group of columns. It can be observed that the thickness of the steel jacket has obvious effects on the hysteretic curves of the segmental columns since it provides important confinement to the concrete segment in the plastic hinge region. With the increment of the steel jacket thickness, the stiffness of the columns after yielding changes from negative to positive. For example, for column C2 (with 3mm thick steel jacket), the maximum strength reaches 200.6 kN at 2% drift ratio. After this, the strength starts to drop and the strength decreases to 180.2 kN at 6% drift level. On the other hand, column C3 (with 9mm thickness steel jacket) shows no strength degradation and the strength reaches 248.9 kN at the drift ratio of 6%. Figure 4-10 (b) shows the cumulative energy dissipation of column C1 to C3. Column C2 with thinner steel jacket dissipates 40.6 kN-m energy at drfit ratio 6%, which is 28.7% higher than that of the reference column C1. Column C3 dissipates 31.2 kN-m energy at drift ratio 6%, which is 23.3% lower than that of column C1. The reason of the above observations is that the base segment is subjected to the largest compressive stress, which causes lateral expansion of the concrete and also bulge in the steel jacket as shown in Figure 4-11. When the thickness of the steel jacket is decreased, the steel jacket is more vulnerable to yield, which leads to a higher energy dissipation. More clear explanations can be made by examining the stress distribution of the steel jacket, as shown in Figure 4-12. It can be seen that for the column C2 with 3mm thick steel jacket, the height of the yielded area is about 390mm which is nearly two times of that of column C1. For column C3 with 9mm thick steel jacket, the height of the yielded area reduces to about 140mm. These results indicate that the confinement of the base segment directly affects the performance of the segmental column. The thinner the steel jacket is, the larger the yielding area occurs in the jacket which results in larger energy absorption but lower ductility. Therefore proper design of the confinement is necessary to achieve the desired performance of the segmental columns.

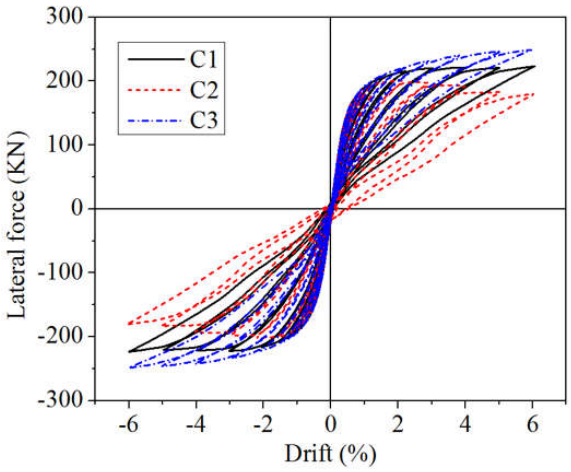

(a)

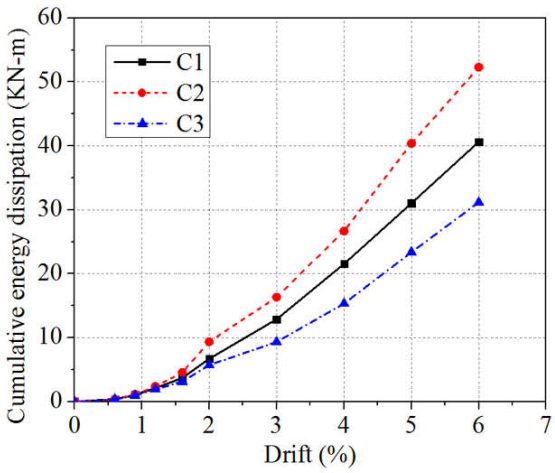

(b)

Figure 4-10 (a) Hysteretic curves of C1-C3; (b) cumulative energy dissipation of C1-C3

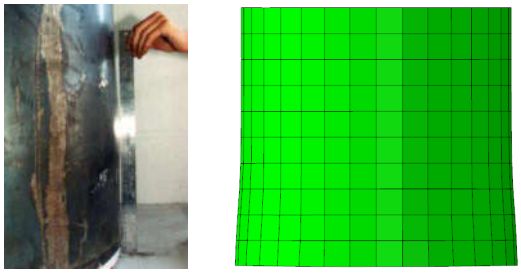

Figure 4-11 Bulge in the steel jacket observed in the test and simulation

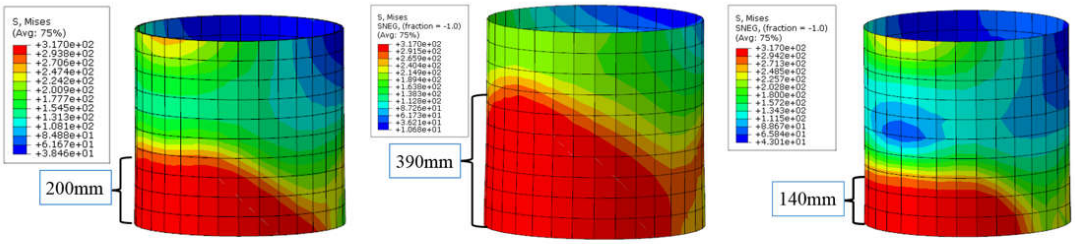

(a) (b) (c)

Figure 4-12 Stress distributions of the steel jackets C1 to C3

4.5.4 Influence of the number of segments

To investigate the influence of the number of segments on the performance of segmental column, columns with different number of segments are investigated in this part. Column S1 is the reference column JH1. Column S2 has two segments, equivalent to combining the bottom two segments, and the top two segments of the reference column JH1 together. Column S3 is a rocking column, equivalent to combining all the four segments of JH1 together to form one segment. Figure 4-13 (a) shows the hysteretic curves of the three segmental columns. It can be seen that the differences of the hysteretic curves among the columns with different number of segments are not significant. Accordingly, the difference among the cumulative energy dissipated by the three columns is insignificant either. It can be seen that column S2 and column S3 dissipate slightly more energy at the same drift ratio than the reference column S1. This is because that at the same drift level, column S1 with four segments is more flexible and has more openings at different joints along the column, while S3 with one segment has only a single opening at the base joint. More concrete damage in S3 is expected and thus increases the energy dissipation.

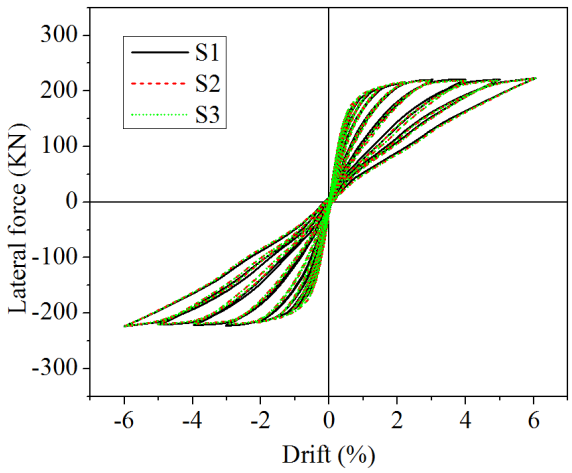

(a)

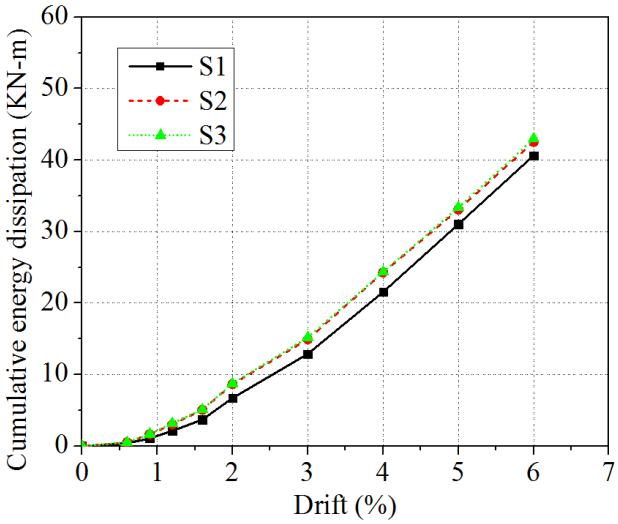

(b)

Figure 4-13 (a) Hysteretic curves of S1-S3; (b) cumulative energy dissipation of S1-S3

4.5.5 Influence of energy dissipation (ED) bars

As reviewed above, previous experimental studies showed that segmental columns connected only with posttensioned tendons showed unsatisfactory energy dissipation capacity (Ou et al., 2009). The column JH1 modelled in this study did not include any energy dissipation device, as a result, the column dissipated limited amount of energy as observed above. In this part, mild steel bars are placed across the segment joints in the numerical model to increase the energy dissipation capacity of the column. Besides, to minimize the residual drift of the columns, mild steel bars are replaced by shape memory alloy (SMA) bars to investigate the effectiveness of using SMA on dissipating seismic energy and minimizing the residual deformation.

4.5.5.1 Mild steel

Eight mild steel bars are added to the column. As detailed in Table 4-4, the specimens are denoted as E1-E6, in which E1 (JH1) has no ED bars and E2-E6 include ED bars with diameters of 10 mm, 16 mm, 20 mm, 24 mm, and 32 mm, respectively, and the corresponding ED bar ratios of these specimens are 0.23%, 0.58%, 0.91%, 1.31% and 2.32%, respectively. These bars start from the footing and extend to the third segment. The ED bars are evenly distributed in the segments with 270 mm distance from the column centre. The arrangement of the ED bars is shown in Figure 4-14. In the numerical model, the ED bars are simulated with truss elements which are embedded in the surrounding concrete, in other words, the bond-slip behaviour between the steel bars and the concrete is ignored. A 50 mm length of the ED bars are unbonded at the joint between the footing and the bottom segment to prevent premature failure of the ED bars (Leitner & Hao, 2016). To make the designated region unbonded in the mild steel in practice, duct tape or small PVC pipe could be used to cover the steel bars and separate the steel bar from the surrounding concrete. After inserting the reinforcement in the precast corrugated ducts, the precast ducts will be filled with grout materials and thus the steel bars is bonded with the surrounding concrete except the unbonded region covered with tape or PVC tube. All the ED bars are defined with a bilinear elastic-plastic stress-strain material model (Nikbakht et al., 2015), with a density of 7800 kg/m^3, a Young's modulus of 206 GPa, a Poisson's ratio of 0.3 and a yield stress of 410 MPa. The hysteretic curves of the columns E1 to E6 are shown in Figure 4-15 (a). As shown, the maximum lateral strength of the column increases with the increment of the ED bar ratios. To compare the hysteretic curves more clearly, a comparison of the hysteretic curves between columns E1 and E6 is shown in Figure 4-15 (b). For the reference column E1, the maximum strength capacity is about 224.6 kN while the maximum strength of column E6 with 2.32% ED bar ratio reaches 358.3 kN. Figure 4-15 also shows that with the increment of ED bar ratio, the residual drifts increase due to plastic deformation of the ED bars. For example, at 6% drift level, the residual displacement of column E6 is about 99.2 mm which equals to a residual drift of 2.7%. For column E1, however, the residual displacement is only about 5.2 mm. The larger strength of the column and larger residual drift result in the larger area enclosed by the hysteretic curve, indicating more energy dissipation. Figure 4-16 shows the cumulative energy dissipated by each specimen. As shown, the cumulative energy

dissipated by column E6 with 2.32% ED bar ratio is 312.9 kN-m at drift ratio 6%, which is 6.7 times the energy dissipated by the reference column E1. To summarize, the numerical results clearly demonstrate that increasing the amount of ED bars increases the energy dissipation capacity of segmental column. It, however, results in larger residual displacement. This is consistent with the experimental results in previous study (Ou et al., 2009). The parametric study can potentially provide guidelines on the optimum amount of ED bars in terms of energy dissipation without losing the self-centring characteristics.

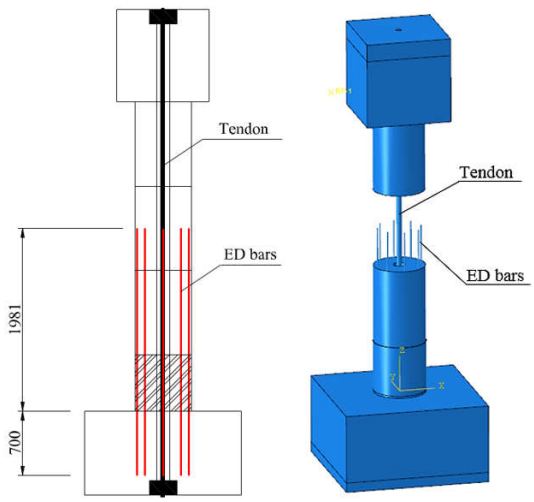

(a) (b)

Figure 4-14 (a) A schematic of arrangement of the added ED bars; (b) ED bars in the FE model

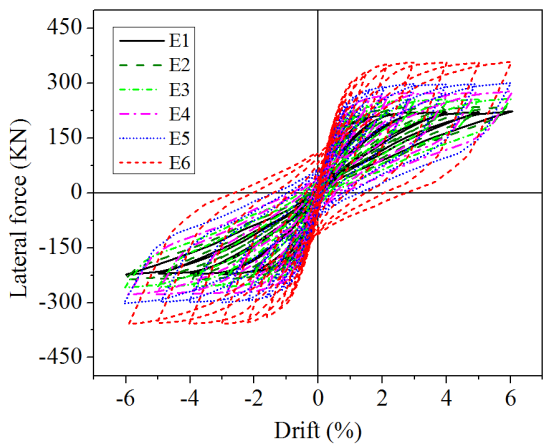

(a)

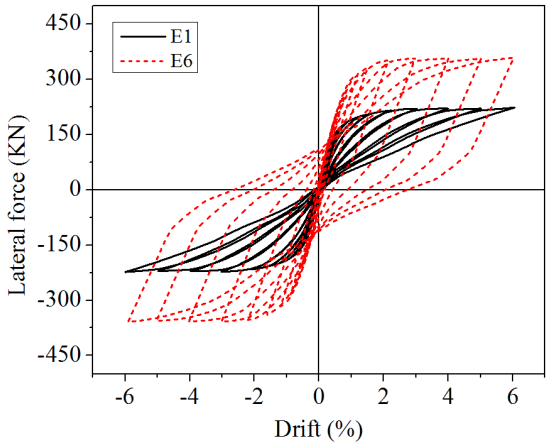

(a)

Figure 4-15 Comparison of hysteretic curves: (a) E1 to E6; (b) E1 and E6

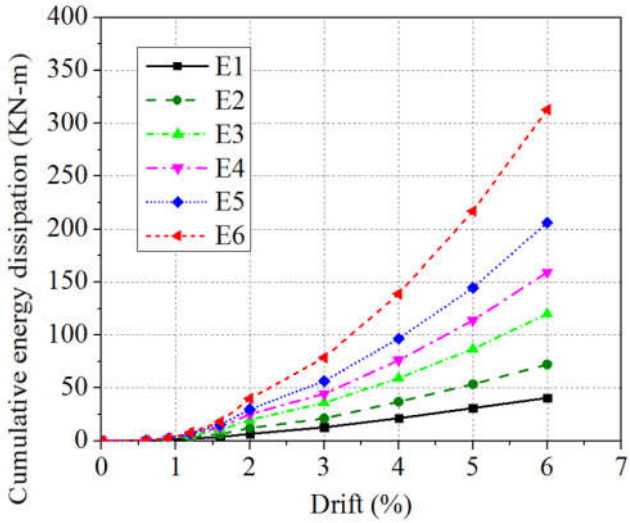

Figure 4-16 Cumulative energy dissipation capacity of E1 to E6

4.5.5.2 SMA

Shape memory alloys (SMA) can undergo large strain and recover to its original shape through heating (shape memory effect) or stress removal (super-elastic effect) (Wilson & Wesolowsky, 2005). This self-centring property can be used to help the structures recover to their original position after an earthquake event and therefore reduce the residual deformation of the structures. Some applications of super-elastic SMA can be found in experimental studies on bridge columns (Saiidi et al., 2009) and bracing system (Gao et al., 2016). Some numerical studies also investigated the effect of SMA on minimising the residual displacement and increasing the energy dissipation capacity (Leitner & Hao, 2016; Nikbakht et al., 2015; Shrestha & Hao, 2015). In this study, SMA bars are used in the segmental column as ED bars to increase the energy

dissipation capacity and reduce the residual drift of the column. To compare the performance of segmental columns with mild steel ED bars and SMA ED bars, the same amount of SMA bars with the same diameters as the mild steel bars are used in the analysis. For the constitutive model of super-elastic SMA, Auricchio-Taylor model is widely used by previous researchers (Auricchio & Taylor, 1997). This material model is implemented in ABAQUS as a user defined material (UMAT) subroutine in this study. Figure 4-17 shows a schematic of the stress-strain relationship of the super-elastic SMA. The mechanical properties of SMA used by Alam et al. are adopted in this study (Alam et al., 2009) and the parameters to define the material properties of SMA bars are listed in Table 4-5.

Table 4-5 Parameters for SMA

Parameter	Symbol	Value
Modulus of elasticity for austenite	E_A	68200 MPa
Modulus of elasticity for martensite	E_M	68200 MPa
Volumetric transformation strain	ε_L	0.062
Start stress of austenite to martensite phase transformation	σ_{sAM}	480 Mpa
Finish stress of austenite to martensite phase transformation	σ_{fAM}	540 Mpa
Start stress of martensite to austenite phase transformation	σ_{sMA}	260 Mpa
Finish stress of martensite to austenite phase transformation	σ_{fMA}	120 Mpa
Start stress of phase transformation during compression	σ_{sCAM}	480 MPa

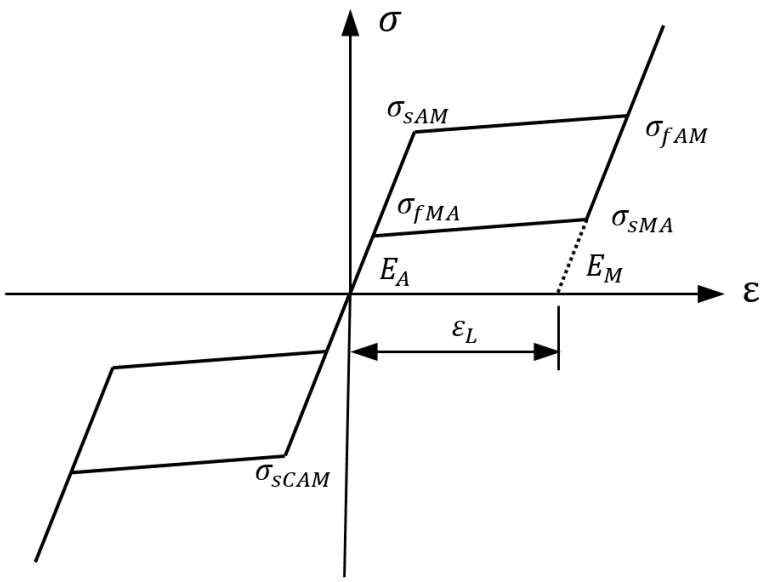

Figure 4-17 Idealized constitutive model of super-elastic SMA

The hysteretic curves of the modelled columns with SMA bars are shown in Figure 4-18 (a). To compare the results more clearly, the hysteretic curves of column SE1 and column SE6 are plotted separately in Figure 4-18 (b). It can be observed that with the SMA bars, the strength of the column is increased. In addition, the area enclosed by the hysteretic curve of column SE6 is also larger than that of column SE1, indicating a higher energy dissipation. Figure 4-19 shows the cumulative hysteretic energy dissipated by the columns. It can be observed that the additional SMA bars are effective to increase the energy dissipation. The cumulative energy dissipated by column SE6 at 6% drift ratio is 121.3 kN-m, which is about three times the energy dissipated by column SE1. Compared with the column with traditional mild steel bars, as shown in Figure 4-20, the energy dissipation capacities of the columns with SMA bars are lower, however, it should be noted that the residual drifs of the columns with SMA bars are also smaller than those of columns with mild steel bars. Table 4-6 gives a quantitative comparison of E6 and SE6 in terms of lateral strength, residual deformation, and energy dissipation at 6% drift ratio. It can be observed that the column with mild steel ED bars dissipated more energy than that of the column with SMA ED bars, however the residual drift is also larger. These differences can be attributed to the material properties of the SMA and steel as mentioned above. Figure 4-21 shows the stress-strain curves of the mild steel and the SMA bars obtained from the bars at the joint between the bottom segment and the footing. It can be observed

that the steel bars experience large plastic deformation which results in a significant residual strain. On the other hand, under the same loading condition, the stress-strain relationship of the SMA bars demonstrates a typical flag shaped curve, which results in a small residual drift of the column. In addition, the area of the stress-strain loops of the SMA bars is smaller compared with that of the mild steel bar, indicating smaller energy dissipation. Figure 4-21 (b) also shows that the stress-strain curve developed in the SMA bars is not symmetric as that in Figure 4-17. This is because the strain shows in Figure 4-21 (b) is the strain from the SMA bars on the left side of the column (Figure 4-22). When the column is pushed in the positive direction as shown in Figure 4-22 (a), the column joint opens and the SMA bar on the left side is in tension and the strain increases in the tensile direction. The tensile stress can reach a large value which makes the SMA yield. On the other hand, when the column is pulled back (Figure 4-22 (b)), the SMA bars on the left side is in compression. The compression stress is not significant in the SMA bars because the surrounding concrete on the left side of the column provides the main resistance in compression.

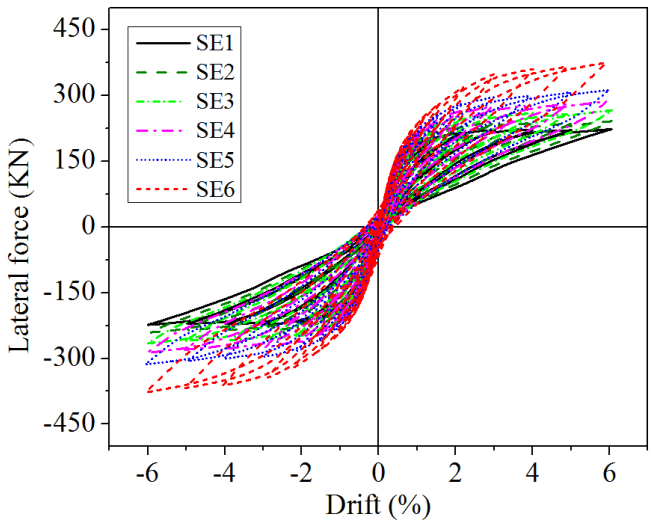

(a)

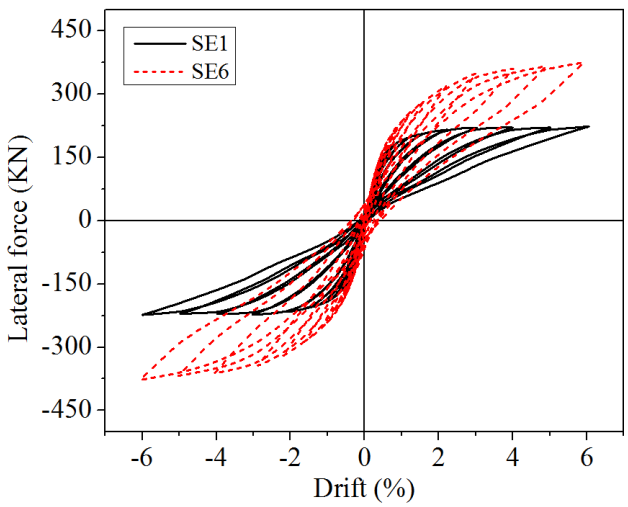

(b)

Figure 4-18 Comparison of hysteretic curves: (a) SE1 to SE6; (b) SE1 and SE6

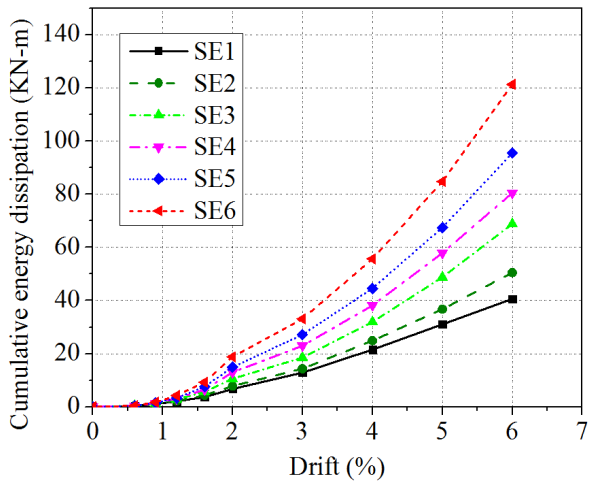

Figure 4-19 Cumulative energy dissipation capacity of SE1 to SE6

Table 4-6 Quantitative comparisons of E6 and SE6

Column	E6	SE6
Lateral strength (kN)	358.6	374.6
Residual deformation (mm)	99.2	15.8
Cumulative energy (kN-m)	312.9	121.3

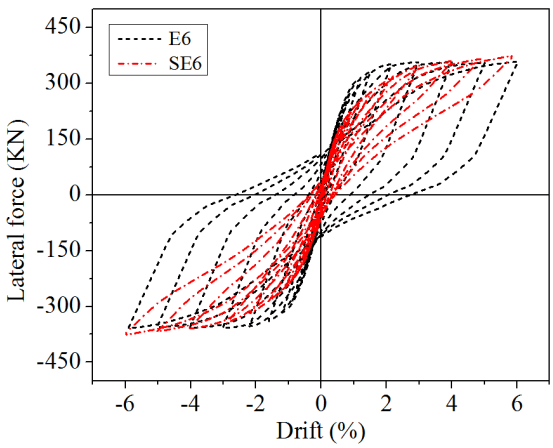

Figure 4-20 Comparison of the hysteretic curves of E6 and SE6

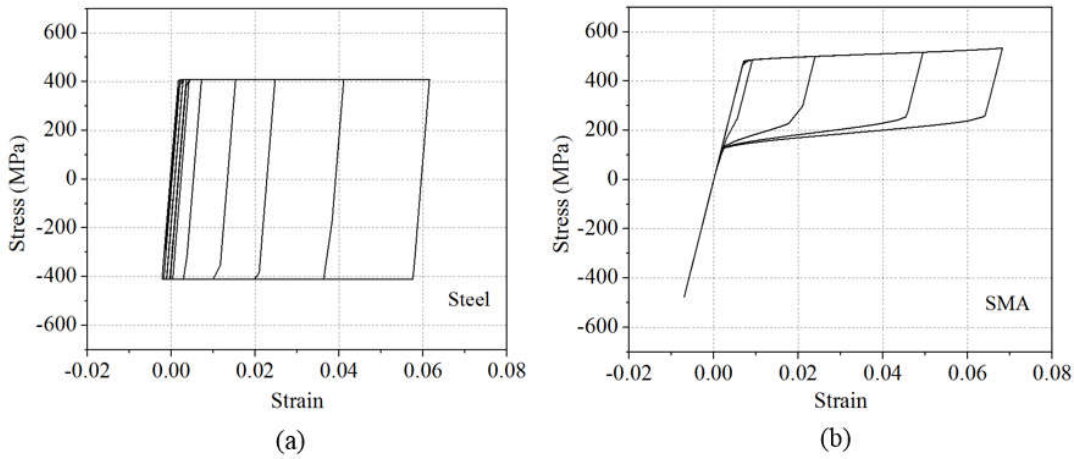

Figure 4-21 Comparison of stress-strain curves of mild steel and SMA bars

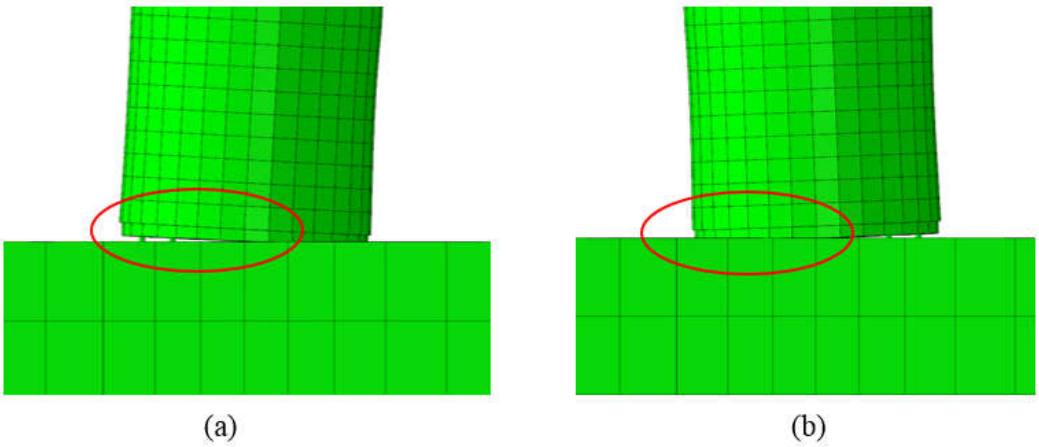

Figure 4-22 Joint openings and deformation of the SMA bars when the column is in push and pull direction

4.6 Conclusions

This paper performs numerical studies on the cyclic performance of precast segmental columns. Three dimensional detailed FE models of two segmental columns with different aspect ratios are developed. These two models are first validated against the experimental results. After validation of the numerical models, comprehensive parametric studies are carried out. Different parameters including the bonding conditions for tendons, axial force ratio, confinement of the segments, the number of segments, and energy dissipation bars are studied to systematically investigate the parameters that may affect the performance of segmental column. Some conclusions are drawn based on the numerical studies:

(1) The numerical models developed in this study are able to capture the general behaviour of precast segmental columns. The modelling results agree well with the experimental results in terms of damage mode and hysteretic curve, indicating the accuracy of the modelling methods. With proper modelling methods and accurate constitutive material model, the FE analysis can be a reliable and efficient tool to capture the nonlinear behaviours of segmental columns.

(2) The numerical models demonstrate that bonded tendons can increase the lateral strength of the column, however, it also results in stress concentration in the tendon. Moreover, the residual drift of the column with bonded tendon is increased and the ductility of the column is reduced compared to the column with unbonded tendons.

(3) Higher initial axial forces in the column results in higher lateral strength and higher energy dissipation of the column, but lower ductility. The initial axial load needs to be carefully designed to achieve a reasonable strength and ductility.

(4) The confinement for the base segment significantly affects the performance of the segmental column. The thinner the steel jacket is, the larger the yielding area is observed in the steel jacket, leading to an increase in the energy dissipation but a decrease in the lateral strength and ductility.

(5) According to the simulated results, the segment number has insignificant influence on the cyclic behaviour of the column.

(6) Adding mild steel bars across the joints between segments increases the energy dissipation of the segmental column. However, with the increase of the steel ED bar ratio, the residual drift is also increased due to the plastic deformation of the mild steel bars. Using SMA bars as ED bars can also increase the energy dissipation capacity while keeping the residual drift small.

4.7 References

Ahn, J.-M., & Shin, S.-W. (2007). An evaluation of ductility of high-strength reinforced concrete columns subjected to reversed cyclic loads under axial compression. *Magazine of Concrete Research, 59*(1), 29-44. doi:10.1680/macr.2007.59.1.29

Alam, M. S., Nehdi, M., & Youssef, M. A. (2009). Seismic performance of concrete frame structures reinforced with superelastic shape memory alloys. *Smart Struct Syst, 5*(5), 565-585.

Auricchio, F., & Taylor, R. L. (1997). Shape-memory alloys: modelling and numerical simulations of the finite-strain superelastic behavior. *Computer Methods In Applied Mechanics And Engineering, 143*(1), 175-194. doi:http://dx.doi.org/10.1016/S0045-7825(96)01147-4

Barrera, A. C., Bonet, J. L., Romero, M. L., & Miguel, P. F. (2011). Experimental tests of slender reinforced concrete columns under combined axial load and lateral force. *Engineering Structures, 33*(12), 3676-3689. doi:http://dx.doi.org/10.1016/j.engstruct.2011.08.003

Billington, S. L., & Yoon, J. (2004). Cyclic response of unbonded posttensioned precast columns with ductile fiber-reinforced concrete. *Journal of Bridge Engineering, 9*(4), 353-363.

Birtel, V., & Mark, P. (2006). *Parameterised finite element modelling of RC beam shear failure.* Paper presented at the Proceedings of the 19th Annual International ABAQUS Users' Conference. Boston:[sn].

Chou, C. C., & Chen, Y. C. (2006). Cyclic tests of post-tensioned precast CFT segmental bridge columns with unbonded strands. *Earthquake Engineering & Structural Dynamics, 35*(2), 159-175.

Dawood, H., ElGawady, M., & Hewes, J. (2011). Behavior of segmental precast posttensioned bridge piers under lateral loads. *Journal of Bridge Engineering, 17*(5), 735-746.

Demir, A., Caglar, N., Ozturk, H., & Sumer, Y. (2016). Nonlinear finite element study on the improvement of shear capacity in reinforced concrete T-Section beams by an

alternative diagonal shear reinforcement. *Engineering Structures, 120*, 158-165. doi:http://dx.doi.org/10.1016/j.engstruct.2016.04.029

ElGawady, M., Booker, A. J., & Dawood, H. (2010). Seismic behavior of posttensioned concrete-filled fiber tubes. *Journal of Composites for Construction, 14*(5), 616-628.

ElGawady, M., & Dawood, H. (2012). Analysis of segmental piers consisted of concrete filled FRP tubes. *Engineering Structures, 38*, 142-152.

ElGawady, M., & Sha'lan, A. (2010). Seismic behavior of self-centering precast segmental bridge bents. *Journal of Bridge Engineering, 16*(3), 328-339.

Gao, N., Jeon, J.-S., Hodgson, D. E., & DesRoches, R. (2016). An innovative seismic bracing system based on a superelastic shape memory alloy ring. *Smart Materials and Structures, 25*(5), 055030. doi:10.1088/0964-1726/25/5/055030

Han, L.-H., Yao, G.-H., & Tao, Z. (2007). Performance of concrete-filled thin-walled steel tubes under pure torsion. *Thin-Walled Structures, 45*(1), 24-36.

Hewes, J. T., & Priestley, M. N. (2002). *Seismic design and performance of precast concrete segmental bridge columns* (No. SSRP-2001/25). Retrieved from University of California, San Diego, CA:

Hu, H.-T., & Schnobrich, W. C. (1989). Constitutive modeling of concrete by using nonassociated plasticity. *Journal of Materials In Civil Engineering, 1*(4), 199-216.

Lee, J., & Fenves, G. L. (1998). Plastic-damage model for cyclic loading of concrete structures. *Journal of Engineering Mechanics, 124*(8), 892-900.

Leitner, E. J., & Hao, H. (2016). Three-dimensional finite element modelling of rocking bridge piers under cyclic loading and exploration of options for increased energy dissipation. *Engineering Structures, 118*, 74-88. doi:10.1016/j.engstruct.2016.03.042

Lubliner, J., Oliver, J., Oller, S., & Oñate, E. (1989). A plastic-damage model for concrete. *International Journal of Solids and Structures, 25*(3), 299-326. doi:http://dx.doi.org/10.1016/0020-7683(89)90050-4

Mander, J. B., Priestley, M. J., & Park, R. (1988). Theoretical stress-strain model for confined concrete. *Journal of Structural Engineering, 114*(8), 1804-1826.

Marriott, D., Pampanin, S., & Palermo, A. (2009). Quasi-static and pseudo-dynamic testing of unbonded post-tensioned rocking bridge piers with external replaceable dissipaters. *Earthquake Engineering & Structural Dynamics, 38*(3), 331-354.

Marriott, D., Pampanin, S., & Palermo, A. (2011). Biaxial testing of unbonded post-tensioned rocking bridge piers with external replacable dissipaters. *Earthquake Engineering & Structural Dynamics, 40*(15), 1723-1741.

Nikbakht, E., Rashid, K., Hejazi, F., & Osman, S. A. (2015). Application of shape memory alloy bars in self-centring precast segmental columns as seismic resistance. *Structure and Infrastructure Engineering, 11*(3), 297-309.

Ou, Y. C., Chiewanichakorn, M., Aref, A. J., & Lee, G. C. (2007). Seismic performance of segmental precast unbonded posttensioned concrete bridge columns. *Journal of Structural Engineering, 133*(11), 1636-1647.

Ou, Y. C., Tsai, M. S., Chang, K. C., & Lee, G. C. (2010). Cyclic behavior of precast segmental concrete bridge columns with high performance or conventional steel reinforcing bars as energy dissipation bars. *Earthquake Engineering & Structural Dynamics, 39*(11), 1181-1198.

Ou, Y. C., Wang, P. H., Tsai, M. S., Chang, K. C., & Lee, G. C. (2009). Large-scale experimental study of precast segmental unbonded posttensioned concrete bridge columns for seismic regions. *Journal of Structural Engineering, 136*(3), 255-264.

Saiidi, M. S., O'Brien, M., & Sadrossadat-Zadeh, M. (2009). Cyclic response of concrete bridge columns using superelastic nitinol and bendable concrete. *ACI Structural Journal, 106*(1), 69.

Shim, C. S., Chung, C. H., & Kim, H. H. (2008). Experimental evaluation of seismic performance of precast segmental bridge piers with a circular solid section. *Engineering Structures, 30*(12), 3782-3792.

Shrestha, B., & Hao, H. (2015). Parametric study of seismic performance of super-elastic shape memory alloy-reinforced bridge piers. *Structure and Infrastructure Engineering, 12*(9), 1076-1089. doi:10.1080/15732479.2015.1076856

Sideris, P., Aref, A. J., & Filiatrault, A. (2014). Quasi-static cyclic testing of a large-scale hybrid sliding-rocking segmental column with slip-dominant joints. *Journal of Bridge Engineering, 19*(10), 04014036.

Simulia, D. S. (2012). Abaqus 6.12 documentation. *Providence, Rhode Island, US.*

Tazarv, M., & Saiid Saiidi, M. (2015). Low-Damage Precast Columns for Accelerated Bridge Construction in High Seismic Zones. *Journal of Bridge Engineering*, 04015056.

Wang, J. C., Ou, Y. C., Chang, K. C., & Lee, G. C. (2008). Large-scale seismic tests of tall concrete bridge columns with precast segmental construction. *Earthquake Engineering & Structural Dynamics, 37*(12), 1449-1465.

Wilson, J. C., & Wesolowsky, M. J. (2005). Shape Memory Alloys for Seismic Response Modification: A State-of-the-Art Review. *Earthquake Spectra, 21*(2), 569-601. doi:10.1193/1.1897384

Yuan, F., Wu, Y.-F., & Li, C.-Q. (2017). Modelling plastic hinge of FRP-confined RC columns. *Engineering Structures, 131*, 651-668. doi:http://dx.doi.org/10.1016/j.engstruct.2016.10.018

Zhu, H., Stephens, M. T., Roeder, C. W., & Lehman, D. E. (2017). Inelastic response prediction of CFST columns and connections subjected to lateral loading. *Journal of Constructional Steel Research, 132*, 130-140. doi:http://dx.doi.org/10.1016/j.jcsr.2017.01.016

CHAPTER 5 SEISMIC PERFORMANCE OF PRECAST CONCRETE-FILLED CIRCULAR TUBE SEGMENTAL COLUMN UNDER BIAXIAL LATERAL CYCLIC LOADINGS

5.1 Abstract

Precast segmental column has been developed in recent years as one of the widely used prefabricated structures to accelerate construction speed. However, its applications are limited in the areas of low seismicity due to insufficient knowledge about its performance under seismic loading. Recently, some research works have been performed to understand the seismic performance of precast segmental columns. However, only the uniaxial cyclic loading was considered. In reality, the seismic excitation is not uniaxial. Considering responses of columns to uniaxial loading only may not accurately reflect the true structural response during an earthquake. In this study, comprehensive numerical analyses are carried out to investigate the seismic performances of circular precast segmental columns under biaxial lateral cyclic loadings. A three-dimensional numerical model is firstly developed and validated against the experimental results of a precast concrete-filled tube (CFT) segmental column under uniaxial cyclic loading. Six biaxial cyclic loading cases are then applied to the validated model. The numerical results indicate that biaxial cyclic loading paths can significantly influence the strength, ductility and energy dissipation of the column. In addition, the residual displacement of the segmental column increases obviously under biaxial cyclic loading compared with that of the column under uniaxial cyclic loading. Shape memory alloy (SMA) is found to be effective to minimize the residual displacement of the segmental column under biaxial loading. Moreover, the axial loading ratio has a more pronounced effect on the strength degradations of the column under biaxial lateral cyclic loading than that of the column under uniaxial loading.

5.2 Introduction

Precast segmental column has attracted a significant amount of research interests recently. The reason is that compared with the traditional cast-in-situ construction methods, this kind of structure has a series of benefits such as shorter on-site construction time, less site disruption, improved quality control and safer working

conditions for construction workers (Ou et al., 2009). Therefore, it is a promising structure that could be used to accelerate construction speed which is especially important in urban areas with heavy traffic. However, due to the limited understanding of its performance under earthquake loading, the applications are still limited to the areas of low seismicity.

A few experimental investigations have been carried out by different researchers in recent years (Billington & Yoon, 2004; Bu et al., 2015; Cai et al., 2018; Chou & Chen, 2006; ElGawady et al., 2010; ElGawady & Sha'lan, 2010; Hewes & Priestley, 2002; Li et al., 2017; Ou et al., 2010; Ou et al., 2009; Shim et al., 2008; Sideris et al., 2014). For example, Hewes and Priestley (2002) presented an experimental study, in which four large-scale segmental columns with the base segment encased in a steel jacket were tested under cyclic loading. Billington and Yoon (2004) tested segmental columns with ductile fibre-reinforced cement-based composite in the potential plastic hinging zones to reduce the concrete damage. Shim et al. (2008) performed an experimental study on the precast segmental piers with bonded prestressing bars and steel tubes which passed across the segmental joints continuously. Ou et al. (2009) carried out large-scale cyclic tests on a series of segmental columns with a hollow square cross section under cyclic loading, and it was concluded that the segmental columns had excellent self-centring ability. The good self-centring is resulted from the tendon in the column which is also beneficial for minimizing the residual displacement of the monolithic column (Sun et al., 2016). Besides these experimental investigations, some numerical studies were also conducted (Cai, et al., 2018; Dawood et al., 2011; Leitner & Hao, 2016; Nikbakht et al., 2014). These studies have greatly advanced the understanding and enriched the knowledge of the seismic performance of precast segmental columns.

It should be noted that all the above studies assumed the column is under uniaxial lateral cyclic loading. Due to the nature of earthquake, the seismic excitations are not uniaxial and columns are inevitably subjected to biaxial horizontal loadings during a severe earthquake event. Therefore it is important to understand the performance of columns under biaxial lateral loadings. A few studies on the biaxial performance of thin wall steel columns (Goto et al., 2006; Goto et al., 2009; Ucak & Tsopelas, 2014) and RC columns (Bousias et al., 1995; Chang, 2009; Qiu et al., 2002; Rodrigues et al.,

2013b; Rodrigues et al., 2015; Rodrigues et al., 2017; Rodrigues et al., 2018) were reported in the literature based on the assumed loading paths. Goto et al. (2006) tested four thin wall steel columns, in which one column was subjected to the uniaxial cyclic loading as a reference and the other three were subjected to the biaxial lateral cyclic loading with a circular loading path. It was found that the biaxial loading accelerated the local buckling and decreased the strength and ductility of the columns in comparison with the uniaxial cyclic loading. Ucak et al. (2014) developed a detailed numerical model to predict the uniaxial cyclic performance of thin wall steel columns. Different loading paths were then used to investigate the effect of loading path on the biaxial behaviour of the columns. The simulated results showed that the ductility and energy dissipation capacity were greatly affected by the loading paths. Bousias et al. (1995) conducted experimental studies on twelve RC columns and investigated the biaxial performance of the tested columns. It was concluded that the degradation of strength and stiffness of the columns under biaxial lateral cyclic loadings were more serious than that of columns under uniaxial lateral cyclic loading. Qiu et al. (2002) tested seven identical RC columns under seven different loading paths to investigate the biaxial performance of RC columns. It was found that the column under biaxial loading had significantly different behaviour as compared with that of the column under uniaxial loading. Chang (2009) tested RC columns under biaxial bending and the hysteretic curves also showed more stiffness and strength degradation. Rodrigues et al. tested a series of columns under different kinds of loading conditions to evaluate the biaxial cyclic performance of rectangular RC columns and the results demonstrated that the responses of the RC columns under biaxial loadings were highly dependent on the loading paths (Rodrigues et al., 2015; Rodrigues et al., 2013a; Rodrigues et al., 2013b). Critical review reveals that most of the previous researches concentrated on investigating the seismic performance of the segmental columns under uniaxial cyclic loading. Limited studies investigated the biaxial cyclic performance and loading path effect on the monolithic reinforced concrete columns and thin wall steel columns. To the authors' best knowledge, there is no study that has investigated the performance of precast segmental column under biaxial cyclic loadings and the effect of different biaxial loading paths on its performance.

The primary objective of this paper is to investigate the biaxial performance of the circular precast segmental columns and the effect of biaxial lateral loading paths on

the performance of precast segmental columns. A detailed three-dimensional (3D) numerical model that can accurately predict the nonlinear cyclic performance of segmental column is first developed based on a previous experimental study. Six biaxial cyclic loading protocols with different paths are then applied to the column. The influence of biaxial cyclic lateral loading on the performance of precast segmental column and the effect of different loading paths on the damage patterns, hysteretic curves, strength degradation, residual displacement and energy dissipation capacity are compared and analysed. The results and discussion can lead to better understanding on the seismic performance of the precast segmental columns.

5.3 Numerical model

As discussed above, no study reports the seismic performance of precast segmental columns subjected to biaxial lateral cyclic loadings. In the present study, a detailed 3D numerical model is developed and validated against a previous experimental study of a precast segmental column under uniaxial cyclic loading. In this part, the design details of the segmental column, the modelling methods and procedures, and the validation of the numerical model are presented.

5.3.1 Model description

The finite element model developed in this study is based on the experimental results (Chou et al., 2013). Figure 5-1 shows the design details. The column consisted of four segments and the total height of the segments was 2030 mm. The footing and the loading block were 850 mm and 840 mm, respectively. The total height of the tested specimen was therefore 3720 mm. The segments had a circular cross section, and the diameter of the cross section was 500 mm. Eight longitudinal steel bars were installed in each segment, the diameter of the steel bars in the upper three segments was 16 mm (#5 steel) and that in the bottom segment was 25 mm (#8 steel). It should be noted that these longitudinal steel bars only existed within the segments, in other words, they were discontinuous at the joints between the segments. #3 steel with the diameter of 10 mm was used as the hoops, and the spacing between the adjacent hoops was 400 mm. Four #6 energy dissipation (ED) bars with the diameter of 19 mm were used to increase the energy dissipation capability of the segmental column. The ED bars started from the footing and extended to the top surface of the bottom segment. To

avoid stress concentration of the ED bars at the joint, a portion (250 mm) of the ED bars was left unbounded in the footing, while the other parts were bonded in the footing and bottom segments, respectively. The column segments were connected and clamped by high strength prestressing tendon. The tendon included nineteen seven-wire high strength prestressing strands with a diameter of 15 mm. Each segment was encased in a steel jacket to mitigate the concrete spalling damage. The thicknesses of the steel jacket for the bottom segment and the upper three segments were 5 mm and 3 mm, respectively. Table 5-1 summarizes the material properties of each component of the simulated precast segmental column.

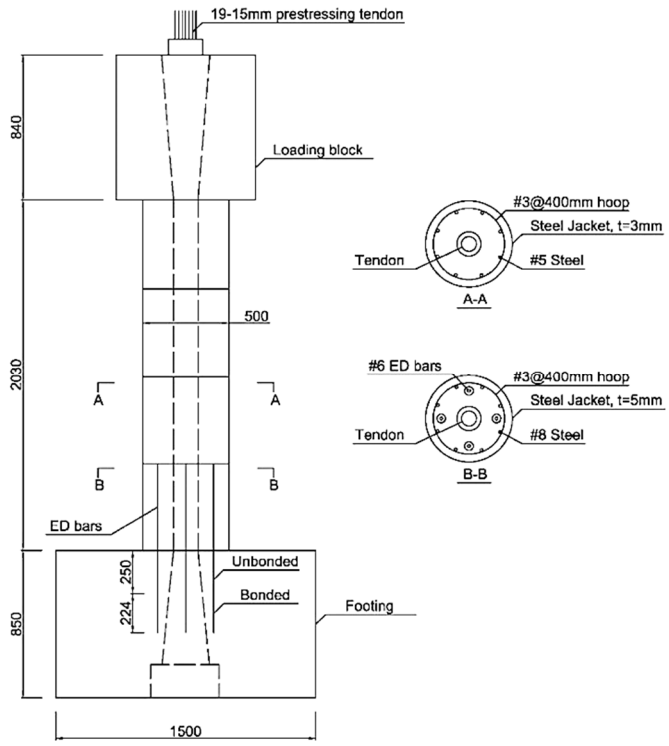

Figure 5-1 Design details of the column (after (Chou et al., 2013))

Table 5-1 Material properties of the column

Items		Values
Concrete	Strength (MPa)	48
	Poisson's ratio	0.2
Steel bars	Diameter (mm)	10/16/25
	Elastic modulus Es (GPa)	203
	Yielding stress (MPa)	474
	Poisson's ratio	0.3
Steel jacket	Thickness (mm)	5mm/3mm
	Elastic modulus Es (GPa)	206
	Yielding stress (MPa)	240/269
	Poisson's ratio	0.3
ED bars	Diameter (mm)	19
	Elastic modulus Es (GPa)	203
	Yielding stress (MPa)	307
	Poisson's ratio	0.3
Tendons	Area (mm^2)	2611
	Elastic modulus Es (GPa)	196.5
	Ultimate stress (MPa)	1860
	Poisson's ratio	0.3
	Prestressing force (kN)	2321

5.3.2 Numerical modelling details

The finite element (FE) model is developed by using the FE code ABAQUS/Standard (Simulia, 2012). Figure 5-2 shows the numerical model. In particular, the precast concrete segments, footing and loading block are modelled by the 3D brick elements (C3D8R), and the longitudinal reinforcements, hoops, and ED bars are modelled by the truss elements (T3D2). The steel jacket is modelled by four-node shell element (S4R). For the mesh size, a mesh convergence test on various mesh sizes (25, 50 and 100 mm) is conducted and it is found that the model with 50 mm mesh for the column and 100 mm for the footing and loading block yields similar results as compared with

that of the model with smaller meshes. These mesh sizes are therefore adopted for the concrete in the numerical simulations. For the longitudinal reinforcements and hoops, they are embedded in the surrounding concrete. For the ED bars, as in the experiment, both ends of the ED bars are also embedded in the concrete and the unbonded region is left unconstrained (i.e. separate) in the model. For the steel jacket, the mesh size is the same as the column, i.e. 50 mm is adopted. Since the diameter of the hole for the tendon in the segments is 130 mm and the diameter of the tendon is only about 58 mm, there is a gap between the tendon and segments. To more realistically consider the contact between the prestressing tendon and the hole, the prestressing tendon is also modelled by the brick C3D8R elements, and a mesh size of 10 mm is adopted for the prestressing tendon based on the mesh convergence test. Surface to surface contact elements are adopted to model the contact between the tendon and the segments which allow the surfaces to separate without any resistance and develop compression when they are in contact. The anchorage of the tendon is modelled by embedding two ends of the tendon in the surrounding concrete.

To simulate the behaviour of the concrete, the concrete damaged plasticity model (CDP) is used to model the concrete behaviour since it is the most suitable model to simulate reinforced concrete structures under cyclic loading among the smeared crack model, brittle cracking model and concrete damage plasticity model that are available in ABAQUS (Simulia, 2012). The CDP model requires the input of five plasticity parameters and the independent uniaxial stress-strain relationships of the concrete in compression and tension. The five plasticity parameters include the dilation angle (ψ), flow potential eccentricity (e), the ratio of initial equibiaxial compressive yield stress to initial uniaxial compressive yield stress (σ_{b0}/σ_{c0}), the coefficient determining the shape of the deviatoric cross-section (K_c), and the viscosity parameter (μ). These parameters define the yield surface function, the potential flow and the viscosity of the material. More detailed descriptions of the definitions of the parameters can be found in the authors' previous paper (Li et al., 2017). In this study, the values of 30°, 0.1, 1.16, 0.6667 and 0.0001 are used for the five parameters (ψ, e, σ_{b0}/σ_{c0}, K_c, and μ).

For the stress-strain relationship of the concrete in compression, the widely used steel tube confined concrete model developed by Han et al. (Han et al., 2007) is adopted to

calculate the uniaxial stress-strain relationship of the concrete. The stress-strain model is defined as follows:

$$y = \begin{cases} 2x - x^2 & (x \leq 1) \\ \frac{x}{\beta_0 (x-1)^\eta + x} & (x > 1) \end{cases} \tag{5.1}$$

in which $x = \frac{\varepsilon}{\varepsilon_0}$, $y = \frac{\sigma}{\sigma_0}$ with $\sigma_0 = f_c'$ representing the cylinder strength of the concrete and ε_0 the corresponding strain; β_0 and η are related to the jacket shape and the material properties of the steel jacket.

For the tensile stress and strain relationship of the concrete, linear elastic behaviour is modelled until the tensile strength $f_t' = 0.62276\sqrt{f_c'}$ MPa is reached. A linear softening behaviour is modelled for the post-cracking behaviour till an ultimate strain of 0.2% (Dawood et al., 2011). For the steel reinforcements, steel jackets and prestress tendon, the classical elastic-perfectly plastic stress-strain material model is adopted (Nikbakht et al., 2015). The properties of each material are listed in Table 5-1.

Under the external loadings, openings at the joints between two adjacent segments might occur. To model the possible joint openings, surface to surface contact elements in ABAQUS are used. The normal contact between the surfaces is modelled by the hard contact, which means the surfaces can develop compression when they are in contact and will separate without tensile resistance when the joints open. For the tangential behaviour, tangential friction is used and the friction coefficient is assumed to be 0.5 as suggested in (Dawood et al., 2011). For the boundary condition, the footing is fixed at the bottom surface. The prestrsssing force in the tendon is modelled by initial stress condition and the prestressing force is given in Table 5-1. The axial load ratio is the same as that in the test, i.e. 24.6%. To be consistent with the experimental setup, the lateral cyclic loading, which is shown in Figure 5-3 (a), is applied to the loading block with predetermined drift ratios. The uniaxial cyclic (UC) loading path is shown in Figure 5-3 (b).

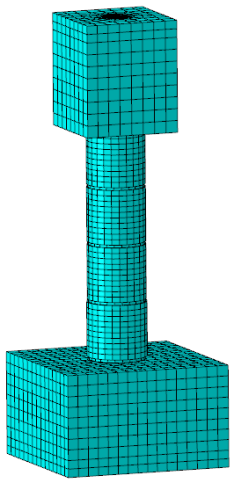

Figure 5-2 Numerical model of the column

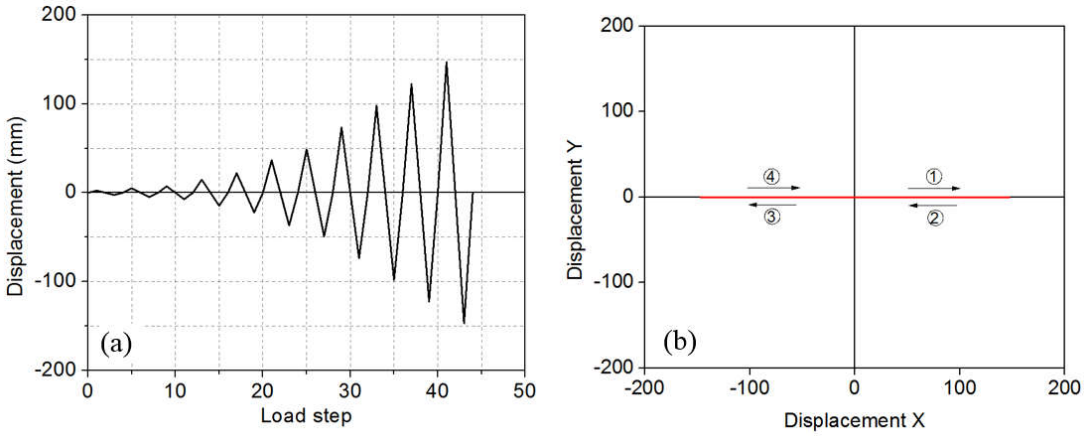

Figure 5-3 Uniaxial lateral loading: (a) displacement amplitude; (b) loading path (UC)

5.3.3 Model validation

Figure 5-4 shows the comparison of the hysteretic curves obtained from the finite element model (the red dash curve) and the experimental result (the black solid curve). It can be observed that the hysteretic loops predicted by the numerical model are in good agreement with the experimental results. The model can well capture the initial stiffness, unloading stiffness, and ultimate load capacity of the tested segmental column, which indicates the accuracy of the numerical model. Figure 5-5 compares the energy dissipations in the experimental tests and numerical simulations at each drift ratio. It can be observed that the energy dissipations from numerical simulations agree well with those from experimental tests, which further proves the accuracy of the numerical model. Since the column was confined by the steel jacket, the damage

was not visible in the test, they are therefore not directly compared. The validated numerical model is used to investigate the biaxial cyclic performance of the precast segmental column in the following sections.

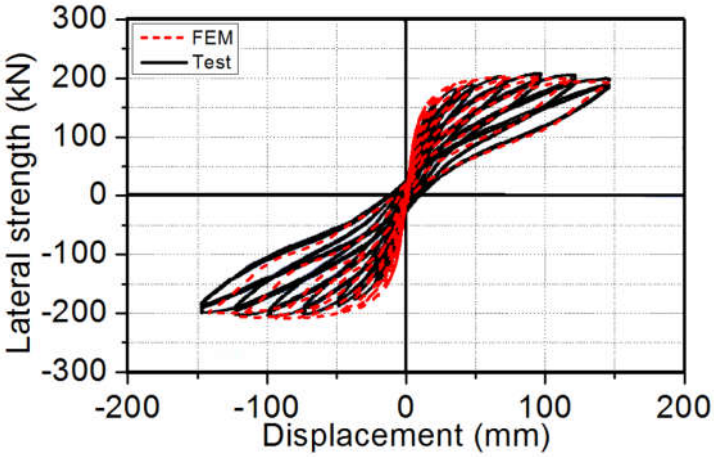

Figure 5-4 Comparison of numerical and experimental hysteretic curves

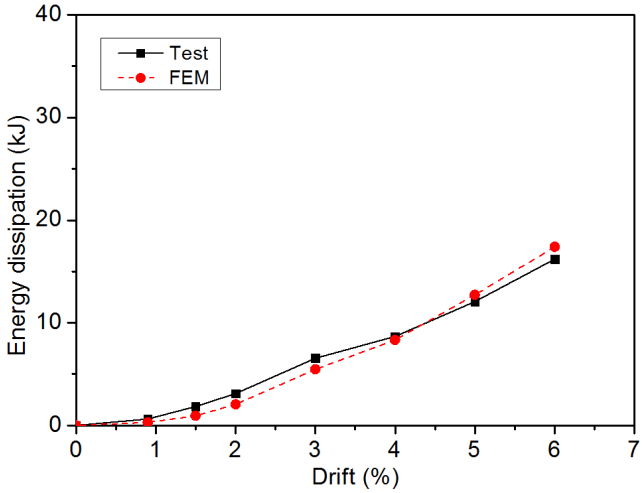

Figure 5-5 Comparison of the energy dissipation at each drift between the numerical and experimental results

It should be noted that the numerical model is only validated under the uniaxial loading due to the lack of data, the validated numerical model is then used to investigate the seismic performances of the circular segmental column under biaxial loadings. This is deemed as a reasonable practice because the only difference is the applied loads. As the 3D brick elements (C3D8R) and truss elements (T3D2) are used to simulate the concrete and rebars in the numerical simulations. These elements are not only able to capture the responses of the column under uniaxial loading but also the responses under biaxial loadings.

5.4 Biaxial loading protocols

The effects of biaxial loadings on the performance of precast segmental column are investigated by applying different types of biaxial lateral loading protocols. The biaxial lateral loadings are modified based on the uniaxial lateral cyclic loading. The displacement amplitudes of the biaxial loadings in each direction are the same as that of the uniaxial loading while the loading path varies for different protocols. Figure 5-3 shows the loading protocol for the UC case, and six commonly used (Bousias et al., 1995; Goto et al., 2006; Khaled et al., 2010; Qiu et al., 2002; Rodrigues et al., 2013b; Rodrigues et al., 2012; Shirmohammadi & Esmaeily, 2015; Ucak & Tsopelas, 2014) biaxial cyclic loading paths (BC1-BC6) as shown in Figure 5-6 are adopted in the present study. The sequence of the loading is represented by the numbers and arrows in Figure 5-6. For the loading path BC1 (Figure 5-6 (a)), the loadings in X and Y directions are applied to the column simultaneously with the same displacement amplitude, forming a diagonal-shape path. The second and third paths BC2, BC3 are both cross-shaped paths. For the loading path BC2 (Figure 5-6 (b)), the loading is first applied in the X direction with positive and negative amplitudes, after the column returns to the original position the Y direction loading is applied. For the loading path BC3 as shown in Figure 5-6 (c), the shape and amplitude are the same as BC2, but the loading firstly goes to the positive X direction and then to the positive Y direction. Paths BC4, BC5, and BC6 are formed with displacement cycles of circular-shape, rhombus-shape and flower-shape, respectively. The corresponding loading protocols are shown in Figure 5-6 (d), (e) and (f) respectively. It should be noted that except the loading protocol, all the modelling methods and parameters (including the axial load ratio) of the column under biaxial loadings are kept the same as those in the uniaxial loading case as presented in Section 5.3.

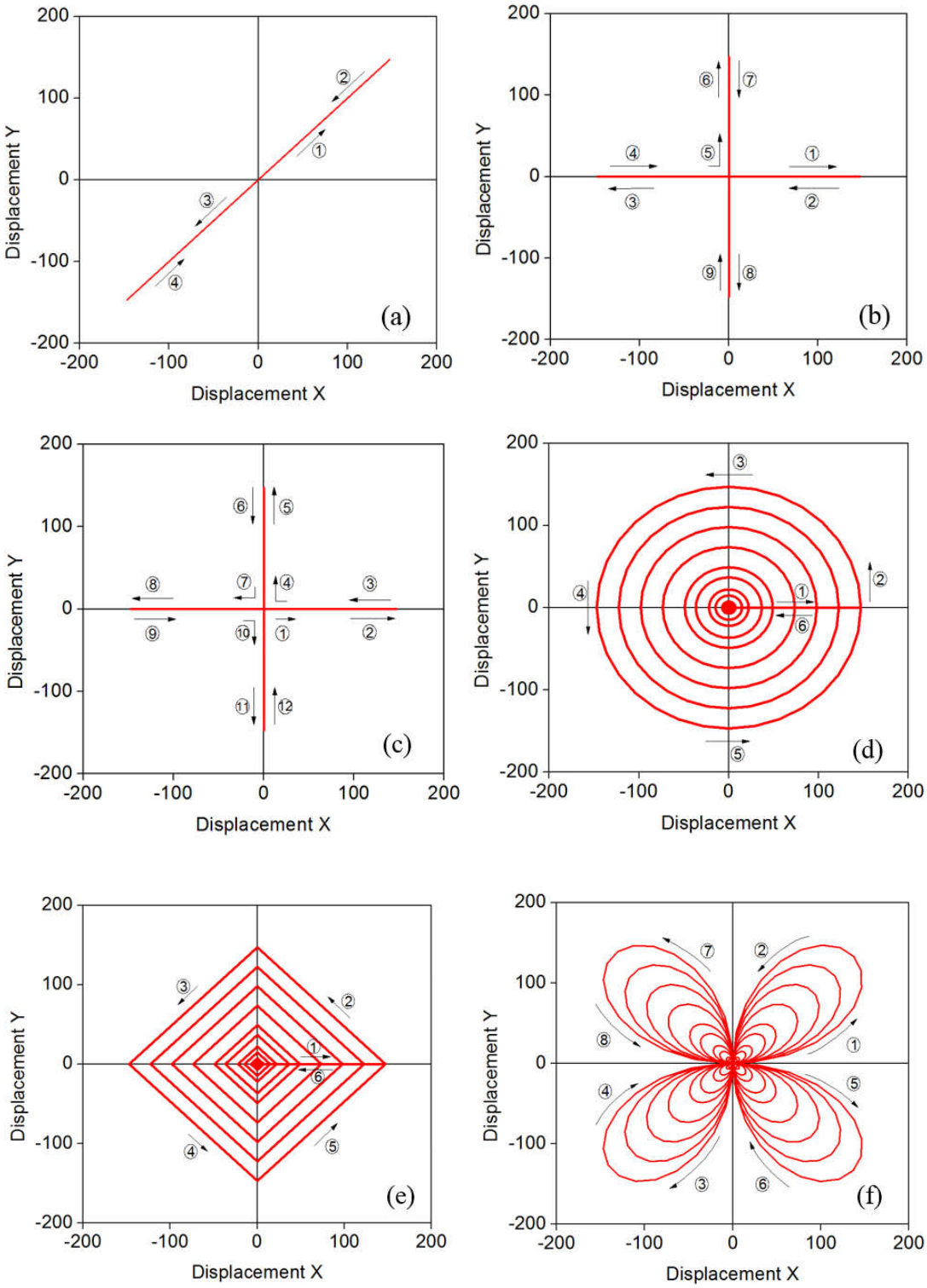

Figure 5-6 Loading protocols for biaxial cyclic load path: (a) BC1, (b) BC2, (c) BC3, (d) BC4, (e) BC5, (f) BC6

5.5 Biaxial modelling results

In this part, the biaxial modelling results are presented. The damage patterns, hysteretic curves, backbone curves, strength degradations, residual displacements, relationships between bidirectional lateral forces and energy dissipation capacities from the results of different loading protocols are analysed and discussed in detail.

5.5.1 Damages and hysteretic curves

Figure 5-7 shows the accumulated damage distribution at the bottom segment of the column under different loading cases at the end of the numerical simulations. In the figure, more severe damage is represented by the larger value of the damage variable 'DAMAGEC'. In particular, the deep red colour means the element is damaged. It can be seen that for the column under UC, since the loading is only applied in one direction, the damage is concentrated at the two bottom corners of the segment in the loading direction. The adjacent region between the two corners remains undamaged. For the column under BC1, the column deforms like a column under uniaxial loading which has a 45-degree angle against the UC loading. Since the displacements in both the X and Y directions are kept the same as UC, the resultant displacement of BC1 is 1.41 times of that of the UC. As shown in Figure 5-7, evident damages are also concentrated at two corners of the segments, but it is 45-degree from the X axis, and the areas are larger as compared to UC due to the larger resultant displacement applied to the column. In the case of the column under loading paths BC2 and BC3, the damage distribution patterns are similar with each other. The most serious damages are developed at the four corners due to the fact that the loadings are now applied in both the X and Y directions, while relatively obvious damage also develops in the adjacent areas. For the column under BC4, BC5 and BC6, it can be observed that more evident damages are formed over the entire section of the segment as compared to the previous four cases. As shown, the damages are fully developed around the column within certain region instead of just at the two corners. The results indicate the coupling effect of the biaxial loadings leads to more damages in the segments. More strength degradations are therefore expected for a column under biaxial loadings.

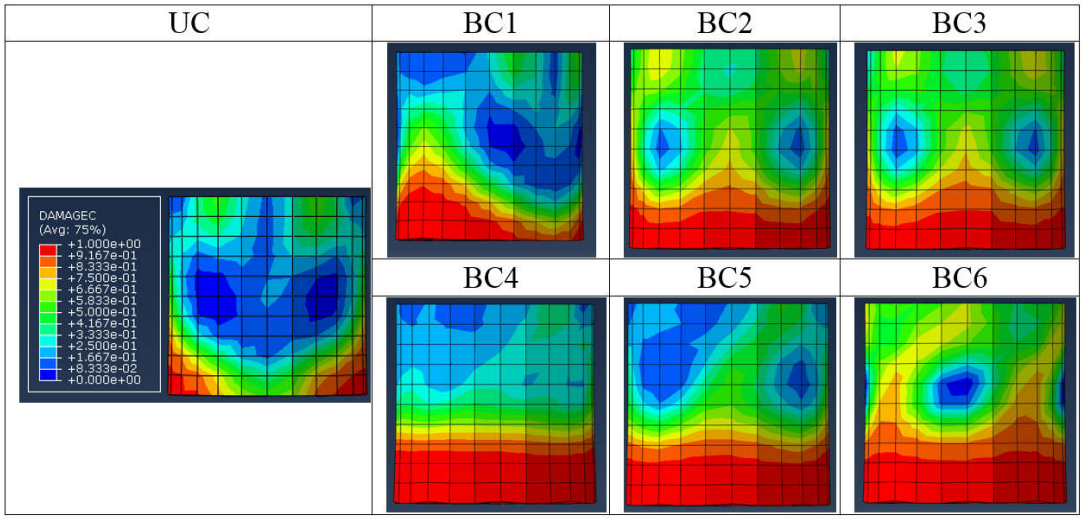

Figure 5-7 Damage distributions at the bottom segment of the column under different loading paths (at the end of the simulation)

Figure 5-8 shows the hysteretic curves in the X and Y directions of the simulated column under six different BC loading paths as described above. The hysteretic curve of the column under UC loading condition is also plotted in the figures for direct comparison. It should be noted that since the column is symmetric, the hysteretic curves in the X and Y directions are the same when the UC loading protocol is applied separately in the two directions. It also should be noted that for loading paths BC1 and BC6, the maximum displacement demand for each cycle is the resultant displacement in both the X and Y directions. To be consistent, the results are still plotted in the X and Y directions separately.

It can be observed that the shape of the hysteretic curves of the column under biaxial cyclic loading are different from that of the column under UC loading due to the coupling effect in the two loading directions. In addition, the hysteretic behaviour of the segmental column under each biaxial loading path differs from each other. For the column under loading path BC1 (Figure 5-6 (a)), the hysteretic curves in the X and Y directions are shown in Figure 5-8 (a-b). It can be observed that the hysteretic curves are almost the same in the X and Y directions since the column section is symmetric in the two directions and the loadings are also the same in both directions. Compared with the column under UC loading, the strengths of the column in both the X and Y directions are smaller than that of the column under uniaxial loading. As shown, the maximum lateral strength of the column under UC is 202.4 kN, while under BC1, the maximum strengths reduce to 137.8 kN and 137.6 kN in the X and Y directions,

respectively. This is because the loadings in the X and Y directions are applied to the column at the same time. When the displacement in the X direction reaches the maximum value, the displacement in the Y direction also reaches the maximum value. The column deforms like a column under uniaxial loading with a 45-degree angle against each axis. Therefore, the strength of the column in each direction is a component of the resultant strength of the column. Figure 5-8 (a-b) also show that the column experiences insignificant strength degradation and the residual displacements in the both directions are small, indicating that the coupling effect of BC1 is insignificant.

The hysteretic curves for the column under loading path BC2 (Figure 5-6(b)) are shown in Figure 5-8 (c-d). Compared with the column under UC, it can be observed that the difference between the hysteretic curves is minor. As shown in Figure 5-8 (c-d), the strength of the column at the maximum displacement under BC2 is only about 5% smaller than that of the column under UC. The reason is that at one particular time, only the loading in one direction is applied and this column deforms in the X and Y directions separately. In other words, the coupling effect between the loadings in the two directions is minor and has insignificant influence on the performance of the column. The hysteretic curves of the column under loading path BC3 are shown in Figure 5-8 (e-f). The same trends are observed compared to loading path BC2. This is because loading path BC3 is similar to BC2 and the only difference is the loading sequence as discussed above. These results indicate that when the loadings applied in the two directions are not coupled with each other, the effects of biaxial loading and the effects of the loading path on the performance of the segmental column are insignificant.

Figure 5-8 (g-h) show the hysteretic curves of the column under BC4, which has a circular shape. It can be observed that the strong coupling between the two orthogonal directions has significant influences on the performance of the column in both the X and Y directions. The strength of the column drops significantly compared with that of the column under UC loading. For example, as shown in Figure 5-8 (h), the final strength in the Y direction of the column at the largest displacement is about 143.3 kN, which is 29.2% smaller than that of the column under UC. In addition, the residual displacement of the column increases evidently. As shown in Figure 5-8 (g-h), the

largest residual displacements in the X and Y directions reach 32.9 mm and 33.4 mm respectively. When the column is under UC, the residual displacement is only 6.3 mm. Similar trends are observed for loading paths BC5 and BC6. As shown in Figure 5-8 (i-l), for the column under BC5, the residual displacements are 23.6 mm and 22.6 mm in the X and Y directions, respectively. The corresponding values for the column under BC6 are 21.5 mm and 20.9 mm. The results reveal that different loading paths result in different hysteretic behaviours, indicating the loading path has significant influence on the biaxial performance of the precast segmental column.

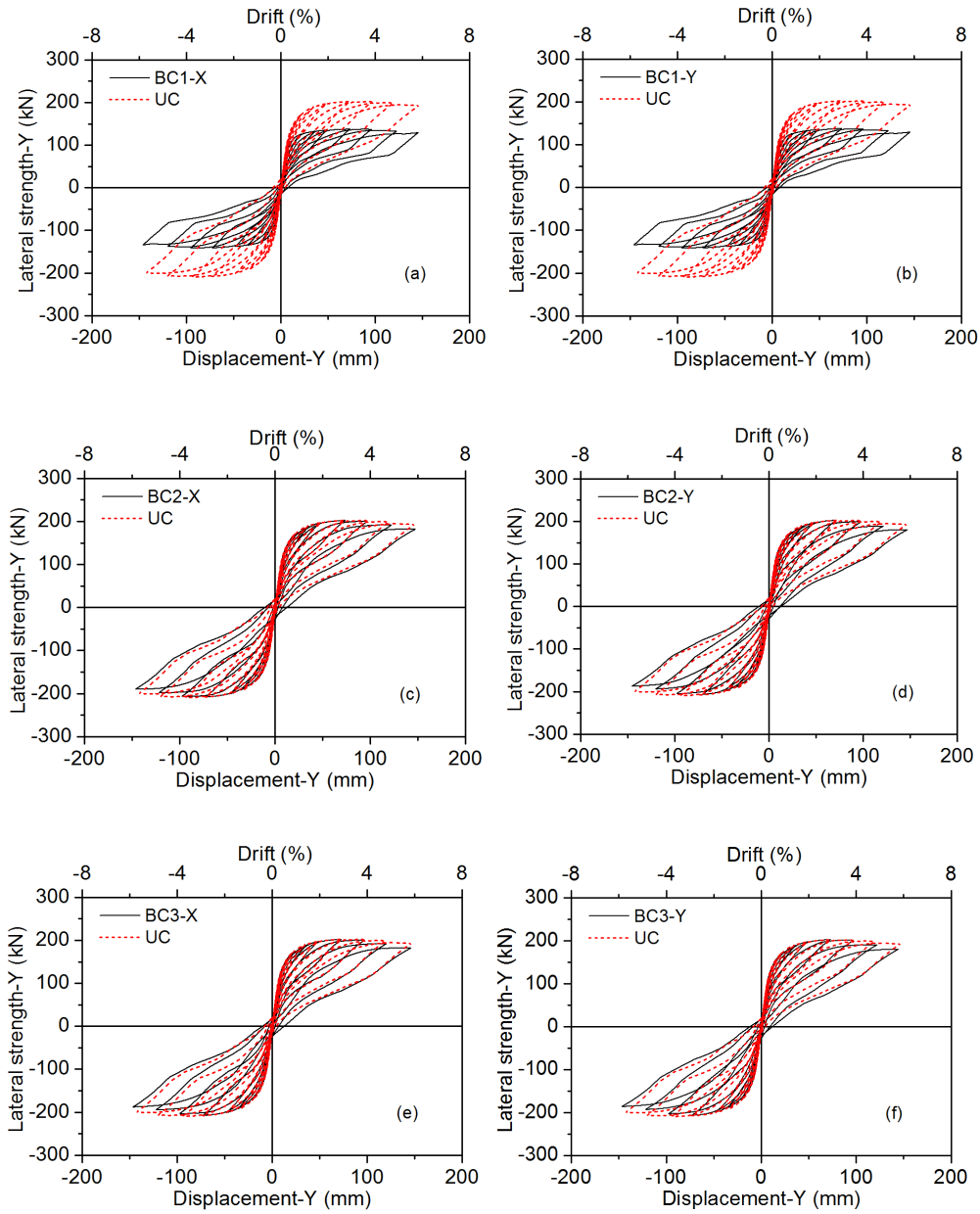

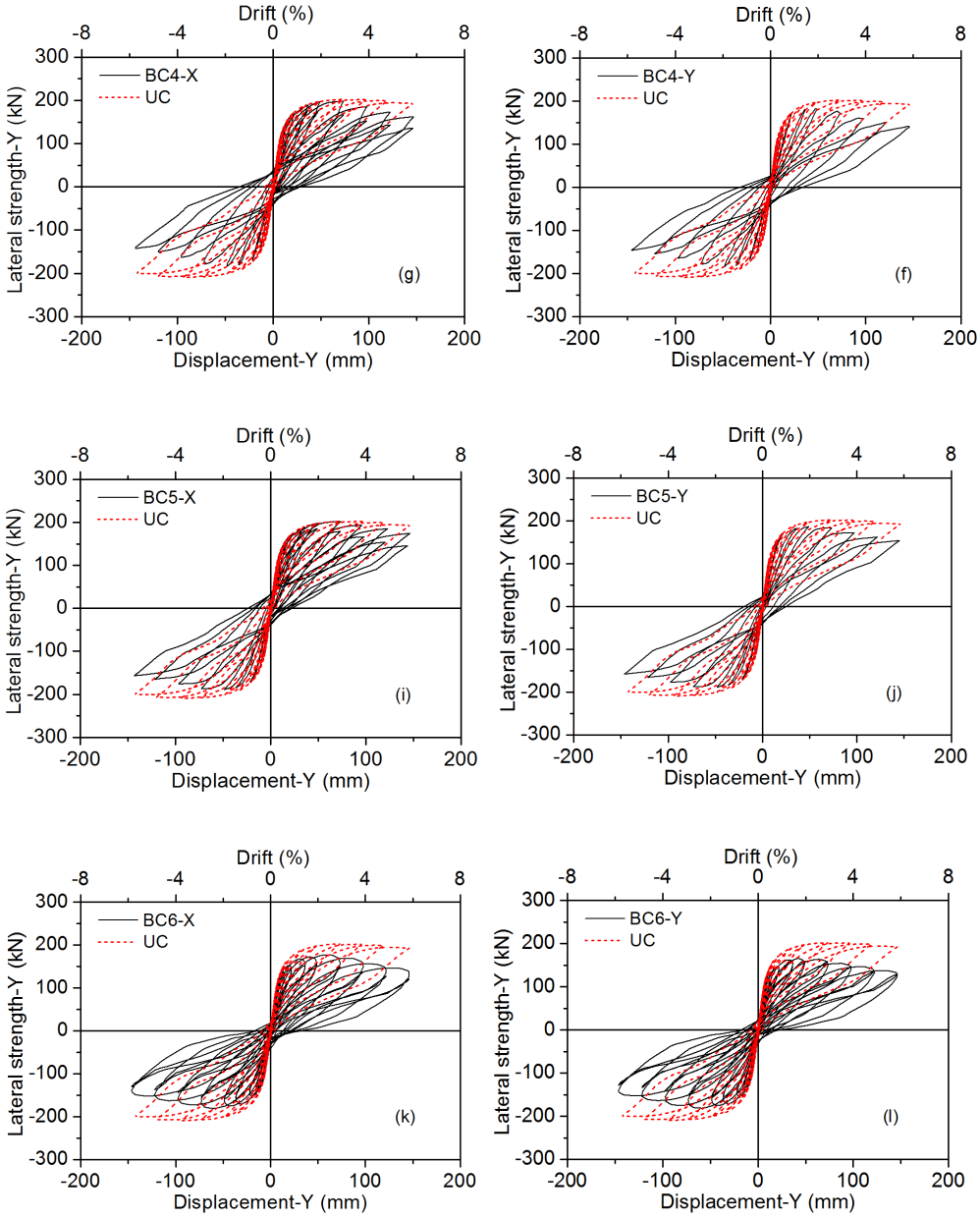

Figure 5-8 Hysteretic curves of segmental column under different biaxial loading paths

5.5.2 Backbone curve

The backbone curves of the hysteretic curves are summarized and plotted in Figure 5-9, in which Figure 5-9 (a) and (b) show the results in the X and Y directions, respectively. For comparison, the backbone for the UC case is also shown in the figure. The solid line in the figure is the result of the column under UC loading and the dashed curves are the corresponding results for the BC cases. According to the backbone curves, it can be observed that the initial stiffness is not significantly affected by the BC loading paths. The initial stiffness for all the cases are similar as shown in the

figure. The figure also shows that when the column is under loading paths UC and BC1, very small strength degradations are observed. Loading paths BC2 and BC3 lead to slightly larger strength degradations as compared to UC and BC1. Loading paths BC4, BC5 and BC6 result in quite obvious strength degradations. Table 5-2 summarizes the strength degradation ratios of the column under different loading paths quantitatively. In which, the strength degradation ratio is calculated as the strength decrease of the column at the end of the simulation compared with the maximum strength of the column during the simulation (Figure 5-10). It can be observed that the maximum average strength degradation reaches 21.6% for the column under the loading path BC4, while for the column under loading path UC, the average strength degradation is only 4.7%. These results can be explained by the damage distributions as shown in Figure 5-7. As shown, under the loading paths UC and BC1, the loading can be regarded as being applied in one direction, only minor damage occurs at the two corners of the segment, which in turn leads to the unobvious strength degradation. However, it should be noted that in the present study each segment is confined by a steel jacket as presented in Section 5.3. If the steel jackets are removed, more damage and more evident strength degradation would be expected. Under loading paths BC2 and BC3, slightly more serious damages occur as shown in Figure 5-7, which lead to the slightly more evident strength degradations. For loading paths BC4, BC5 and BC6, obvious damages appear at the bottom of the segment as shown in Figure 5-7, and they therefore result in the most evident strength degradations.

The above results indicate that using the uniaxial behaviour of the segmental column in the analysis of the whole structure under biaxial lateral seismic excitation may overestimate the performance of the structure in terms of the strength and ductility. The biaxial performance of the segmental column should be carefully considered in the structural response analysis to avoid overestimating the performance of the structural system.

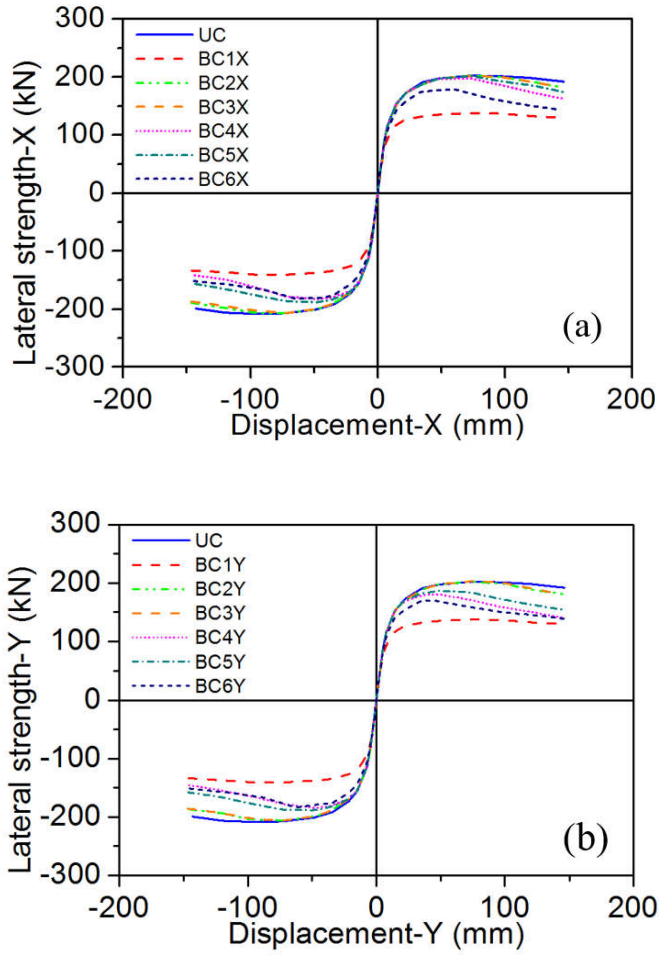

Figure 5-9 Backbone curves of the columns (a) X direction, (b) Y direction

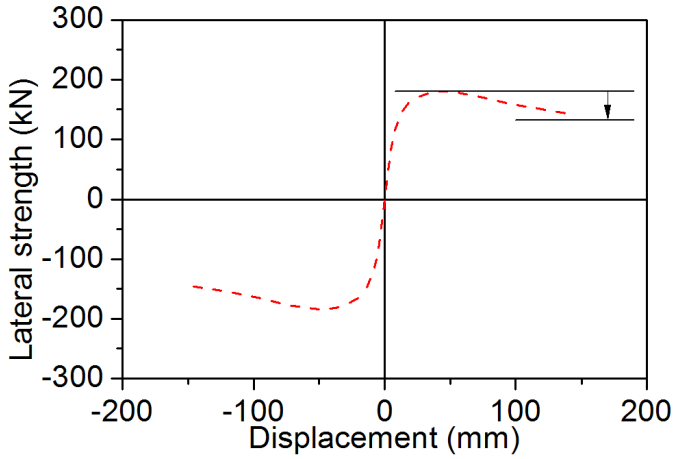

Figure 5-10 Schematic of the strength degradation

Table 5-2 Strength degradation in comparison with the maximum strength (%)

Direction	UC	BC1		BC2		BC3		BC4		BC5		BC6	
		X	Y	X	Y	X	Y	X	Y	X	Y	X	Y
Positive	5.0	6.1	6.0	10.0	10.9	10.0	11.2	18.0	22.2	13.6	17.3	20.1	18.4
Negative	4.4	5.1	4.8	8.8	9.2	9.5	9.9	22.2	20.9	16.9	16.1	16.8	17.6
Average	4.7	5.6	5.4	9.4	10.1	9.8	10.6	20.1	21.6	15.3	16.7	18.5	18.0

5.5.3 Residual displacement

The residual displacement is another important parameter to evaluate the seismic performance of the column. Large residual displacement after an earthquake event will make it difficult or even impossible to retrofit the structure. In this part, the residual displacements of the column under uniaxial and biaxial loadings are summarized and compared. Figure 5-11 shows the residual displacement of the column under different loading paths. As shown, different loading paths result in different residual displacements in the column. For example, under the UC loading path, the residual displacement is 6.3 mm, while under the loading path BC4, the maximum residual displacements reaches 32.9 and 33.4 mm in the X and Y directions, respectively, equalling to around 1.6% drift ratio. They are more than 5 times of that when the column is under the UC loading path. Further analyses indicate that the residual displacement shows the same trend with the strength degradation percentage as summarized in Table 5-2. This is actually understandable since the strength degradation reflects the damage extent of the column. More serious damage (thus larger strength degradation) makes the column more difficlut go back to its original position, and therefore leads to the larger residual displacement.

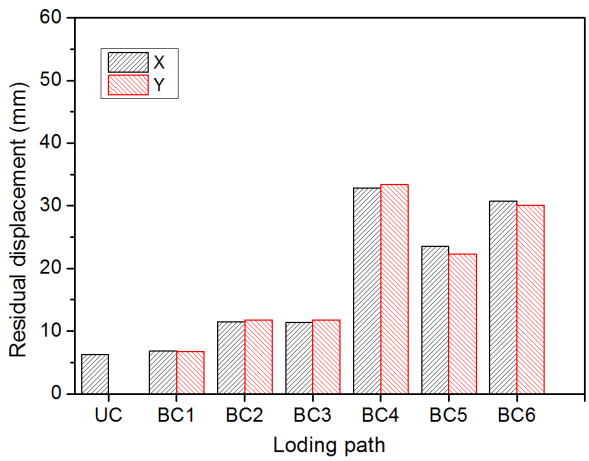

Figure 5-11 Maximum residual displacements of the column under different loading paths

5.5.4 Relationships between bidirectional lateral forces

To investigate the coupling effect of the loadings in the two directions, the relationship between the biaxial lateral forces of the column under BC1 to BC6 are shown in Figure 5-12. The red dash circle represents the maximum lateral strength of the column under uniaxial loading path UC. As shown in Figure 5-12 (a), for the first loading path BC1, the force path shows almost the same shape as that of the loading path (Figure 5-6 (a)). This is because the loading path and cross section of the column are both symmetric, it deforms like a column under uniaxial loading path. The shapes of the force path of the column under BC2 and BC3 differ slightly from the shapes of the applied loading paths (Figure 5-6 (b-c)) due to the nonlinear behaviour of the column. For the column under loading paths BC4, BC5 and BC6, the shapes of the force path show similar shapes to the applied loading displacement shapes at the initial several loading cycles since the response of the column is essentially elastic at small drift ratios. After that, the shapes of the lateral force relationship grow and differ from the applied loading displacement shape due to plastic deformation of the column and strong coupling effect in the X and Y directions. With the blue dash lines and red dash lines representing the symmetric axes of the imposed displacement path and the lateral force relationship respectively, it can be seen from Figure 5-12 (d-e) that the lateral force trajectories for the column under BC4 and BC5 rotate anti-clockwise slightly, which results in a phase shift compared with the applied displacement trajectories. The phase shift is caused by the damage of the column and it results in a large residual displacement. This result is consistent with that observed in the thin walled steel

column (Ucak & Tsopelas, 2014) and monolithic reinforced concrete columns (Bousias et al., 1995).

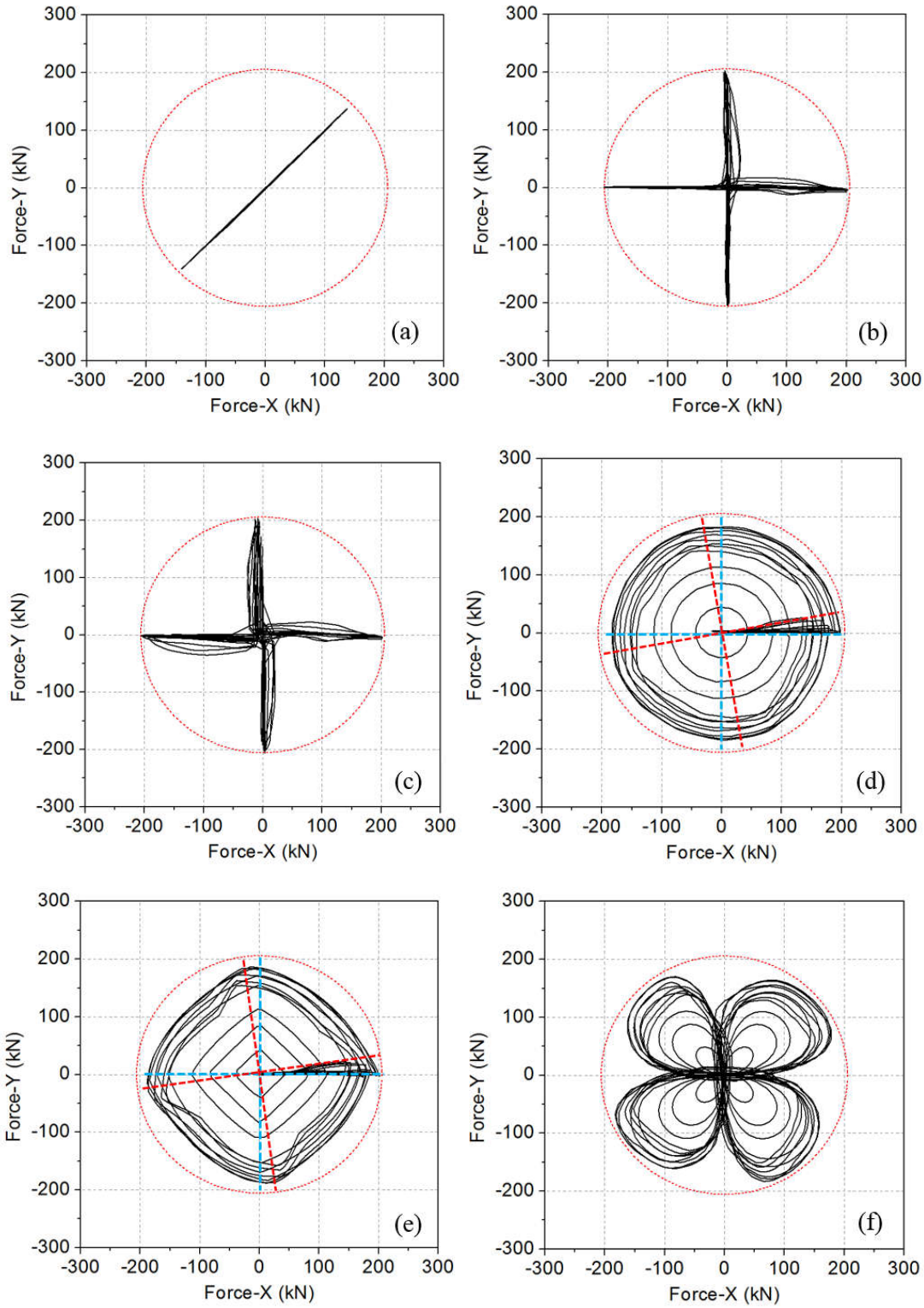

Figure 5-12 Relationships between the forces in the X and Y directions (red dash circle: maximum lateral strength of the column under UC; solid line: biaxial loading relationships in the X and Y directions)

5.5.5 Energy dissipation

The energy dissipation capacities of the column under different loading paths are investigated in this section. It is obvious the energy dissipation capacity of the column under cyclic loading can be calculated by integrating the area of the hysteretic curve. For the biaxial loading cases, the total energy dissipated by the column is therefore calculated by summing up the integrated areas of the hysteretic curves in the X and Y directions respectively as commonly did by other researchers (Qiu et al., 2002; Rodrigues et al., 2015; Rodrigues et al., 2017). Figure 5-13 shows the comparisons of the dissipated energies of the column under uniaxial and biaxial lateral loading paths. For the column under loading paths BC1 and BC6, the value shown in the figure corresponds to the maximum resultant drift of the column at each cycle. It can be observed that the energy dissipation of the column under UC reaches 47.3 kJ at the end of the simulation. For the column under biaxial loadings, different loading paths result in different energy dissipations of the column. The column under BC1 dissipates about 76.9 kJ energy at the end of the simulation, which is 62.6% higher than that of the column under UC. For the same drift ratio, the column under loading paths BC2 and BC3 dissipates similar amount of energy due to the similar shapes and lengths of the loading paths. Among all the loading paths, the column under loading path BC6 dissipates the largest amount of energy, reaching 185.8 kJ at the end of the simulation, which is about 4 times of that when the column is under UC. The reason is that for the same amplitude, BC6 has a longer loading path length, leading to a larger amount of energy dissipation. In summary, the amount of energy dissipation of the precast segmental column varies with the change of loading path. The column under BC loading paths dissipates more energy than the column under UC loading path because of the coupling effects of the loading in the X and Y directions and also the larger length of the loading path. Different BC loading paths also result in different energy dissipations. It may underestimate the performance of the column in terms of energy dissipation when using the uniaxial behaviour of the column in the seismic analysis of a structure with segmental columns.

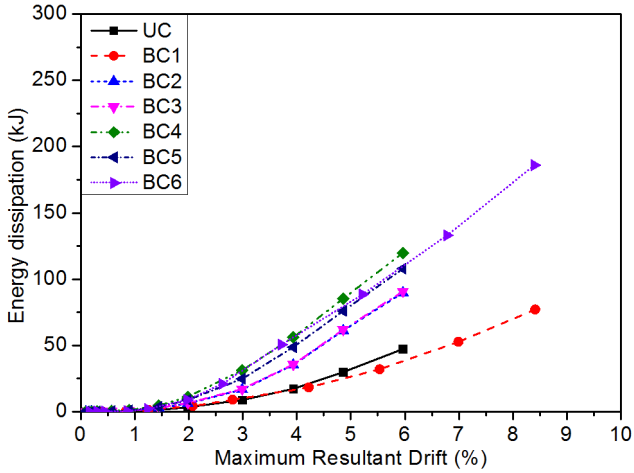

Figure 5-13 Cumulative energy dissipation of the column under different loading paths

In order to investigate the influence of the loading path length on the energy dissipation capacity of the column, the energies dissipated by the column at different drift ratios are normalized by the length of the loading path at each maximum resultant drift ratio. Figure 5-14 shows the results. As shown, in general the normalized energy dissipation capacities of the column differ from each other for different loading cases. For columns under loading cases BC1, BC2 and BC3, the normalized energy dissipation capacities are close to that of the column under UC. This is reasonable because for these loading paths, the loadings in the X and Y directions induce insignificant coupling effect to the column as shown in Figure 5-7 and discussed in section 5.5.1. For the column under loading paths BC4, BC5 and BC6, the energy dissipation capacities of the column start to increase faster than that of the column under other loading paths after about 1.5% drift ratio. This is also consistent with the previous observations in section 5.5.1, i.e., the loading paths BC4, BC5 and BC6 cause more damage to the column due to the strong coupling effect of the loadings in the X and Y directions. Interestingly, the results also show that the normalized energy dissipation capacities of the column start to decrease when the drift ratio reaches 3% (for BC4) or 4% (for BC5 and BC6). This can be attributed to the strength degradation as observed in the hysteretic curves (Figure 5-8).

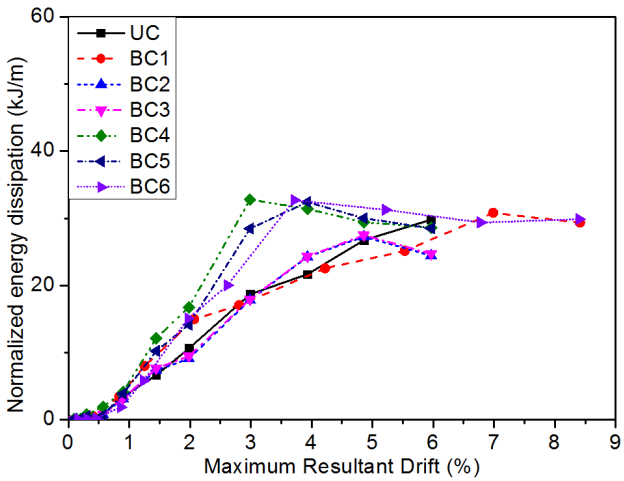

Figure 5-14 Normalized energy dissipation of the column under different loading paths at different drift ratios

5.6 Discussion

5.6.1 Minimize the residual displacement

As observed in the numerical simulations, the biaxial loading increases the residual displacement of segmental column. Large residual displacement often makes the retrofitting difficult after an earthquake event. Some previous studies have used shape memory alloy (SMA) to minimize the residual displacement of bridge columns (Leitner & Hao, 2016; Nikbakht et al., 2015; Saiidi et al., 2009; Shrestha & Hao, 2015) because it can undergo large strain and recover to its original shape after removing the stress (Wilson & Wesolowsky, 2005). In this section, the mild steel ED bars are replaced by SMA bars in order to mitigate the residual displacement of the column under biaxial loading. Numerical simulations are carried out to investigate the effectiveness of the proposed method.

The numerical model is exactly the same as that presented in section 5.3, the only difference is the mild ED bars are replaced by the SMA bars. The SMA bars are also modelled with the truss elements. The material model for the SMA is the Auricchio-Taylor model (Auricchio et al., 1997). Figure 5-15 shows the stress-strain relationship of SMA (Li et al., 2017), and the corresponding material parameters are listed in Table 5-3. As shown in Figure 5-11, loading path BC4 results in the largest residual displacement, therefore this case is selected as an example to demonstrate the effectiveness of using SMA bars.

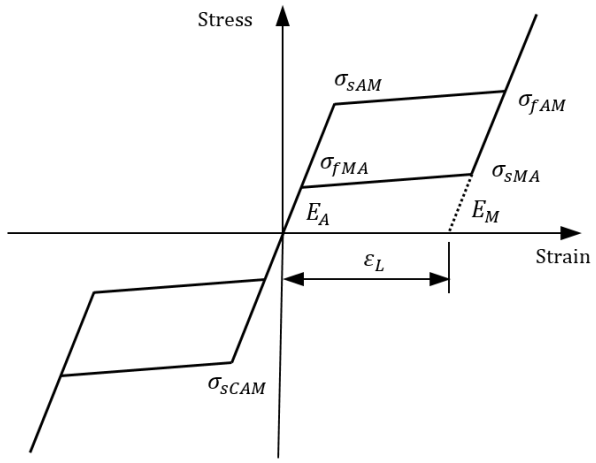

Figure 5-15 Constitutive model for SMA

Table 5-3 Material properties of SMA

Symbol	Value	Parameter
E_A	68200 MPa	Modulus of elasticity for austenite
E_M	68200 MPa	Modulus of elasticity for martensite
ε_L	0.062	Volumetric transformation strain
σ_{sAM}	480 Mpa	Start stress of austenite to martensite phase transformation
σ_{fAM}	540 Mpa	Finish stress of austenite to martensite phase transformation
σ_{sMA}	260 Mpa	Start stress of martensite to austenite phase transformation
σ_{fMA}	120 Mpa	Finish stress of martensite to austenite phase transformation
σ_{sCAM}	480 MPa	Start stress of phase transformation during compression

Figure 5-16 shows the comparison of the hysteretic curves of the column with mild steel bars and SMA bars. It can be seen that the residual displacement of the column can be reduced significantly by using SMA bars. When the conventional ED bars are used, the maximum residual displacement reaches about 33.4 mm as discussed above. When SMA bars are used, the value reduces to 12.7 mm, with a reduction ratio of 61.9%. Figure 5-16 also shows that when SMA bars are used, the area of the hysteretic

loops in the X and Y directions become slightly smaller compared to the case with conventional steel ED bars due to the innate mechanical properties of the SMA. Figure 5-17 compares the cumulative energy dissipation of the column with mild steel bars and SMA bars. It can be seen that the total energy dissipated by the column with SMA is reduced by 30.8% compared with that of the column with mild steel ED bars. The numerical results clearly demonstrate the effectiveness of using SMA bars to reduce the residual displacement of the column. However, a balance might need to be made since this design will decrease the energy dissipation of the column.

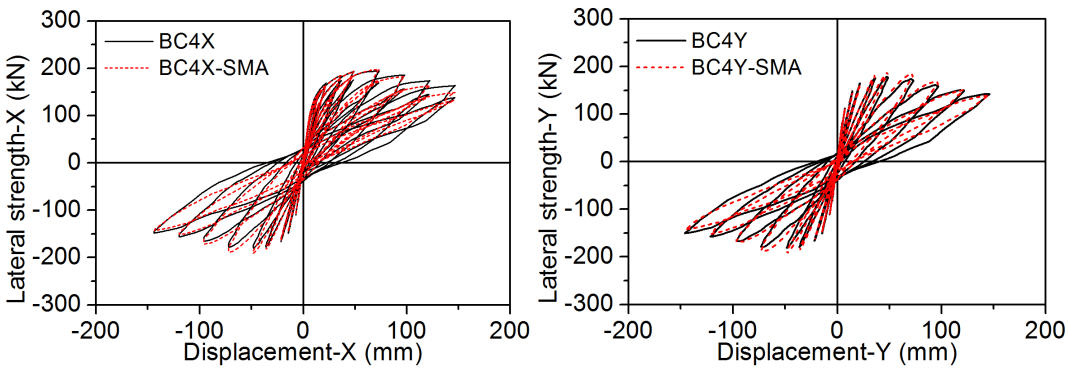

Figure 5-16 Hysteretic curves of segmental column with mild steel and SMA bars under biaxial loading path BC4.

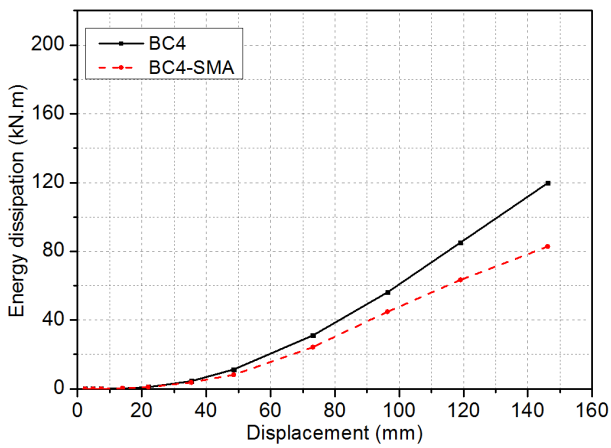

Figure 5-17 Comparison of the cumulative energy dissipation of the column with mild steel and SMA bars

5.6.2 Effect of axial loading ratio

Some previous studies (e.g.(Li et al., 2017)) showed that under uniaxial lateral loading, increasing the axial loading ratio could increase the strength of the precast segmental column but it could also cause more damage in the segments and reduce the ductility

of the column. Under biaxial lateral loading, the effect of axial loading ratio on the performance of the precast segmental column, however, has not been investigated yet. Different axial loading ratios are applied to the column under uniaxial loading path UC and biaxial loading path BC4 in this section to investigate the effect of axial loading on the seismic performance of segmental column. Without loss of generality, seven axial loadings, i.e. 10%, 15%, 20%, 25%, 30%, 35%, and 40% of the axial loading capacity of the column, are considered in the present study. The backbone curves and strength degradations are compared and analysed.

Figure 5-18 shows the backbone curves of the column under uniaxial lateral loading with different levels of axial loading ratios. It can be observed that the increase in the axial loading leads to the increases in the column lateral load resistance capacity. However, the column with higher axial loading ratio shows more strength degradation, indicating that the increase of the axial loading ratio results in the decrease in the ductility of the column. As shown in Figure 5-18, the strength degradation of the column under the uniaxial loading path UC with 40% axial loading ratio is about 16.5%, while it is only 0.7% when the axial loading ratio is 15%.

Figure 5-19 shows the backbone curves of the column under biaxial lateral loading path BC4 with different levels of axial loading ratios. Similar to the observations on the column under uniaxial loading, increasing the axial loading ratio increases the strength of the column but decreases the ductility of the column under biaxial lateral loadings. By comparing the backbone curves of the column under biaxial loading (Figure 5-19) with that under uniaxial loading (Figure 5-18), it can be found that the axial loading ratio has more significant effect on the column under biaxial loading in terms of the strength degradation. Table 5-4 summarizes the maximum strengths, final strengths and strength degradations of the column under uniaxial and biaxial loading paths. When the axial loading ratio is 40%, the strength degradations of the column under biaxial loading path BC4 reach 30.1% and 33.1% in the X and Y directions, respectively, which are much higher than that of the column under uniaxial loading (16.5%). These results indicate that the axial loading ratio has more pronounced effect on the precast segmental column under biaxial loadings compared with the column under uniaxial loading. The reason is that the biaxial loading results in more plastic deformation in the column, while the high axial loading aggravates the accumulated

damage. Therefore, axial loading ratio should be carefully considered during the seismic analysis of the columns under bidirectional excitations.

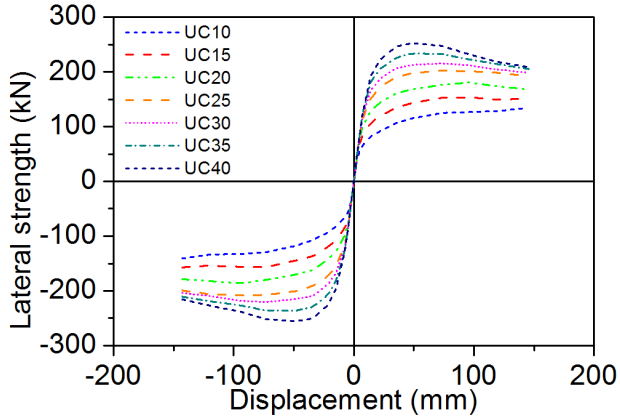

Figure 5-18 Backbone curves of the column under uniaxial loading with various levels of axial loading ratios

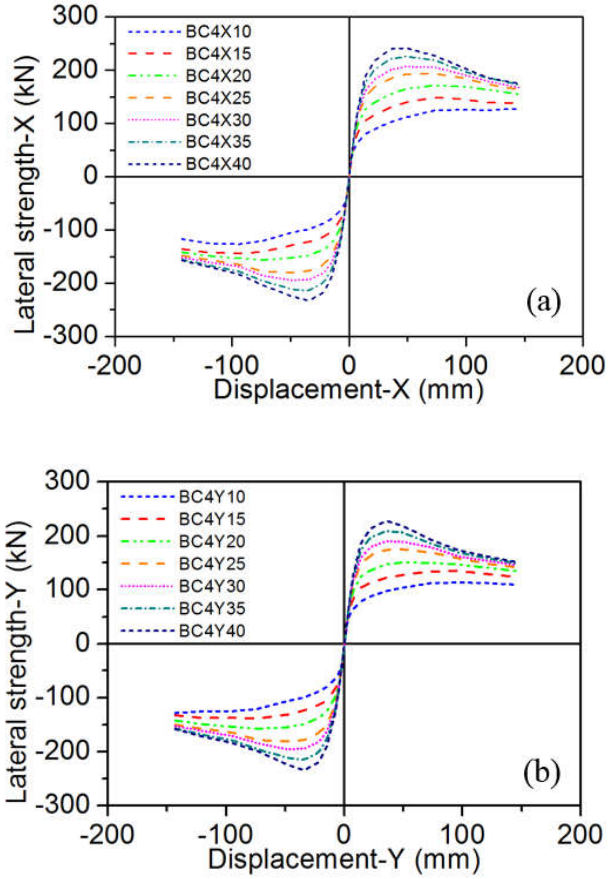

Figure 5-19 Backbone curves of the column under biaxial loading with various levels of axial loading ratios: (a) X direction (b) Y direction

Table 5-4 Summary of the strengths and strength degradations of the columns under different loading cases

Loading path	Strength	Axial loading ratio (%)						
		10	15	20	25	30	35	40
UC	Max. (kN)	137.63	155.48	183.53	205.31	218.06	234.73	253.91
	Final (kN)	137.63	154.42	173.23	195.72	200.68	207.99	211.92
	Degradation	0.0%	0.7%	5.6%	4.7%	8.0%	11.4%	**16.5%**
BC4-X	Max. (kN)	127.09	146.33	163.90	186.63	200.42	219.87	237.27
	Final (kN)	122.39	137.32	148.35	155.76	159.44	163.97	165.94
	Degradation	3.7%	6.2%	9.5%	16.5%	20.4%	25.4%	**30.1%**
BC4-Y	Max. (kN)	121.14	136.53	154.14	177.93	192.44	212.36	231.25
	Final (kN)	118.92	127.96	138.65	145.74	149.39	153.35	154.75
	Degradation	1.8%	6.3%	10.1%	18.1%	22.4%	27.8%	**33.1%**

5.7 Summary and conclusions

The performance of the precast concrete-filled circular tube segmental column under biaxial cyclic loading and the load path effect on the biaxial performance of the column are comprehensively investigated in this study through numerical simulations. Six biaxial lateral cyclic loading paths are considered and applied to the validated numerical model. Based on the numerical results, the following conclusions are made:

1. Different biaxial loading paths result in different damage patterns and hysteretic behaviours, indicating the loading paths have significant influence on the biaxial performance of segmental columns.

2. The initial stiffness of the columns is not significantly affected by the loading paths. However, the coupling effect of the biaxial loading results in strength degradation and larger residual displacement of the column as compared to the uniaxial loading case.

The largest strength degradation and residual displacement are observed on the column under loading path BC4, in which the strength degradation reaches about 22% of its maximum strength and the residual displacement is more than 5 times larger than that of the column under uniaxial loading path UC.

3. The force relationships in the X and Y directions show obvious nonlinear behaviours compared with the applied loading path. Phase lag between the loading path and the force relationship is observed in the column under BC4 and BC5.

4. The energy dissipation of the column varies with the change of loading paths. The column under loading path BC6 dissipates more energy than the columns under other loading paths due to longer length of the loading path.

5. For the column under BC4, BC5 and BC6, the normalized energy dissipation capacities of the column are larger than that of the column under UC and other BC loading cases due to the strong coupling effects of the biaxial loadings which cause more damage to the column. However, when the drift of the column reaches a certain level, the energy dissipation capacities normalized by the drift of the column begin to decrease due to the strength degradation of the column.

6. The residual displacement of the column can be reduced significantly by using SMA instead of mild steel bars.

7. The increase of the axial loading ratio increases the strength of the column but decreases the ductility of the column under both uniaxial and biaxial lateral loadings. For the column under biaxial loading, this effect is more pronounced.

Though this study revealed some important information about the biaxial performance of precast segmental columns, it is a preliminary step to fully understand the performance of precast segmental column under biaxial loading. Experimental studies are needed to further investigate the biaxial behaviours of precast segmental columns.

5.8 References

Auricchio, F., Taylor, R. L., & Lubliner, J. (1997). Shape-memory alloys: macromodelling and numerical simulations of the superelastic behavior. *Computer Methods In Applied Mechanics And Engineering, 146*(3), 281-312.

Billington, S. L., & Yoon, J. (2004). Cyclic response of unbonded posttensioned precast columns with ductile fiber-reinforced concrete. *Journal of Bridge Engineering, 9*(4), 353-363.

Bousias, S. N., Verzeletti, G., Fardis, M. N., & Gutierrez, E. (1995). Load-path effects in column biaxial bending with axial force. *Journal of Engineering Mechanics, 121*(5), 596-605.

Bu, Z. Y., Ou, Y. C., Song, J. W., Zhang, N. S., & Lee, G. C. (2015). Cyclic Loading Test of Unbonded and Bonded Posttensioned Precast Segmental Bridge Columns with Circular Section. *Journal of Bridge Engineering*, 04015043.

Cai, Z.-K., Wang, Z., & Yang, T. Y. (2018). Experimental testing and modeling of precast segmental bridge columns with hybrid normal- and high-strength steel rebars. *Construction and Building Materials, 166*, 945-955. doi:https://doi.org/10.1016/j.conbuildmat.2018.01.159

Cai, Z.-K., Zhou, Z., & Wang, Z. (2018). Influencing factors of residual drifts of precast segmental bridge columns with energy dissipation bars. *Advances in Structural Engineering*, 1369433218780545.

Chang, S.-Y. (2009). Experimental studies of reinforced concrete bridge columns under axial load plus biaxial bending. *Journal of Structural Engineering, 136*(1), 12-25.

Chou, C. C., Chang, H. J., & Hewes, J. T. (2013). Two-plastic-hinge and two dimensional finite element models for post-tensioned precast concrete segmental bridge columns. *Engineering Structures, 46*, 205-217.

Chou, C. C., & Chen, Y. C. (2006). Cyclic tests of post-tensioned precast CFT segmental bridge columns with unbonded strands. *Earthquake Engineering & Structural Dynamics, 35*(2), 159-175.

Dawood, H., ElGawady, M., & Hewes, J. (2011). Behavior of segmental precast posttensioned bridge piers under lateral loads. *Journal of Bridge Engineering, 17*(5), 735-746.

ElGawady, M., Booker, A. J., & Dawood, H. (2010). Seismic behavior of posttensioned concrete-filled fiber tubes. *Journal of Composites for Construction, 14*(5), 616-628.

ElGawady, M., & Sha'lan, A. (2010). Seismic behavior of self-centering precast segmental bridge bents. *Journal of Bridge Engineering, 16*(3), 328-339.

Goto, Y., Jiang, K., & Obata, M. (2006). Stability and Ductility of Thin-Walled Circular Steel Columns under Cyclic Bidirectional Loading. *Journal of Structural*

Engineering, 132(10), 1621-1631. doi:doi:10.1061/(ASCE)0733-9445(2006)132:10(1621)

Goto, Y., Muraki, M., & Obata, M. (2009). Ultimate state of thin-walled circular steel columns under bidirectional seismic accelerations. *Journal of Structural Engineering, 135*(12), 1481-1490.

Han, L.-H., Yao, G.-H., & Tao, Z. (2007). Performance of concrete-filled thin-walled steel tubes under pure torsion. *Thin-Walled Structures, 45*(1), 24-36.

Hewes, J. T., & Priestley, M. N. (2002). *Seismic design and performance of precast concrete segmental bridge columns* (No. SSRP-2001/25). Retrieved from University of California, San Diego, CA:

Khaled, A., Massicotte, B., & Tremblay, R. (2010). Cyclic testing of large-scale rectangular bridge columns under bidirectional earthquake components. *Journal of Bridge Engineering, 16*(3), 351-363.

Leitner, E. J., & Hao, H. (2016). Three-dimensional finite element modelling of rocking bridge piers under cyclic loading and exploration of options for increased energy dissipation. *Engineering Structures, 118*, 74-88. doi:10.1016/j.engstruct.2016.03.042

Li, C., Hao, H., & Bi, K. (2017). Numerical study on the seismic performance of precast segmental concrete columns under cyclic loading. *Engineering Structures, 148*, 373-386. doi:https://doi.org/10.1016/j.engstruct.2017.06.062

Li, C., Hao, H., Zhang, X., & Bi, K. (2017). Experimental study of precast segmental columns with unbonded tendons under cyclic loading. *Advances in Structural Engineering*, 1369433217717119.

Nikbakht, E., Rashid, K., Hejazi, F., & Osman, S. A. (2014). A numerical study on seismic response of self-centring precast segmental columns at different post-tensioning forces. *Latin American Journal of solids and structures, 11*(5), 864-883.

Nikbakht, E., Rashid, K., Hejazi, F., & Osman, S. A. (2015). Application of shape memory alloy bars in self-centring precast segmental columns as seismic resistance. *Structure and Infrastructure Engineering, 11*(3), 297-309.

Ou, Y. C., Tsai, M. S., Chang, K. C., & Lee, G. C. (2010). Cyclic behavior of precast segmental concrete bridge columns with high performance or conventional steel reinforcing bars as energy dissipation bars. *Earthquake Engineering & Structural Dynamics, 39*(11), 1181-1198.

Ou, Y. C., Wang, P. H., Tsai, M. S., Chang, K. C., & Lee, G. C. (2009). Large-scale experimental study of precast segmental unbonded posttensioned concrete bridge columns for seismic regions. *Journal of Structural Engineering, 136*(3), 255-264.

Qiu, F., Li, W., Pan, P., & Qian, J. (2002). Experimental tests on reinforced concrete columns under biaxial quasi-static loading. *Engineering Structures, 24*(4), 419-428.

Rodrigues, H., Arêde, A., Furtado, A., & Rocha, P. (2015). Seismic behavior of strengthened RC columns under biaxial loading: An experimental characterization. *Construction and Building Materials, 95*, 393-405. doi:http://dx.doi.org/10.1016/j.conbuildmat.2015.07.149

Rodrigues, H., Arêde, A., Varum, H., & Costa, A. (2013a). Damage evolution in reinforced concrete columns subjected to biaxial loading. *Bulletin of Earthquake Engineering, 11*(5), 1517-1540.

Rodrigues, H., Arêde, A., Varum, H., & Costa, A. G. (2013b). Experimental evaluation of rectangular reinforced concrete column behaviour under biaxial cyclic loading. *Earthquake Engineering & Structural Dynamics, 42*(2), 239-259. doi:10.1002/eqe.2205

Rodrigues, H., Furtado, A., & Arêde, A. (2015). Behavior of rectangular reinforced-concrete columns under biaxial cyclic loading and variable axial loads. *Journal of Structural Engineering, 142*(1), 04015085.

Rodrigues, H., Furtado, A., & Arêde, A. (2017). Experimental evaluation of energy dissipation and viscous damping of repaired and strengthened RC columns with CFRP jacketing under biaxial load. *Engineering Structures, 145*, 162-175. doi:https://doi.org/10.1016/j.engstruct.2017.05.021

Rodrigues, H., Furtado, A., Arêde, A., Vila-Pouca, N., & Varum, H. (2018). Experimental study of repaired RC columns subjected to uniaxial and biaxial horizontal loading and variable axial load with longitudinal reinforcement welded steel bars solutions. *Engineering Structures, 155*, 371-386. doi:https://doi.org/10.1016/j.engstruct.2017.11.043

Rodrigues, H., Varum, H., Arêde, A., & Costa, A. (2012). A comparative analysis of energy dissipation and equivalent viscous damping of RC columns subjected to uniaxial and biaxial loading. *Engineering Structures, 35*, 149-164. doi:http://dx.doi.org/10.1016/j.engstruct.2011.11.014

Saiidi, M. S., O'Brien, M., & Sadrossadat-Zadeh, M. (2009). Cyclic response of concrete bridge columns using superelastic nitinol and bendable concrete. *ACI Structural Journal, 106*(1), 69.

Shim, C. S., Chung, C. H., & Kim, H. H. (2008). Experimental evaluation of seismic performance of precast segmental bridge piers with a circular solid section. *Engineering Structures, 30*(12), 3782-3792.

Shirmohammadi, F., & Esmaeily, A. (2015). Performance of reinforced concrete columns under bi-axial lateral force/displacement and axial load. *Engineering Structures, 99*, 63-77. doi:http://dx.doi.org/10.1016/j.engstruct.2015.04.042

Shrestha, B., & Hao, H. (2015). Parametric study of seismic performance of super-elastic shape memory alloy-reinforced bridge piers. *Structure and Infrastructure Engineering, 12*(9), 1076-1089. doi:10.1080/15732479.2015.1076856

Sideris, P., Aref, A. J., & Filiatrault, A. (2014). Quasi-static cyclic testing of a large-scale hybrid sliding-rocking segmental column with slip-dominant joints. *Journal of Bridge Engineering, 19*(10), 04014036.

Simulia, D. S. (2012). Abaqus 6.12 documentation. *Providence, Rhode Island, US.*

Sun, Z., Wang, D., Bi, K., & Si, B. (2016). Experimental and numerical investigations on the seismic behavior of bridge piers with vertical unbonded prestressing strands. *Bulletin of Earthquake Engineering, 14*(2), 501-527.

Ucak, A., & Tsopelas, P. (2014). Load Path Effects in Circular Steel Columns under Bidirectional Lateral Cyclic Loading. *Journal of Structural Engineering, 141*(5), 04014133.

Wilson, J. C., & Wesolowsky, M. J. (2005). Shape Memory Alloys for Seismic Response Modification: A State-of-the-Art Review. *Earthquake Spectra, 21*(2), 569-601. doi:10.1193/1.1897384

CHAPTER 6 SEISMIC PERFORMANCES OF PRECAST SEGMENTAL COLUMN UNDER BIDIRECTIONAL EARTHQUAKE MOTIONS: SHAKE TABLE TEST AND NUMERICAL EVALUATION

6.1 Abstract

Precast segmental concrete column, as one of the prefabricated structures used to accelerate the construction speed in the urban areas with heavy traffic, has been more and more widely used recently. Current applications of such structures are mainly limited to the low seismicity areas due to the lack of knowledge on its seismic performances. Recently, extensive research efforts have been made to understand the force-displacement relationship of such columns under quasi-static cyclic loading through experimental and numerical investigations. The behaviours of the column under real dynamic earthquake motions were, however, rarely investigated. Moreover, only the uniaxial motion was considered in the limited shake table tests of such columns despite earthquake excitations have three components in reality. This study carries out shake table tests on the seismic performances of precast segmental concrete column, and bidirectional earthquake motions were used as inputs. For comparison, the behaviours of the traditional cast-in-situ monolithic column were also experimentally investigated and compared with the segmental column. Interestingly, the experimental results showed that obvious twisting occurred to the segmental column under the bidirectional earthquake motions. To prevent the adverse twisting response, shear keys between the segments are proposed. The effectiveness of the proposed method is demonstrated through numerical simulations after the model is validated by the experimental results.

6.2 Introduction

Prefabricated structures have been proposed to accelerate construction speed in the congested urban areas. Precast segmental column, as one of the prefabricated structures, can be used to shorten construction time, reduce traffic delays, improve quality control and minimize environmental impact. Despite these advantages, its applications are mainly limited to the low seismicity areas due to the insufficient knowledge on its performance under extensive seismic loading.

To understand the seismic performance of precast segmental column, some research works have been carried out in recent years (Billington & Yoon, 2004; Cai et al., 2018; Chou & Chen, 2006; ElGawady et al., 2010; ElGawady & Sha'lan, 2010; Guo et al., 2015; Hewes & Priestley, 2002; Hung et al., 2017; Ichikawa et al., 2016; Li et al., 2018; Li et al., 2017; Nikoukalam & Sideris, 2017; Ou et al., 2010; Ou et al., 2009; Tazarv & Saiid, 2015; Wang et al., 2018; Yang & Okumus, 2017; Zhao et al., 2017; Zhao et al., 2018). According to these studies, some advantages of segmental column were observed, such as the excellent self-centring ability and good deformation capability. However, it was also found that the segmental column has limited energy dissipation capacity. Therefore, some studies were carried out to increase the energy dissipation capacity of the segmental column by using additional energy dissipation (ED) devices. Commonly studied ED devices included the internal ED bars and external ED devices. In the internal ED bar system, mild steel bars were normally embedded in the footing and extended to the segments across the joints. Such design was found effective to increase the energy dissipation capacity of the segmental column (Cai et al., 2018; Ou et al., 2010; Ou et al., 2009). However, these internal ED bars might increase the residual displacement (Ou et al., 2009). Moreover, they are not easy to be replaced if damaged during a severe earthquake, which can delay the retrofit activities after the earthquake. To overcome this problem, external ED devices were proposed and it was found the external ED devices were able to increase the energy dissipation capacity of the column while keeping the residual displacement small (Chou & Chen, 2006; ElGawady & Sha'lan, 2010; Guo et al., 2015; Nikoukalam & Sideris, 2017). Another observation was the concrete damage near the joints. Due to the joint openings between the segments, excessive compressive stress can be developed in the toes of the concrete segments, and concrete spalling damages were observed during the tests. Therefore, some other researches concentrated on mitigating the concrete spalling near the joints by confining the segments with steel jacket (Chou & Chen, 2006; Hewes & Priestley, 2002), fibre-reinforced polymer jacket (FRP) (ElGawady et al., 2010), or using advanced materials such as ductile fiber-reinforced concrete (DFRCC) (Billington & Yoon, 2004), engineered cementitious composite (ECC) (Tazarv & Saiid, 2015), and ultrahigh-performance concrete (UHPC) (Ichikawa et al., 2016; Wang et al., 2018; Yang & Okumus, 2017).

It should be noted that almost all the above-mentioned researches focused on the quasi-static performance of the segmental column under cyclic loading. To fully understand the real dynamic behaviours of such column, shake table tests are essential. Up to now, very limited shake table tests (Motaref et al., 2013; Moustafa & ElGawady, 2018; Varela & Saiidi, 2016; Yamashita & Sanders, 2009) have been carried out to investigate the performance of precast segmental columns under seismic ground motions. Yamashita et al. (2009) carried out shake table tests on a precast segmental column with rectangular hollow cross section. It was found the specimen showed limited damage, good ductility and small residual drift. Motaref et al. (2013) tested several segmental columns with damage resilient material such as elastomeric pad, ECC and carbon fibre-reinforced polymer (CFRP) in the plastic hinge region. The test results showed that the damage and residual displacement could be reduced by using these materials. Moustafa et al. (2018) tested the segmental hollow-core FRP-concrete-steel (HC-FCS) columns on the shake table and it was found that the HC-FCS columns sustained minor damage and smaller residual displacement compared to the reference RC column. Varela and Saiid (2016) conducted shake table tests on two 1/4-scale resilient bridge columns with replaceable plastic hinges incorporating ECC and two types of SMA bars. It was concluded that the concept of disassemble and reassemble connection could be achieved and the use of ECC and SMA bars could reduce the damage and residual displacement of the column.

It is worth mentioning that only the uniaxial earthquake excitation was applied in all the above shake table tests. During a severe earthquake, the columns are inevitably subjected to the multi-component earthquake motions, and the performances of the column under multi-component earthquake motions might be different from those obtained from the uniaxial earthquake motion. A few previous studies investigated the bidirectional performance of the traditional monolithic columns (Acosta et al., 2011; Hachem et al., 2003; Kitajima et al., 1992). Kitajima et al. (1992) tested several 1/9-scale columns under bidirectional earthquake motions. It was found that under bidirectional motions, the strength and stiffness of the monolithic columns decreased more significantly compared with those subjected to unidirectional motion. Hachem et al. (2003) tested four columns under seismic ground motions and it was concluded that the residual displacements of the column under bidirectional motions could be larger than those under unidirectional motion. Acosta et al. (2011) carried out shake

table tests on several monolithic oblong columns with interlocking stirrups subjected to two horizontal motions. It was found that after yielding, the bidirectional motions caused more stiffness and strength degradation and thus larger displacement responses compared to uniaxial excitations.

This paper carries out shake table tests on the seismic performances of precast segmental columns. The column was subjected to the bidirectional seismic motions with different peak ground accelerations (PGAs) until the failure of the column. For comparison, a conventional monolithic column was also experimentally investigated and the results were compared in detail with the segmental column. For the segmental column, it was generally believed that the friction forces between the joints were sufficient to resist the shear force during the earthquake event, and no shear keys across the joints were necessary (e.g. (Chou & Chen, 2006; Hewes & Priestley, 2002)). During the shake table tests in this study, it was interesting to observe that obvious twisting occurred to the segmental column under bidirectional seismic excitations, demonstrating that the friction forces at the joints were not enough to resist the shear force. This phenomenon has never been reported in the previous quasi-static and unidirectional shake table tests. To resist the adverse twisting, steel shear keys are proposed to be installed at the joints of the segments. To demonstrate the effectiveness of the proposed method, detailed three-dimensional (3D) finite element (FE) model is developed and numerical simulations are performed after the numerical model is validated by the experimental results. This article is organized as follows: Section 6.3 introduces the design and construction of columns; Section 6.4 presents the test setup. The test results are discussed in Section 6.5; In Section 6.6, a detailed 3D model is developed and the effectiveness of using steel shear keys between the segments to resist the twisting of the column is discussed; and finally some concluding remarks are drawn in Section 6.7.

6.3 Column designs and constructions

The shake table tests were performed in the Structural Dynamics Lab at Curtin University by using the recently commissioned four-shake table system. Each table has a platform with the dimension of 1000 × 1000 mm (length × width). The maximum payload, frequency range and stroke of each table are 8 kN, 0.1-50 Hz, and ±150 mm, respectively. The specimens were scaled down based on a bridge pier prototype

adopted from (Schoettler et al., 2012). In this part, the design of the columns, the construction process and material properties are presented.

6.3.1 Column design

One monolithic column (RC) and one segmental column (S1) were designed and tested in this study. The prototype column has a diameter of 1.22 m and a height of 7.32 m. A geometry scale factor of 1/12 was selected for both columns considering the capacity of the shake tables. The diameter and height of the scaled columns were therefore chosen as 100 mm and 600 mm, respectively. Table 6-1 summarises the geometry and other scale factors based on the similitude rules (Dove & Bennett, 1986). Figure 6-1 shows the general dimensions and design details of the columns. As shown, each column had a footing and a cap with the dimensions of 400 × 400 × 150 mm (length × width × height) and 500 × 500 × 150 mm (length × width × height), respectively. For the reference monolithic column (Figure 6-1 (a)), four steel bars with a diameter of 6 mm were used as the longitudinal reinforcements. The diameter and spacing of the stirrups were 3 mm and 35 mm, respectively. In contrast, for the segmental column, as shown in Figure 6-1 (b), the column was divided into three segments and each segment had a height of 200 mm. The steel reinforcements were the same as the monolithic column except that the longitudinal bars were discontinuous across the joints between the segments. A posttensioned strand with a cross sectional area of 54.7 mm^2 was used to clamp all the segments together. The tendon was anchored at the footing and the top surface of the cap. Two pieces of concrete blocks were fixed on the top of the column cap to mimic the weight of the superstructures. The dimension of the two blocks was 1000 × 1000 × 150 mm (length × width × height) and the weight of each block was 375 kg. The total weight of the whole specimen was 1456 kg. In particular, the weight of footing, column and cap were 60 kg, 12 kg and 94 kg, respectively. The total weight of the two mass blocks on the top of the column was 750 kg and the base slab was 540 kg. It should be noted that the sizes of the aggregates and rebar should be selected based on the scaling law as well. However, it could be very difficult to have the steel reinforcement and concrete aggregates uniformly scaled down. The maximum aggregate size used in the test was 7 mm and the smallest diameter of the rebar was 3 mm, which were the best available sizes from the local suppliers.

Table 6-1 Scale factors for the column

Physical Quantities			Scale Factors, S_i	
			Scale rule	Values
Geometry	Length of superstructure	l	S_l	12
	Displacement	δ	S_l	12
Material properties	Modulus of elasticity	E	S_E	1
	Stress	σ	S_E	1
	Strain	ε	1	1
	Poisson's Ratio	ν	1	1
Dynamic properties	Acceleration	α	S_a	1
	Mass	m	$S_E S_l^2/S_a$	144
	Frequency	ω	$(S_a/S_l)^{0.5}$	0.29
	Velocity	v	$(S_l S_a)^{0.5}$	3.46
	Time	t	$(S_l/S_a)^{0.5}$	3.46
Loadings	Force	F	$S_E S_l^2$	144
	Moment	M	$S_E S_l^3$	1728

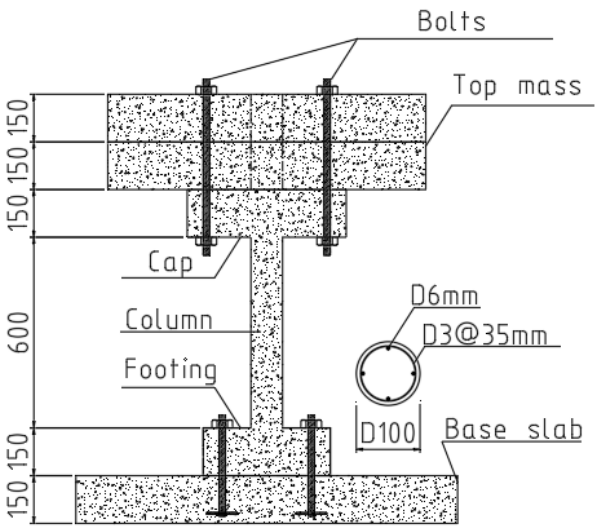

(a)

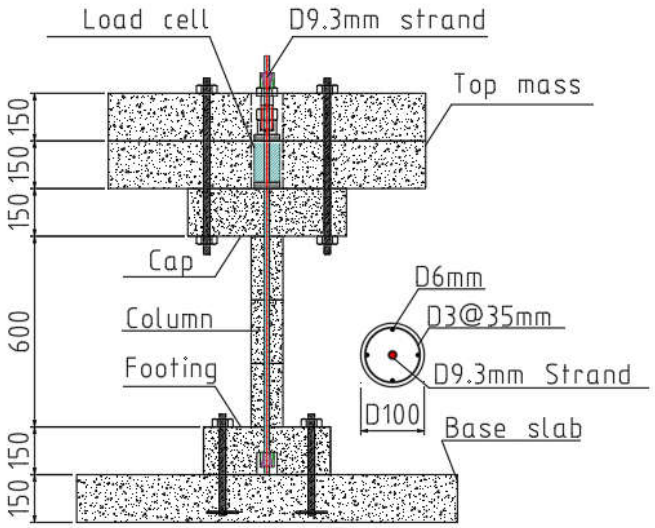

(b)

Figure 6-1 Design details of the tested columns (a) monolithic column; (b) segmental column

6.3.2 Construction and material properties

For the monolithic column, the footing, column and the cap were cast together as a whole, while for the precast segmental column, each part was cast separately. Figure 6-2 shows some of the construction procedures of the specimens. After curing of the concrete, the segments of the segmental column were camped together by the posttensioned tendon, and the posttensioning force was applied to the segmental column through the hydraulic jack. Figure 6-2 (e) shows the posttensioning setup of

the segmental column. In the design of the posttension force of the segmental column, normally two aspects should be considered. Firstly, the posttension force should be able to provide the column with flexural and shear strengths at the joints. To satisfy this requirement, Ou et al. (2010) applied the posttension force with a value around $0.072f_c'A_g$, in which f_c' is the compressive strength of the concrete, A_g is the cross sectional area of the column. Cai et al. (2018) applied a force to the tendon with the value around $0.1f_c'A_g$. Another consideration is the initial posttension load level corresponding to the strength of the tendon. During the earthquake excitations, the posttension force of the segmental column will increase due to the joint opening. To minimize the occurrence of yielding of the tendon so to preserve the column with self-centring ability, the initial posttension force is designed at a low level. For example, ElGawady et al. (2010) used the prestressing force corresponding to 30% of the ultimate strength of the tendon. In the present study, the initial posttension force was designed to be around $0.087f_c'A_g$, and the size of the tendon was chosen based on the available smallest strand from the local supplier, which resulted in the initial posttension load level equalling to 24% of the ultimate strength of the tendon. The measured compressive strength was 37.0 MPa on the testing day (41 days). The ultimate strengths of the longitudinal rebar and stirrups were 616 MPa and 430 MPa, respectively, as provided by the supplier. The seven-wire high strength steel strand was used as the tendon to clamp the segments. Details of the material properties are summarized in Table 6-2.

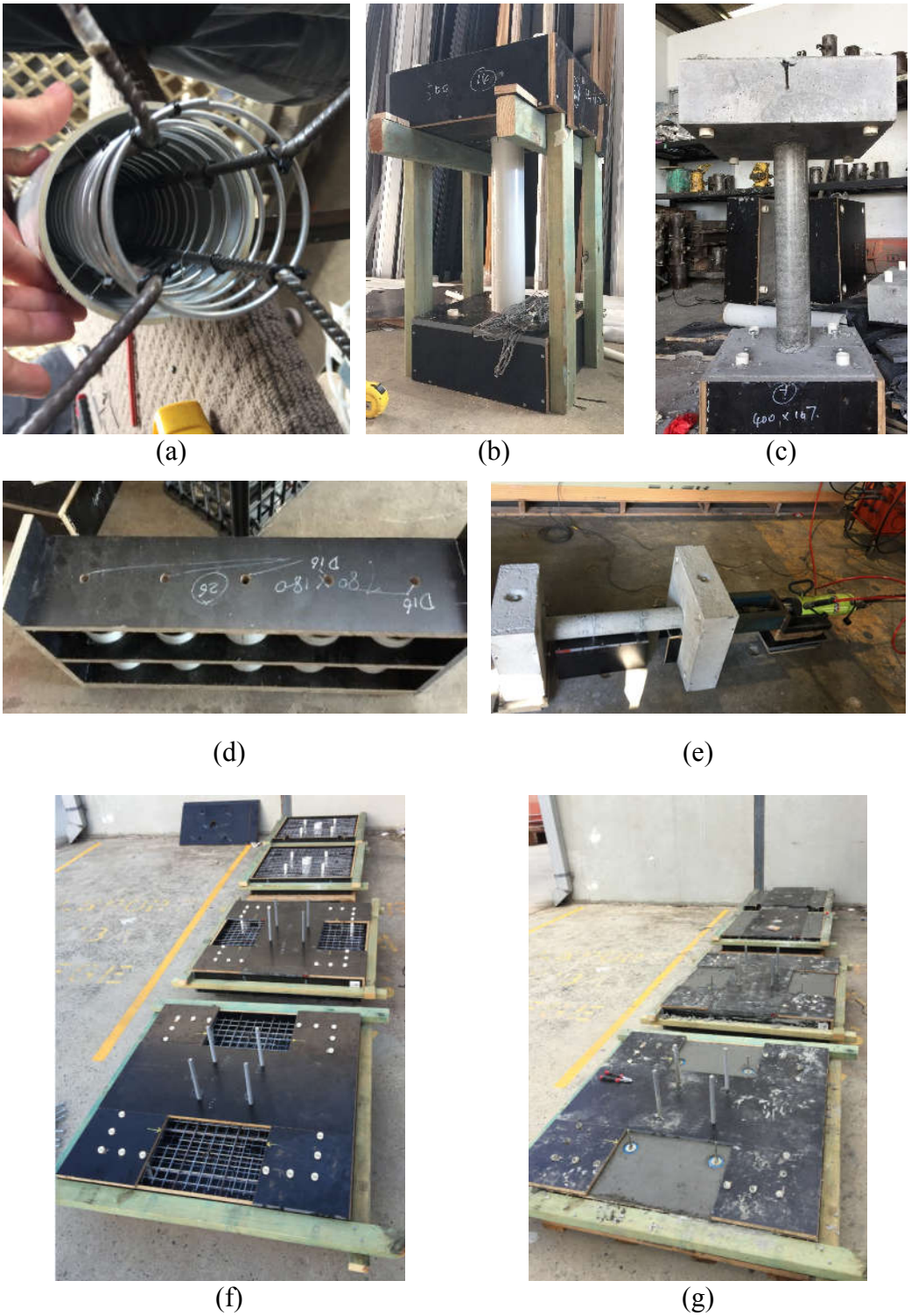

Figure 6-2 Construction of the specimens: (a) arrangement of rebars for the monolithic column, (b) formwork for the monolithic column, (c) monolithic column after curing, (d) formwork for the segmental column, (e) posttensioning setup of the segmental column, (f) base slabs and top mass slabs before casting, (g) base slabs and top mass slabs after casting

Table 6-2. Properties of the materials

Material	Diameter mm	Area mm^2	Elastic modulus (GPa)	Yield strength (MPa)	Ultimate strength (MPa)
Longitudinal rebar	6	28.3	200	555	616
Stirrup	3	7.1	200	346	430
Prestress tendon	9.3	54.7	195	1674	1860

6.4 Shake table test setup

6.4.1 Shake table and column installation

As mentioned above, the total mass applied on the column, including the mass blocks and the cap was 844 kg, which was larger than the capacity of a single shake table. The four shake tables in the lab were therefore combined together to form a big table. A base concrete block with dimension of 1500 × 1500 × 150 mm was used to connect to the four tables together. This concrete block also served as the base to support the specimen. Figure 6-3 (a-b) show the arrangement of the shake tables and the installation of the base concrete block. It should be noted since the four tables were used together, the alignment and synchronization of the tables are essential. Special attention was paid to align the shake tables in the horizontal and vertical directions before the installation of the base slab to ensure their levelling and alignment. In addition, the four tables were carefully controlled during the tests and the recorded data from the four tables showed that good synchronization was achieved. This will be demonstrated later in section 6.4.3. After tying the base slab to the shake tables, the column was installed and fixed to the base slab through four D22 mm thread bars that were embedded in the base slab. Figure 6-3 (c) shows the column that was ready to be installed. After installing the column, as shown in Figure 6-3 (d), the mass blocks were stacked on top of the column cap and connected with the cap through four bolts. A catching frame was built to prevent the column from collapsing after failure. Figure 6-3 (e) shows the final setup of the whole test system before testing.

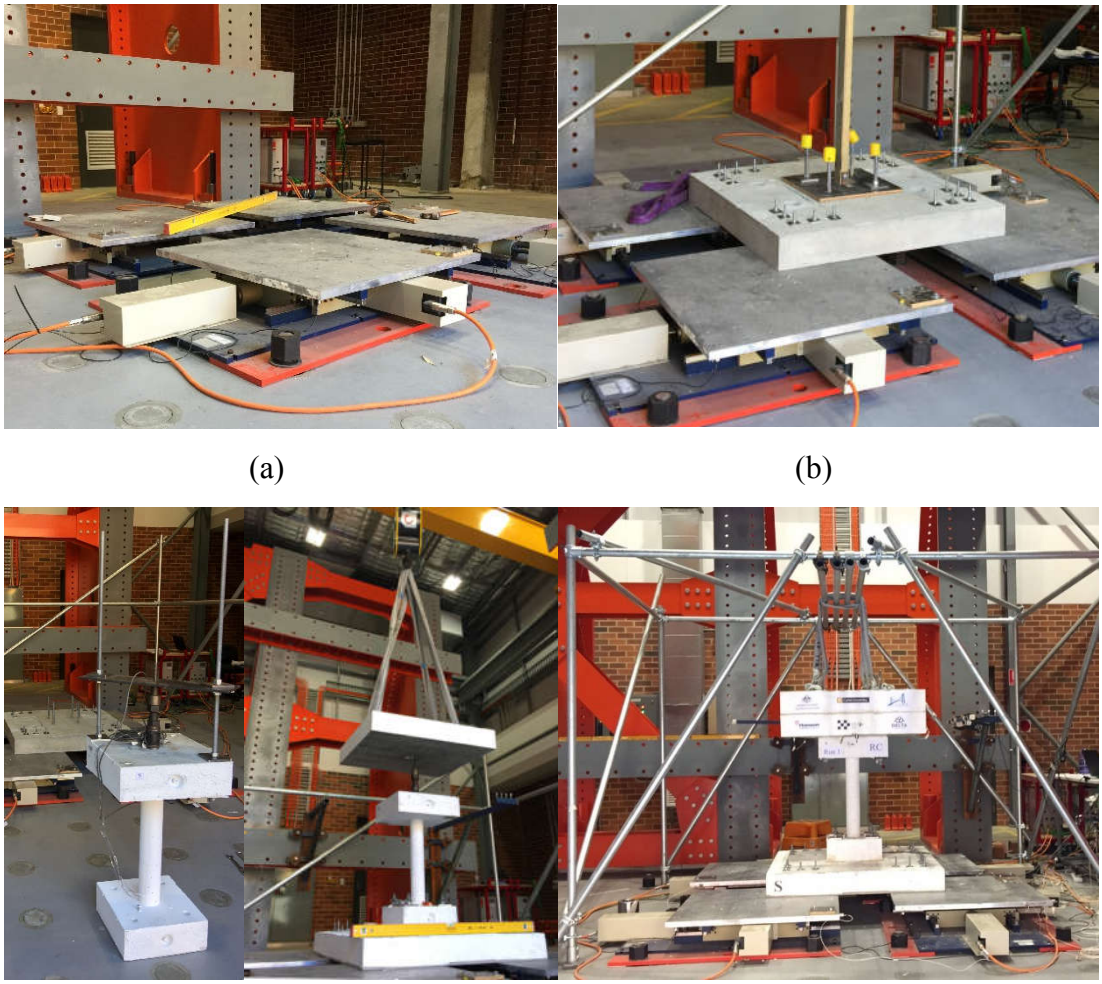

(a) (b)

(c) (d) (e)

Figure 6-3 (a) Shake tables alignment and levelling, (b) base concrete block installed, (c) column ready to be installed, (d) installation of the mass blocks, (e) final setup of the column

6.4.2 Instrumentation

Sensors including accelerometers, LVDTs and load cell were used to measure the responses of the columns under seismic motions. Table 6-3 summarizes the names and locations of the sensors and Figure 6-4 illustrates the front and top views of the sensor locations. As shown in Figure 6-4, two accelerometers (A0 and A1) were placed on the mass block to measure the accelerations in the North-South and East-West directions and another two accelerometers (A2 and A3) were installed on the footing to record the input accelerations. For simplicity, the North-South and East-West directions will be named as X and Y directions respectively in the following context. The accelerometers have a measurement range of ±5g and a frequency range of 0.06 Hz to 450 Hz. Three LVDTs were used to measure the displacements of the mass

block. Among which, the LVDT L0 was installed in the X direction and LVDTs L1 and L2 were installed in the Y direction. These LVDTs were made by Keyence (IL series) and have a measurement range of ±140mm. The measurement sensitivity of the LVDTs is 30 μm, which is accurate enough to capture the small displacements in the tests. A load cell was placed at the top of the segmental column to measure the change of the post-tensioning force in the tendon. In addition to these sensors, each shake table itself has integrated displacement and acceleration sensors in both directions which are not shown here. All the sensors were wired to QuantumX, a data acquisition system made by HBM, and the data were recorded with a sampling frequency of 200 Hz.

During the test, three cameras were also used to record the videos. One of the cameras was used for tracking the general overall behaviour of the column. The other two were placed perpendicular to the specimens in the X and Y directions to record the videos and derive the displacement of the footing and column in each direction through Digital Image Correlation (DIC) analysis for backup. Some tracking points were made on the base concrete block, column footing and mass block for the DIC analysis before the tests. The locations are also shown in Figure 6-4.

Table 6-3. Sensor details

Device	Name	Note
Accelerometers	A0	North-South (X) Acceleration at Top Mass
	A1	East-West (Y) Acceleration at Top Mass
	A2	North-South (X) Acceleration at Column Base
	A3	West-East (Y) Acceleration at Column Base
LVDTs	L0	North-South (X) Displacement
	L1	West-East (Y) Displacement-1
	L2	West-East (Y) Displacement-2
Load Cell	LC	Post-Tension Force in the Tendon

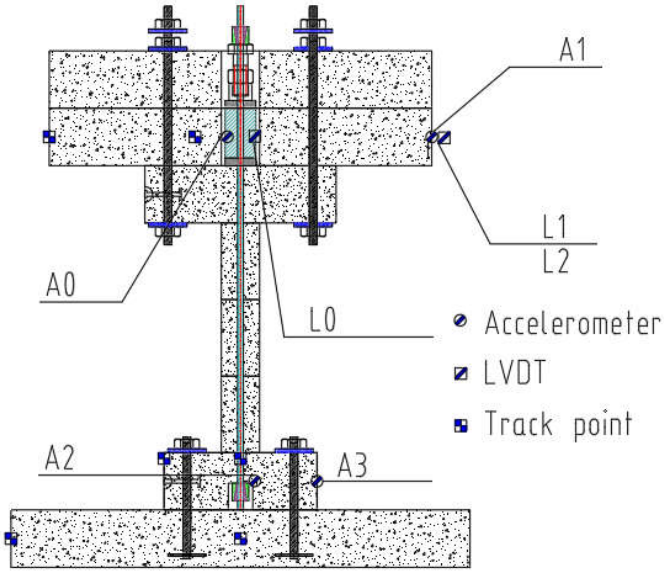

(a)

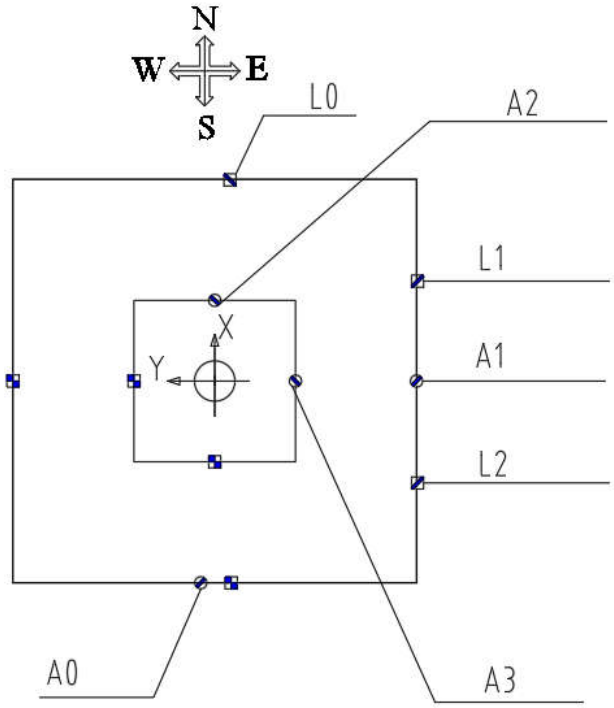

(b)

Figure 6-4 Arrangement of the sensors: (a) front view; (b) top view

6.4.3 Input ground motions

The columns were subjected to the two directional earthquake motions that were recorded at the Niland Fire Station during the 1979 Imperial Valley Earthquake. The

PGAs of the original data were 0.108g and 0.068g in the N-S (X) and E-W (Y) directions, respectively. In the present study, the specimens were designed to be tested up to failure. The original earthquake ground motions therefore should be scaled. During the tests, the original earthquake motions were scaled with the maximum PGA varying from 0.2g up to the collapse of the column with an interval of 0.1g. The same scaling factor was used for both the X and Y directions. To account for the scale factor of the tested column, the time duration of the input accelerations was compressed by a factor of $\sqrt{12} = 3.46$ according to the scaling rules as illustrated in Table 6-1. Figure 6-5 shows one pair of the earthquake motions with the maximum PGA of 0.2g in X direction and the corresponding response spectra.

It is worth noting that this pair of ground motions were selected mainly because of the following two reasons: Firstly, the two specimens (i.e. the segmental column and monolithic column) were designed to be tested up to failure. The specimens should be able to fail before the tables achieving the maximum achievable PGA. Secondly, due to the special arrangement of the four tables (i.e. using the four shake tables as a whole), the initial positions of the tables' centres were shifted from their original physical zero positions to allow the connections of the shake tables to the strong floor and the concrete slab on the top of the four tables. As a result, the allowable displacements of the tables were only about 95 mm though the stroke of the tables could reach 150 mm. The displacements of the ground motions should be smaller than 95 mm during the testing case with the maximum PGA.

It should be noted that since the four shake tables were used together as a whole, it is important to ensure that the four tables were well synchronized. Figure 6-6 shows the comparisons of the input and outputs in the X direction of the four shake tables when the PGA was 0.2g. In particular, the displacements, accelerations and Fourier spectra of the corresponding accelerations are compared. It can be seen that the output displacements of the four shake tables were exactly the same as the input displacement (Figure 6-6 (b)) due to the fact that displacement control was used in the controlling system of the shake tables. For the accelerations (Figure 6-6 (a)), slight discrepancies could be found between the input and outputs. This was also reflected in the Fourier spectra of the accelerations (Figure 6-6 (c)). For the other direction and other PGAs, the same observations can be drawn. After the tests, the slab that connecting the four

tables and the bolt holes on the slab were also checked carefully, no damage to the slab/holes was observed, implying very good control of the four tables that they had synchronized movements. To measure the change of the dynamic characteristics of the columns with the increase of the ground motion intensities, white noise excitations were used as inputs between the earthquake motions. The white noise inputs had duration of 40 s and a small amplitude of 0.02g.

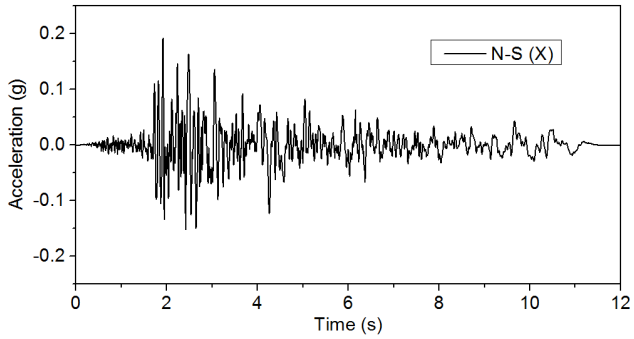

(a)

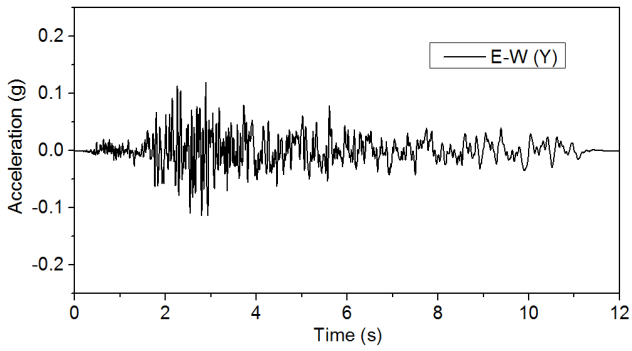

(b)

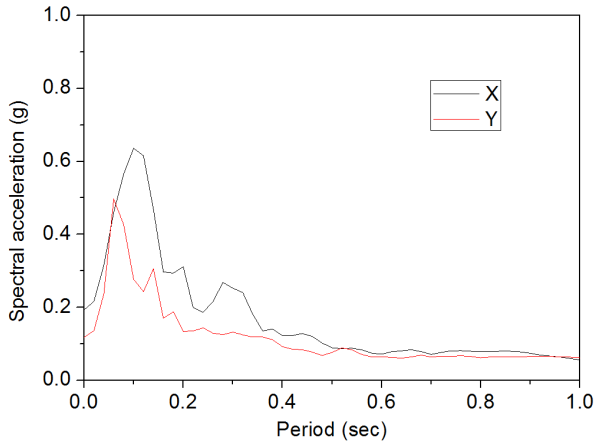

(c)

Figure 6-5 One pair of the bidirectional inputs (maximum PGA=0.2g): (a) N-S (X) direction; (b) E-W (Y) direction; (c) Acceleration response spectra

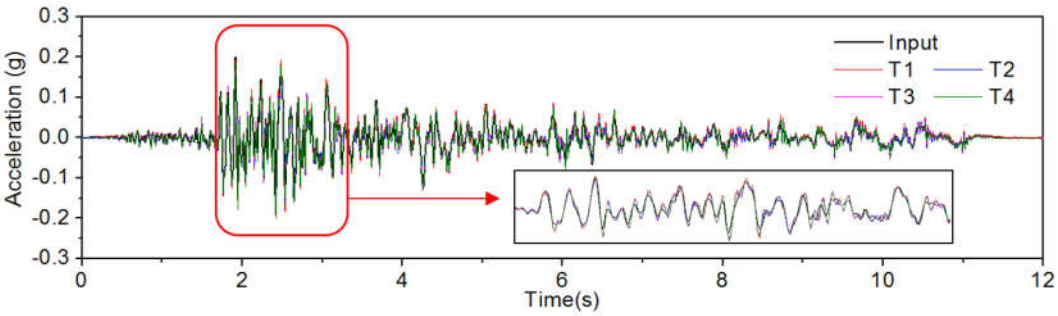

(a)

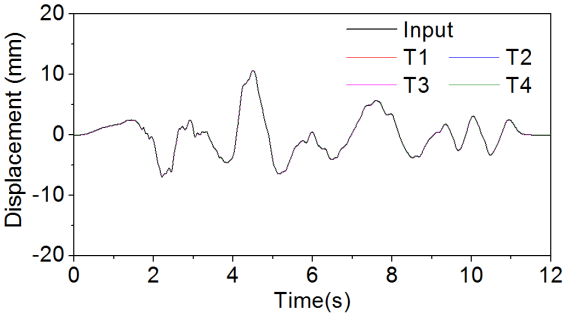

(b)

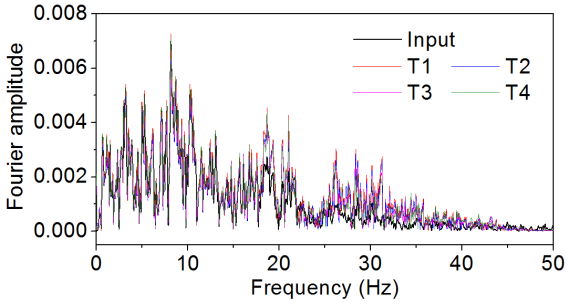

(c)

Figure 6-6 Comparisons of the input and outputs: (a) accelerations; (b) displacements; (c) Fourier spectra

6.5 Test results

The monolithic column collapsed when the maximum PGA reached 1.0g and the segmental column collapsed at 0.8g. In the following sections, most of the results were compared when the PGA was up to 0.7g before the collapse of the two columns.

6.5.1 Observed damage

Figure 6-7 and Figure 6-8 show the damages and final failures of the two columns. For the monolithic column, the main damage mode of the column was the concrete tensile cracks, concrete cover spalling and fracture of the internal longitudinal steel bars. Figure 6-7 (a) illustrates the damage patterns of the monolithic column at the PGA of 0.9g. It can be observed that concrete cracks distributed along the column from the bottom of the column and developed to about half height of the column. Figure 6-7 (b-c) show the final collapse views of the column (at 1.0g) and the local

damage near the footing-column joint. It can be found that the longitudinal bars fractured and the concrete crushed at the bottom of the column.

The segmental column experienced rocking and joint opening responses during the test, and no tensile crack was observed. This is because the segments could rock against each other and opening could be formed at the joints instead of forming tensile cracks as observed in the monolithic column. No visible concrete damage was observed before the PGA reached 0.6g. Due to the rocking behaviour, the toes of the bottom segment experienced significant compressive stress. As a result, concrete spalling damage started to appear at the PGA of 0.6g and further developed with the increase of PGA. Figure 6-8 (a-b) show the concrete spalling and crushing damages near the joint between the footing and the bottom segment when the PGA was 0.7g. It can be observed that severe concrete damages occurred in the bottom segment. Figure 6-8 (c-d) show the final collapse views of the segmental column when the PGA reached 0.8 g. It can be found the concrete was seriously damaged due to the excessive compressive stress in the segments.

As mentioned above the monolithic and the segmental columns collapsed at the maximum PGA of 1.0g and 0.8g, respectively. The segmental column collapsed earlier than the monolithic column. This could be attributed to the large axial force from the posttensioned tendon in the segmental column. On one hand, the tendon could pull the column to its initial position after deformation, so that the residual displacement of the segmental column is small (details will be presented in Section 6.5.4). On the other hand, the prestressed tendon increased the axial stress of the column and the bottom segment experienced excessive compressive stress resulting from the rocking of the column. Concrete crushing damages were therefore induced and developed in the segment. Therefore, the posttensioning force should be carefully chosen in the design and the bottom segments might need to be confined by FRP or steel jackets to minimize the concrete crushing and spalling damages. With such treatments, less concrete damages would occur and the segmental column might be able to fail at the same or even higher PGA level compared to the monolithic column.

Another interesting observation during the test was that obvious twisting occurred in the segmental column while almost no twisting was observed in the monolithic column. This is because the segmental column had no continuous steel bars across the

joints except a post-tensioned tendon at the centre of the column. The only resistance of the column to the torsional moment and shear was the friction between the interfaces of the segments. The observation of the twisting during the test indicated that the friction was not enough to resist the torsional moment in the segmental column when it was subjected to bidirectional seismic motions. No previous literature has reported such phenomenon yet. Further quantitative discussions and method to prevent this adverse twisting will be presented in Sections 6.5.4 and 6.6, respectively.

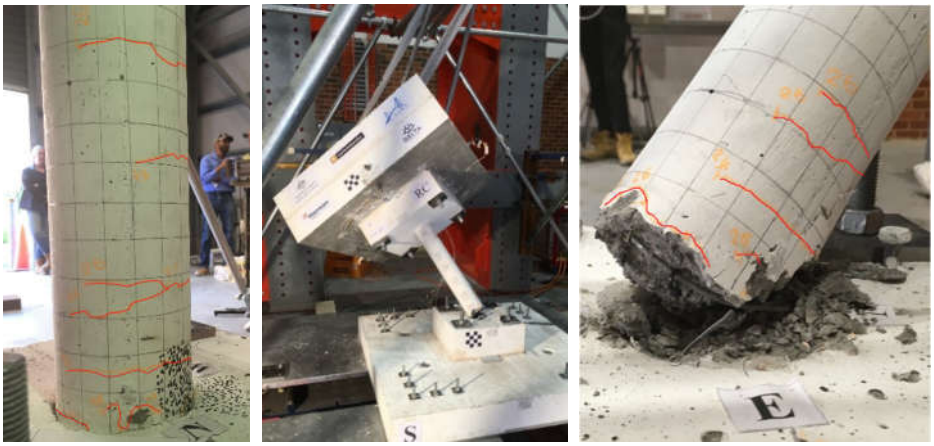

(a) (b) (c)

Figure 6-7 Damage of the monolithic column: (a), PGA 0.9g; (b-c), PGA 1.0g

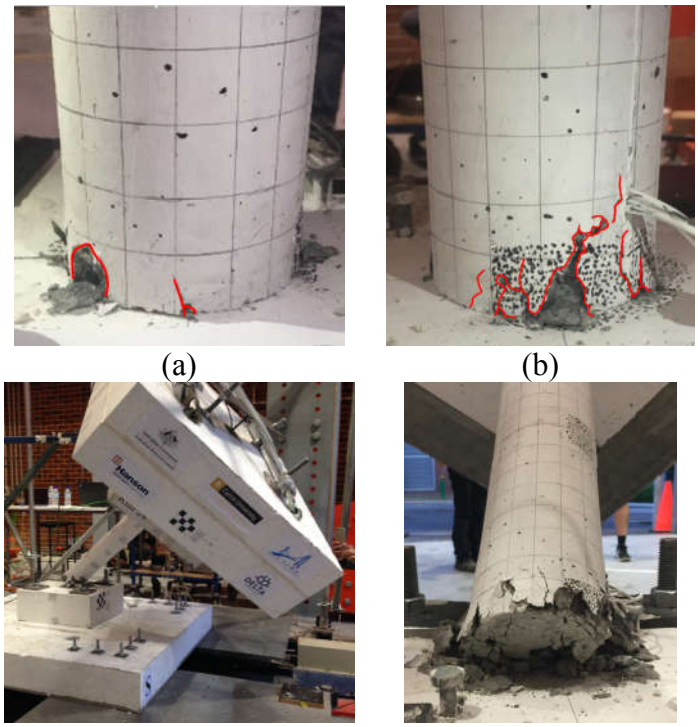

(a) (b)

(c) (d)

Figure 6-8 Damage of the segmental column: (a-b), PGA 0.7g; (c-d), PGA 0.8g

6.5.2 Variations of the fundamental periods

As described in section 6.4.3, white noise tests were carried out between each earthquake input. The periods of the columns then can be obtained by transforming the time domain data into the frequency domain through the Fourier transform. Figure 6-9 shows the variations of first vibration periods of the two columns during the tests. As shown, the segmental column has smaller initial vibration period compared to the monolithic column. As the mass of the mass blocks at the top of the two columns is the same, the results indicate that the segmental column has larger initial stiffness than the monolithic column. This is because the stiffness of the segmental column depends on the posttensioning force in the tendon, and the variation of the posttensioning force directly changes the stiffness of the segmental column. Trono et al. (Trono et al., 2014), when testing a damage-resistant posttensioned bridge column rocking at the interface of its foundation, also observed that the period of the posttensioned column was smaller than the reference monolithic column. Figure 6-9 also shows that when the PGA increased from 0.2g to 0.6g, the periods of the segmental column (S1) were almost a constant with an increment of 8.2% only. In comparison, for the monolithic column (RC), the period increased from 0.42s to 0.52s, with an increment of 21.6%. These results indicated that the monolithic column experienced more intensive damages than the segmental column owing to the concrete tensile cracks and steel bar yielding, which did not occur in the segmental column since the joints could open under tensile force. The primary damage of the segmental column was the crushing damage to the concrete segments as shown above, which was not prominent under these excitation levels. When the PGA became larger, both the vibration periods of the segmental and monolithic columns increased due to the damages developed in the columns. However, the increment was more obvious in the monolithic column as shown in Figure 6-9. This means that compared to the conventional monolithic column, the segmental column is less vulnerable to the small to medium seismic excitations that may be experienced during its whole lifecycle.

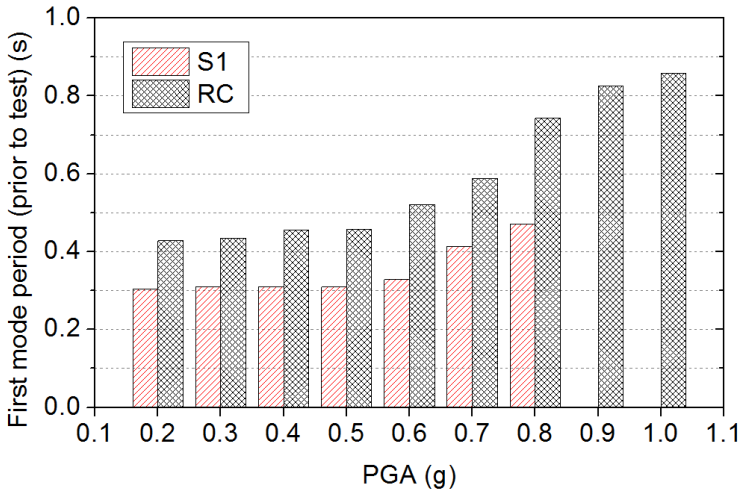

Figure 6-9 Measured first vibration periods of the columns prior to each test

6.5.3 Drift responses

The displacements of the column were recorded by the LVDTs in the two directions. The relative displacements were calculated by subtracting the displacement of the shake table from the measured displacements. Figure 6-10 shows the lateral relative drift response time histories of the columns in the both directions. It can be observed that when the PGA was 0.2g, the two columns had similar drift responses. When the PGA reached 0.7g, the maximum drifts of the segmental column were larger than those in the monolithic column. As shown, the maximum drifts reached 4.49% and 4.45% in the X and Y directions respectively for the segmental column. In contrast, the corresponding values for the monolithic column were 3.42% and 2.64%. Figure 6-11 shows the maximum resultant drift responses of the two columns at different PGAs. Similar observations can be obtained, i.e. the two columns had similar drift responses at small input intensities, while under large intensities the segmental column experienced larger drift responses than the monolithic column due to the openings at the joints. It should be noted that both the columns showed very small residual drift even the maximum PGA reached 0.7g (Figure 6-10 (c) and (d)). For the segmental column, this was attributed to the restoring force provided by the posttensioned tendon that could pull the column back to its original position after deformation. For the monolithic column, the concrete mainly experienced tensile cracks and almost no crushing damage, no obvious plastic hinge was formed during the tests and the residual drift of the monolithic column was therefore also very small. More quantitative analysis will be presented in Section 6.5.4.

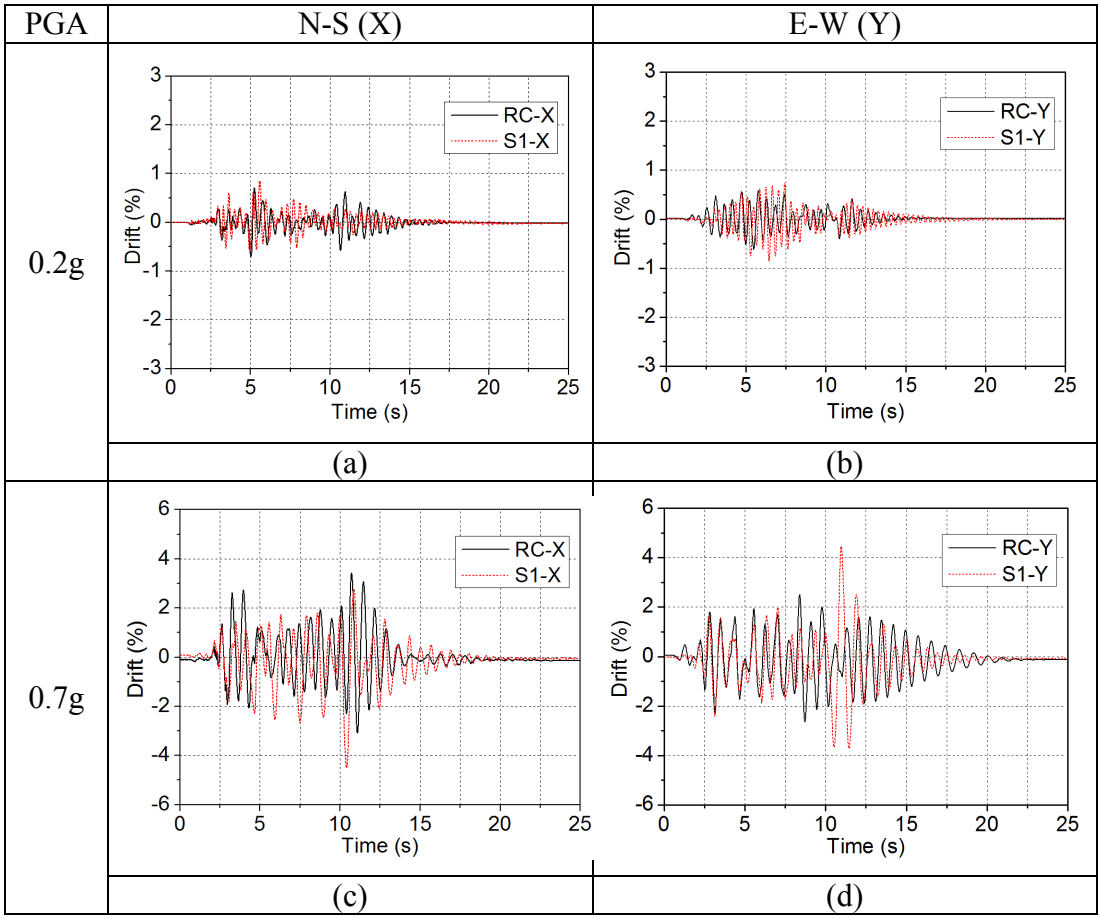

Figure 6-10 Drift time histories of the two columns (a-b), PGA 0.2g; (c-d), PGA 0.7g

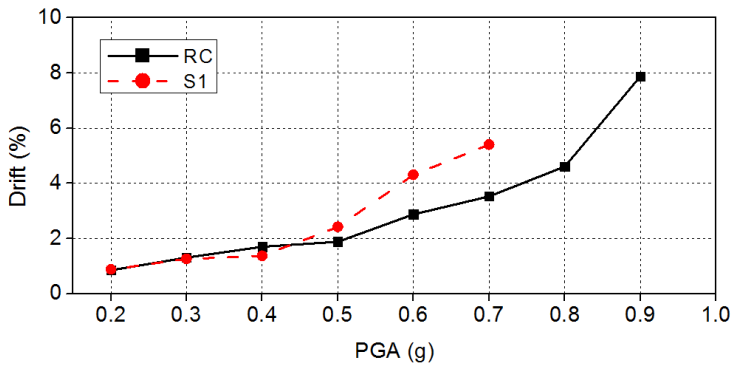

Figure 6-11. Intensity vs resultant drift responses of the two columns

6.5.4 Residual twisting angle and residual displacement

As mentioned above, obvious twisting was observed in the segmental column during the tests. Figure 6-12 shows the residual twisting angles of the two columns after each test. It can be observed that the residual twisting angles of the monolithic column were almost zero during the tests. In contrast, the twisting angles of the segmental column S1 gradually increased from zero to around 5.5 degrees when the maximum PGA

reached 0.7g. The cause of the twisting can be explained as follows. As shown in Figure 6-13 (a), when the column was intact, the stiffness centre was the same as the mass centre because the column was symmetric, no torsional moment would be developed in the column. When the column was subjected to earthquake motions, the column had different displacement responses in each direction during the test due to the different earthquake motions, and even in the same direction, the displacement amplitudes in the two sides of the column could be different, unsymmetrical damages therefore could be formed in the column as illustrated in Figure 6-13 (b), resulting in the change of the stiffness centre of the column. When the stiffness centre and the mass centre were not coincident, the bidirectional earthquake motions applied to the column could induce torsional moment to the column. For the segmental column, the only resistance to the torsional moment was the friction between the interfaces of the segments at the joints. Once the friction was not enough to resist the shear stress caused by the torsional moment, twisting between the interfaces occurred. In contrast, the monolithic column was cast as a whole, no such problem existed and the twisting angle was thus small.

It should be noted that such phenomenon has never been reported in previous studies. This is because previous studies mainly focused on the quasi-static cyclic tests or only the uniaxial earthquake motion was used as input when shake table tests were performed. It was therefore commonly believed that the friction forces between the joints were enough to resist the shear forces (Chou & Chen, 2006; Hewes & Priestley, 2002), and no special treatment was needed to increase the shear resistant capacity of the segmental column. This study, on the other hand, shows that the friction forces between the joints was not enough to resist the shear forces caused by the torsional moment and severe residual twisting was observed. Therefore, shear resistant designs (e.g. concrete shear keys, steel shear keys) between joints need to be provided. The effectiveness of using shear keys to decrease the adverse twisting effect will be discussed in Section 6.6 through numerical simulations.

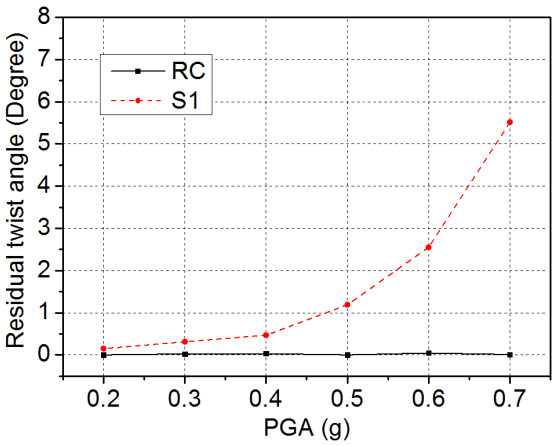

Figure 6-12 Residual twisting angles of the two columns

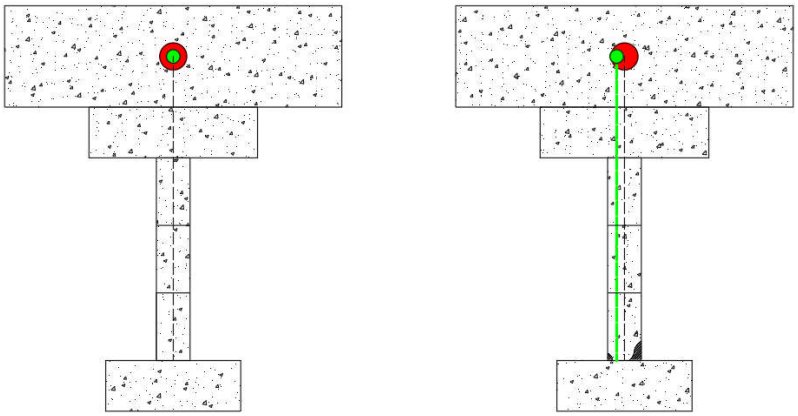

(a) (b)

Figure 6-13 Schematic drawing of the stiffness centre change due to asymmetric damage

The residual displacements of the two columns are compared and evaluated in this part. It is obvious that the twisting would influence the residual displacement recorded in the tests, and the influence should be removed before assessing the results. Figure 6-14 shows a schematic view of the twisting of the mass block at the top of the column. The solid lines show the original position of the column and the dash lines represent the column without any lateral residual displacement but with a twisting angle φ. The red short lines ME in the E-W direction and RR' in the N-S direction are the lateral displacements resulting from twisting, which should be removed. Figure 6-15 (a) shows the residual displacements of the both columns in each direction after the influence of twisting was removed. It can be found that the residual displacements of the monolithic column in the X direction were larger than those in the Y direction. This is because that the PGA of the inputs in the X direction was larger than that in

the Y direction as illustrated in Figure 6-5, resulting in more damage in the X direction. The same trend was found for the segmental column S1 except when the PGA reached 0.7g, at which severe damages occurred to the bottom segments. Figure 6-15 (b) shows the resultant residual displacements of the columns. It can be found that the maximum resultant residual displacements were 1.4 mm and 0.7 mm for the monolithic column and segmental column, respectively, which were very small for the both columns. The reason is that the monolithic column experienced insignificant concrete spalling and crushing damages before collapse and no obvious plastic hinge was formed in the monolithic column as shown in Figure 6-7 (a). It also can be seen that the resultant residual displacements of the segmental column were smaller than those of the monolithic column due to the fact that the posttensioned tendon could pull the segmental column back to the original position, which demonstrated the most widely recognized advantage of precast posttensioned segmental column.

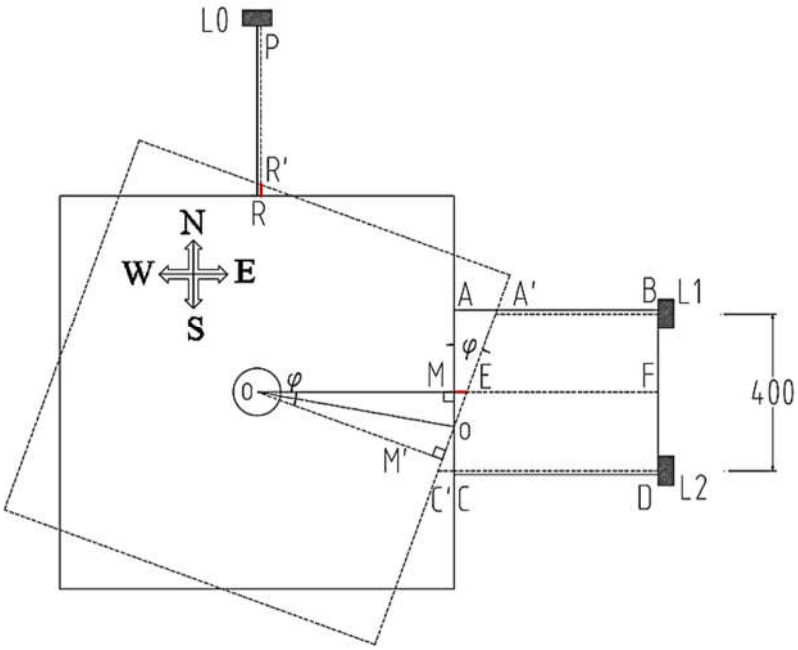

Figure 6-14 Schematic drawing of the influence of twisting on the residual displacement

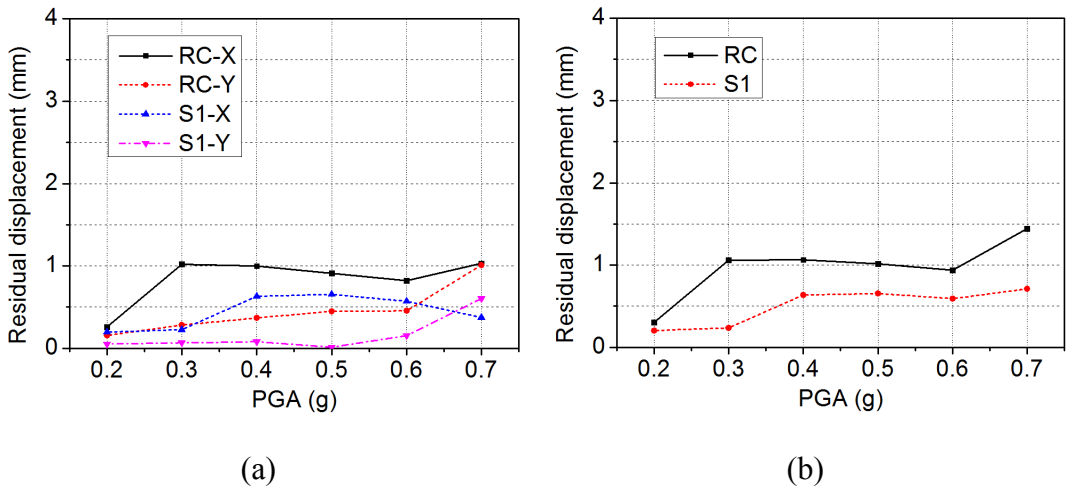

Figure 6-15 Residual displacements of the two columns: (a) in each direction; (b) resultant residual displacements

6.5.5 Posttension force

As mentioned above, the posttension forces in the segmental column were recorded by the load cell at the top of the column. Figure 6-16 shows an example of the relationship between the posttension forces and the displacements of the column when the PGA was 0.7g. In the figure, the black line represents the posttension force corresponding to the actual deformation of the column in the X and Y directions, and the green and blue lines are the projections of the black line to the X and Y directions, respectively. As shown, the posttension forces increased with the increase of the lateral displacement and showed a V-shape relationship with the displacement, which was similar to those observed in the previous cyclic test (Li et al., 2017). Due to the damage of the column, posttension force loss was observed. Figure 6-17 summarizes the maximum and minimum posttension force during the tests. It can be observed that the maximum posttension forces increased with the increase of PGA due to the larger displacement responses and joint openings. The maximum posttension force reached 33.3 kN at 0.7g, the corresponding stress in the tendon was around 608.8 MPa, which was smaller than the yielding stress of the material, indicating the posttensioned tendon did not yield. The minimum stress decreased with the increase of the PGA. When the PGA reached 0.7g, the minimum posttension force was 23.2 kN, which was reduced by 6.4% compared with the initial posttension force (24.8 kN). As mentioned above, the tendon did not yield during the test, the loss of posttension force was therefore caused by the damages accumulated in the column during the tests, which

shortened the height of the column and in turn reduced the existing posttension force in the tendon.

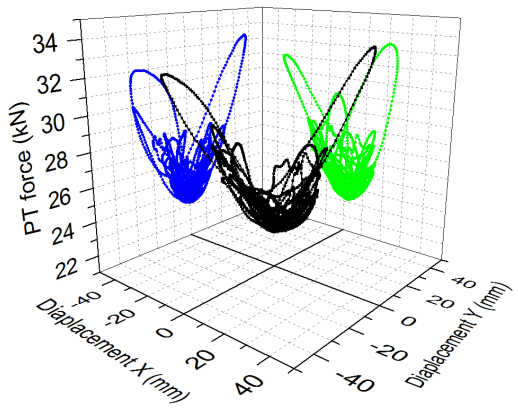

Figure 6-16 The posttension force versus displacements of the segmental column (PGA=0.7g)

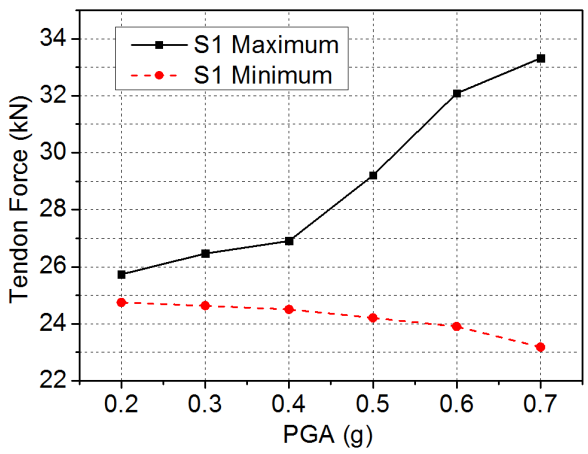

Figure 6-17 The Maximum and minimum posttension forces in the tests

6.6 Numerical study

In this part, a detailed 3D numerical model of the segmental column is developed to simulate the dynamic behaviours of the column under seismic excitations. The model is validated against the test results first, and then steel shear keys between the segments are then proposed to minimize the twisting of the column.

6.6.1 Numerical model

To realistically simulate the joint opening and twisting behaviour of the segmental column under earthquake ground motions, a detailed 3D FE model is developed by adopting the commercially available FE software ABAQUS/Standard (Simulia,

2012). The concrete segments, footing and mass blocks are modelled by the 3D eight-node solid elements (C3D8R in ABAQUS). The mesh sizes of the segments, footing and mass are chosen as 10 mm, 40 mm and 50 mm, respectively by conducting mesh convergence test. Details regarding the concrete and steel modelling can be found in the authors' previous work (Li et al., 2017).

As observed in the tests, joint openings and twisting were developed at the interfaces between the segments. To model these behaviour, surface to surface contact elements are used. Hard contact is used for the normal contact behaviour between the two contact surfaces of the segments. The tangential behaviour is modelled as tangential friction with Coulomb friction model. Different values of the friction coefficient (μ) have been used in the previous studies. For example, the value of 0.5 was used in the simulations of the quasi-static cyclic performance of segmental columns (Dawood et al., 2011; Ou et al., 2007). In another study, the value of 0.4 was used (Pitilakis et al., 2017). Tassios and Vintzēleou carried out systematic experimental studies on the friction behaviour between concrete interfaces (Tassios & Vintzēleou, 1987). It was found that the friction coefficient was dependent on the normal compressive stress and loading conditions. For example, under monotonic loading, when the compressive stress increased from 0.5 MPa to 2 MPa, the friction coefficient decreased from 0.5 to 0.4. Moreover, under the repeated cyclic loading, the friction coefficient could further decrease. In the current study, the axial compressive stress was around 3.2 MPa and the interfaces experienced repeated loading during the test, the friction coefficient could be smaller than 0.4 according to the observations from the reference (Tassios & Vintzēleou, 1987). The friction coefficient is selected as 0.3 in the present study. The damping is modelled as Rayleigh damping and a damping ratio of 1.8% is adopted as determined based on the half-power bandwidth method through analysing the response of the column under the white noise excitations (Motaref, 2011).

For the loadings, three loading steps are defined in the model, including the prestressing force, gravity load, and the earthquake inputs. The posttensioning force is applied to the tendon with initial stress condition and the gravity load is applied to the model by assigning gravity acceleration to the whole model. The bidirectional earthquake motions are imposed to the column footing with the recorded displacements in the two horizontal directions. For the boundary condition, the footing

was totally constrained during the prestressing and gravity loading steps. In the earthquake loading step, the lateral displacements of the two horizontal directions are released to allow the movements of the footing. After the earthquake loadings are finished, the footing is constrained again to allow the free vibration of the column. Figure 6-18 shows the whole numerical model.

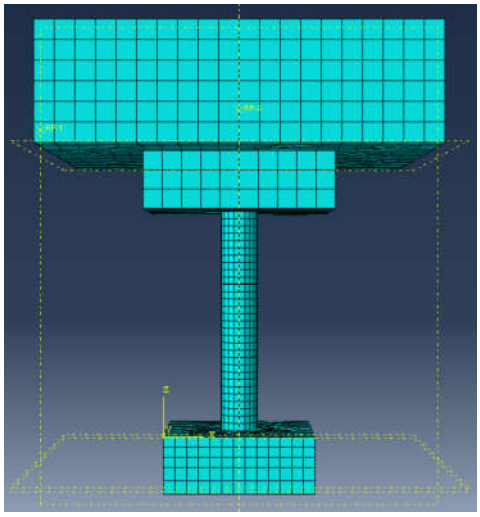

Figure 6-18 Numerical model

6.6.2 Model validation

The numerical model is calibrated by the experimental results. Firstly, eigenvalue analysis is carried out to determine the vibration periods of the column. It is found that the fundamental vibration period of the numerical model is 0.29 s, which is close to the measured value of 0.30 s. Then more detailed comparisons are made. Figure 6-19 (a-d) show the comparisons of the lateral displacement time histories of the column in the two horizontal directions when the maximum PGA of the inputs is 0.2g. It can be seen that the displacement responses of the simulated results agree well with the test results. Figure 6-19 (e-h) show the comparisons of the displacement responses when the PGA reaches a relatively large value of 0.5g. It can be seen that in general good matches can be obtained. The discrepancies might be caused by the construction uncertainties, the bidirectional coupling damages in the segments and the accuracy of the material models in the simulation. As shown in Figure 6-20, the residual twisting is also observed in the numerical simulation and the trend of the residual twisting angle in the simulation is similar to that in the test but with smaller values. This might be because the selected friction coefficient (0.3) is still slightly larger than the real value,

and it changes during the tests with the change of the interface conditions, which is not considered in the present study. The experimental result (the black curve in Figure 6-20) also shows that obvious twisting is observed at the very beginning of the test (at the first 2.5s), this is however not observed in the numerical simulation (the red curve). This is because the mass centre and stiffness centre of the specimen could not be exactly coincident with each other in the real test due to the minor construction error, though the structure was designed to be symmetrical. In the numerical simulation, no such problem exists. Other than these, the above comparisons show that the developed numerical model can capture the dynamic performances of the precast segmental column when it is subjected to the bidirectional earthquake excitations.

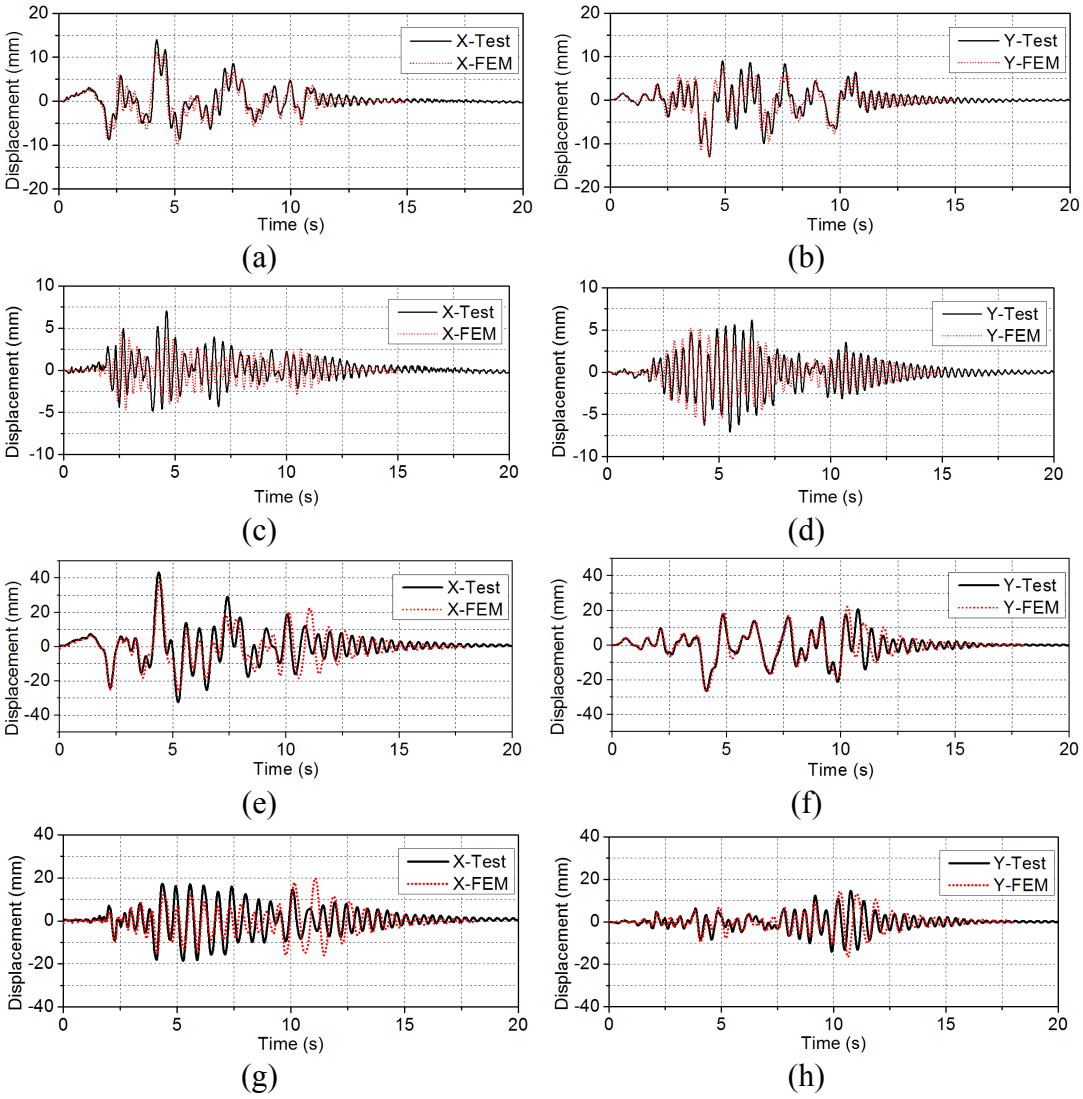

Figure 6-19 Absolute displacement response comparisons: (a-b) PGA=0.2g; (e-f) PGA=0.5g; relative displacement response comparisons: (c-d) PGA=0.2g; (g-h) PGA=0.5g

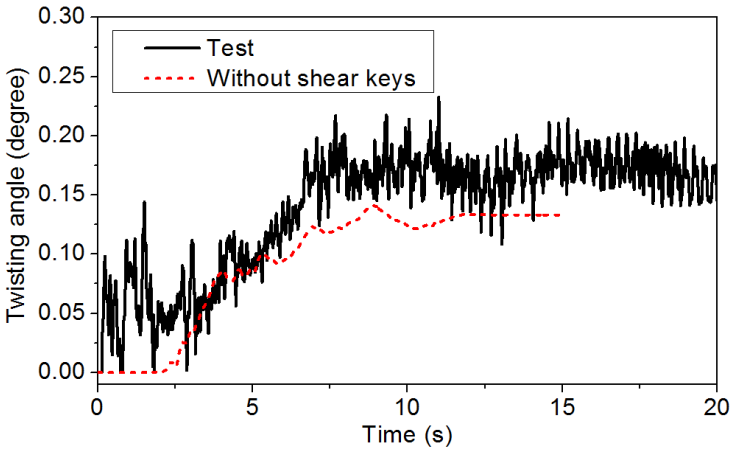

Figure 6-20 Twisting angles of the column from the test and numerical simulation

6.6.3 Shear keys to mitigate torsional responses

Both the experimental and numerical results show that the frictions between the joints are not enough to resist the torsional moment in the earthquake event. Some measurements need to be implemented to increase the torsional resistant capacity of the segmental column at the joints. In this part, shear keys are proposed to be added between the segments to minimize the adverse twisting, and the effectiveness of the proposed shear key is demonstrated through numerical simulations.

Recently, Hung et al. proposed installing a single steel shear key at the centre of the cross section between the neighbouring segments to increase the lateral shear resistance of the segmental columns, so as to reduce the high prestressing force in the tendon that was usually used to increase the friction between the segments to resist the lateral shear force (Hung et al., 2017). It should be noted that the single shear key at the centre of the column cannot resist the adverse twisting phenomenon. To resist the torsional moment, the method suggested by Hung et al. is slightly modified in the present study. Instead of using one large shear key at the centre of the cross section, multiple smaller shear keys are proposed to be installed. Figure 6-21 (a-b) show a schematic drawing of the column with four shear keys. As shown, the shear key system includes four holes that are symmetrically reserved in the segments and four protruded shear keys that can be fitted into the holes. Figure 6-21 (c) shows the FE model of one segment with shear keys. In the numerical simulation, the steel shear keys are modelled as solid elements and the material property is the same as the longitudinal steel bars as shown in Table 6-2. Surface to surface contact elements are used to

simulate the interaction between the concrete segments and the shear keys. Figure 6-22 compares the twisting of the columns with and without shear keys when the columns are subjected to the same bidirectional earthquake motions. It can be seen that the twisting angles of the column with the proposed shear keys are reduced to almost zero, demonstrating that the proposed method is effective to minimize the twisting angle of the segmental column.

It should be noted that during the service life of the structure with segmental columns, besides earthquake loading, it may also subjected to the other types of dynamic loads such as impact and blast. Previous experimental and numerical studies (e.g. (Li et al., 2017; Zhang et al., 2016)) revealed that shear keys in the segmental column could reduce the lateral slippages between segments resulting from these impact and blast loads. The experimental and numerical results in this study as shown above demonstrate the necessity and effectiveness of installing shear keys between the segments to reduce the twisting of the segmental column under seismic excitations. The proper design of shear keys so that it can be used to resist multi-hazard could be an interesting topic. This is, however, out of the scope of the present study, which will be further investigated in the future studies.

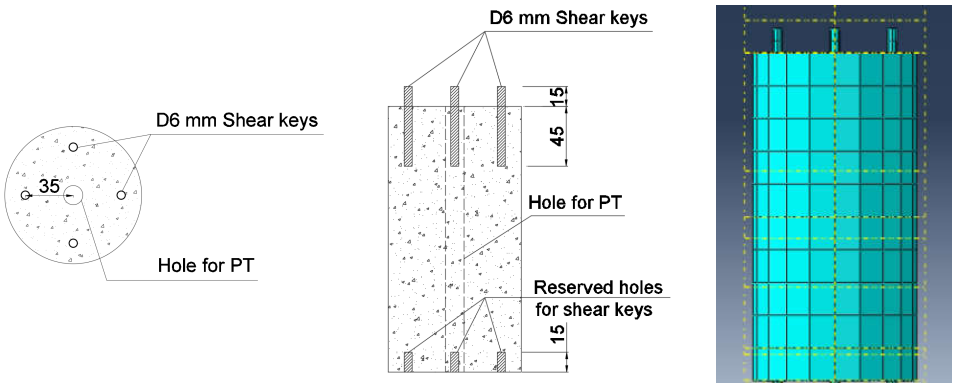

(a) (b) (c)

Figure 6-21 Steel shear key system between the segments: (a-b) schematic drawing of the shear keys, (c) modelling of the shear keys

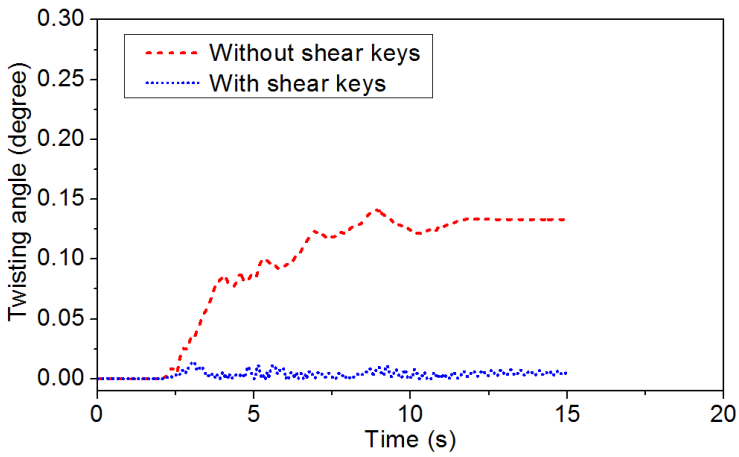

Figure 6-22 Twisting angles of the column with and without shear keys

6.7 Summary and conclusions

Previous studies on the seismic performances of segmental column mainly focused on the quasi-static cyclic tests. Limited studies investigated the dynamic behaviours of segmental column subjected to the earthquake motions. In the present study, the dynamic responses of the segmental column under bidirectional earthquake motions are experimentally investigated through shake table tests. For comparison, the behaviours of the conventional monolithic column is also investigated. Moreover, a detail 3D FE model is developed to simulate the behaviours of the segmental column under bidirectional earthquake motions. Multiple shear keys are proposed to mitigate the adverse twisting response, and the effectiveness of the proposed method is examined through numerical simulations. According to the test and numerical results, the following conclusions are drawn:

1. Tensile cracks could widely develop along the traditional monolithic column, while in the segmental column, the main damage pattern was the concrete crushing at the toes of the segments.

2. The fundamental vibration period of the segmental column after repeated seismic excitations varied much less compared to the monolithic column, indicating less damages developed in the segmental column after low to medium level earthquake ground motions. The segmental column failed earlier than the monolithic column due to excessive compressive stress resulting from the posttensioned tendon and rocking of the bottom segment.

3. Segmental column experienced significant twisting under bidirectional earthquake motions. The friction force between the joints was not enough to resist the torsional moment associated with eccentricities induced by the unsymmetrical damages in the segments and the bidirectional earthquake motions.

4. The developed 3D FE model can capture the seismic performances of the segmental column under bidirectional seismic motions including the twisting effect.

5. For the segmental column investigated in the present study, shear keys are effective to reduce the twisting response of the segmental column subjected to the bidirectional earthquake motions. Further study could be carried out to investigate the performance of different types of shear keys.

6.8 References

Acosta, J. G. A. (2011). *Seismic Performance of Circular and Interlocking Spirals RC Bridge Columns under Bidirectional Shake Table Loading*: University of Nevada, Reno.

Billington, S. L., & Yoon, J. (2004). Cyclic response of unbonded posttensioned precast columns with ductile fiber-reinforced concrete. *Journal of Bridge Engineering, 9*(4), 353-363.

Cai, Z.-K., Wang, Z., & Yang, T. Y. (2018). Experimental testing and modeling of precast segmental bridge columns with hybrid normal- and high-strength steel rebars. *Construction and Building Materials, 166*, 945-955. doi:https://doi.org/10.1016/j.conbuildmat.2018.01.159

Chou, C. C., & Chen, Y. C. (2006). Cyclic tests of post-tensioned precast CFT segmental bridge columns with unbonded strands. *Earthquake Engineering & Structural Dynamics, 35*(2), 159-175.

Dawood, H., ElGawady, M., & Hewes, J. (2011). Behavior of segmental precast posttensioned bridge piers under lateral loads. *Journal of Bridge Engineering, 17*(5), 735-746.

Dove, R., & Bennett, J. (1986). *Scale modeling of reinforced concrete category i structures subjected to seismic loading*. Retrieved from

ElGawady, M., Booker, A. J., & Dawood, H. (2010). Seismic behavior of posttensioned concrete-filled fiber tubes. *Journal of Composites for Construction, 14*(5), 616-628.

ElGawady, M., & Sha'lan, A. (2010). Seismic behavior of self-centering precast segmental bridge bents. *Journal of Bridge Engineering, 16*(3), 328-339.

Guo, T., Cao, Z., Xu, Z., & Lu, S. (2015). Cyclic Load Tests on Self-Centering Concrete Pier with External Dissipators and Enhanced Durability. *Journal of Structural Engineering, 142*(1), 04015088.

Hachem, M. M., Moehle, J. P., & Mahin, S. A. (2003). *Performance of circular reinforced concrete bridge columns under bidirectional earthquake loading*: Pacific Earthquake Engineering Research Center.

Hewes, J. T., & Priestley, M. N. (2002). *Seismic design and performance of precast concrete segmental bridge columns* (No. SSRP-2001/25). Retrieved from University of California, San Diego, CA:

Hung, H.-H., Sung, Y.-C., Lin, K.-C., Jiang, C.-R., & Chang, K.-C. (2017). Experimental study and numerical simulation of precast segmental bridge columns with semi-rigid connections. *Engineering Structures, 136*, 12-25.

Ichikawa, S., Matsuzaki, H., Moustafa, A., ElGawady, M. A., & Kawashima, K. (2016). Seismic-Resistant Bridge Columns with Ultrahigh-Performance Concrete Segments. *Journal of Bridge Engineering*, 04016049.

Kitajima, K., Koizumi, T., Akiyama, H., Kanda, M., Nakanishi, M., & Adachi, H. (1992). *Response characteristics of reinforced concrete columns under bi-directional earthquake motions.* Paper presented at the Proc., 10th World Conf. on Earthquake Engineering.

Li, C., Hao, H., & Bi, K. (2017). Numerical study on the seismic performance of precast segmental concrete columns under cyclic loading. *Engineering Structures, 148*, 373-386. doi:https://doi.org/10.1016/j.engstruct.2017.06.062

Li, C., Hao, H., & Bi, K. (2018). Seismic performance of precast concrete-filled circular tube segmental column under biaxial lateral cyclic loadings. *Bulletin of Earthquake Engineering*. doi:10.1007/s10518-018-0443-4

Li, C., Hao, H., Zhang, X., & Bi, K. (2017). Experimental study of precast segmental columns with unbonded tendons under cyclic loading. *Advances in Structural Engineering*, 1369433217717119.

Li, J., Hao, H., & Wu, C. (2017). Numerical study of precast segmental column under blast loads. *Engineering Structures, 134*, 125-137. doi:http://dx.doi.org/10.1016/j.engstruct.2016.12.028

Motaref, S. (2011). *Seismic response of precast bridge columns with energy dissipating joints*: University of Nevada, Reno.

Motaref, S., Saiidi, M. S., & Sanders, D. (2013). Shake table studies of energy-dissipating segmental bridge columns. *Journal of Bridge Engineering, 19*(2), 186-199.

Moustafa, A., & ElGawady, M. A. (2018). Shaking Table Testing of Segmental Hollow-Core FRP-Concrete-Steel Bridge Columns. *Journal of Bridge Engineering, 23*(5), 04018020.

Nikoukalam, M., & Sideris, P. (2017). Resilient Bridge Rocking Columns with Polyurethane Damage-Resistant End Segments and Replaceable Energy-Dissipating Links. *Journal of Bridge Engineering, 22*(10), 04017064.

Ou, Y. C., Chiewanichakorn, M., Aref, A. J., & Lee, G. C. (2007). Seismic performance of segmental precast unbonded posttensioned concrete bridge columns. *Journal of Structural Engineering, 133*(11), 1636-1647.

Ou, Y. C., Tsai, M. S., Chang, K. C., & Lee, G. C. (2010). Cyclic behavior of precast segmental concrete bridge columns with high performance or conventional steel reinforcing bars as energy dissipation bars. *Earthquake Engineering & Structural Dynamics, 39*(11), 1181-1198.

Ou, Y. C., Wang, P. H., Tsai, M. S., Chang, K. C., & Lee, G. C. (2009). Large-scale experimental study of precast segmental unbonded posttensioned concrete bridge columns for seismic regions. *Journal of Structural Engineering, 136*(3), 255-264.

Pitilakis, K., Tsinidis, G., & Karafagka, S. (2017). Analysis of the seismic behavior of classical multi-drum and monolithic columns. *Bulletin of Earthquake Engineering, 15*(12), 5281-5307.

Schoettler, M., Restrepo, J., Guerrini, G., Duck, D., & Carrea, F. (2012). A full-scale, single-column bridge bent tested by shake-table excitation. *Center for Civil Engineering Earthquake Research, Department of Civil Engineering, University of Nevada*.

Simulia, D. S. (2012). Abaqus 6.12 documentation. *Providence, Rhode Island, US.*

Tassios, T. P., & Vintzēleou, E. N. (1987). Concrete-to-concrete friction. *Journal of Structural Engineering, 113*(4), 832-849.

Tazarv, M., & Saiid Saiidi, M. (2015). Low-Damage Precast Columns for Accelerated Bridge Construction in High Seismic Zones. *Journal of Bridge Engineering*, 04015056.

Trono, W., Jen, G., Panagiotou, M., Schoettler, M., & Ostertag, C. P. (2014). Seismic response of a damage-resistant recentering posttensioned-HyFRC bridge column. *Journal of Bridge Engineering*, 04014096.

Varela, S., & Saiidi, M. (2016). Resilient deconstructible columns for accelerated bridge construction in seismically active areas. *Journal of Intelligent Material Systems and Structures*, 1045389X16679285.

Wang, J., Wang, Z., Tang, Y., Liu, T., & Zhang, J. (2018). Cyclic loading test of self-centering precast segmental unbonded posttensioned UHPFRC bridge columns. *Bulletin of Earthquake Engineering*, 1-29.

Wang, Z., Wang, J., Liu, T., & Zhang, J. (2018). An explicit analytical model for seismic performance of an unbonded post-tensioned precast segmental rocking hollow pier. *Engineering Structures, 161*, 176-191.

Yamashita, R., & Sanders, D. H. (2009). Seismic performance of precast unbonded prestressed concrete columns. *ACI Structural Journal, 106*(06).

Yang, C., & Okumus, P. (2017). Ultrahigh-Performance Concrete for Posttensioned Precast Bridge Piers for Seismic Resilience. *Journal of Structural Engineering, 143*(12), 04017161.

Zhang, X., Hao, H., & Li, C. (2016). The effect of concrete shear key on the performance of segmental columns subjected to impact loading. *Advances in Structural Engineering*, 1369433216650210.

Zhao, L., Bi, K., Hao, H., & Li, X. (2017). Numerical studies on the seismic responses of bridge structures with precast segmental columns. *Engineering Structures, 151*, 568-583. doi:https://doi.org/10.1016/j.engstruct.2017.08.018

Zhao, L., Hao, H., Bi, K., & Li, X. (2018). Numerical Study of the Seismic Responses of Precast Segmental Column Bridge under Spatially Varying Ground Motions. *Journal of Bridge Engineering, 23*(12). doi:10.1061/(asce)be.1943-5592.0001319

CHAPTER 7 CONCLUSIONS AND RECOMMENDATIONS

7.1 Main findings

The thesis has investigated the seismic performance of precast posttensioned segmental column. Quasi-static cyclic tests were conducted to evaluate the performances of monolithic and segmental columns. In addition, to improve the seismic performance of the segmental column, BFRP was used to mitigate the damage of the concrete segments and TEED devices were used to increase the energy dissipation capacity of the segmental column. Moreover, detailed 3D numerical model of the segmental columns were developed. Systematical parametric studies were carried out to assess the effects of different design configurations on the seismic performance of such columns. Furthermore, the performance of the segmental column under biaxial cyclic loading was also studied and compared with that of the column subjected to the uniaxial cyclic loading through numerical simulation. Finally, shake table tests on the monolithic and segmental columns were conducted. Bidirectional seismic excitations were used as inputs. The main findings from these works are summarized below.

Quasi-static performance of monolithic and segmental columns

The performance of the traditional monolithic column and the segmental columns under cyclic loading are investigated through quasi-static tests. One monolithic column and five segmental columns with different designs have been tested. It is found that the damages of the monolithic column are the concrete crushing, concrete flexural cracks, and fracture of longitudinal reinforcements. In contrast, the damages of the segmental columns are the concrete spalling and crushing due to the excessive compressive stress caused by the rocking between the segments. Moreover, the segmental columns show better ductility and smaller residual drift, but less energy dissipation capacity compared with the monolithic column. The use of ED bars between the joints of the segments is found effective in increasing the energy dissipation capacity of the segmental column. The number of segments has limited influence on the performance of the segmental column. The shear keys between the segments is found effective in increasing the shear resistance and reduce the relative slip between the segments, but they also cause stress concentration around the concrete shear key, resulting in more severe damages in the segments.

Effectiveness of using BFRP and TEED devices

The BFRP is used to wrap the segments to mitigate the damages of the segments and the TEED device is proposed and used to increase the energy dissipation capacity of the segmental column and minimize the residual displacement of the column. The combination of these two methods aims to improve the seismic performance of the precast segmental column. The use of BFRP is found to be effective to prevent the concrete compressive failure such as spalling and crushing damages. No visible damages can be observed in the columns with BFRP wrap. The newly proposed TEED device can increase the energy dissipation capacity of the segmental column. Due to the special design, buckling is prevented, the design therefore ensures full functionality of the TEED for energy dissipation. Furthermore, the design does not prevent the segmental column to recover the deformation although TEED experiences plastic deformation, therefore the residual displacement of the column with TEED is small.

Influences of different design details on the seismic performance of segmental columns

Detailed 3D none-linear FE models are developed for the segmental columns. The modelling results are validated against the test results and it is found that the model can capture the response of the segmental column in terms of damage mode and hysteretic curves. Parametric studies on the seismic performance of the segmental column under cyclic loading are conducted based on the validated models. It is found that the bonding condition significantly affects the behaviour of the segmental column. The bonded tendon causes stress concentration in the tendon and reduces the ductility of the column. The column with higher axial force has higher strength and energy dissipation capacity but lower ductility compared to the column with lower axial force. In addition, the confinement to the bottom segment significantly influences the strength, energy dissipation capacity and ductility of the column. Moreover, though the use of internal ED bars can increase the energy dissipation capacity of the segmental column, it also results in the increase of the residual drift. The use of SMA can increase the energy dissipation of the segmental column and keep the residual displacement small due to the advanced mechanical properties of the SMA.

Biaxial performance of segmental columns

The biaxial cyclic performance of the segmental column is investigated. Six different biaxial lateral cyclic loading paths are used to investigate the effect of load path on the performance of the segmental column. It is found that the loading paths have obvious influences on the biaxial performance of the segmental column. In addition, the coupling effects of the biaxial loading result in more strength degradation as well as larger residual drift in the column subjected to biaxial loadings than those under uniaxial loading. Moreover, different loading path results in different amount of energy dissipation. The column under the circular shaped loading path dissipates the largest amount of energy compared with the column under other five loading paths. Furthermore, it is also found that increasing the axial loading ratio decreases the ductility of the segmental column subjected to both uniaxial and biaxial cyclic loadings, and this effect is more pronounced on the column under biaxial cyclic loadings.

Shake table studies of monolithic and segmental column under bidirectional excitations

Shake table tests on the monolithic and segmental column are carried out to investigate the dynamic responses of the two columns. Different from previous shake table tests on the segmental columns, bidirectional seismic excitations are used as inputs to more realistically represent the real earthquake excitations in this study. It is found that the segmental column show less increase in fundamental vibration period than the monolithic column after repeated seismic excitations, indicating less damages developed in the segmental column after low to medium level excitations. In addition, it is interesting to find that the segmental column experiences obvious twisting under bidirectional earthquake motions while almost no twisting is found in the monolithic column. It indicates that the friction between the segments is not enough to resist the torsional moment induced by the damages in the segments and bidirectional excitations. Furthermore, the developed numerical model is able to capture the displacement responses as well as the twisting behaviour of the segmental column. According to the numerical simulation, the proposed multiple shear keys between the segments are effective to reduce the twisting response of the segmental column.

7.2 Recommendations for future works

Extensive experimental studies and numerical simulations have been carried out in this research to investigate the seismic performance of the precast segmental columns. Further studies that are needed for effective applications of the segmental columns in constructions to resist earthquake ground motions are identified. The following are some of the possible further research topics:

1. Small scale experimental tests are conducted to investigate the seismic performance of the precast segmental columns. Some design details such as the connections at the joints, which are critical for prefabricated construction, are not considered due to the small size of the columns. Further study with larger scale columns can take the connection details into consideration.

2. The influences of different design factors on the seismic performance of the precast segmental column are investigated through comprehensive numerical studies, simplified design procedures is needed to allow engineers to design the segmental column.

3. The biaxial performance of the precast segmental column is investigated in this study through numerical simulations. More experiments are required to further understand the performance of the segmental column under biaxial loading since such kind of test on the segmental column is not available in the literature yet. Moreover, different design factors such as shape of the cross section which can affect the biaxial performance of the column need to be considered in future tests.

4. Residual twisting is observed in the segmental column when it is subjected to bidirectional seismic excitations. Multiple shear keys are proposed to mitigate such twisting through numerical simulations. Experimental tests are necessary to examine such design in the future study.

5. The shake table test on the dynamic performance of the segmental column is conducted by idealizing the superstructures as a mass block on the top of the column. The interaction between the column and the superstructure need to be considered in future studies. The testing of a whole bridge system with precast segmental columns is suggested.

BIBLIOGRAPHY DISCLAIMER

Every reasonable effort has been made to acknowledge the owners of copyright material. I would be pleased to hear from any copyright owner who has been omitted or incorrectly acknowledged.

APPENDIX I

STATEMENTS OF THE CO-AUTHORS

To Whom It May Concern

I, Chao Li, contributed (conducted the experimental study with help of the co-authors and wrote the manuscript which was revised and edited by the co-authors) to the paper/publication entitled (Experimental study of precast segmental columns with unbonded tendons under cyclic loading).

(Chao Li)

I, as a Co-Author, endorse that this level of contribution by the candidate indicated above is appropriate.

(Prof. Hong Hao) ( )

(Dr. Xihong Zhang) ( )

(Dr. Kaiming Bi) ( )

To Whom It May Concern

I, Chao Li, contributed (conducted the experimental study with help of the co-authors and wrote the manuscript which was revised and edited by the co-authors) to the paper/publication entitled (Cyclic test and numerical study of precast segmental concrete columns with BFRP and TEED).

(Chao Li)

I, as a Co-Author, endorse that this level of contribution by the candidate indicated above is appropriate.

(Prof. Hong Hao) ( )

(Dr. Kaiming Bi) ( )

(Dr. Xihong Zhang) ( )

(Mr. Do Van Tin) ( )

To Whom It May Concern

I, Chao Li, contributed (conducted the numerical investigation, experimental tests with help of the co-authors and then wrote the manuscripts which were further revised and edited by the co-authors) to the paper/publications entitled:

1. Numerical study on the seismic performance of precast segmental concrete columns under cyclic loading
2. Seismic performance of precast concrete-filled circular tube segmental column under biaxial lateral cyclic loadings
3. Seismic performances of precast segmental column under bidirectional earthquake motions: shake table test and numerical evaluation

(Chao Li)

I, as a Co-Author, endorse that this level of contribution by the candidate indicated above is appropriate.

(Prof. Hong Hao) (_____)

(Dr. Kaiming Bi) (_____)

APPENDIX II

COPYRIGHT CLEARANCE

The proof of the rights, granted by publisher for the publication that forms the chapters of this thesis, to reproduce the contribution in the thesis are attached below.

Copyright Clearance Center RightsLink®

Home | Create Account | Help | LIVE CHAT

SAGE Publishing

Title: Experimental study of precast segmental columns with unbonded tendons under cyclic loading

Author: Chao Li, Hong Hao, Xihong Zhang, et al

Publication: Advances in Structural Engineering

Publisher: SAGE Publications

Date: 02/01/2018

Copyright © 2018, © SAGE Publications

LOGIN

If you're a copyright.com user, you can login to RightsLink using your copyright.com credentials.

Already **a RightsLink user** or want to learn more?

If you are a SAGE journal author requesting permission to reuse material from your journal article, please note you may be able to reuse your content without requiring permission from SAGE. Please review SAGE's author re-use and archiving policies at https://us.sagepub.com/en-us/nam/journal-author-archiving-policies-and-re-use for more information.

If your request does not fall within SAGE's reuse guidelines, please proceed with submitting your request by selecting one of the other reuse categories that describes your use. Please note, a fee may be charged for reuse of content requiring permission. Please contact permissions@sagepub.co.uk if you have questions.

BACK | CLOSE WINDOW

Copyright © 2019 Copyright Clearance Center, Inc. All Rights Reserved. Privacy statement. Terms and Conditions.
Comments? We would like to hear from you. E-mail us at customercare@copyright.com

SPRINGER NATURE LICENSE
TERMS AND CONDITIONS

Jun 11, 2019

This Agreement between 178 Thelma st. como ("You") and Springer Nature ("Springer Nature") consists of your license details and the terms and conditions provided by Springer Nature and Copyright Clearance Center.

License Number	4605751494753
License date	Jun 11, 2019
Licensed Content Publisher	Springer Nature
Licensed Content Publication	Bulletin of Earthquake Engineering
Licensed Content Title	Cyclic test and numerical study of precast segmental concrete columns with BFRP and TEED
Licensed Content Author	Chao Li, Kaiming Bi, Hong Hao et al
Licensed Content Date	Jan 1, 2019
Licensed Content Volume	17
Licensed Content Issue	6
Type of Use	Thesis/Dissertation
Requestor type	academic/university or research institute
Format	print and electronic
Portion	full article/chapter
Will you be translating?	no
Circulation/distribution	501 to 1000
Author of this Springer Nature content	yes
Title	Mr. Chao Li
Institution name	Curtin University
Expected presentation date	Jun 2019
Requestor Location	178 Thelma st. como 178 Thelma st. como, WA 6152 Australia Attn: 178 Thelma st. como
Total	0.00 USD

Copyright Clearance Center RightsLink®

Home | Create Account | Help

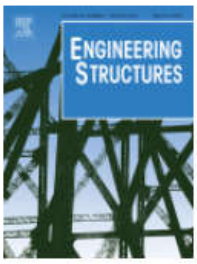

Title: Numerical study on the seismic performance of precast segmental concrete columns under cyclic loading

Author: Chao Li,Hong Hao,Kaiming Bi

Publication: Engineering Structures

Publisher: Elsevier

Date: 1 October 2017

© 2017 Elsevier Ltd. All rights reserved.

LOGIN

If you're a copyright.com user, you can login to RightsLink using your copyright.com credentials.

Already **a RightsLink user** or want to learn more?

Please note that, as the author of this Elsevier article, you retain the right to include it in a thesis or dissertation, provided it is not published commercially. Permission is not required, but please ensure that you reference the journal as the original source. For more information on this and on your other retained rights, please visit: https://www.elsevier.com/about/our-business/policies/copyright#Author-rights

BACK | CLOSE WINDOW

Copyright © 2019 Copyright Clearance Center, Inc. All Rights Reserved. Privacy statement. Terms and Conditions.
Comments? We would like to hear from you. E-mail us at customercare@copyright.com

SPRINGER NATURE LICENSE
TERMS AND CONDITIONS

Nov 01, 2018

This Agreement between 178 Thelma st. como ("You") and Springer Nature ("Springer Nature") consists of your license details and the terms and conditions provided by Springer Nature and Copyright Clearance Center.

License Number	4460130128483
License date	Nov 01, 2018
Licensed Content Publisher	Springer Nature
Licensed Content Publication	Bulletin of Earthquake Engineering
Licensed Content Title	Seismic performance of precast concrete-filled circular tube segmental column under biaxial lateral cyclic loadings
Licensed Content Author	Chao Li, Hong Hao, Kaiming Bi
Licensed Content Date	Jan 1, 2018
Type of Use	Thesis/Dissertation
Requestor type	non-commercial (non-profit)
Format	print and electronic
Portion	full article/chapter
Will you be translating?	no
Circulation/distribution	501 to 1000
Author of this Springer Nature content	yes
Title	Mr. Chao Li
Institution name	Curtin University
Expected presentation date	Jan 2019
Order reference number	18078147
Requestor Location	178 Thelma st. como 178 Thelma st. como, WA 6152 Australia Attn: 178 Thelma st. como
Billing Type	Invoice
Billing Address	178 Thelma st. como 178 Thelma st. como, Australia 6152 Attn: 178 Thelma st. como
Total	0.00 USD

Copyright Clearance Center RightsLink®

Home | Create Account | Help

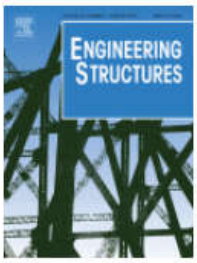

Title: Seismic performances of precast segmental column under bidirectional earthquake motions: Shake table test and numerical evaluation

Author: Chao Li,Kaiming Bi,Hong Hao

Publication: Engineering Structures

Publisher: Elsevier

Date: 15 May 2019

© 2019 Elsevier Ltd. All rights reserved.

LOGIN

If you're a copyright.com user, you can login to RightsLink using your copyright.com credentials.

Already **a RightsLink user** or want to learn more?

Please note that, as the author of this Elsevier article, you retain the right to include it in a thesis or dissertation, provided it is not published commercially. Permission is not required, but please ensure that you reference the journal as the original source. For more information on this and on your other retained rights, please visit: https://www.elsevier.com/about/our-business/policies/copyright#Author-rights

BACK | CLOSE WINDOW

Copyright © 2019 Copyright Clearance Center, Inc. All Rights Reserved. Privacy statement. Terms and Conditions.
Comments? We would like to hear from you. E-mail us at customercare@copyright.com